A geometry independent integrated method to predict erosion wear rates in a slurry environment

Abinesh Balasubramaniam Gnanavelu

Submitted in accordance with the requirements for the degree of
for the degree of Doctor of Philosophy

The University of Leeds
School of Mechanical Engineering

December 2010

The candidate confirms that the work submitted is his own, except where work which has formed part of jointly-authored publications has been included. The contribution of the candidate and the other authors to this work has been explicitly indicated below. The candidate confirms that appropriate credit has been given within the thesis where reference has been made to the work of others.

Sections 5.4, 6.1.3, 7.2, 7.3 and 7.4 contain work published in:

Gnanavelu, A., N. Kapur, A. Neville, and J.F. Flores, **An integrated methodology for predicting material wear rates due to erosion.** *Wear, 2009. 267(11): p. 1935-1944.* Attached in appendix A.

Sections 8.2 and 8.3 contain work submitted for publication in:

A. Gnanavelu, N. Kapur, A. Neville, J. F. Flores, N. Ghorbani, **A numerical investigation of a geometry independent integrated method to predict erosion rates in slurry erosion,** *submitted to the journal of wear and currently under review.* Attached in appendix B.

All the work in both the papers mentioned above is a contribution of the candidate, under the supervision of the co-authors.

Acknowledgements

Abstract

Material wear due to erosion-corrosion in slurry transport equipment is prevalent in process industries such as the oilsands industry. Damage to equipment can cost a typical oilsands industry nearly £200 million annually, along with an associated health and safety risk to man and environment [6]. New materials are continuously developed in order to endure wear under adverse erosion-corrosion conditions better and laboratory testing offers a good option to test new materials prior to commission. Traditionally the performance of a set of new materials are assessed based on their overall wear behavior in a laboratory test and is ranked accordingly, with the best performing material generally used for application. However, due to differences in prevailing conditions on the material surface and geometrical variations between actual and test geometry, accurately correlating data from a laboratory test to field scenario can be highly complex. Also the ranking system is not capable of predicting wear profiles for specific conditions and hence a new wear prediction method was developed and is presented in this thesis.

This method has been developed, using a combination of standard laboratory based experiments and Computational Fluid Dynamic (CFD) simulations. As a starting point only wear due to erosion is considered and this thesis provides validation of such an approach. The method involves two stages in which (i) a universal wear map is generated for the material and abrasive combination in question using a standard laboratory test (jet impingement test) to generate a wear scar on a simple geometry. The local wear rate from this is interpreted using a CFD simulation of the test to generate a map giving local wear as a function of particle impact velocity and angle; (ii) a CFD solution is calculated for a series of different erosion configurations giving the particle impact data at each point on the surface. The wear map from the first stage is then used to give the local wear rate. The power of this method is that once a material-specific map has been generated then wear on any geometry can be calculated through the simulation of flow using CFD. As validation of this, wear on a typical plant geometry (1.5D 90° elbow bend) is undertaken and the general applicability of this method is demonstrated.

Contents

Figures

Tables

Notation

E_0	Mass loss due to pure erosion component
C_0	Mass loss due to pure corrosion component
ΔE_C	Corrosion enhanced erosion loss component
ΔC_E	Erosion enhanced corrosion loss component
η	Fluid Dynamic Viscosity (Pa-s)
ρ_f	Fluid density (kg/m^3)
F_s	Shape/angularity factor
d_p	Particle Diameter (μm)
ρ_p	Particle density (kg/m^3)
H_p	Particle hardness (kgf/mm^2)
N_p	Number of impact
V_p	Particle impact velocity (m/s)
θ	Particle impact angle (degree)
E	Material strength (Mpa)
H	Material hardness (kgf/mm^2)
V_f	Local fluid velocity (m/s)
C_d	Drag co-efficient
A	Frontal area (mm^2)
F_d	Drag force (N)
Re_p	Particle Reynolds number
$\ddot{a}_p$	Acceleration of a particle (m/s^2)
F_p	Force required to accelerate a particle (N)
m_p	Particle mass (kg)
E_R	Erosion loss due to a single particle impact (kg)

$\vec{V_f}$	Characteristic mean fluid velocity (m/s)
$\vec{L}$	Characteristic length scale (m)
λ, S_t	Momentum equilibrium constant
Q_p	Volume of material removed per particle impact (mm^3)
P	Material plastic flow stress constant
κ	Ratio of vertical to horizontal force component on a particle
Ψ	Ratio of the depth of contact to depth of cut
Q_t	Volume of material removed for a specific quantity of abrasive mass (mm^3)
V_n	Normal velocity component below no erosion occurs (m/s)
A, n, x, y, z, β	Material constants
$K_{1,2,3}, C_{1,2,3}, \alpha,$	Experimental constants
a, b, c, d, e, f	Numerical coefficients
$\emptyset$	Cutting wear factor
δ	Deformation wear factor
θ_{p0}	Impact angle at which the horizontal velocity is zero (degree)
E_d	Volume loss due to deformation mechanism
E_{c1}, E_{c2}	Volume loss due to cutting mechanism
ϵ, γ	Energy required to remove unit mass of material due to primary erosion and secondary erosion processes respectively (N)
V_0	Impact velocity below which no erosion takes place (m/s)
d_0	Particle diameter below which no erosion takes place (mm)
F	Degree of fragmentation
E_B and σ_B	Stiffness, hardness and of the material surface (MPa)
ε_B	Elongation of the test material (mm)

B	Stiffness ratio of target to erodent materials
R_t	Co-efficient of restitution or restitution factor
δv	Finite volume of a fluid particle (mm^3)
$\delta x, \delta y$ and δz	Finite lengths of each side of a cubic fluid particle (mm)
u, v and w	Normal flow velocities in the x, y and z directions (m/s)
τ	Viscous shear stress (MPa)
P	Pressure on the fluid element (Pa)
Re	Reynolds number of a fluid regime
$\bar{u}$	Steady mean component of the local flow velocity (m/s)
$u'(t)$	Fluctuating or turbulent component of the local flow velocity (m/s)
k	Turbulent kinetic energy (m^2/s^2)
η_t	Turbulent or eddy viscosity (m^2/s)
l_m	Turbulent mixing length (m)
τ_w	Turbulent wall shear stress (MPa)
r_p and r_f	Volume fraction of particle and fluid phases respectively
F_p	Pressure on a particle due to existing pressure gradient (Pa)
F_b	Force due to buoyancy of the fluid medium on a particle (Pa)
F_a	Added/Virtual force required by the particle to overcome (Pa)
τ_p and τ_f	Particle and fluid response times respectively (s)
g	Acceleration due to gravity (m/s^2)
h	Radial distance from the inner surface of the bend (m)
D	Inner diameter of the pipe cross-section (m)
r	Quoted radius of curvature (m)
r_o and r_i	Outer and inner radius of curvature respectively (m)

Abbreviations

AFS	American foundry society
Al_2O_3	Aluminium oxide
CFD	Computational fluid dynamic
CP	Cathodic protection
JIT	Jet impingement test
LHS	Left hand side
MSDM	Micro scale dynamic model
NG	Neilson and Gilchrist
NS	Navier-Stokes
PIV	Particle image velocimetry
RANS	Reynolds averaged Navier-Stokes
Re	Reynolds number
RHS	Right hand side
RKE	Realizable K-ε equation
RNG	Renormalization group
RSM	Reynolds stress model
SAE	Society of automotive engineers
SEM	Scanning electron microscope
SiC	Silicon carbide
SiO2	Silicon dioxide
SKE	Standard K-ε equation
TWL	Total weight loss
UNS	Unified numbering system

Chapter 1

Introduction

1.1 Oilsands industry and the extraction process

Utilization of conventional oil sources across the World has led to diminished resource levels. This coupled with increasing oil prices and technological advancements has led to a surge in the demand for crude oil production from oilsand deposits which, as on August 2006, was estimated to comprise 30% of the total World Oil reserves [1]. Oilsands typically consist of around 10% bitumen (a semi solid form of crude oil) 83% Silica sand and 7% of mineral rich clays and water. Bitumen in its raw state is a sticky, tar-like form of petroleum which when processed can be upgraded to produce commercial synthetic crude oil [2]. Oilsand deposits are shallow but huge and spread over several thousand square kilometres, especially in parts of Canada. It is usually covered by overburden (plant deposits, clay and barren sand) which are less than 50m by depth in most of the regions, making surface mining the most efficient method of extraction. Several industries mine the oilsands deposits and the world's largest producers of crude oil from oilsands are Syncrude Canada Limited. It requires approximately 2000 kilograms of oilsands to recover a barrel of oil and in 2008 Syncrude Ltd. reportedly produced 290,000 barrels of oil every day, accounting for more than half a million tonnes of mined oilsands [3].

Oilsands at Syncrude Ltd. are recovered by mining involving truck and shovel operations and a simple representation of the entire process is shown in Figure 1.1. Large amounts of oilsands are mined from the surface and hauled to crushing stations where an average sand size distribution is obtained. A slurry is then formed by mixing the oil sand with hot water and caustic soda, which is then conveyed using a hydro-transport system to

extraction facilities where bitumen and sand particles are separated. A vibrating impact screen is used to filter any large particles or boulders present in the slurry. Extracted bitumen is transferred to refineries and redundant sand particles from the extraction facilities are transported to storage (tailings) deposits using hydro-transport facilities.
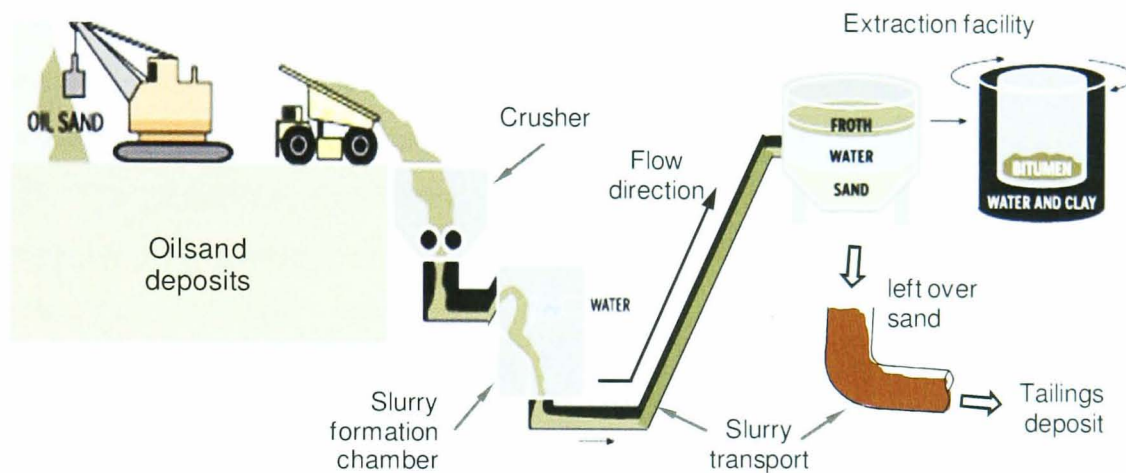
Figure 1.1 A typical oilsand extraction process using surface mining techniques and hydro-transport equipment [2]. This figure is only a schematic and hence the geometry and the orientation of the hydro-transport system is not of accurate representation.

The hydro-transport system provides an economic means to transport oilsands for processing and is mainly made up of a network of pipelines spanning kilometres in length, pumps, valves, joints and bends, etc. However, the adverse conditions encountered in the process has had detrimental effects on material integrity of the equipment involved [4, 5] and has cost the largest oilsands extractor nearly £200 million annually, along with an associated health and safety risk to man and environment [6]. A consortium of material degradation mechanisms can prevail within the equipment involved [7] and are discussed in subsequent sections.

1.2 Wear mechanisms in hydro-transport equipment

Transportation of large quantities of Oilsand results in higher production of oil and hence Oilsand slurries are highly concentrated with sand particles, usually greater than 35% by weight (defined as the total weight of sand particles to total weight of fluid) and the average size of a particle is generally between 0.18 to 0.3 mm. The solid suspension is transported at reasonably high velocities (3.5 to 5.5 m/s) for good productivity and also to prevent particles from settling along the base of the pipelines [8, 9] and also at high temperatures to reduce the effects of viscous drag on pipe walls [7, 10]. The prevailing conditions, however, offer a very good foundation for material degradation to occur which is primarily due to the mechanical interaction between sand and the inner surface of an equipment and corrosive attack due to thermodynamic imbalance [6, 11, 12].

Material loss due to sand particle/wall interactions can be broadly grouped into two main categories, wear due to sliding/rolling action of the particles or wear due to particle impacts. At certain conditions (low bulk flow velocity) particles tend to settle along the length of a pipeline base forming a bed of sand particles moving at low velocities (a fraction of the mean flow velocity) recreating a wear process equivalent to three body abrasion known as sliding or rolling wear [7, 13, 14]. Under certain conditions (non settling conditions), sand particle motion within the flowing fluid is significantly influenced by the local hydrodynamics. The combination of high particle velocities and diameters prompts the particles to cross fluid streamlines and collide with the inner wall surfaces leading to material loss due to particle impact, and this effect is predominant when an obstruction or any geometrical variation is encountered in flow [15, 16]. This variation can be due to the presence of either flow measurement, control or directional devices such as orifices, venturi-meters, valves, T-bends, U-bends, joints, elbows, etc. and the consequences are shown in Figure 1.2.

The presence of oxygen in the slurry renders it corrosive to several plant equipment materials leading to material loss which is further enhanced due to high temperatures and the flow dynamics. The effect of corrosion can be intensified by particle impacts leading to greater damage and this

phenomenon is known as erosion-corrosion synergy [6, 17-20]. Conversely, corrosion can influence the kinetics of local erosion damage as reported by Li et al [21].
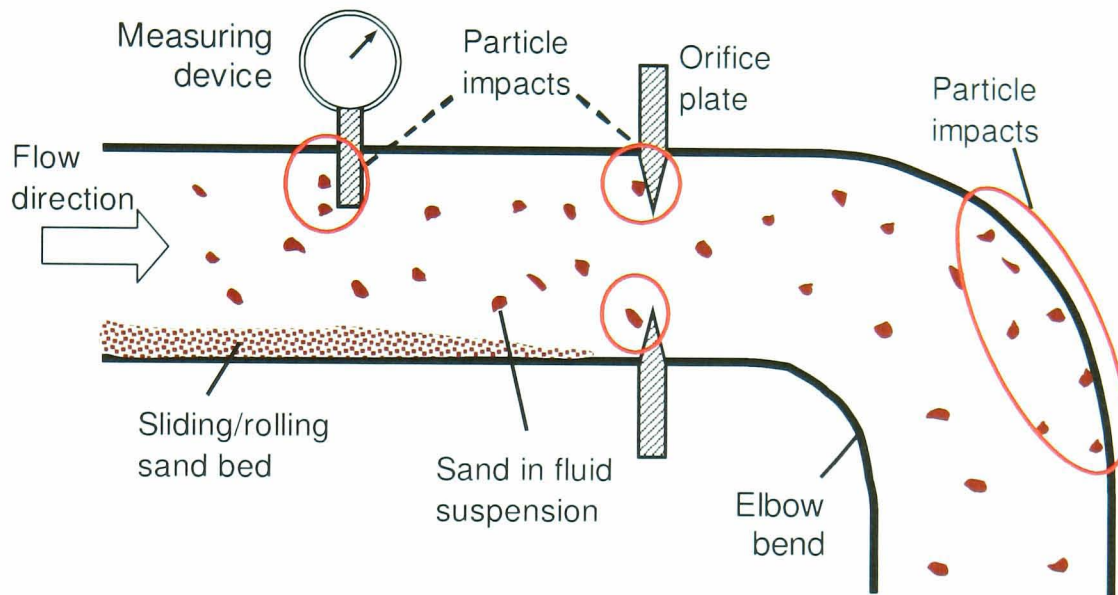
Figure 1.2 A schematic of a pipeline used in slurry transportation indicating sand particle impacting flow devices and the inner wall.

Figure 1.3 shows the photographs of a damaged centrifugal pump and a pipe bend after three months into service in an oilsand industry and the cause of failure was attributed mainly to erosion-corrosion which suggests the severity of the problem [22]. Erosion by impact, corrosion, erosion-corrosion synergistic effects and sliding/rolling wear are all influenced by the prevailing local conditions and under suitable conditions, it is possible that all the these mechanisms can exist at a certain cross-section in an equipment [15, 23]. Thus it is vital to understand the prevailing conditions which lead to wear in order to prevent or minimise the negative effects of wear processes on material integrity and these prevailing conditions are discussed within the framework of this work in chapter 2.
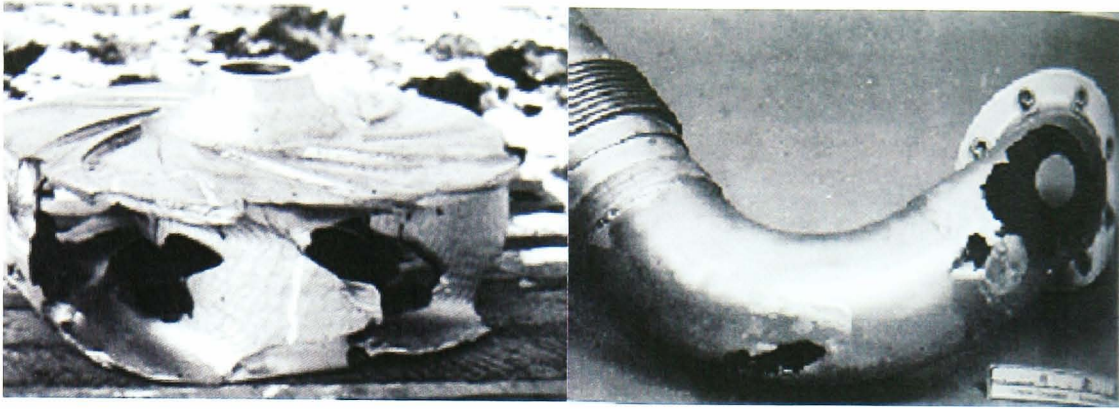
Figure 1.3 A slurry pump component and an u-bend from a pipeline after three months in service in an oilsand industry [2].

1.3 Material selection in the oilsand industry

Extensive research has been conducted to minimise material damage and several methods are currently been implemented. Controlling the operational conditions and redesigning the plant layout offers opportunities to reduce material wear losses, however, the extent of these measures are limited. Another approach is to develop and implement advanced materials with greater endurance to adverse conditions and this has revolutionised modern day material design and development [24-26].

The average operating conditions, flow rates in particular, within the entire plant equipment might remain uniform across a section; however variations in local flow conditions are extensive due to the changes in equipment size and functionality. This presents a complex scenario of the occurrence of any wear mechanisms previously stated [23] and the material commissioned for application should be capable of enduring wear due to these mechanisms by sustaining its integrity. A combination of high values of material properties such as strength, abrasion wear resistance, toughness, anti-corrosion behaviour, hardness, etc. are basic necessities for a service material. However, a material having high values of all these properties has yet to be developed and there has always been trade-offs between various properties during material development. Researchers and industrialists historically have preferred the approach of manipulating the properties of

materials by modifying the constituent elements to provide for its operational needs and hence the standard for material design is set by the local conditions which dictate material degradation modes [27, 28].

Prior to implementation, newly designed materials are required to be tested under a controlled environment simulating actual plant conditions. Full scale testing offers an ideal opportunity due to its ability to closely reproduce actual plant conditions and to undertake material testing, however, this option is rarely adopted due to its practical and economic constraints. Laboratory based experiments provide an economical and time efficient opportunity to reproduce these conditions under a controlled environment to test and analyse newly developed materials. Several laboratory based experiments are being used today and the common most laboratory tests and the conditions reproduced during these tests are discussed in chapter 2.

1.4 Laboratory conditions and plant equipment

Laboratory tests are accelerated wear tests performed on materials under a controlled environment to provide sufficient wear data for a range of operating conditions. The challenge during laboratory testing is to recreate local conditions similar to prevailing conditions in plant equipment and be able to accurately interpret laboratory test wear data to predict actual material loss. It has been reported that materials behaved quantitatively differently during field trails in comparison with results obtained from laboratory tests. Tests are generally conducted at operating conditions similar to field but recreation of local plant conditions at the surface of the test specimen has proven not to be straightforward [29]. This has been mainly attributed to geometrical variations between laboratory and slurry transport equipment. Dimensional ratios of plant geometry to test geometry are generally greater than ten and merely scaling the results does not truly represent actual damage.

It was mentioned previously that geometrical changes can affect flow dynamics influencing transport of sand particle and corrosive species within a specific geometry. To illustrate this, particle motion (indicated by line-

arrows) as predicted by computational methods (described later), within three geometries of different size and shapes for similar bulk operating conditions (bulk flow velocities, particle and fluid properties, temperature, etc.) are shown in Figure 1.4. All the geometries illustrated in Figure 1.4 are simplified 2-D representation of actual 3-D plant geometry. The angle subtended by the particle trajectory prior to impact with the inner wall is defined as the local impact angle and particles on impact are assumed to transfer almost all their energy instigating damage (each line represents a particle motion path-those that end at the surface indicate impact) and for simplicity particle rebound action are not indicated.
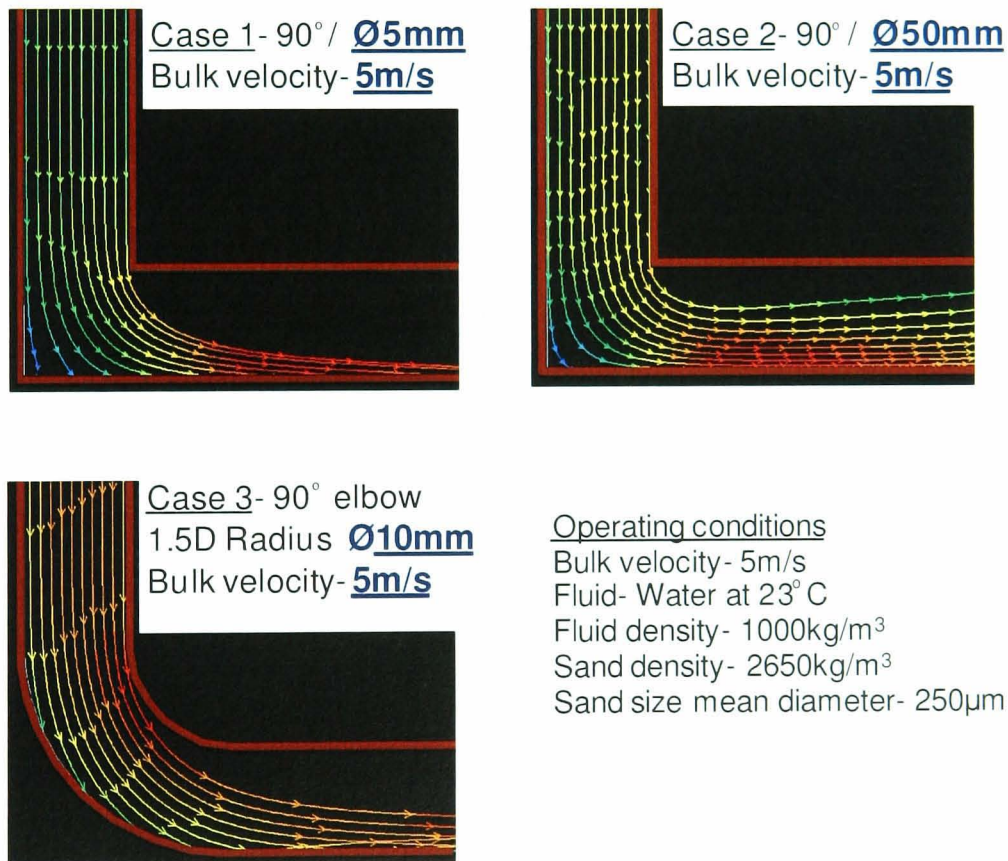
Figure 1.4 Line arrows indicate particle motion within three flow geometries (either of different size or shape) as predicted using CFD (Computational fluid dynamic) methods. All geometries are 3-dimensional but only a cross-section is represented here and also note the figure is not to scale.

Visual observation of particle motion close to the inner wall for all cases suggests that impacts occur at a wide range of angles and the three cases can be categorised as,

Case 1: High to very low angles (70° to 10°),

Case 2: Predominantly sliding angles (<10°),

Case 3: Medium to low angles (10° to 30°).

Levy [12, 27] and Tilly [30] conducted erosion experiments on various materials to study the influence of impact angle on erosion wear and confirmed that impact angles directly affect wear rates depending on the nature of the material, with materials ductile in nature wearing significantly at angles between 15-30° and brittle material wear peaking at angles greater than 70°. As demonstrated by Figure 1.4, for similar bulk operating conditions changes in geometrical shape and size affect local impact dynamics and this change is brought about by different local hydrodynamic regimes prevailing in all the three cases. Changes in hydrodynamic conditions also influence corrosion by affecting the transport of fresh corrosive species to the surface and removal of corrosion products. Efird et al. [31] pointed out that corrosion rates are significantly higher when the diffusion boundary layers are destroyed due to local flow disturbances though mean steady state hydrodynamics prevail. It was suggested that laboratory equipment should accurately recreate local diffusion boundary layer disturbances to accurately analyse corrosion [23, 32].

Consequently the behaviour of a material under laboratory-based experiments can be entirely different to its performance in field trials if the local conditions influenced by mean flow conditions vary between the two and hence the complication in predicting absolute wear rates in service equipment. Thus prediction methods should be independent of the influence of geometrical variations between plant and laboratory and the ultimate aim of the research is to be able to accurately predict material durability in aggressive slurries where the damage mechanism is primarily erosion-corrosion and to optimise material selection through provision of a selection

tool developed based on experimental and theoretical calculations (numerical methods).

1.5 Prediction of erosion-corrosion material loss

Material performance has been analysed by several researchers using various methodology and a brief overview of which is provided in this section. Traditionally experimental techniques were followed and wear data from standardised bench tests has been interpreted to predict erosion-corrosion wear loss in field applications. Theoretical prediction methods were sought after to minimise the cost of testing and to advance the knowledge of wear mechanism. In 1960, Finnie [33] developed breakthrough erosion wear models for metals based on classical metal cutting theories and validated these models using controlled laboratory experiments. These models were further evolved and modified by various researchers to accurately capture various intricate wear processes supplemented by laboratory testing [30, 34, 35]. With advancements in technology and computational power resulting in better mathematical understanding of the importance of hydrodynamics on erosion-corrosion, Computational Fluid Dynamic (CFD) methods are gaining popularity in this field. Brown et al. [36] and Wang et al. [37] used CFD methods to predict the location of maximum erosive wear in plant geometry. Similarly Nesic [38] and Bozzini et al. [39] used CFD to determine the cause of local corrosion attack in a heat exchanger due to flow disturbances and successfully improved the design to minimise corrosion. Roco [7] and Tian et al. [40] used flow modelling equations to correlate laboratory wear data to predict wear loss in hydrotransport equipment. Whereas Shook et al. [41] and Wang et al. [42] improved prediction methodology by combining numerical models and CFD simulations to predict quantitative material loss with reasonable accuracies.

Predicting erosion-corrosion wear presents a complex task considering the enormity of parameters involved as suggested by Pulson [23] and constant fluctuations in operating conditions as reported by Schaan [43] and hence substantial research in this subject area is still fundamentally based

on laboratory testing. However, with improvements in mathematical understanding of erosion-corrosion, increasing testing costs and wear predictions based on laboratory tests still not entirely representative of field conditions, modelling techniques have gained impetus in the last decade and this forms an integral part of the wear prediction methodology presented in this thesis.

1.6 Research methodology

The deliverables of this research form part of an integral programme to develop a robust methodology to be able to accurately predict absolute wear rates as a function of time and position in plant equipment under the action of aggressive slurries. Although wear in hydro-transport equipment can be due to various mechanical and chemical processes, the focus here is on wear due to impact alone. It is proposed that this method could potentially be advanced to include the effects of corrosion in the future. The foundation of this work will be on developing a methodology to extract a wide range of erosion parameters from a minimum set of experiment and correlate these to field conditions in a way in which computational models can be used to predict erosion wear on more complex geometries. This involves two key stages to build a material specific wear map using a combination of standard experimentation and CFD. The objective is to generate a wear map that is universal for a specific material and sand combination; once generated, actual wear in complex geometry of that material eroded by that particular abrasive can be predicted using further CFD simulations and this wear map.

Stage 1 – generating a material-specific wear map

A minimal set of tests (under standardised conditions) are carried out using a flat coupon of the test material orientated at 90° to the flow in a standard Jet Impingement Test (JIT) [44]. Following the test, the coupon is analysed to give the local wear rate as a function of radial position from the centre of the wear scar.

A CFD simulation of the standard test, incorporating the motion of the sand particles, is run under the exact conditions as the standard tests, to provide local particle impact velocity, angle and frequency as a function of radial position from the centre of the test surface.

The final part of stage 1 is to generate a universal wear map for the material-sand combination under test. This gives wear rate as a function of local particle impact velocity and angle.

Stage 2 – predicting wear rates in specific geometries

A CFD simulation is run for the specific geometry of interest in plant operation. This gives impact velocity, angle and frequency at each position within the geometry.

The wear map from stage 1 is then used to predict the local wear rate at each point. This allows the final scar depth and shape to be determined as a function of position, together with the overall wear of the component.

Ultimately any geometry may be examined in Stage 2, where hydrodynamic impact erosion is prevalent.

1.7 Thesis outline

The thesis describes the work carried out in developing the wear map methodology linking laboratory wear data interpreted by computational methods to predictions on complex plant geometry and is explained in subsequent chapters detailed as follows;

Chapter 2 presents the review of the wide range of research conducted relating to erosion wear in hydro-transport equipment and the various factors influencing it. Several standard laboratory test methods in practice and its versatility in accurately predicting erosion-corrosion damage are also discussed. Also a review of various numerical equations developed with the motive of predicting erosion wear is presented.

Computational fluid dynamics (CFD) forms an integral part of the work undertaken and **chapter 3** is dedicated to the description of the scientific background of CFD and its approach in studying engineering problems.

Chapter 4 presents the work done using computational fluid dynamic (CFD) methods to numerically simulate the configuration of the slurry jet impingement test (JIT) facility at the University of Leeds. Sand particle impact data (impact velocity, impact angle and frequency) were obtained and are presented in this chapter.

Chapter 5 describes the experimental work conducted on a standard material using a standard configuration of the JIT to provide local wear data to develop a material-sand specific wear map. To ensure the fidelity of the experimental results, various measures and procedures were followed and are presented in this section.

In **chapter 6** the local particle impact data and test wear data obtained are systematically linked to develop a material specific wear map. The results of CFD simulations are qualitatively validated using micrographs of post test surface in correlation with local deformation theories.

Chapter 7 demonstrates the originality of the wear map method by predicting erosion damage with CFD on complex geometry by associating wear data obtained from tests on simple configurations and predictions are validated against actual wear data. Wear predictions on an elbow bend is presented and its accuracy in relation with measured wear data is discussed.

A numerical analysis of the prediction capabilities of various other existing models is conducted and the behaviour of each model is compared with the experimental data and the CFD based wear-map predictions and is presented in **Chapter 8.**

Chapter 9 summarises various findings of the project and the advantages and disadvantages of the method developed. The novelty of the wear map method and progress made in predicting erosion wear is discussed.

Chapter 2

Literature Review and Theoretical Background

2.1 Damage mechanisms in oil transport equipment

Extensive research work has attributed material degradation within an oil transport equipment to one of four wear mechanisms, (1) erosion, (2) corrosion, (3) erosion-corrosion and (4) abrasion/sliding wear [5, 15, 45]. These four types of wear mechanisms in the context of an oil transport (also referred to as hydro-transport) system are discussed in the following sections.

2.1.1 Wear by erosion

Wear by erosion generally occurs when a solid surface is in relative motion to solid particles contained within a multiphase environment (fluid and solid particles). It is defined as an irreversible process resulting in progressive loss of material from a surface due to mechanical interaction by particle impacts between the surface and solid particles entrained by the fluid phase, and the conditions leading to this are strongly influenced by the local hydrodynamics of the flow [46, 47]. A particle within a confined geometry is generally influenced by several forces, as illustrated in Figure 2.1 [5] and the subsequent particle motion is dictated by the balance of these forces. Particles acquire energy due to the drag imparted on it by the moving surrounding fluid and due to inter-phase cohesive forces [48]. Any changes in this force balance brought about by change in local flow dynamics can instigate particles to cross fluid path lines leading to impact and material wear [35]. This illustrates the prominence of the flow field on erosion process and this process is identified as erosion by impact [16].
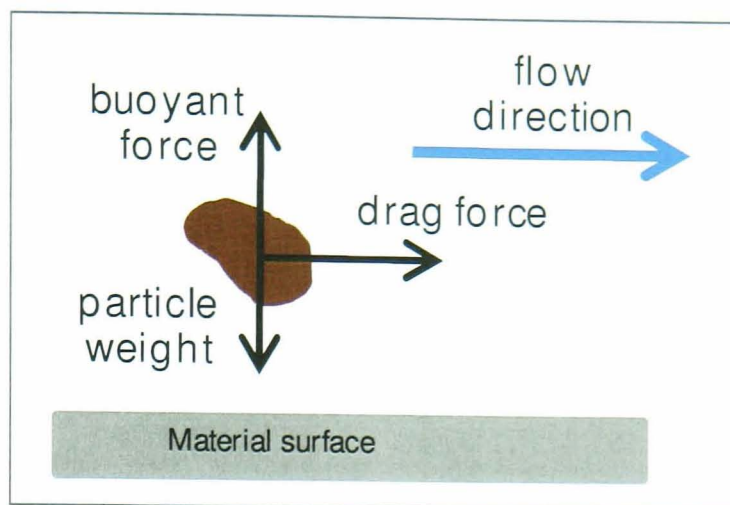
Figure 2.1 Illustration of the major forces acting on a solid particle within a moving fluid medium (reproduced and modified from Hutchings [5]).

2.1.2 Loss due to corrosion

According to Fontana [49], Corrosion can be defined as an irreversible electrochemical reaction between a metallic surface and the surrounding environment leading to degradation of material integrity and eventual dissolution in fluid. Losses can occur either due to atomic, molecular or ionic transport processes occurring at the surface. Depending upon the environment, corrosion is often classified as either 'wet' or 'dry' corrosion, the presence of liquid pertaining to wet corrosion. It has been suggested that wet corrosion can be severe relative to dry conditions [48, 49]. Corrosion loss rates are determined by the kinetics of electrochemical reactions, however, the initiation of corrosion processes is dictated by the thermodynamic state of the system [17].

The driving force that causes metals to corrode is a natural consequence of their temporary existence in metallic form, this form brought about by providing a certain amount of energy. Metals tend to return to their natural form and the rate at which this transpires is dependent on several factors [18]. Several forms of corrosion can occur depending upon the environment and although corrosion can be significant in hydro-transport equipment, further discussions are not pursued.

2.1.3 Erosion-corrosion synergy

Total loss in a slurry environment can be significantly higher than the sum of individual loss due to pure erosion and pure corrosion. Either pure erosion or pure corrosion losses are measured under conditions promoting only pure erosion wear or pure corrosion wear respectively. The additional component is known as the *'Synergistic effect'* and has been accounted to the enhancement of corrosion loss due to erosion and vice-versa [17, 50-53]. The total weight loss (TWL) in an erosion-corrosion environment can be represented by equation (2.1) [19, 51];

$$TWL = E_0 + C_0 + \Delta E_c + \Delta C_E, \qquad (2.1)$$

where, E_0 is due to pure erosion, C_0 is pure corrosion loss, ΔE_c is corrosion enhanced erosion loss and ΔC_E is the erosion enhanced corrosion loss.

2.1.3.1 Erosion enhanced corrosion loss (ΔC_E)

Several materials at certain conditions on reacting chemically with the environment form a layer on the surface (product of the chemical reaction) with the function of inhibiting corrosion and thus reducing corrosion loss. This layer can be locally damaged or ruptured due to particle impacts in a slurry environment, leaving the underlying surface unprotected and vulnerable to corrosive attack. The passive layer reforms to attain its previous full grown condition using up the parent material. The repassivation times are dependent on the behaviour of a material in that environment. The erosion enhanced synergy component (ΔC_E) is due to the rupture and exposure of parent material to corrosive conditions and also due to the consumption of material for repassivation. This leads to an increase in the overall corrosion loss rate which is attributed to particle impacts and is illustrated by Figure 2.2. Erosion also affects surface roughness and can increase the overall surface area in contact with the corrosion environment which also can increase corrosion losses [54, 55].

(a) Stable passive layer   (b) Passive layer damage
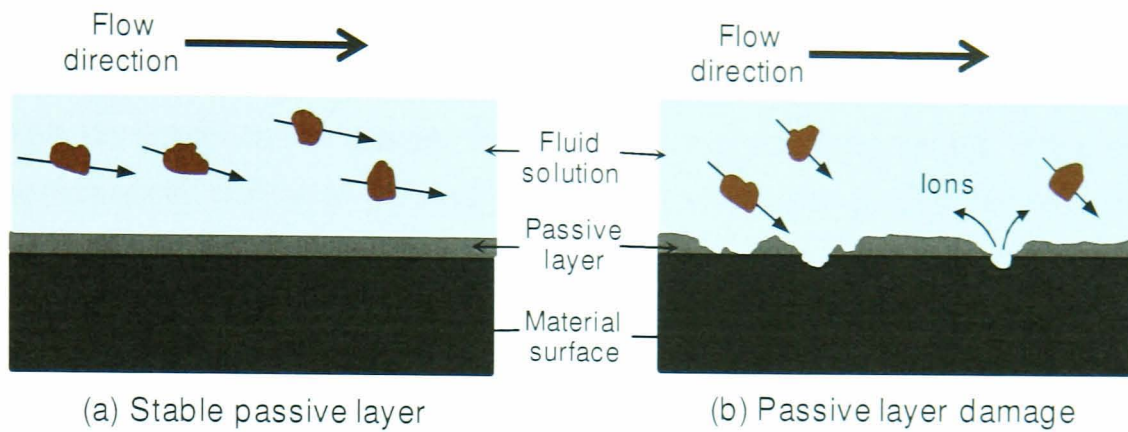
Figure 2.2 The schematic representation of **(a)** a fully grown stable passive layer inhibiting corrosion loss and **(b)** acceleration of corrosion due to particle impacts rupturing the passive layer.

2.1.3.2 Corrosion enhanced erosion loss (ΔE_c)

Li et al. [21] proposed that the effect of corrosion was to increase surface roughness by the dissolution of material and influence erosion rates through its sensitivity to particle impingement angles. Dissolution of material can deteriorate surface integrity leading to reduced erosion resistance as pointed by Matsumara et al. [56]. Li et al. [21] compared the morphology of wear surfaces and observed a major difference in material removal mechanisms in pure erosion and erosion-corrosion conditions and reported greater total losses in erosion-corrosion conditions.

Erosion-corrosion as a phenomenon is complex in nature and studying the interactions between erosion and corrosion can be intensive. Masden [52] reported 23-33 % of the total weight loss of low-alloy steels in slurry flow was attributed to synergistic effects and this increased to 55-62 % in the case of austenitic stainless steels. Whereas, Lu and Luo [53] pointed out that the relative contribution of erosion enhanced corrosion is minimal in slurries with low sand concentration and with relatively low flowing velocity. This may be due to the fact that the material repassivates fully between impacts, suggesting that the contributions of erosion-corrosion synergistic effects are specific to working conditions.

2.1.4 Wear by abrasion

Particle concentrations within hydro-transport pipelines can be very high; in some cases greater than 50% by weight (total weight of sand particles/total weight of the fluid phase) which translates to 30% by volume for particles with an average diameter of 250μm and spherical in shape (particle and liquid densities are 2650kg/m^3 and 1000kg/m^3 respectively). Distributions of particles across a pipeline cross-section can be non-uniform as proved by Ekambara et al. [57] who also reported that this asymmetric distribution increases with sand concentrations, with more particles concentrated at the bottom of the pipeline. This was accounted for by the dominance of gravity over drag forces on a particle in transport, particular at low flow velocities [57, 58].

This presents a unique situation where particles tend to settle at the bottom of the pipelines (particularly in long straight sections) leading to the formation of a slow moving particle bed. Wear under this situation is severe at the base of the pipeline and the degradation mechanisms according to Hutchings [5] can be described to be similar to that of a three-body abrasion as illustrated in Figure 2.3, where two surfaces slide over each other separated by a bed of free rolling particles [5]. The degree of particles settling at the bottom can be minimised by increasing the bulk flow velocity, however, this in turn can increase erosion rates due to impact (erosion rates increased with impact velocity [59-62].

Although wear by abrasion/sliding and by impact are both due to mechanical interactions between particles in relative motion with the surface a clear distinction exists between sliding wear and impact erosion. In the case of impact erosion (Section 2.1.1) the fluid phase dominates particle motion and any minor changes in local flow conditions can have a significant effect. On the contrary, the influence of flow field on particles in a rolling or sliding bed cases can be minimal.
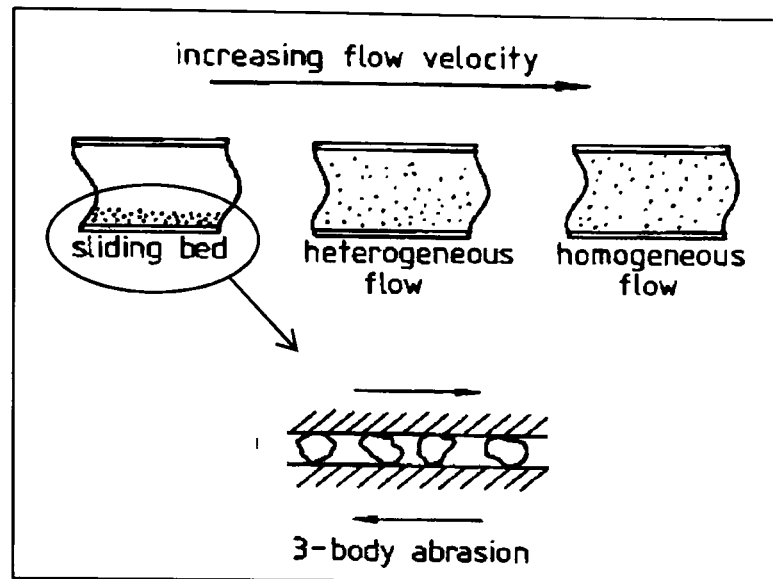
Figure 2.3 Illustration of non-homogenous particle distribution within a straight pipeline section and the effect of flow velocity on this distribution. A schematic representation of three body abrasion process is also provided (reproduced from Hutchings [5]).

At Syncrude Canada Limited, a typical pipeline is of 750mm internal diameter and run up to a length of 10km. These are operated at a bulk flow velocity of 3-6 m/s, transmitting particle concentrations ranging between 35-55 % by weight and at fluid temperatures of 50°C. Slurry conditions can be very aggressive on plant equipment and in the case of Syncrude Canada Limited, equipment has been damaged within weeks of commission. A material able to resist wear under all conditions throughout its intended service lifetime stills eludes the industry, due to the intricacy of the wear mechanisms and thus a selective design approach is implemented. A common material selection practice is to identify the wear mechanisms prevailing at a particular location and to commission a material with superior endurance to that particular wear mechanism. This drives the requirement for accurate material selection tools with the capability of translating wear data from material test onto an industrial application. A starting point to this is by developing a prediction method for a particular wear phenomenon and then incorporating various other wear mechanisms. Wear by impact erosion is chosen as the initiation point in this research and hence forms the theme of following sections.

2.2 Factors affecting solid particle impact erosion

Meng and Ludema [63] in their review reported that more than 30 parameters can affect wear rates and Clark [16] separated the majority of these factors into four groups as presented by Table 2.1. These parameters either influence particle transport, the behaviour of the surface materials to particle-surface interactions and for certain properties (for example particle shape, fluid temperature) both. Following sections discuss the influence of each factor specified in Table 2.1 on erosion wear rates.

Table 2.1 Significant parameters of an erosion system which can influence material removal rates due to impact erosion [16].

Erosion parameters	affecting particle transport	affecting material response
Fluid medium properties	Dynamic Viscosity (η), density (ρ_f).	-
Abrasive particles	Shape/angularity factor (F_s), size distribution (d_p), density (ρ_p),	Shape/angularity factor (F_s), hardness (H_p),
Flow dynamics	Flow regime, temperature, particle rebound and collisions.	Number of impact (N_p), impact velocity (V_p), impact angle (θ), temperature.
Target surface	-	Strength (E), hardness (H), residual stress levels, work-harden ability, ductility-brittleness, toughness.

In the following section, the term 'conform' of a particle to a pathline represents the ability of the flow to change direction and the particle to respond; a particle that conforms to a pathline will follow it closely (Figure 2.4a) whilst a particle that does not conform to fluid pathlines will cross the pathlines and can impact the surface (Figure 2.4b). The ability of a particle to conform to a fluid pathline rests on the control of the flow regime over a particle and this can be determined using the momentum equilibrium constant which is described later.

(a) conforming particle   (b) non-conforming particle
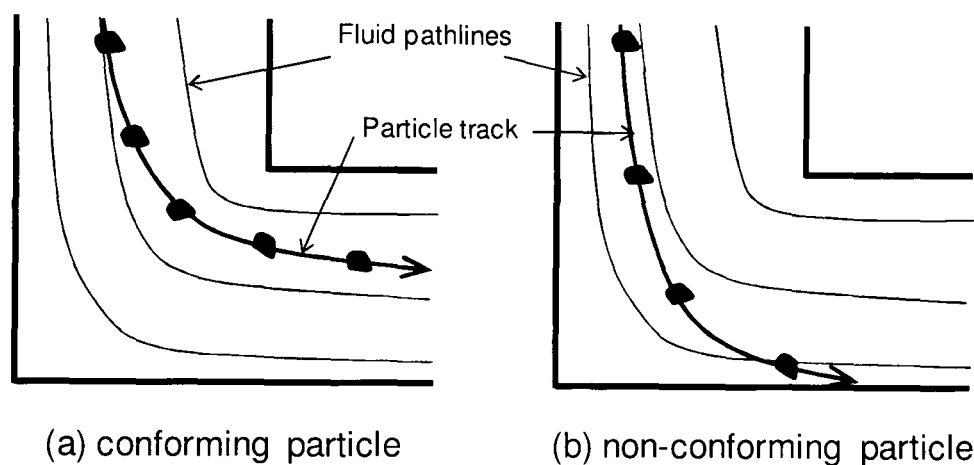
Figure 2.4 Illustration of particle motion within a confined geometry.

2.2.1 Properties of fluid medium

The effect of the viscosity and density of the fluid medium on erosion rates has been investigated; a reduction in erosion rates with increasing fluid viscosity and density has been reported [12, 15, 16, 64]. Levy [64] compared erosion wear rates of mild steel surfaces in two fluid mediums (water and a process solvent with dynamic viscosities of 0.89×10^{-3}Pa-s and 52×10^{-3}Pa-s respectively) by maintaining the other variables (flow geometry, particle size and properties, target material, etc.) constant. Clark [65] measured erosion rates of steel samples in a slurry containing 3% by weight of Al_2O_3 (Aluminium oxide) particles using a slurry pot tester (described later). In both cases significant reduction in erosion rates were observed with higher fluid

viscosities. Similarly increasing fluid density results in lower erosion rates but only by a fraction in comparison to the effects of viscosity [15, 66].

The effects of fluid properties on particle dynamics and hence erosion rates can be understood by studying the fluid dynamics involved. Moving fluid exerts drag on a particle along the direction of fluid motion and this force is accountable for providing the energy required for particle transport. A numerical expression for the drag force, F_d, in the form of equation (2.2) was provided by Hojo et al. [67].

$$F_d = \frac{1}{2}\rho_f C_d A(V_f - V_p)|V_f - V_p|, \tag{2.2}$$

where ρ_f is the fluid density, V_f and V_p is local fluid and particle velocities, A is the frontal area of the particle, C_d is the coefficient of drag which is expressed by the empirical equation (2.3).

$$C_d = \frac{24}{Re_p}(1 + Re_p^{2/3}), \tag{2.3}$$

where Re_p is the particle Reynolds number defined by equation (2.4).

$$Re_p = \frac{\rho_f}{\eta}(V_f - V_P)d_P, \tag{2.4}$$

where d_p is particle diameter and η is the dynamic viscosity of fluid and the significance of Reynolds number is described later. From equations (2.2 to 2.4) the drag force on a particle can be approximately written as follows,

$$F_d = 3\pi(V_f - V_p)^{2/3}|V_f - V_p|\rho_f^{2/3}d_P^{5/3}\eta^{1/3}, \tag{2.5}$$

Equation 2.5 implies that increasing the viscosity or density (with all other parameters being equal) gives a greater drag force on the particle and hence good conformance between fluid and particle phases. This minimises

the probability of particle crossing the pathlines (due to changes in local flow conditions) and impacting with the wall. This contributes to an overall reduction in erosion wear rates.

2.2.2 Properties of abrasive particles

2.2.2.1 Particle size and density

The conformance of particles to the flow is resisted by the inertia of a particle and numerically this force can be represented by equation (2.6).

$$F_p = \frac{\pi}{12} \times d_p^3 \times \rho_p \times \ddot{a}_p , \qquad (2.6)$$

where, $\ddot{a}_p$ is particle acceleration and F_p is the force required to accelerate a particle of mass m_p in the direction of this force. It is assumed here that the particle is spherical in shape. If $\frac{F_d}{F_p} \gg 1$, then the conformance between particle and fluid would be sustained and particles will strictly adhere to fluid streamlines. This sweeps particles away from the surface leading to lesser number of impacts and hence lower wear. However, when $\frac{F_d}{F_p}$ is small, particles travel straight on and there exists a possibility of particles crossing fluid pathlines leading to collisions and the tendency of which is increased with increasing F_p. Thus the significance of particle density ρ_p and diameter d_p is to influence F_p; larger and denser particles increase F_p (the force associated with particle mass) which also increases particle kinetic energy. This relates to greater energy transferred to the surface on impact and hence increased erosion rates.

The effect of increasing particle size can be illustrated by Figure 2.5 reproduced from Benchaita et al. [68] who numerically predicted particle trajectories approaching a planar target normal to flow direction and observed particles with larger diameter experienced little deviation from a collision path with the surface whereas smaller particles (200μm) failed to contact the surface.
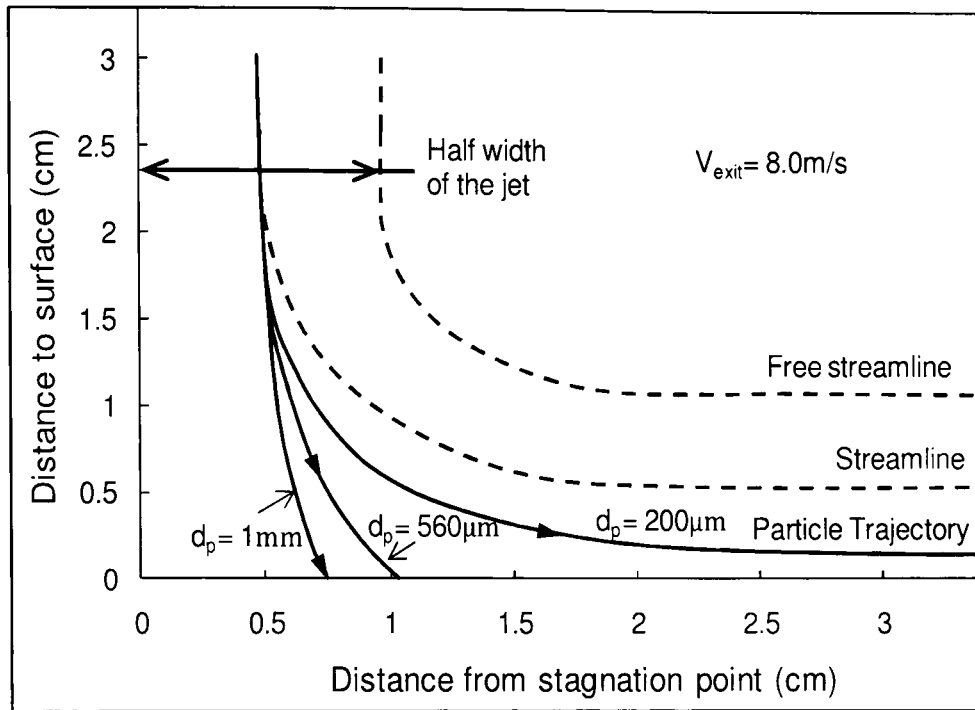
Figure 2.5 Calculated trajectories of spherical particles of different diameters in a water jet, 20mm wide and a bulk velocity of 8m/s directed at a flat plate [68].

Lynn et al. [69] conducted short duration erosion tests with various particle sizes and measured wear rates of steels specimens in an erosion pot tester using 1.2 weight % suspension of SiC (silicon carbide) particles in oil (ρ_f = 858kg/m³ and dynamic viscosity η = 2.1×10⁻³Pa-s) and observed that particle impact velocities increased with increasing particle sizes (Figure 2.6). Similar observations were also reported with increasing particle density accounting for greater wear rates [69-71].

From equation (2.2) it could be inferred that fluid drag on particles increases with size and hence better affinity between fluid and particle which can lead to lower erosion rates. However, the extent of this is lower relative to the effect of increasing particle inertia with size [16, 72].
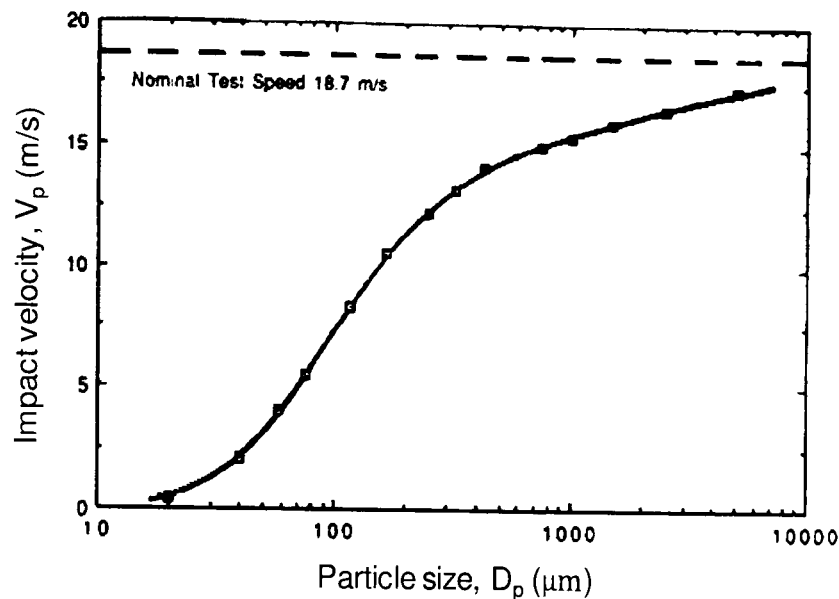
Figure 2.6 Variation of particle impact velocity as calculated based on experimental wear data obtained from a slurry pot erosion tester and irregular shaped SiC (silicon carbide) particles in a 1.2 weight % suspension of oil on steel surfaces [69]. Image reproduced from Lynn et al. [69] and please note the use of logarithmic scale for particle size.

2.2.2.2 Particle shape factor

Particle shape can affect the drag force acting on the particle and also the wear mechanism by influencing particle wall interaction event. Generally particle studies are conducted using spherical shaped objects since it offers good control over other particle variables, however, in real circumstances the shape and orientation of a particle can be entirely different and random. The general conclusion is that sharper objects inflict greater damage [73] and Desale et al. [71] suggested that a smaller particle-target contact region (for the case of sharper abrasives) results in higher local stresses in comparison to spherical particle impact events as illustrated by Figure 2.7, thus modifying the local wear pattern which can eventually lead to greater losses. It must be noted that the shape of a particle can change as a result of breakage due to constant impact and sharper particles can be rounded leading to significant reduction in wear rates as reported [11, 52]. This again confirms that sharper particles inflict more damage when compared to rounded or smoother particles.

Spherical
particle

Actual
particle

2r

2r'
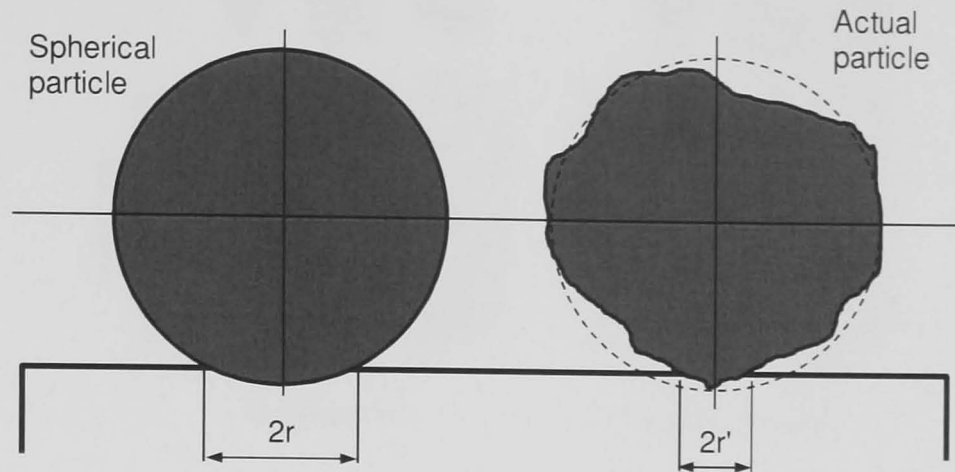
equal mass and density; similar diameter
Contact radius 2r > 2r'

Figure 2.7 Effect of particle shape on surface contact and hence overall wear. Here two abrasive particles of exact same mass and density with minor variation in geometry are shown in contact with the same material surface. Reproduced from Desale et al. [71].

Also for a particular shape, particle rotation can be a key factor since it changes the orientation with the surface and determines its eventual contact surface area [73]. Chen and Li [74] numerically studied the effect of shape and orientation on wear rates with single and multiple impacts (a better representation of actual phenomenon) and the predictions are illustrated in Figures 2.8 and 2.9. It can be deduced that particle shape affects erosion rates significantly with sharper objects contributing to greater losses, but the effect of different orientations is not so significant. This has been accredited to modifications in the roughness of the surface after several impacts which can alter wall-abrasive contact areas and hence reduce erosion rate variations with orientations. The issue here is the effect of local contact surfaces changing with surface roughness and thus to study the effect of particle shape and orientation quantitatively can be intricate due to its random nature.
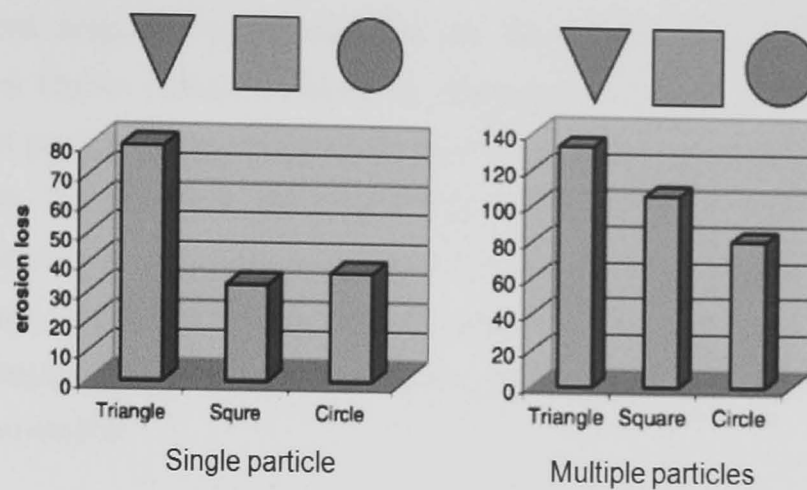
Figure 2.8 Variation of erosion wear of copper by SiC particles of particular size such that the mass of each particle is relatively similar but with three different shapes as predicted by Chen and Li [74]. Note the figure is not to scale.
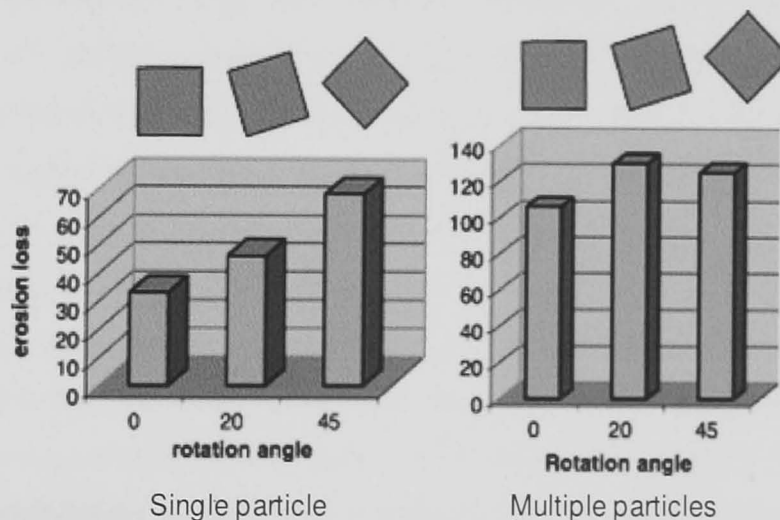
Figure 2.9 Variation of erosion wear of copper by square shaped SiC particles but at different orientations to the surface as predicted by Chen and Li [74]. Note the figure is not to scale.

Particle shape also affects the drag co-efficient, C_d, and hence the fluid drag forces over the particle. Particle with streamlined shaped such as an ellipse or a pear has a lower C_d compared to spherical particles [75]. This transpires to lower drag on streamlined shaped particles (at certain

orientations, angular shaped particles can be considered to be streamlined) and hence higher collision efficiency. Collision efficiency is defined as the number of particles impacting to the number of particles present in the fluid stream [16, 72]. However, Goossens [76] reported that the C_d of an irregular shaped particle is dependent on the initial orientation of that particle in the fluid stream. Hence accurate determination of drag coefficient of particles can be impossible and approximations are used to describe the C_d of particles in motion.

2.2.2.3 Particle hardness

Hardness of a particle does not play a role in controlling particle motion; however, it has been proved to be factor in erosion wear studies [77-79]. Levy and Chik [80] eroded 1020 steel with particles (calcite, apatite, sand, alumina and silicon carbide) of different hardness and observed an increase in measured erosion rates with particle hardness. Low erosion rates were observed for particles with low hardness (these particles were thought to shatter during contact and hence leading to lower erosion losses). However, beyond a particular particle hardness ($700kgf/mm^2$ for this case), additional increases in erosion rates were not observed (Figure 2.10). Fracture of particles was a phenomenon specific to particular operating conditions and depends on target surface hardness and particle velocity. It was proposed that beyond this particular hardness, particles were strong enough not to shatter during impact and erosion rates essentially remain constant [80]. Surface examinations suggested shattered particles might be adhered to the surface resulting in a net gain of mass [78, 80] and can also act as an protective layer against oncoming particles.

2.2.3 Flow Dynamics

For fixed properties of fluid medium, abrasive and target surface the variable factors that influence erosion rates are associated to the local flow conditions and the surrounding environment and are discussed here.
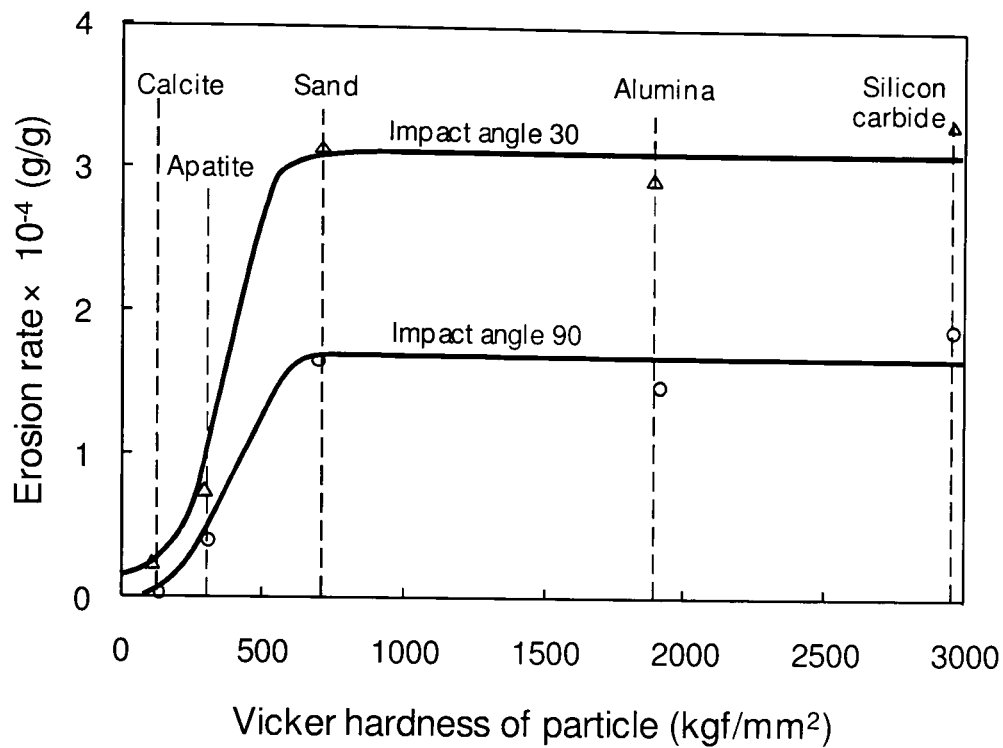
Figure 2.10 Variation of erosion rates of 1020 steel eroded using different types of abrasive particles with varying hardness with the particulate stream oriented at 30° and 90° to the surface as observed by Levy and Chik [80]. Image reproduced from Levy and Chik [80].

2.2.3.1 Impact velocity

Impact velocity of a particle is defined as the velocity magnitude of a particle just prior to contact. The variation of erosion rates with impact velocity has been shown to take the form of equation (2.7) [81].

$$E_r \propto V_p^n ,$$ (2.7)

where V_p is the particle impact velocity, E_R is the average erosion loss due to a single particle impact and n is an experimental constant (also referred to as velocity exponent). The velocity exponent has been experimentally determined for various materials and erodent properties and found to vary between 1 to 5 as reported by Clark [16], however, an exponent of 2 to 3 is generally used [63].

The local particle impact velocities are different from the bulk flow velocity; for a liquid erosion system the differences can be significant. For a

gas phase containing solid particles, wear rates in air-borne studies were analytically determined by presuming impact velocity of particles to be similar to mean fluid flow velocities [33, 82]. This assumption was considered valid since the viscous drag forces on particles were negligible, which is attributed to low viscosity of air. However, this assumption is invalid for a fluid with relatively high viscosities, for example water and hence accurate definition of particle impact velocities is a criterion for good predictions [24, 83, 84]. Nevertheless, for viscous systems, it is acknowledged that increases in local particle impact velocity correspond to an increase in erosion wear.

2.2.3.2 Impact angle

The local particle impact angle can be defined as the angle subtended by the velocity vector of a particle to the surface just prior to imminent collision. For an air-borne erosion system, this angle can be considered to be similar to the angle subtended by the impinging jet to the target surface. Oka et al. [85] conducted air borne erosion studies on aluminium surfaces at various impingement angles and observed vast differences in the wear scar and overall erosion loss (Figure 2.11). Material removal due to impact erosion is predominantly either due to *'cutting'* or *'deformation'* mechanisms and material responses to these mechanisms are varied [33, 34, 82, 86]. According to Finnie [33], cutting wear predominates at low angles of impacts (horizontal component) whereas Bitter [34, 86] suggested that wear by deformation dominates at high impact angles (vertical force component). The effectiveness of each mechanism and hence total mass losses are directly related to horizontal and vertical components of the total impact energy which is connected to the impact angle. A very detailed review of the effect of local impact angles on material behaviour is presented subsequently (Section 2.2.4).
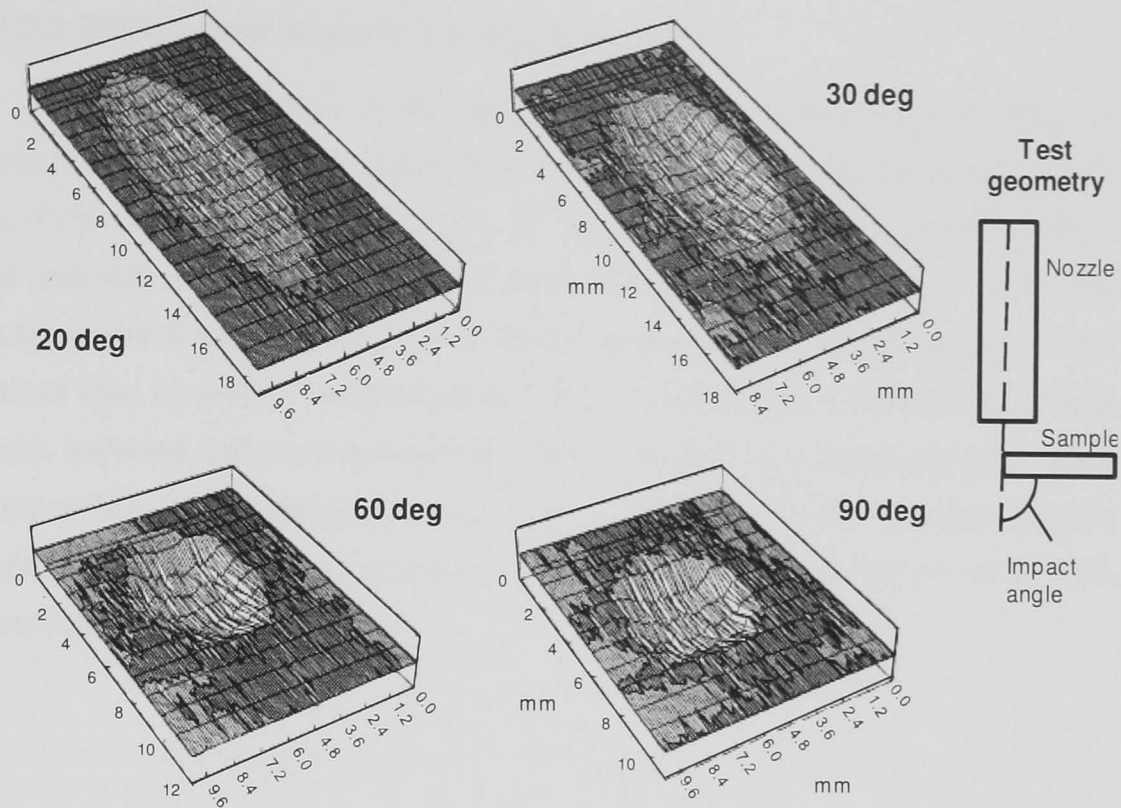
Figure 2.11 Variation of wear scars on aluminium surfaces due to impingement by air-borne SiO$_2$ (silicon dioxide) particles at various nominal impingement angles (reproduced from Oka et al. [85]).

Determining the effects of impact angle on the erosion is generally an indicative of the basic mechanism of erosion [12, 63] since erosion wear peaks at specific local impact angles for a particular material [30, 33, 87]. Clark [88] reported that for ductile materials, only a small measurable erosion rate at 90° nominal impingement angle was observed. The wear reached a maximum at 30°; further reduction in the angles led to lower wear which was in accordance with Oka et al. [85]. In the case of a brittle material, the maximum overall wear was observed for 90° impingement angles and reduced to zero at low angles of impingement [88]. Due to the sensitivity of materials to impact angles, knowledge of this can be valuable in material specification for plant equipment.

2.2.3.3 Number of impacts/ particle rebound

Experimental data of erosion wear rates measured using a range of experimental methods suggest that increasing particle concentrations leads to increased erosion rates [16, 24, 27, 40, 65, 89]. Reza [6] studied the effect of particle concentration on erosion loss of steel samples using an impingement based erosion test facility and observed an increase in total mass loss for concentrations up to 7.5% by weight and recorded total mass loss reduced with concentrations. Oka et al. [85] conducted erosion tests using SiO_2 (silicon dioxide) particles on an iron specimen at various speeds and observed reduced erosion rates as illustrated in Figure 2.12 with increasing particle flux [85].
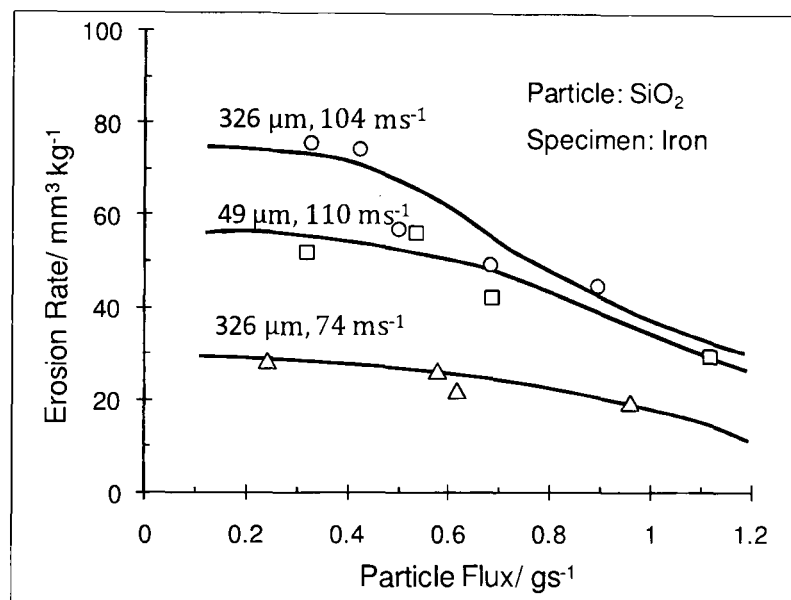
Figure 2.12 Variation of erosion rates of Iron samples for different particle flow rates and velocities suggesting the effect of solid concentrations on erosion rates as observed by Oka et al. [85].

This reduction in average erosion loss per impact with concentrations beyond a certain limit was observed by several others and is collectively attributed to collisions between particles occurring around the vicinity of a surface [7, 24]. Post impact particles during rebound can impede oncoming particles by altering its subsequent motion and reducing the kinetic energy of those particles, leading to reduced losses. This effect can be prominent with

increasing particle concentrations [15, 16, 28]. Particle-particle collisions are specific to test geometries and operating conditions. At low concentrations the effect of inter particle collisions can be neglected but can be pronounced at higher concentrations [28, 36] and it is also possible that a layer of post-impact particles develops at the surface which can shield the surface from subsequent impacts. Hence it is vital to understand the extent to which a particle interfering with an oncoming particle influences erosion wear for qualitative and quantitative wear analysis.

2.2.3.4 Flow temperature

Dosanjh and Humphrey [90] numerically analysed erosion rates for a multi-phase flow (air and solid particles) at high and low temperatures (1200 and 300 K). It was reported that the primary effect of higher temperature was to increase fluid viscosities (air in their case). A consequence of which was better conformance to fluid pathlines and hence lower number of particle impacts leading to a reduction in erosion rates (section 2.2.5). Conversely, the effect of increasing the temperature of a liquid medium is to reduce viscosities and hence leading to an overall increase in erosion rates. Levy and Man [91] conducted erosion tests on various steel surfaces using kerosene as the fluid medium at two different flow temperatures (95 and 175 °C) and observed that erosion rates were nearly 6 times higher at 175 °C for all test samples and attributed this effect mainly to reduction in viscosities of the fluid medium with temperature [91]. It is argued that rise in the operating temperature can affect the local property of a surface by softening the material which could lead to change in erosion wear mechanisms and hence wear rates [15]. However, the primary effect in the case of liquid medium (presuming no corrosion) is to change fluid viscosities and indirectly affect wear rates.

2.2.3.5 Hydrodynamic regime

An extensive review of the effects of flow regime on erosion was conducted by Humphrey [15] and summarised that erosion rates are strongly

coupled to the overall flow field, particular for the case of slurry erosion. A general knowledge of the flow regime can provide enough evidence to suggest the qualitative nature of erosion wear behaviour. The measure of the control of local flow field over a particle can be obtained by calculating the momentum equilibrium constant given by equation (2.8) [90].

$$\lambda = \frac{\rho_p \, d_p^2 \, \vec{V_f}}{18 \, \eta \, \vec{L}} ,$$
(2.8)

where ρ_p and d_p are particle density and diameter respectively, $\vec{V_f}$ and $\vec{L}$ are the characteristic mean fluid velocity and length scales and η is the dynamic viscosity of the fluid medium.

The quantity, λ was defined by Brown [36] as the ratio of the particle response time due to viscous drag to a characteristic turbulent eddy time in the fluid medium. The effect of the ensuing fluid flow regime on particle motion for an impingement erosion case using momentum equilibrium constant as a reference is schematically shown in Figure 2.13.

Impingement jet flow
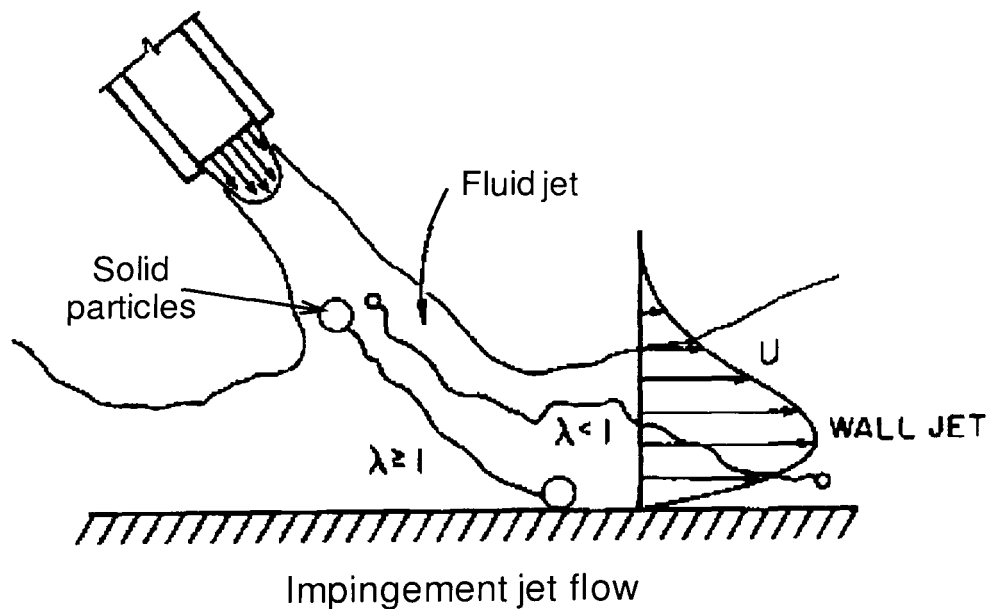
Figure 2.13 Schematic illustration of an impingement scenario with different particle momentum equilibrium constant (reproduced from Humphrey [15]).

For values of λ≥2, particle motion is dominated by inertia and particles are very slow to respond to changes in fluid velocity, which in a confined geometry would be dominated by particle-wall interactions. For values of λ<0.25, particles conform better to fluid pathlines and hence minimal particle-wall interactions can be expected. This was also observed by Zhang et al. [92], who suggested that turbulent flows have a higher λ (momentum equilibrium constant) number and the multi-phase flow would be dominated by particle-wall interactions [15].

2.2.4 Influence of material properties

Numerous erosion studies of materials caused by impacting particles including several comprehensive reviews of this subject are reported [12, 27, 30, 33-35, 64, 78, 82, 86, 93-98]. The emphasis in these studies was on the material-related aspects and the physical properties dependence of erosion wear in attempting to postulate wear mechanisms and formulate models with physical significance. The major observation was the variance in wear behaviour with properties (such as hardness, toughness, stress levels, temperature, ductility, brittleness) addressing the crucial role played by material properties in dictating overall wear.

A classical illustration of the difference in material properties on the resulting wear mechanisms and rates can be retrieved from Figure 2.14. Chen and Li [74] used mathematical deformation models to predict erosion losses on two different materials (ductile and brittle) using similar abrasives (material property, geometrical feature and orientation) at exact local particle impact conditions and observed the variation of erosion loss with impact angles. For the ductile material type, maximum erosion occurred at an impact angle around 30° whereas for the brittle type material erosion rate peaked at 90° impact angle [74].
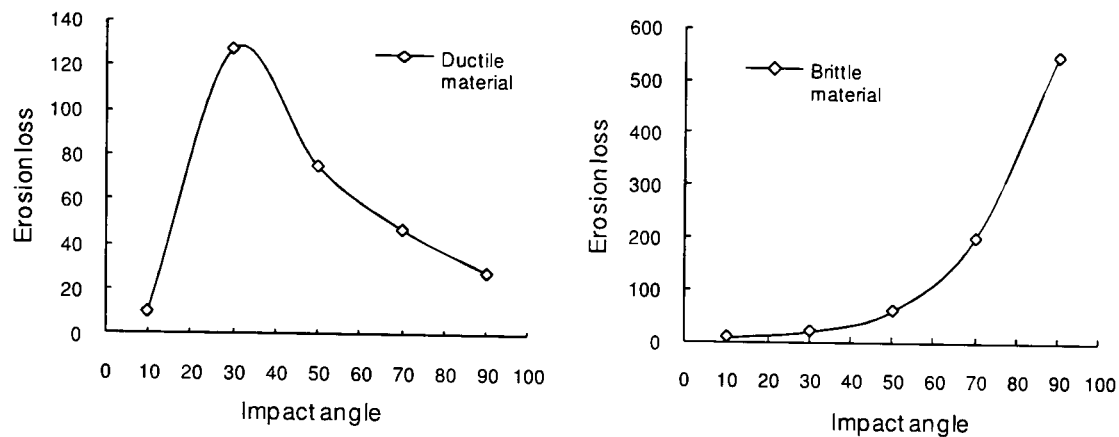
Figure 2.14 Variation of erosion loss for two different types of material (ductile and brittle) as numerically predicted by Chen and Li [74] using the MSDM (Micro scale dynamic model) approach.

Finnie [33] conducted various particle impact erosion tests on different ductile materials (copper, aluminium and steel) at various impact angles. Measured erosion loss per particle impact suggested peak erosion occurred at angles in the range of 20-30°. Tilly [78, 99] conducted impingement tests on materials classed as brittle and reported that maximum weight losses occurred at impact angles greater than 80°. The variation of maximum erosion loss with impact angle with different material types has been reported to support these findings [27, 30, 78, 82, 99]. The difference in material behaviour is critical in the application of a specific material in an industrial context. The design of hydro-transport equipment using a brittle material can be detrimental if particle impacts occur predominantly at high angles. Equally, ductile materials would be a poor material selection if the majority of particle impacts occur between 20-30° local angles.

Alongside the ductility/brittleness of a material, the material hardness is a major factor which affects erosion rates. Erosion wear usually occurs if the particle hardness is greater that the target surface hardness and increased target surface hardness can enhance erosion endurance [100-102]. Chauhan et al. [103] conducted impingement based erosion tests on two different steel samples (martensitic and austenitic) and the observed damage was relatively lower on harder target and this was concurred by several other reported studies. On the contrary, Sundararajan [104] reported

that increases in target surface hardness had minimal effect on erosion resistance. It was argued that increasing hardness can lead to brittle behaviour (brittle materials are vulnerable to high angle impacts) and hence the material may not perform as expected. Goretta [105] investigated the erosion resistance of copper, nickel and stainless steels against sharp alumina particles and concluded that work hardening improved the erosion resistance of these materials. It was asserted that increasing hardness can improve erosion resistance provided the ductility of the target is sustained and hence careful material manufacturing processes and surface treatment has to be followed [100, 106].

Generally a material developed for subsequent application in an oil industry is required to be able to endure wear due to erosion, corrosion, erosion-corrosion and abrasion mechanisms. Increasing hardness has been associated with improved resistance to abrasion wear and corrosion under certain conditions [6, 19]. However, this can lead to reduction in erosion endurance at high impact angles. Along with the ductility, brittleness and hardness of a material, several other factors can influence wear performance of a material and studying the effects of these factors is an exhaustive task.

During the process of selecting an appropriate material to construct hydro-transport equipment, the prevailing local particle impact conditions are to be carefully considered. A material which exhibits ductile behaviour can be used for better erosion resistance provided impacts occur predominantly at high angles and conversely brittle materials if local particle impact angles are low. However, if particle impacts occur at a wide range of angles then selective application of ductile and brittle materials can be practised. However, other possible wear mechanisms should also be taken into consideration. At this juncture it is concluded that material property does play a major role in influencing material wear rates and choosing a material for application in hydro-transport industry has to be done with careful consideration to local impact conditions and hence the prior knowledge of local impact conditions and wear mechanisms is a criterion for good material design.

2.2.5 A summary of factors affecting erosion by impact

A review of various factors influencing particle transport within a slurry medium and the eventual response of a material to particle-wall interactions was presented in the previous sections. Based on this it can be inferred that the effects of majority of the factors are intertwined, for example increasing particle size leads to larger mass and thus greater losses. Also increasing particle sizes can increase the fluid drag over the particle leading to reduction in wear rates as mentioned earlier. Studying the individual contribution of each factor to the overall wear process can be extremely exhausting and in cases such as particle shape can be impossible due to the random shape variations involved. Hence a statistical approach is involved to assess the contribution of each parameter to wear rates. All major parameters can be segmented into four groups, three of which are associated with the properties and features of either the material, abrasive or the fluid. These three groups in a slurry medium are connected together by the fourth group, flow dynamics and hence forms a crucial link in studying and predicting the ensuing erosion behaviour.

It was previously illustrated through Figure 1.4 that for similar material-abrasive combinations, fluid properties and nominal working conditions different flow regimes can be prevail which can lead to disparities in wear behaviour. It is thus proposed that studying the local flow field can provide an insight and subsequently be able to analytically predict wear rates in different geometries and thus establishing a link between standard laboratory tests and plant geometry.

2.3 Erosion prediction methodologies

Erosion wear behaviour analysis and prediction methodologies can be broadly classified into three types; experimental, numerical and empirical methods all of which are described in the following sections.

2.3.1 Experimental methods

The behaviour of newly developed materials has been studied using laboratory based, purpose built testing facilities for several decades. A vast majority of these laboratory tests by nature are designed to be fast and aggressive in comparison with actual plant conditions in order to provide sufficient wear data in short time periods and thus reducing lead times during material design and developmental stage. Another beneficial aspect of laboratory tests is the ability to recreate and control a wide range of material degradation conditions without the added safety risk associated with an industrial setting. Traditionally, various materials are tested under several erosion conditions and the better performing material is proposed for commission.

It has been stated that erosion wear can be prevalent in a wide range of local conditions and the sub-modes of wear can differ depending upon the prevailing conditions [23]. A minimum criterion for meaningful translation of data from laboratory tests to plant environment is that the local wearing modes has to be similar [31]. Using this as a prerequisite, a range of laboratory tests were developed to specifically regenerate conditions prevailing within hydro-transport equipment and the prominent ones are briefly described as follows.

2.3.1.1 Coriolis tester

The Coriolis tester comprises a rotating bowl enclosing the multi-phase fluid and a flow channel attached to the circumference of this bowl. The material to be tested is strategically inserted within this flow channel. A schematic representation of the coriolis tester is shown in Figure 2.15 and further detailed description of this facility is provided elsewhere [107, 108]. The multi-phase fluid is centrifuged within this bowl and is made to pass through the flow channel (which also acts as exit for flow). Solid particles slide (impact angles can be very low <10°) along the sample surface at low velocities (only a fraction of the bulk fluid velocity) instigating material wear. It has been reported that the condition recreated at the test surface is similar to those expected within particular parts of pumps and in certain sections of

pipe bends with large radius of curvatures [109-111]. Advancements were incorporated to reproduce conditions with high particle impingement angles and velocities [40, 112].
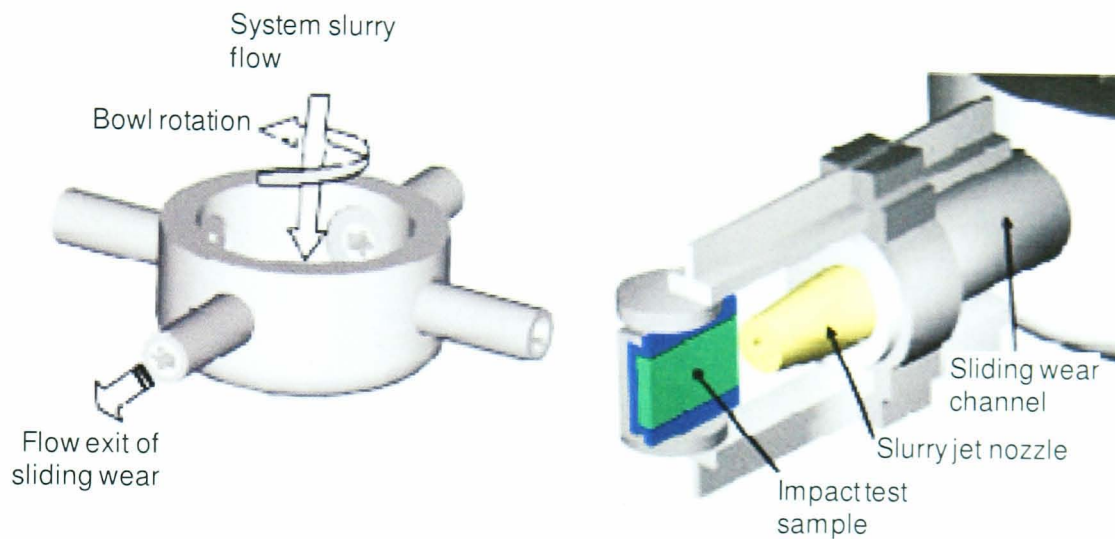
Figure 2.15 Schematic representation of a coriolis tester with a sliding wear channel and equipped with an impingement nozzle to reproduce slurry erosion-corrosion conditions. Image reproduced from Tian et al. [40, 112].

2.3.1.2 Slurry pot erosion tester

The test specimens, generally cylindrical in shape are housed strategically within a cylindrical container or pot comprising the fluid suspension. The specimens are made to revolve about the container axis, agitating the encapsulated fluid suspension leading to particle-specimen collisions [65, 72, 113]. A schematic representation of a version of the slurry pot tester developed by Desale et al. [114] is shown in Figure 2.16 and detailed description of this device is provided elsewhere [114]. A numerical study of particle trajectories and impact data within a slurry pot erosion tester predicted the recreation of particle impacts at very low angles and velocities for small particle sizes [115]. Clark [72] demonstrated that high impact velocities and angles can also be reproduced by the slurry pot using particles with larger densities and sizes. Particles would settle at the bottom

of the pot during operation which could be avoided by the introduction of baffle plates within the pot.
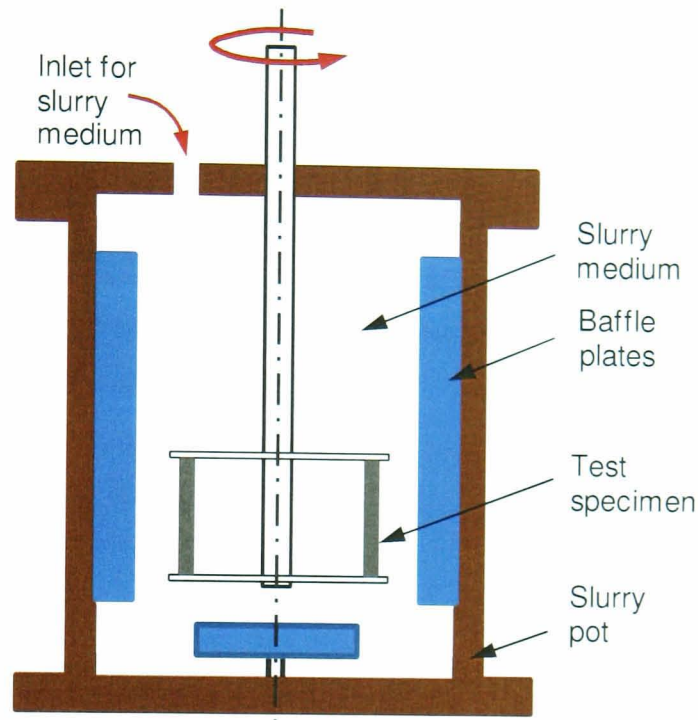
Figure 2.16 A cross-sectional representation of a slurry pot tester with two cylindrical test samples contained within a slurry medium. The baffle plates are used improve circulation of sand within the pot by agitating the medium.

2.3.1.3 Slurry Jet Impingement tester

The slurry jet impingement test (JIT) is described in detail later (section 5.2.1) and it has been demonstrated by Benchaita et al. [68] that a wide range of local particle impact conditions can be reproduced using this facility. Two configurations of the slurry jet impingement tests, the free jet and the submerged jet. In the free jet impingement test, a slurry stream is made to impinge the surface and is surrounded by air whereas in the submerged jet the test surface and the nozzle are both fully submerged in the fluid medium. The submerged jet impingement test is widely used in studies related to slurry conditions and hence this configuration is discussed here. The submerged JIT recreates erosion conditions prevailing in geometries with sudden obstructions where severe wear can be prevalent, however, it does

not effectively describe wear at conditions prompting minimal or no changes in flow directions (for example: Straight sections of pipes, bends with a very large radius of curvature) [116]. This facility is therefore most applicable to predictions where erosion by impact is the dominant mechanism. Using CFD (computational fluid dynamics) methods the findings of Benchaita et al. [68] is exemplified and is described within this thesis (section 4.3.1).

2.3.1.4 Pipe Loop tests

These are generally small scale versions of an actual piping layout, with certain sections made of materials to be tested and were developed with the motive of capturing closely the hydrodynamics in an actual pipe network. Various versions of pipe loop tests were developed [41, 58, 116, 117] and one such configuration is represented in Figure 2.17. In order to obtain credible material wear data it was required to continuously run these tests for several days. Despite the huge setup and functioning costs incurred, only reasonable correlations has been reported [117] and this facility also limits the amount of parametric wear studies to be conducted.
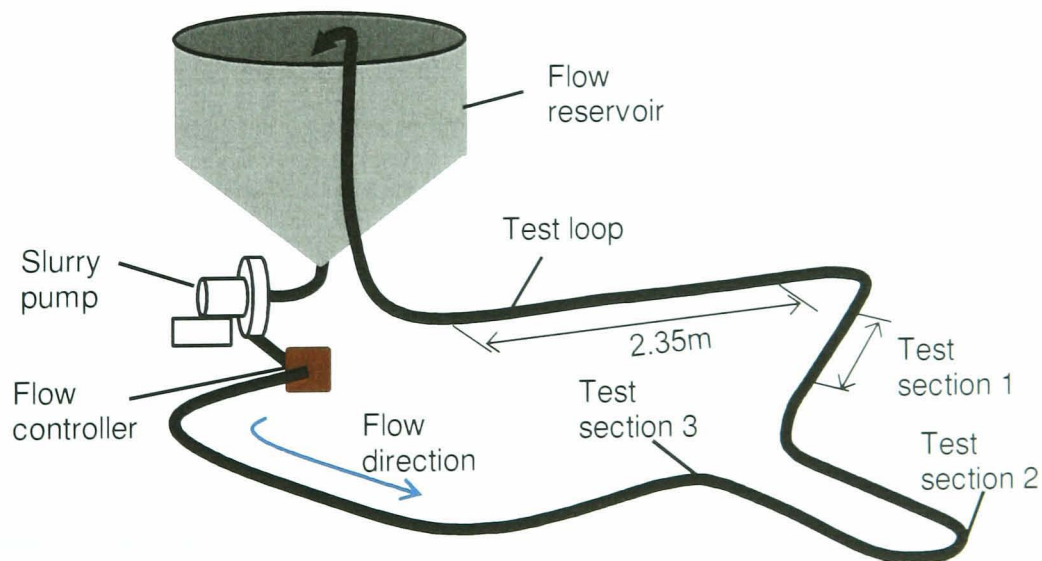
Figure 2.17 A schematic of pipe loop test rig developed by Wood et al. [117] to validate wear predictions made using CFD simulations on pipe geometry. Image reproduced from Wood et al. [117].

It can be said that no single standard test equipment can recreate all the range of conditions instigating all material degradation mechanisms. Although the slurry jet can produce a wide range of local impact angles, it is argued that wear phenomenon at very low impact angles are not adequately described. Whereas it is proposed that the coriolis tester recreates particle impacts at low velocity and angles but fails to reproduce high impingement angles. The coriolis tester was advanced to recreate high angle impacts (Figure 2.15), but it was reported that estimating particle impact velocities and angles were complicated due to the added effect of the centrifuge. The slurry pot on the other hand has been claimed to reproduce the entire range of particle impact conditions; however, to accomplish this various parameters had to be controlled. For instance, high impact angles were achieved by using particles with large densities and smaller sized particles for low impact angles, thus limiting the applicability of this apparatus. The pipe loop apparatus, as mentioned earlier, closely resembles the plant layout and although may not recreate the entire envelope of wear mechanisms, it can adequately capture the behaviour of a particular plant geometry. However, the immense costs and operational times associated limit the value of this apparatus.

Other than the above factors, the major challenge is translating laboratory wear data to meaningful correlations for plant conditions and to eventually predict wear profiles for a given plant geometry. Generally correlations between laboratory and plant conditions are based on mean flow data obtained from conducting field tests. A prerequisite for similarities between test and field wear data, is the mean flow data- flow shear stresses, flow rates, bulk velocities, average particle impact energies- in both the cases should be similar [7, 31]. Based on this premises numerically formulations were pursued and formulated to establish a link between laboratory and plant. Irrespective of the inherent limitations of laboratory test methods due to the complexity of erosion mechanism, it is still actively pursued as the initial step material design and to provide material wear data for analytical formulations of erosion wear as described in the ensuing sections.

2.3.2 Numerical methods

The importance of material properties was earlier discussed (section 2.2.4) and the significance of accurately capturing its behaviour at various impact conditions. Mathematical equations which profess to predict erosion wear characteristics quantitatively as a function of material properties and impact conditions have been formulated based on different wear theories. Several numerical formulations have been proposed and descriptions of a select few are provided as follows.

2.3.2.1 Finnie formulation

One of the earliest erosion models was developed by Finnie [33]. The proposed model was developed on metal cutting phenomenon and based on the mechanisms of kinetic energy exchange during the impact of a single solid particle where material is removed predominantly by 'cutting wear' (described later) in dry conditions. Equation (2.9) predicted erosion volume loss due to a single abrasive grain in contact with the surface and was developed on the assumption that local impact conditions were similar to nominal impact conditions (an assumption which was considered valid under air borne conditions).

$$Q_p = \frac{m_p V_p^2}{P \psi \kappa} \left(\sin(2\theta) - \frac{6}{\kappa} \sin^2 \theta \right), \qquad \text{for } \tan \theta \leq \frac{\kappa}{6},$$

$$Q_p = \frac{m_p V_p^2}{P \psi \kappa} \frac{\kappa \cos^2 \theta}{6}, \qquad \text{for } \tan \theta \geq \frac{\kappa}{6},$$

(2.9)

where Q_p is the volume of material removed, m_p is the mass of a single particle, V_p is the impact velocity, θ is the impact angle, P is a constant associated with the material plastic flow stress, κ is the ratio of vertical to horizontal force component on a particle, Ψ= ratio of the depth of contact to depth of cut (a value of 2 was used in accordance with metal cutting phenomenon). It was proposed that the numerical values for these constants were to be experimentally determined.

Since erosion phenomenon involves several particle impacts, equation (2.9) was modified to incorporate the effects of multiple impacts to equation (2.10). Taking into account surface changes due to multiple impacts K was assumed to be 2 (obtained from force measurement tests) and Q_t volume removed due to a mass of M of angular abrasive particles as,

$$Q_t = \frac{MV_p^2}{8P}(\sin(2\theta) - 3\sin^2\theta) \qquad \text{for } \tan\theta \leq 18.5°,$$

$$Q_t = \frac{MV_p^2}{24P}\cos^2\theta \qquad \text{for } \tan\theta \geq 18.5°. \tag{2.10}$$

The general erosion wear of ductile materials at various impingement angles were predicted by equation (2.10) and compared with experimental wear data for copper, SAE 1020 steel and aluminium surfaces (SAE- society of automotive engineers) obtained at exact conditions as illustrated in Figure 2.18. Tests were conducted in air-borne conditions and hence the nominal impingement and local particle impact angles were considered similar. These predictions agreed closely with measured data for angles between 0 to 30° where erosion rates were greatest. However, with increasing impact angles, predictions differed from experimental values and significantly varied at very high angles (predictions were zero as compared to measured wear). Equation (2.10) was developed for an idealised case of cutting where only the leading face of the particle is in contact with the surface which is realized only during low impact angles (where the length/depth ratio of the impact crater is of the order of 10) and impacts at high angles were not considered to be significant. Discrepancies were attributed to this fundamental flaw in the Finnie formulation as stated by Bitter [34, 86] and modifications were made as described in the next section. It was suggested by Finnie [33] that for erosion studies with majority of impacts occurring at low angles, equation (2.10) can be used without any modifications, but for high angles of impact empirical coefficients were necessary to match wear data.
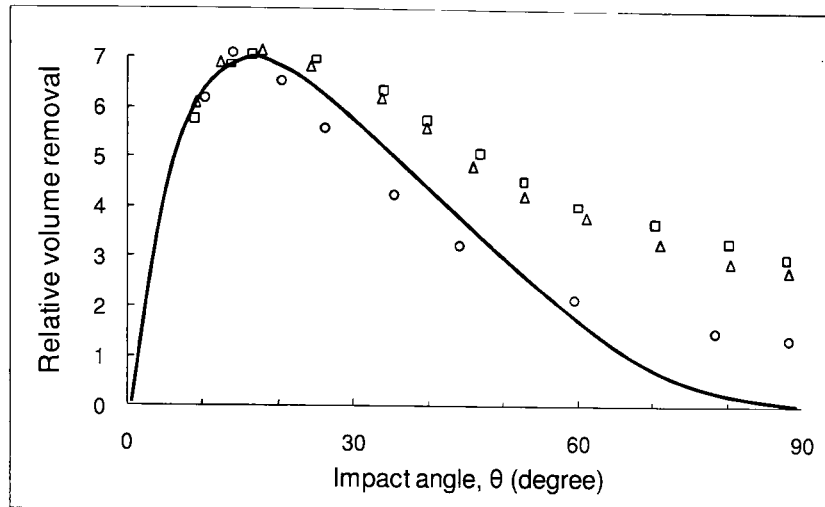
Figure 2.18 The general trend of erosion wear of ductile materials for various impingement angles as predicted by equation (2.10) is represented by the solid line. Experimental data for erosion for different materials (Δ-Copper; □-SAE 1020 Steel, O-Aluminium) are also shown for comparison. Image reproduced from Finnie [33].

2.3.2.2 Combined Finnie-Bitter formulation

Bitter proposed that at high impact angles material removal by 'cutting action' is minimal and wear due to 'deformation' predominates [34, 86]. The Finnie model equations (2.9 and 2.10) does not consider this 'deformation' component and hence the observed large deviations at high impact angles. Based on post test surface observations Bitter [34, 86] pointed that material was plastically deformed due to severe impacts at high impingement angles and formulated a numerical expression for this component.

$$E_d = \frac{1}{2} \frac{M(V_P \sin\theta - V_n)^2}{\delta},$$ (2.11)

where E_d is volume loss due to deformation mechanism, M is the total mass of impinging particles, V_n is the velocity component normal to the surface below which erosion does not occur (critical velocity and is material specific) and δ is deformation wear factor (energy required to remove unit volume of material due to deformation).

At low impact angles, a possibility of particles exiting the surface with a residual velocity exists and hence only a fraction of particle kinetic energy is transferred to the surface during impact for wear [34, 86]. Modifications of the Finnie equations were proposed as given by equations (2.12 and 2.13).

$$E_{c1} = \frac{2MV_p(V_p \sin\theta - V_n)^2}{(V_p \sin\theta)^{1/2}} \left(V_p \cos\theta - \frac{C(V_p \sin\theta - V_n)^2}{(V_p \sin\theta)^{1/2}} \emptyset \right), \quad \theta \leq \theta_{p0}, \quad (2.12)$$

$$E_{c2} = \frac{1/2M \left[V_p^2 \cos^2\theta - K_1(V_p \sin\theta - V_n)^{3/2} \right]}{\emptyset}, \quad \theta \geq \theta_{p0}, \quad (2.13)$$

where K_1 and C are material and experimental constants respectively, $\emptyset$ is the cutting wear factor (the quantity of energy needed to remove a unit volume from a surface) and θ_{p0} is the impact angle at which the horizontal velocity component has just become zero when the particle leaves the body.

The total wear component at any instant is given by;

$E_r = E_d + E_{c1}$ (when $\theta \leq \theta_{p0}$);

$E_r = E_d + E_{c2}$ (when $\theta \geq \theta_{p0}$):

Values for C, V_n, K_1, δ and $\emptyset$ were determined based on data obtained from erosion tests conducted by Finnie [33]. Erosion rates were predicted for the same materials as conducted by Finnie [33] and good correlations between experiments and calculations were reported.

2.3.2.3 Model of Neilson and Gilchrist

The theoretical work of Bitter was considered extensive and extremely intricate due to the inclusion of elastic and plastic behaviour of the surface material [82, 118]. The complexity of equations (2.11 to 2.13) prompted the need for simpler analytical solutions. Neilson and Gilchrist [82] proposed an erosion wear equation analogous to Finnie and Bitter formulations,

incorporating both the cutting (Ø) and deformation (δ) wear components. The behaviour of erosion rates were dependent on the relative magnitudes of cutting and deformation wear constants (Ø and δ) and a simpler wear equation (2.14) was proposed.

$$E_r = \frac{m_p V_p^2}{2} \frac{(\cos^2 \theta \sin n\theta)}{\emptyset} + \frac{m_p}{2} \frac{\left(V_p \sin \theta - V_n\right)^2}{\delta}, \qquad \theta \leq \theta_{p0},$$

$$(2.14)$$

$$E_r = \frac{m_p V_p^2}{2} \frac{\cos^2 \theta}{\emptyset} + \frac{m_p}{2} \frac{\left(V_p \sin \theta - V_n\right)^2}{\delta}, \qquad \theta \geq \theta_{p0},$$

where n is a constant. The values for parameters δ, Ø and n are dependent on various factors such as material-abrasive properties, impact velocity and within this framework are obtained from experimental data.

2.3.2.4 Two Stage ductile erosion model by Tilly [30]

The previously discussed models were reported to have resulted in good correlations, however, according to Tilly [30, 78] the experimental observations were not in accordance with the established velocity and particle size dependence on erosion wear. Theoretical models described erosion wear as a function of the square of the velocity (contrary to experiments [30, 78, 99]) and were predicted to be independent of particle size, whereas particle size has been reported to be major factor (section 2.2.2.1). Tilly eroded steel surfaces using 700μm quartz particles at very high velocities using air as the continuous phase and observed the indentation under a scanning electron microscope (SEM). Along with the primary indentation, secondary damage around the impact site was observed which was attributed to particle fragmentation, with these fragments causing secondary impacts and hence greater overall damage. Thus a two stage erosion wear mechanism was proposed, in which primary wear and secondary wear both are associated with the transfer of kinetic energy to the surface due to impact. The novelty of this study therefore is it

incorporates the effect of particle fragmentation and the erosion caused by these fragments. It was observed that below a certain particle size, wear due to particle fragments were not observed and a numerical equation (2.15) was formulated by Tilly [30].

$$E_r = \frac{V_P^2}{\epsilon}\left[1 - \left(\frac{d_0}{d_p}\right)^{3/2}\frac{V_0}{V_P}\right]^2 + \frac{V_P^2}{\gamma}F, \tag{2.15}$$

where ϵ and γ are defined as the energy required to remove unit mass of material due to primary erosion and secondary erosion process respectively, F is the degree of fragmentation which is a function of velocity, particle size and impact angle, V_0 and d_0 are the threshold velocity and diameter below which no erosion takes place.

For implementation of this model, it was required to determine threshold values for particle diameter and velocity, along with the degree of fragmentation (F), ϵ and γ values. This demanded several tests to be conducted for different particle velocity and diameters and coefficients to be determined from experimental data. Despite this only reasonable agreement between experimental and material studies were reported by Tilly [30], with a lot of scatter at high velocities.

2.3.2.5 Huang et al. [24] model correlations

A new phenomenological model was theoretically derived for erosion of materials in slurry jet flow and was implemented in conjunction with CFD by Wang et al. [42]. The analysis was based on numerically determining indentation volumes and the force required to remove this material volume. According to Huang et al. [42], erosion wear can be described by equation (2.16) and a detailed derivation is presented elsewhere [24].

$$E_r = \frac{K_1 m_p^{1.125} V_p^{2.25} (\cos\theta)^2 (\sin\theta)^{0.25}}{(1+B)^{0.125} \, E_B^{0.125} \, \sigma_B^{0.7} \, \varepsilon_B^{1.2}} + \frac{K_2 E_B^{1.1} d_p^{0.05}}{\sigma_B^{0.98} \, \varepsilon_B^{1.44}} \left(\frac{m_p V_p^2 \sin^2\theta}{1+B} \right)^{1.15} \qquad (2.16)$$

where E_r is the material removed per impact, K_1 and K_2 are material coefficients associated with plastic flow stress and values of which are to be experimentally determined. For instance, for 44W carbon steel, experimentally determined values were K_1= 7.48 ×10^{-4} and K_2= 0.283 ×10^{-6}.

It is suggested that for equation (2.16) to be applicable for a different material, a new set of K_1 and K_2 values must be determined. E_B, σ_B and ε_B are the stiffness, hardness and elongation of the target material, respectively; B= E_B/ E_P is defined as the stiffness ratio describing relative strength of target to erodent materials; ε_B is the ductility of eroded material; m_p is the particle mass; V_p and θ are the local impact velocity and angle respectively.

Equation (2.16) is a combination of two physical erosion degradation mechanisms, the first part representing cutting wear and the second part representing deformation wear components. Wang et al. [42] used equation (2.16) in conjunction with CFD to predict wear due to impingement for flow exit velocities of 9m/s and nominal impingement angle of 90°. In the case study of Wang et al. [42], the application of CFD enabled local particle impact data to be predicted as a function of position. This data was then fed into equation (2.16) and erosion profiles were predicted, which were qualitatively similar to experimental data. However, quantitatively the size (wear scar region) and the maximum wear depth were both under predicted by nearly 50%. Prediction errors were attributed to a combination of factors, namely, misalignments between test surface and the exit of the nozzle, particle size distributions and turbulence effects (note the turbulence effects on particles were neglected).

Several other conceptual numerical models were purported to provide numerical wear data as a function of mechanical properties of abrasive-target materials and local conditions [35, 98, 119-121]. These models, despite the ability to predict erosion phenomenon under certain circumstances, fail to do so at all conditions and can also be difficult to adopt

it to many practical applications [42, 84, 122, 123]. A relatively simpler approach to predicting wear was also pursued and empirical models were developed, a few of which are described in the next section.

2.3.3 Empirical wear models

Erosion wear rates for a material in a chemically inert medium depends on the number of particle impacts, the angle and velocity of these impacts and the behaviour of the material to these impacts [33]. This can be numerically represented by equation (2.17).

$$E_r = A \times V_P^n \times f(\theta), \tag{2.17}$$

where E_r is the erosion rate (defined as the average mass lost to the average mass of impacting particles), V_p and θ are local particle impact velocity and angle, n is the velocity exponent which is generally in between 2 to 3 (section 2.2.3.1). 'A' is associated with the mechanical properties of the abrasive-material combination. Empirical coefficients obtained from testing provide a value for 'A' as an alternative to analytically predicting material behaviour. The angular dependency of erosion wear is described as a trigonometric function of local impact angle.

Using equation (2.17) as the basic frame work, numerical equations were postulated and coefficients which provided wear correlations were determined from experimental data. These models can provide accurate correlations as long as the applied scenario is similar to the conditions that generate the empirical coefficients [63]. Examples of which are models of Alhert [124], McLaury et al. [125], Grant and Tabakoff [126] and the energy approach of Roco and Addie [7] are briefly described in the following section.

2.3.3.1 Wear model of Alhert [124]

Wang and Shirazi [37] predicted erosion rates on pipe bends using a CFD based approach and an erosion model developed by Alhert [124] for sand particle impacts in water given by equation (2.18),

$$E_r = A \, F_s \, V_p^{1.73} f(\theta) B^{-0.59}, \tag{2.18}$$

where F_s is the particle shape coefficient, (F_s=1.0 for sharp particle, 0.53 for semi-rounded or 0.2 for fully rounded sand particles; particles used in testing had sharp geometrical features), V_p is the local impact velocity; 'A' is an empirical constant related to the mechanical properties of surface and abrasive and the value of which is 1.2246×10^{-7} (obtained from experiments) while 'B' is the Brinell's Hardness number of the test material. Alhert [124] used two functional forms for angular dependence, with matching conditions applied at 15°. The dependence on impingement angle, $f(\theta)$ is given by equation (2.19), in which a, b, x, y and z are all empirical constants to be determined from experiments.

$$f(\theta) = a\theta^2 + b\theta, \qquad \text{for } \theta \leq 15°, \tag{2.19}$$

$$f(\theta) = x \cos\theta^2 \sin\theta + y \sin\theta^2 + z, \qquad \text{for } 90° > \theta > 15°.$$

The equation is very similar in comparison to the model suggested by McLaury et al. [125] which was built on experimental observations of high silica sand impacts on carbon steels. The only difference between these two model is the inclusion of an additional term, 'Z' in the angle dependence equation [125].

Haugen et al. [127] developed an empirical model based on equation (2.17) and applied that equation to predict wear as a function of flow velocity on various configurations of valves made of different materials. A different angle dependence function comprising 8 empirical constants was developed, the coefficients were obtained from experimental test data. Using the new equation, Haugen et al. [127] predicted wear on different materials (coefficients for these materials were obtained from experimental data reported elsewhere) and testing suggested reasonable correlations. It was suggested that discrepancies were seen due to the lack of well refined tests results and hence the inability to accurately describe the impact angle dependence of a particular material. Hence a further number of additional testing was suggested. It was reported that this technique developed on the

premises of equation (2.17) can be used to successfully extrapolate data from laboratory to plant, provided careful selection of empirical constants.

2.3.3.2 Empirical correlations of Grant and Tabakoff [126]

A particle can impact a surface more than once and both the occasions can lead to wear and numerical equations should consider wear due to secondary impacts of a particle. This can be predominant within a geometry where particles impact at sliding angles (very low angles with high velocities) and hence an empirically developed restitution factor was proposed [126]. Grant and Tabakoff eroded 410 stainless steel using silica sand in dry conditions (air) and developed an erosion equation (2.20) based on empirical coefficients [126]. The *Co-efficient of Restitution* R_t, (also termed restitution factor) is defined as the ratio of the post and pre collision impact velocities [128]. Grant and Tabakoff observed that introduction of a restitution factor made predictions closer to experimental wear and the proposed equation (2.20) is as follows.

$$E_r = K_1 \left\{ 1 + C \left[K_2 \sin\left(\frac{90}{\theta_{po}}\theta\right) \right] \right\}^2 V_p^2 (\cos^2 \theta)(1 - R_t^2)$$
$$+ K_3 (V_p \sin\theta)^4,$$

$$C = 1 \text{ if } \theta \leq 3\theta_{po} \quad \textbf{(2.20)}$$
$$C = 0 \text{ if } \theta \geq 3\theta_{po}$$

and $R_t = 1 - 0.0016 V_p \sin\theta$,

where ϵ is the average mass removed by a single particle, $K_{1,2,3}$ are all proportionality constants, R_t is the tangential restitution factor, θ_{po} is the impact angle at which the horizontal velocity component has just become zero when the particle leaves the body.

2.3.3.3 Energy approach for wear correlations

Roco and Addie [7] used an energy based approach to determine the erosion wear from average flow parameters and concentration distributions in the proximity of exposed surfaces. Mechanistic and stochastic models

provided a numerical description of wear mechanism at particle scale. Average threshold energy for the initiation of wear due to a particular mechanism was determined from laboratory experiments conducted on small scale devices. The mechanical energy dissipated by particle-wall interactions is assumed proportional to the amount of material removed. Flow modelling on practical geometries provided information regarding particle-wall interaction energy which was then correlated to actual wear based on coefficients obtained previously.

2.3.4 Difficulties in implementing wear models in an industrial context

The majority of the models purported for erosion predictions were developed and validated in dry conditions (conditions in which the viscous effects of the fluid medium had negligible effect of particle motion). Before proceeding further, the impact parameters need to be clearly defined since confusion exists in the literature regarding impact angle and velocity [92] and a clear distinction should be drawn between local and nominal conditions. Local impact conditions are defined as those associated with the abrasive particle just prior to impact, while nominal conditions are those which are used to define mean flow parameters and can be distinguished as illustrated in Figure 2.19, where V is the average flow velocity at the exit of the nozzle, α is the nominal impingement angle (90° in this case), V_p and θ are particle impact velocity and angle respectively; also h here is the stand-off or sample nozzle separation distance. Thus for slurry erosion the individual local impact particle velocities can approximately vary between 0 to 5 m/s for a bulk velocity of 5m/s, but for the case of an air borne condition, the local impact velocities of every particle is taken to be a constant and equal to the bulk flow velocity and the same is applicable to impact angles.

During the formulation stage of both conceptual and empirical models, the constants (deformation and cutting wear factor, threshold velocity and diameter, restitution factors, velocity exponent, proportionality constants) were developed for nominal (bulk) flow conditions. Huang et al. [24] and Haugen et al. [127] pointed out that for equations (2.12 to 2.16), Ø (cutting)

and δ (deformation) coefficients were determined from experimental values for nominal impact angles of 30° and 90° respectively. It was argued that a different set of δ and Ø values would have resulted if the correlations were made at; for example, 20° and 70°, which also contradicts the statement that δ and Ø are associated with material constants. Lester et al. [84] remarked that conceptual models (equations 2.13 to 2.17) works for an air-borne system since the average local impact conditions are similar and hence the resulting local wear, however, directly applying these models for a slurry erosion system maybe inappropriate. Huang et al. [24] thus developed a conceptual model professed to capture wear at various impact conditions, taking into account the local variation of impact dynamics in a slurry medium. Only reasonable correlations resulted from this model as reported by Wang et al. [42] and the range of applicability of the model is still to be tested.
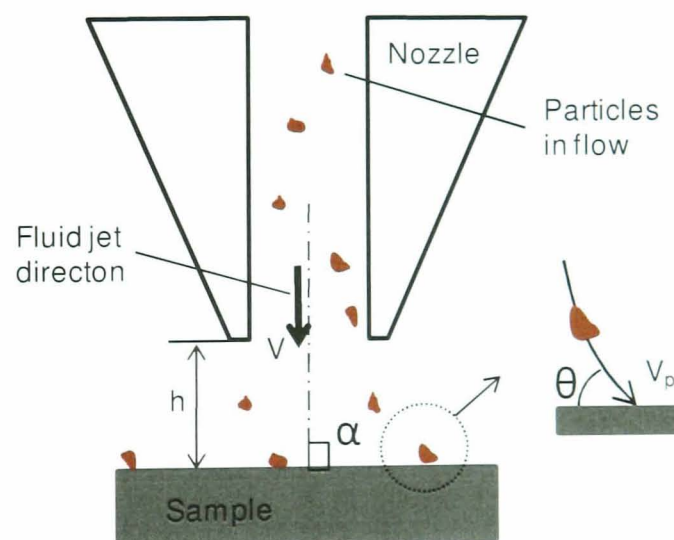
Figure 2.19 Diagram of particle impacts as generated by a JIT illustrating the difference between nominal impact data and local impact data.

Empirical models based on the simple background of equation (2.17) were developed which has reported in good correlations. Lester et al. [84] developed an empirical wear function based on equation (2.17) and correlation factors for that equation was obtained from test data. Good fits of the observed erosion data were found when a general fitting function was used, however, non-physical behaviour was observed when predicting wear

outside the envelope of experimental data. It was suggested that although the behaviour of empirical models are satisfactory, extrapolation can, in general be a dangerous practice. The issues in developing models were presented due to the difficulty in attaining high precision erosion data at various impact regimes. Dobrowolski and Wydrych [123] compared the performance of various erosion models (both theoretical and empirical) in an industrial setting and concluded by stating that erroneous predictions were made by all models at different sections and none of the models behaved uniformly (qualitatively if not quantitatively precise). Meng and Ludema [63] attributed this to inability of the wear models to accurately encapsulate the effect of various wear mechanisms occurring in an industrial setting. This is further complicated by the behaviour of a material in a particle impact event.

Furthermore the numerous experiments required to be conducted to procure data for constants in order to effectively use these equations, limits their beneficial aspects. The fitting functions, material and experimental constants which are required for a specific wear model to work are not universal for all particle/material combinations and herein lay the issue of predicting wear rates.

2.4 Summary

A brief introduction to the major wear mechanisms was presented and it is emphasized that all these mechanisms can prevail in slurry transport equipment and the interactions between individual mechanisms can be sophisticated. Keeping to the theme of this work only wear by impact erosion and the numerous factors affecting wear rates were discussed in detail. Also various methods (experimental, numerical and empirical) adapted to analyse and predict material behaviour was reviewed. Although several experimental techniques have been practised, none of the test equipments can accurately reproduce the entire range of conditions in which erosion wear can be prevalent. Numerical and empirical equations profess to predict wear over a wide range of conditions and as a function of material can be very subjective and the applicability of which are limited.

Chapter 3

An overview of the Computational Fluid Dynamics method

3.1 Introduction

The effects of fluid flow on particle motion and subsequent erosion mechanism was reviewed in chapter 2 which emphasises the significance of local flow regime and hence an accurate description of the flow field is vital. The study of the flow field leading to erosion in this study is pursued using Computational Fluid Dynamics (CFD) methods which also forms a critical part of the developed wear prediction method. Hence the need to understand the theoretical (governing laws of physics) and functional aspects of CFD. An overview of the entire CFD process in a general context is presented in this chapter.

3.2 Computational Fluid Dynamics- An introduction

CFD can be described as an engineering method integrating the discipline of fluid mechanics with mathematics and computer science. Traditionally, experimental and analytical (mathematical) methods have been used to study the various aspects of fluid dynamics and to aid in the design of equipment involving fluid flow. The advent of computational (numerical) methods has provided a simple yet robust method to solve flow problems, particularly when the involved flow physics is very complex. Since CFD is predominantly dependent on the performance of computational resources, faster solutions with better accuracies (described later) incurs higher computing costs. Nevertheless CFD has several unique advantages and finds its application in various fields of engineering such as research,

design, aerospace, automotive, biomedical science, chemical and process industries, civil and environmental, power generation, sports science, etc [129].

3.2.1 An overview of the CFD process

CFD codes (programs) are structured around numerical algorithms that can solve fluid problems. Various commercial codes are available and all codes contain the three main elements: (1) a pre-processor, (2) a solver and (3) a post-processor. These three elements are structured in a particular way depending upon the functional aspects of each stage and for operational ease. These elements are described briefly as follows;

3.2.1.1 CFD Pre-processor

Pre-processing consists of the submitting a flow problem to a CFD code by means of an interface and the transformation of this entry into a suitable form for use by the program. The majority of the user activities involved in the entire CFD process are performed during this stage, which comprises,

- Defining the geometry of interest which is referred to as the computational domain (flow domain).

- Grid generation- consisting the sub division of the entire flow domain into a number of smaller but inter-connected domains. The sub-domains are termed cells for a 2-D geometry and volumes for a 3-D geometry for a finite volume method (strictly control elements for a finite element method) and the resulting grid of numerous interconnected small cells generates the computational grid or mesh.

- Selection of the appropriate physical and chemical (if any) phenomenon that needs to be studied and definition of the fluid properties.

- Specification of appropriate boundary conditions at the edges or faces of the computational cells which coincide or touch the domain boundaries. This is done to associate a physical condition to the geometry to represent the actual flow process.

The pre-processing stage is discussed later in further detail by considering the CFD simulation of the impingement based erosion problem.

3.2.1.2 CFD Solver

The governing flow equations are solved over the computational mesh generated in the pre-processing stage to obtain discrete values for the flow parameters studied. Typically, flow equations are solved using one of the three numerical techniques: finite difference, finite element and spectral methods. The finite volume method, a particular finite difference formulation is fundamental to most of commercial CFD packages such as *CFX/ANSYS*, *FLUENT INC*, *PHOENICS* and *STAR-CD*. *FLUENT INC* is used in our study and hence only the finite volume method is described here. The numerical solution technique using finite volume method consists of the following steps;

- Integration of the governing equation of fluid flow over all the control volumes (cells for 2-D geometry) of the flow domain.

- Discretization- converting the resulting equations into a system of algebraic equations.

- Solving the algebraic equations by an iterative method to obtain a solution for the formulated flow problem.

The flow phenomenon covered by these algebraic equations is complex and non-linear. A special iterative approach the SIMPLE technique is used to solve these equations to obtain the flow solution.

3.2.1.3 Post-Processor

Discrete values for flow parameters at each data point (centre of the computational cell) during the processing stage are converted into a simple form for meaningful interpretation. This conversion is usually into various graphical forms such as vector plots, line and shaded contour plots, surface plots, line graphs, particle motion tracks, fluid streamlines, etc. The numerical calculations performed in this stage are related to extracting data from the solution and does not influence the obtained flow solution.

3.3 Governing flow equations

The governing equations of fluid flow describe the physical laws of conservations in a mathematical form. The equations pertaining to our case study are listed below followed by its description.

- Mass of fluid is conserved (Continuity equation)
- Momentum is conserved and the rate of change of momentum equals the sum of the forces on a fluid element (Momentum equation)

A primary assumption in all our flow analysis is regarding the nature of the fluid and is treated as a continuum.

3.3.1 Fluid as a continuum

A medium is defined as a continuum (concepts of averaging and average aspects) if the behaviour of a small volume can be considered as a representative for the entire volume (Figure 3.1). This small volume is regarded as the control or limiting volume. However, real materials are not a continuum (at molecular level the effects of molecular motion cannot be ignored) and hence a limiting volume cannot be taken as zero. The limiting volume for a fluid is usually taken to be 1µm above which the events at molecular levels can be ignored and flow medium larger than this are considered a continuum [128]. Another factor to be considered for a continuum is the relative scales of a limiting volume and the flow domain size. If the size of a cube representing a limiting volume is less than ten times smaller than the flow channel then the medium cannot be considered a continuum and this flow is called rarefied flow which has to be treated on a molecular basis.
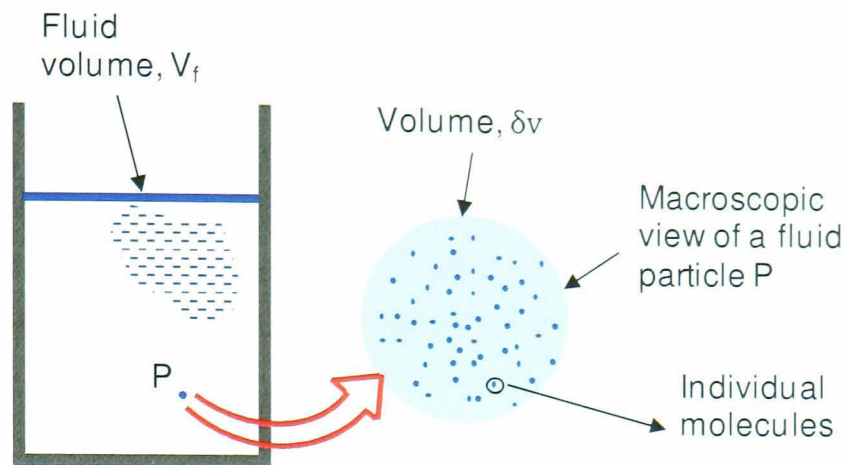
Figure 3.1 An illustration of fluid as a continuum. V_f is the volume of the fluid, P is a fluid particle of a volume δv. For this fluid volume to be treated as a continuum, the volume δv should be greater than the limiting volume.

A small element of fluid with its centre located at (x, y, z) and with sides δx, δy and δz is defined in Figure 3.2 and u, v and w are the normal flow velocities in the x, y and z directions. This fluid element is considered as representative of the fluid medium, i.e., control volume and the flow governing equations subsequently described are with respect to this volume. Fluid density is denoted by ρ and t represents time.
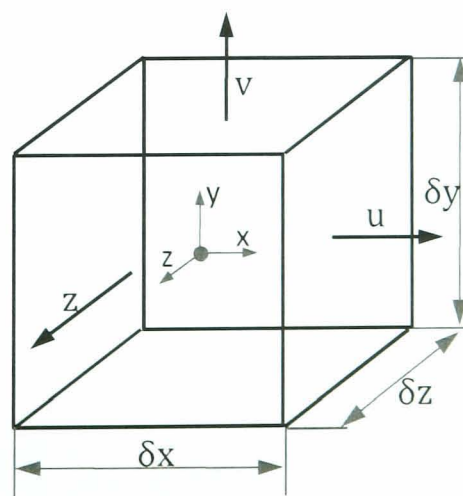
Figure 3.2 Description of flow parameters within a control volume of sides' δx, δy and δz used in the numerical equation described later.

3.3.2 Conservation of mass (Continuity equation)

One of the conservation laws that are relevant to fluid flow is that 'matter may neither be created nor destroyed'. The law of mass conservation states that the rate of accumulation of mass within a control volume is equal to the net flow of mass into the control volume. For a small fluid element (control volume) as defined in Figure 3.2, the continuity equation (3.1) is given by,

$$\frac{\partial \rho}{\partial t} + \frac{\partial (\rho u)}{\partial x} + \frac{\partial (\rho v)}{\partial y} + \frac{\partial (\rho w)}{\partial z} = 0,$$

or in a vector notation,   (3.1)

$$\frac{\partial \rho}{\partial t} + \text{div}(\rho u) = 0.$$

Equation (3.1) is for an unsteady and 3-D flow at a point in a compressible fluid. A flow is considered to be unsteady if the flow variables (such as velocity, density, etc) fluctuate with time. Almost all fluid flows are unsteady in nature due to turbulence, but the majority of these flows are considered to be steady since the local variations can be statistically averaged with time as described later. The continuity equation for a steady and incompressible flow (density remains constant) becomes,

$$\text{div } U = 0 \text{ or } \nabla.U,$$

which can also be written (in cartesian co-ordinates) as,   (3.2)

$$\frac{\partial u}{\partial x} + \frac{\partial v}{\partial y} + \frac{\partial w}{\partial z} = 0.$$

3.3.3 Conservation of momentum (Force balance equation)

Newton's second law states that the rate of change of momentum of a fluid particle equals the sum of the forces on the particle and for a particular direction (x in this case) is given by equation (3.3),

$$\sum F_x = ma_x, \qquad (3.3)$$

where F_x and a_x are the force and acceleration along x direction and m is the mass of the fluid element for an incompressible fluid.

The forces on a fluid element are grouped into two: body forces and surface forces. The body forces that can influence fluid momentum are gravity, centrifugal, Coriolis and electromagnetic forces. The surface forces which affect fluid momentum are the pressure and viscous forces, the effect of which is to deform the fluid element. The mathematical derivation of the 3-Dimensional momentum conservation equation (3.4) is provided elsewhere [130] and the equation can be written (in cartesian coordinates) as,

$$\frac{\partial \rho u}{\partial t} + \frac{\partial (\rho uu)}{\partial x} + \frac{\partial (\rho uv)}{\partial y} + \frac{\partial (\rho uw)}{\partial z} = -\frac{\partial p}{\partial x} + \frac{\partial \tau_{xx}}{\partial x} + \frac{\partial \tau_{yx}}{\partial y} + \frac{\partial \tau_{zx}}{\partial z} + S_{Mx}, \qquad (3.4a)$$

$$\frac{\partial \rho v}{\partial t} + \frac{\partial (\rho vu)}{\partial x} + \frac{\partial (\rho vv)}{\partial y} + \frac{\partial (\rho vw)}{\partial z} = -\frac{\partial p}{\partial y} + \frac{\partial \tau_{xy}}{\partial x} + \frac{\partial \tau_{yy}}{\partial y} + \frac{\partial \tau_{zy}}{\partial z} + S_{My}, \qquad (3.4b)$$

$$\frac{\partial \rho w}{\partial t} + \frac{\partial (\rho wu)}{\partial x} + \frac{\partial (\rho wv)}{\partial y} + \frac{\partial (\rho ww)}{\partial z} = -\frac{\partial p}{\partial z} + \frac{\partial \tau_{xz}}{\partial x} + \frac{\partial \tau_{yz}}{\partial y} + \frac{\partial \tau_{zz}}{\partial z} + S_{Mz}, \qquad (3.4c)$$

where S_M is the overall effects of body forces and S_M for that particular axis is denoted by a suffix. P is the pressure on the fluid element (pressure at a point in a fluid is independent of direction) and the viscous stresses are denoted by τ, with the suffix denoting the plane on which that particular stress is acting.

3.3.4 The Navier-Stokes Equation

Equation (3.4) contains viscous components, τ, and suitable models are introduced to obtain useful forms of the conservation equation (3.4). Assuming the fluid is Newtonian (viscous stresses are proportional to the rate of deformation and the proportionality constant is defined as the dynamic viscosity, η) and that continuity equation is satisfied, the stress terms in equation (3.4) can be expressed as,

$$\tau_{xx} = 2\eta \frac{\partial u}{\partial x}, \qquad \tau_{yy} = 2\eta \frac{\partial v}{\partial y}, \qquad \tau_{zz} = 2\eta \frac{\partial w}{\partial z},$$

$$\tau_{xy} = \tau_{yx} = \eta \left(\frac{\partial u}{\partial y} + \frac{\partial v}{\partial x} \right); \qquad \tau_{xz} = \tau_{zx} = \eta \left(\frac{\partial u}{\partial z} + \frac{\partial w}{\partial x} \right); \qquad (3.5)$$

$$\tau_{yz} = \tau_{zy} = \eta \left(\frac{\partial v}{\partial z} + \frac{\partial w}{\partial y} \right).$$

Substitution of the above viscous terms into the momentum conservation equation (3.4) yields the complete set of Navier-Stokes (NS) equation (3.6) in cartesian coordinates as:

$$\frac{\partial \rho u}{\partial t} + \frac{\partial (\rho u u)}{\partial x} + \frac{\partial (\rho u v)}{\partial y} + \frac{\partial (\rho u w)}{\partial z} = -\frac{\partial p}{\partial x} + \eta \left(\frac{\partial^2 u}{\partial x^2} + \frac{\partial^2 u}{\partial y^2} + \frac{\partial^2 u}{\partial z^2} \right) + S_{Mx},$$

$$\frac{\partial \rho v}{\partial t} + \frac{\partial (\rho v u)}{\partial x} + \frac{\partial (\rho v v)}{\partial y} + \frac{\partial (\rho v w)}{\partial z} = -\frac{\partial p}{\partial y} + \eta \left(\frac{\partial^2 v}{\partial x^2} + \frac{\partial^2 v}{\partial y^2} + \frac{\partial^2 v}{\partial z^2} \right) + S_{My}, \qquad (3.6)$$

$$\frac{\partial \rho w}{\partial t} + \frac{\partial (\rho w u)}{\partial x} + \frac{\partial (\rho w v)}{\partial y} + \frac{\partial (\rho w w)}{\partial z} = -\frac{\partial p}{\partial z} + \eta \left(\frac{\partial^2 w}{\partial x^2} + \frac{\partial^2 w}{\partial y^2} + \frac{\partial^2 w}{\partial z^2} \right) + S_{Mz}.$$

The Navier-Stokes equation used in CFD codes to solve fluid problems can be represented in vector form as,

$$\underbrace{\frac{\partial (\rho \vec{u})}{\partial t}}_{\substack{\text{Local} \\ \text{acceleration}}} + \underbrace{(\vec{u}.\nabla)\rho\vec{u}}_{\substack{\text{Advection} \\ \text{term}}} = \underbrace{-\nabla p}_{\substack{\text{Pressure} \\ \text{gradient}}} + \underbrace{\eta \nabla^2 \vec{u}}_{\text{Diffusion}} + \underbrace{S_M}_{\substack{\text{Body} \\ \text{force}}}. \qquad (3.7)$$

3.4 Turbulence and its modelling

3.4.1 Flow regimes and Reynolds number

Osborne Reynolds [131] observed the nature of fluid flow within a glass tube by injecting dye into the water column at different flow velocities. For small flow velocities, the dye followed a continuous and undisturbed (laminar regime) path along the centre of the tube. As velocities increased, the dye began to disperse and mix downstream (transitional regime) of the tube. Further increases in velocity produced a repeating curling pattern but random in nature (turbulent regime). These observations led to the general classification of different flow regimes (illustrated in Figure 3.3); in laminar regime, the flow structure is characterized by smooth and stable motion between fluid layers and turbulent regime is characterized by random, chaotic motion of fluid particles in addition to the mean motion. In between the two lies the transitional regime in which flow instabilities begin to set in and if conditions permitting can develop into a fully turbulent regime.
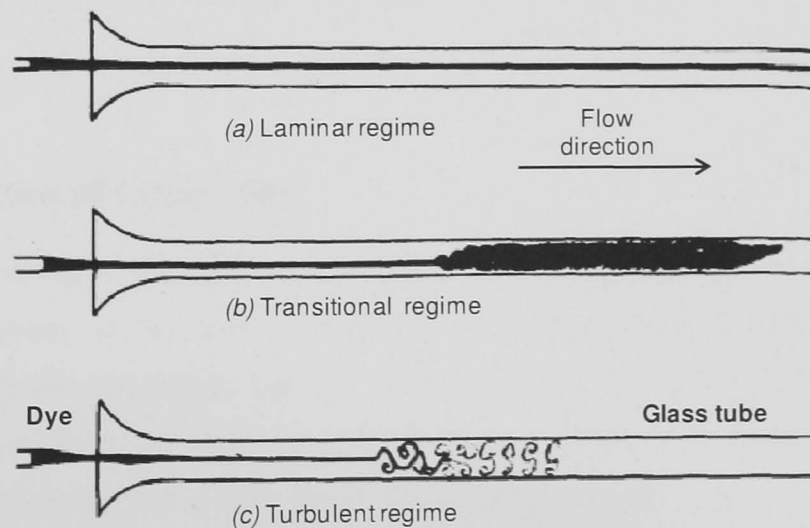
Figure 3.3 Illustrations showing (a) laminar, (b) transitional and (c) turbulent flows. Reported by Reynolds and reproduced from Gilkeson [132].

Reynolds proposed a non dimensional number known as the Reynolds number (Re) given by equation (3.8) which is used to characterize a flow regime. The onset of turbulence depends on the ratio of inertia force to

viscous force which is indicated by Re. At low Re (<2000), inertia forces are smaller than the viscous forces and naturally occurring disturbances are dissipated away and flow remains laminar. At high Re (>4000), the inertia forces are sufficiently large to amplify any disturbances and transition to turbulence occurs. For Re values between 2,000 and 4,000 the flow regime is said to be transitional [133].

$$Re = \frac{\rho \times v \times l}{\eta},$$
(3.8)

where Re is the non-dimensional Reynolds number, l and v are the characteristic length and velocity of the flow domain and η is the fluid viscosity. Re is low for the flow of highly viscous oil through a pipe at low velocities but for the impingement erosion scenario, the Re can be very high (for example in a pipe with water flowing: density $\rho = 1000$ kg/m^3, viscosity $\eta = 1 \times 10^{-3}$ Pa-s, characteristic length $l = 0.1$m for diameter and flow velocity $v = 10$m/s the Re is 1×10^6) hence the flow turbulent. Re can hence be used to serve as a guideline to determine the suitable approach for studying a fluid regime.

3.4.2 Nature of turbulence

According to Davidson [134] there is no proper definition of turbulent flow, however, a number of characteristic features are associated with turbulent flows and hence can be described as a *"chaotic and random state of motion in which the velocity and pressure changes continuously with time in substantial regions of the flow"*. The majority of the flows of engineering significance are turbulent in nature and therefore there is a need to capture the effects of turbulence. An attribute of a turbulent flow is that the velocity field is unpredictable at local instantaneous level and a minute change to the initial conditions can produce a large change to the subsequent motion. This is illustrated by Figure 3.4 which presents the variation of local flow velocities with time on two different occasions at exact location for exact nominal initial conditions. Despite the identical settings, the numerical behaviour of

measured local flow velocities with time was different on each occasion. It was suggested that minute variations in initial conditions can be amplified by turbulence and hence the resulting variation in flow parameters [134, 135].

For precise determination of a turbulent flow field, it is necessary to capture these minute variations which can occur over various length and time scales. For a typical flow field with $Re = 10^5$, large eddies (turbulent flow structures) can be of the size of $l = 0.01$m and the smallest eddies can be around 320nm. To directly solve a turbulent flow problem with a $Re = 10^5$, it is required to resolve the computational domain down to the size of smallest eddies and also the time step would be similarly small to resolve the time fluctuations. It was estimated that with modern computational ability, it would take approximately 960 years to solve this flow problem and hence the complexities in analysing turbulent behaviour [132, 134].
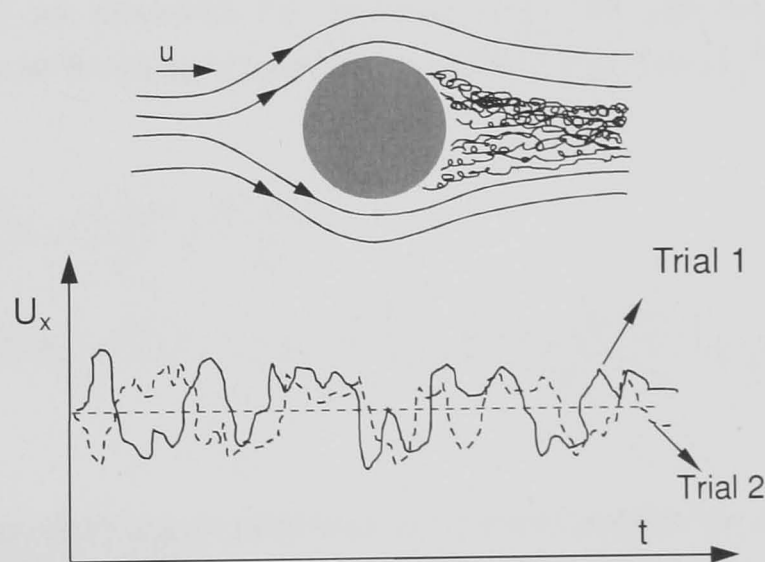
Figure 3.4 A cylinder in a flow filed with an upstream flow velocity of u. Measurements of local velocity at a fixed position behind the solid body with time for the two nominally identical conditions are also shown.

3.4.3 Closure problem of turbulence

Although the nature of turbulence, based on the local variations of flow parameters with time (Figure 3.4), appears to be random and unpredictable, its statistical properties are not, i.e. the local variations over time can be

averaged and the instantaneous velocity can be decomposed into a steady mean value ū, with a fluctuating or turbulent component u'(t) superimposed on it: u(t)= ū+ u'(t). Similarly other flow variables of interest can be represented as averages as shown;

x-velocity: $u = \bar{u} + u'$

y-velocity: $v = \bar{v} + v'$

z-velocity: $w = \bar{w} + w'$

pressure: $p = \bar{p} + p'$,

where u' denotes turbulence fluctuations from the mean values represented as $\bar{u}$ for the x direction and p stands for pressure. Substituting these into the x-direction momentum conservation equation (3.4) yields the Reynolds Average Navier-Stokes (RANS) equation for the x-direction (in cartesian coordinates) as described by equation (3.9). The derivation and the complete set of RANS equations can be obtained from Wilkes [130].

$$\frac{\partial \rho \bar{u}}{\partial t} + \frac{\partial (\rho \bar{u}\bar{u})}{\partial x} + \frac{\partial (\rho \bar{u}\bar{v})}{\partial y} + \frac{\partial (\rho \bar{u}\bar{w})}{\partial z} \tag{3.9}$$

$$= -\frac{\partial \bar{p}}{\partial x} + \frac{\partial (\tau_{xx} - \rho \overline{u'u'})}{\partial x} + \frac{\partial (\tau_{yx} - \rho \overline{u'v'})}{\partial y} + \frac{\partial (\tau_{zx} - \rho \overline{u'w'})}{\partial z} + S_{Mx}.$$

Equation (3.9) has six additional terms in comparison to equation (3.4a) which are associated with the average turbulent fluctuations and are referred to as *Reynolds Stresses*. The six additional terms are,

$$-\rho \overline{u'u'}, \ -\rho \overline{u'v'}, \ -\rho \overline{u'w'}, \ -\rho \overline{u'v'}, \ -\rho \overline{u'w'}, \ -\rho \overline{v'w'}.$$

With complex algebraic manipulation of the NS and RANS equations, expressions for these Reynolds Stresses can be obtained, which leads to further unknown turbulent terms. This is known as the closure problem of turbulence in which further generation of equations to determine unknown terms introduces more unknowns. There have been a multitude of attempts

to plug this gap by introducing additional, ad hoc equations, which are empirical in nature. The resulting closed set of equations are referred to as *turbulence closure models*, however, these models tend to work only for a narrow class of flow problems [136].

3.4.4 Turbulence modelling

The closure problem means that it is impossible to develop a predictive statistical model of turbulence by simply manipulating the equations of motion. To close the gap additional information is needed which are essentially empirical. Attempts to close this gap are made using the *'Eddy Viscosity Hypothesis'* proposed by Boussinesq in 1877 (as presented by Davidson [134]), forms the foundation of many engineering turbulence models. The hypothesis proposes that Reynolds Stresses are proportional to the mean rates of deformation and can be described by equation (3.10):

$$-\rho\overline{U'_i U'_j} = \eta_t\left(\frac{\partial \overline{U_i}}{\partial x_j} + \frac{\partial \overline{U_j}}{\partial x_i}\right) - \frac{2}{3}\rho k\delta_{ij}, \qquad (3.10)$$

here, $\delta_{ij}=1$ if $i = j$ and $\delta_{ij} =0$ if $i \neq j$; with $i,j = 1, 2, 3$ corresponding to x, y and z axes. In equation (3.10) η_t is the turbulent or eddy viscosity, k is the turbulent kinetic energy and U represents velocity in general. For instance, if i=1 and j=2, then equation (3.10) reduces to

$$-\rho\overline{u'v'} = \eta_t\left(\frac{\partial \overline{u'}}{\partial y} + \frac{\partial \overline{v'}}{\partial x}\right); \quad \text{And for i=j=1, we get} \quad -\rho\overline{u'u'} = 2\eta_t\left(\frac{\partial \overline{u'}}{\partial x}\right) - \frac{2}{3}\rho k;$$

Several models which provide mathematical relations (also known as transport equations) for η_t and k have been proposed and some of which are listed in Table 3.1.

Table 3.1 Various available models proposed to provide closure for the turbulence problem and a few commercially available models are specified this table.

Name	No. of extra transport equations
Mixing length model	Zero
Spalart-Allmaras model	One
k-ε Model	Two
Reynolds stress model	Seven

3.4.4.1 Mixing length model (Zero equation)

Ludwig Prandtl, based on the kinetic gas theory proposed rough approximate equations for Reynolds stresses. It was advocated that if one velocity scale (v) and one length scale (l) can adequately describe the majority of turbulence effects, then η_t, can be written as,

$$\eta_t = C_1 \, \rho \, v \, l, \tag{3.11}$$

where C_1 is a constant of proportionality, v and l are characteristic turbulent velocity and length scales. It is assumed that only eddies of these length and velocity scales have a major effect on the mean flow, the flow is 2-D and where the significant Reynolds Stresses is $-\rho \overline{u'v'}$. The Reynolds stresses can then be determined using the relation,

$$-\rho \overline{u'v'} = \rho \, l_m^2 \, \left| \frac{\partial U}{\partial y} \right| \frac{\partial U}{\partial y} , \tag{3.12}$$

where $l_m = C_1 C_2 l$ and is the *mixing length* (empirically obtained), C_2 is another constant and l is the turbulent length scale. It is assumed here that $\partial U / \partial y$ is the only significant mean velocity gradient.

For different flows which fits these assumptions, it is required to change the values of mixing length and for a substantial category of simple turbulent

flows, the mixing lengths can be described by simple algebraic equations provided by Rodi (1980) as reported by Versteeg and Malalasekera [137].

3.4.4.2 Spalart-Allmaras model (One equation)

This one equation model was developed by the employees of Boeing in the early 1990's and finds its application predominantly in the aerospace industry. It involves only one transport equation for the calculation of the turbulent viscosity parameter. However, the length scale is not calculated and has to be specified which is accomplished by the means of an algebraic formula similar to the mixing length hypothesis [136, 138].

This model contained constants which were tuned (by comparison with experiments) for external aerodynamic flows and hence its ability to give good performance for boundary layers with adverse pressure gradients, which is vital for the prediction of stalled aerodynamic flows. Hence it is used extensively in the aerospace industry and in the design of turbo-machinery (also note the relatively low computational resources required to solve only one additional equation). However, due to the difficulty in defining the length scale, this model is unsuitable for more general internal flows [139].

3.4.4.3 k-ε Model (two equation model)

One of the earliest and 'complete' turbulence models applicable to high Re flows was the standard two equation k-ε model (SKE) proposed by Launder and Spalding [135] which invokes two additional transport equations to close the RANS equations. The advantages of the SKE model are that it exhibits robust performance across a wide range of industrial relevant flows and it has been extensively validated. The performance of the k-ε model has been reported to be particularly good for confined flows such as those applicable to industrial sectors [139]. In spite of the numerous successes, the SKE has been reported to show only moderate agreement in some unconfined flows, flows with large strains and severe curvature such as axi-symmetric impinging jets [140, 141].

To account for these deficiencies in the SKE, changes were made by Yakhot et al. [142] and Shih et al. [143] giving the updated Renormalization group (RNG) *k-ε* model and the realizable *k-ε* model (RKE) respectively. The numerical simulations of the impingement jet based erosion case was conducted using the RNG *k-ε* model due to the ability of this model to capture the impingement flow characteristics better [59, 144-146]. The mathematics involved is the derivation is highly profound and only the model equations derived by Yakhot et al. [142, 147] for high Reynolds numbers are quoted here,

$$\frac{\partial(\rho k)}{\partial t} + \text{div}(\rho k U) = \text{div}\left[\alpha_k \eta_{eff} \, \text{grad} k\right] + \tau_{ij}.S_{ij} - \rho\varepsilon \ , \tag{3.13}$$

$$\frac{\partial(\rho\varepsilon)}{\partial t} + \text{div}(\rho\varepsilon U) = \text{div}\left[\alpha_k \eta_{eff} \, \text{grad}\varepsilon\right] + C_{1\varepsilon}^* \frac{\varepsilon}{k}\tau_{ij}.S_{ij} - C_{2\varepsilon}\rho\frac{\varepsilon^2}{k} \ , \tag{3.14}$$

where,

$$\tau_{ij} = \rho\overline{u_i' v_j'} = 2\eta_t S_{ij} - \frac{2}{3}\rho k \delta_{ij} \ , \tag{3.15a}$$

$$\eta_{eff} = \eta + \eta_t \ , \quad \eta_t = \rho C_\eta \frac{k^2}{\varepsilon} \ , \tag{3.15b}$$

$$C_{1\varepsilon}^* = C_{1\varepsilon} - \frac{\gamma(1 - \gamma/\gamma_0)}{1 + \beta\gamma^3} \ , \quad \gamma = \frac{k}{\varepsilon}\sqrt{\left(2S_{ij}.S_{ij}\right)} \ , \tag{3.15c}$$

C_η=0.0845; α_k=α_ε=1.39; $C_{1\varepsilon}$=1.42; $C_{2\varepsilon}$=1.68; γ_0=4.377; β=0.012;

where S_{ij} is the rate of deformation, τ_{ij} is the shear stresses, δ_{ij}=1 if i = j and δ_{ij} =0 if i ≠ j. Here i,j = 1, 2, 3 corresponding to x, y and z axes. The values for the numerical constants were chosen such that good correlation between experiments and numerical solutions were obtained [142] and these coefficients are also used in Fluent as the standard value.

3.4.4.4 The Reynolds Stress Model (Seven equation model)

The Reynolds stress model (RSM) is the most elaborate and complex turbulence model yet developed. It abandons the eddy-viscosity hypothesis which presumes isotropic behaviour of Reynolds stresses and provides a set

of transport equations (total 7 equations) for closure of the RANS equation which takes into account the anisotropic behaviour of turbulence. For the RSM to do this, several unknown turbulence processes need to be modelled, and the computer storage requirements and run times are significantly increased in comparison with two-equation models. Examples of flows where the RSM might be very effective are cyclone flows, highly swirling flows in combustors and rotating flow passages. Despite the elaborate description of turbulence, the RSM might not always yield results that are of better-quality to simple models in all classes of flows, thus nullifying the additional computational costs incurred. Similar to the SKE model it performs poorly when dealing with axi-symmetric jets [137].

3.5 CFD solution procedure and essentials in Fluent

CFD simulations in this study are conducted using Fluent which is based on the finite volume method and the solution scheme used by Fluent to solve a flow problem consists of various steps as described;

1. The integral form of governing flow equations (conservation, Navier-Stokes and turbulence models) are discretized over all control volumes using the finite volume method to obtain approximate linearised set of equations.
2. The governing algebraic equations are then solved through to obtain an initial flow solution.
3. The initial problem is then updated using the values obtained in 2 using an iterative scheme until a solution with the required accuracy is obtained.

In the following sections, the Finite volume discretization method, the pressure-velocity linkage and solution techniques such as under-relaxation and convergence criterion are briefly described.

3.5.1 Finite Volume method

The finite volume method discretizes the integral form of the conservation equations directly in the physical space. The subdivided computational domain is made up of a finite number of adjoining control volumes so that the grid point lies at the centre of a control volume as shown in Figure 3.5. At the centroid of each of the control volumes, the variable values are calculated and stored. Next the differential equations describing the flow are discretized for each control volume [Patankar, 1980]. These equations are then numerically integrated over each individual control volume to evaluate the fluxes through each of the cells. For instance the integration process would yield a solution variable flux through faces n, e, s and w for the shaded control volume (Figure 3.5).
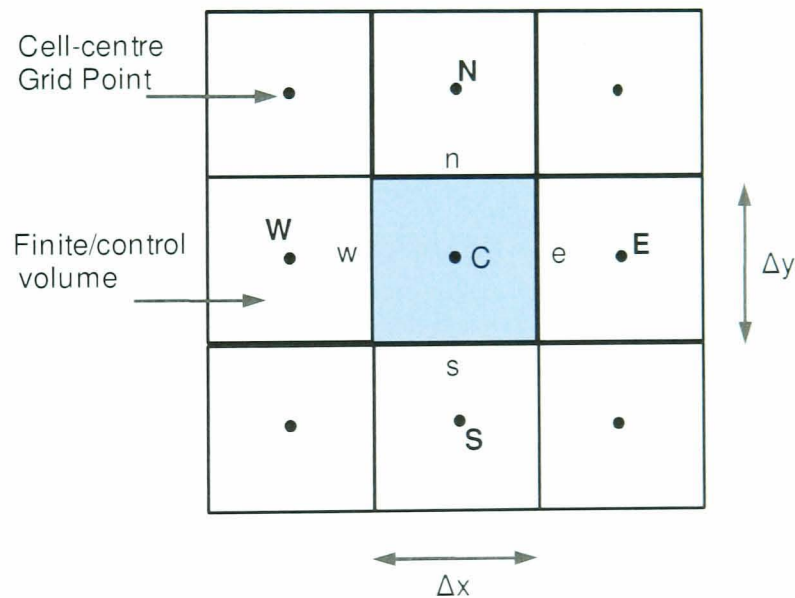
Figure 3.5 Illustration of the finite volume method for a two dimensional structure grid.

Interpolation is used to express variable values at the control volume surfaces in terms of the centroid values and suitable formulas are used to approximate surface and volume integrals. This approximation leads to numerical errors which can be reduced by reducing the inter node distances (Δx and Δy). An algebraic equation for each of the control volumes/surfaces

can be obtained in which a number of the neighbouring nodal values appear. What makes this approach so attractive is that the integration of the conservation quantities, ensure that mass and momentum are conserved locally to each control volume. The implication is that global conservation is ensured so that the grid, whether fine or coarse will produce solutions which exhibit exact integral balances.

3.5.2 Pressure-Velocity Coupling

Due to the incompressible assumption, the solution to the governing equations is complicated by the lack of an independent equation for pressure. In each of the momentum equation for a 3-D geometry, the fluid flow is driven by the contribution of pressure gradients. With the additional equation provided by the continuity equations, this system of equations is self-contained; there are four equations for four dependent u, v, w and p but no independent transport equation for pressure. The implication here is that the continuity and momentum equations are required to solve for the velocity and pressure fields in an incompressible flow and linkage of pressure and velocity can be constructed by different possible methods, one such method used in our study is the SIMPLE scheme, which stands for Semi-Implicit Methods for Pressure-Linkage Equations. This was introduced by Patankar and Spalding (1972).

3.5.3 Convergence Criterion and Residuals

The goal of a numerical solution is to achieve solution convergence of a desired degree of accuracy. The residuals are the imbalance between the LHS (left hand side) and RHS (right hand side) of the discretized momentum and transport equations summed over all the computational cells in the domain. If the residuals of a particular flow parameter is below the convergence criterion, the flow solution is said to be converged or has reached a state beyond which further iterations does not greatly affect the solution. For a flow solution with various parameters the residuals of all concerned flow variables should drop below the criterion to obtain a

converged solution and the iteration process terminates. Fluent recommends a default criterion of 10^{-3} which is sufficient for the majority of flow studies [129]. However, the default criterion may not necessarily yield accurate solutions in all cases because convergence is dependent upon several factors including the degree of computational grid refinement achieved, discretization schemes and complexity of the flow.

3.5.4 Under-Relaxation factors

Under-relaxation factors are used to control the change of flow variable, $\emptyset$, during the iterative solution process which aids flow convergence. Because the governing equations are non linear, it is important to control the extent of change of $\emptyset$ during each iteration. An appropriate setting for under-relaxation factor, α, accelerates solution convergence as described by equation (3.16).

$$\emptyset_{new} = \emptyset_{old} + \alpha(\emptyset_{new} - \emptyset_{old}). \tag{3.16}$$

For a value of $\alpha = 1$ represents no under relaxation and can cause divergence of the flow field. On the other hand, a value of $\alpha = 0$ represents zero progress from one iteration to the next step. Thus an optimum values lies in between these two extremes and depends invariably on the particular problem under investigation. Recommendations of a value between 0.3 and 0.8 for transport equations are suggested in Fluent's user manual [129].

3.5.5 Source of solution errors

It is to be recognised that errors are inherent during the entire CFD procedure and this section serves to address the possible sources of errors that an awareness and appropriate measures to counter it can lead to flow solutions with minimum errors. Some prevalent source of errors associated with numerical solutions includes the following classification:

- <u>Discretization error:</u> These errors are due to the difference between the exact solution of the modelled equations and the numerical solution with a space and time (if the solution is time dependent) resolution. These errors arise because the discretized equations are approximate equations and not exact solutions, i.e., to recover the actual equation from the discretized versions of momentum equations. a truncated part which is a function of the space and time resolution has to be added. Discretization errors arise since the truncated part is neglected during the solution process and the degree of this error can be reduced by using smaller length and time scales.

- <u>Round-off error:</u> These errors exist due to the difference between the accuracy of the computing system and the true value of a variable. A computational system stores only finite number of significant digits for a particular variable, with the default value been seven (referred to as single precision). It has been reported that by performing calculations using single precision can account to a solution error of 25% in comparison to a double precision solver (15 significant digits) [132]. Hence to reduce round-off errors, it is recommended to use the double precision facility, however this does increase computational expense.

- <u>Iteration or convergence error:</u> These errors occur due to the difference between a fully converged solution of a finite number of grid points and a solution that has not fully converged but the iterative process was terminated prematurely. Convergence errors can therefore occur because of either the solution algorithm requires a greater time for completion or the convergence criterion was set to large tolerances to prematurely terminate the CFD process when the solution may still be considerably far from its converged state. To reduce these errors, it is recommended for the iteration process to run its full course towards convergence as dictated by the convergence criterion.

- <u>Physical-modelling errors:</u> These errors are more of an uncertainty which is defined as a potential deficiency due to lack of knowledge.

Although Navier-Stokes equations are considered to be exact, solving them is impossible for most flows of engineering interest. The sources of uncertainties are due to the lack of thorough knowledge of the flow phenomenon; uncertainties of some degree within model parameters, and experimental confirmation of the models are not always possible or is incomplete. The possible ways to reduce these uncertainties is by improving the robustness of turbulence models and by extensive validations.

3.5.6 Validation and verification

Additionally to the errors described previously, uncertainties can also arise while performing a numerical simulation which could be due to improper modelling of the physics involved or incorrect computational design due to inappropriate approximations and simplifications (neglecting certain minor geometrical features which can significantly affect the solution). Verification and validation provides a means to assess the credibility of a CFD solution through quantitatively estimating the inherent errors and uncertainties.

Verification can be defined as a process for assessing the numerical simulations uncertainty and conditions permissible, estimating the sign and magnitude of the numerical simulation error and the uncertainty in that estimated error. This procedure concerns primarily to the input parameters used for defining the geometry, initial conditions, computational grid size, the numerical discretization scheme.

Validation on the other hand can be defined as a process assessing simulation model uncertainty by using benchmark experimental data and when conditions permit, estimating the magnitude of the simulation modelling itself. This means validating the simulation results by direct comparison with experimental evidence at the exact range of conditions. It is essential to validate a CFD simulation using practical data to evaluate the performance of the turbulence model used.

3.6 Summary

An overview of the CFD process and a mathematical representation of governing laws were presented. The effect of turbulence can be significant and predicting its exact nature can be impossible. However, the statistical behaviour can be captured using various approximate models. Using various numerical techniques the governing flow equations can be solved for a particular flow problem to obtain a solution. Although errors are inherent in the system, it is possible that through a systematic modelling procedure and a bit of practical knowledge about the studied flow problem, good credible solutions can be obtained using CFD.

Chapter 4

CFD simulations slurry jet impingement erosion

The primary developmental stage of the wear prediction method involves the accurate definition of local particle impact conditions leading to material degradation. Using Computational Fluid Dynamic (CFD) methods, a standard sand based erosion test (JIT) is recreated and information relating to prevailing particle impact conditions are extracted. The impetus in choosing CFD methods to predict impact conditions is mentioned in section 4.1 and a complete account of the approach adopted in numerically recreating an impingement based erosion case is presented in section 4.2 and 4.3 of the chapter. The final part (section 4.4) summarizes vital findings and presents impact data contributing to the initial development phase of the wear-map.

4.1 Effect of numerical methods (CFD) on Erosion studies

The effects of flow dynamics on particle motion within an enclosed geometry was reviewed in section 2.2.3 and the outcome on erosion rates was typified by Clark [16] and Humphrey [15]. Initial studies, such as Finnie [33], Bitter [34], Neilson and Gilchrist [82], Sundararajan [35], were intended towards capturing the behaviour of an erosion system analytically and were based on the observations from air-borne erosion tests. The impetus here was to improve material behaviour in pneumatic process equipment. With increasing use of hydro-transport equipment and need to minimize material loss the effects of fluid flow on erosion wear mechanisms were studied. The primary difference between air and fluid based erosion systems is the extent to which particle impact conditions can be affected by fluid viscosity [15].

Particle impact conditions (angle, velocity and rate) in a liquid erosion system can vary widely with position and this could account for the existence of different types of erosion wear modes [15], which was in contrast to the predominance of a particular wear mode in an air based erosion systems [78]. Hence accurate definition of local impact conditions are required for numerical wear predictions.

Advancements in optical measuring instruments and techniques have driven forward the progress made by researchers in determining local impact conditions. Wood et al. [117, 148] studied the effect of flow disturbances introduced in the upstream of a transparent pipe bend section on the motion of sand particles using high speed visualization techniques. The purpose of this study was to acquire qualitative knowledge of particle motion. Feyerl et al. [149] designed an elaborate impingement cell within a protected cage with thick glass windows at one side to enable particle image velocimetry (PIV) measurements. The purpose of the cage was to prevent particles damaging the expensive PIV equipment. This provided numerical data relating impact conditions around the test surface. Optical imaging techniques have proven to be effective in determining the relevant data [83], however, this can be extremely difficult considering the harsh environmental conditions and high expenditures incurred. More importantly, the effort needed to analyse visual data obtained from these measurements can be tremendous. For instance, in an actual JIT particle size/shape and their location in flow field can vary. This affects subsequent particle motion and hence impact data. A particular particle motion track visually recorded has to be related to a specific shape/size and location. Considering the range of particles size/shape and possible location in flow field, large amounts of data can be obtained and processing this can be close to impossible. Numerical methods provide an alternative to practical measurements which has progressed with advancements in computing power and improved the mathematical understanding of erosion behaviour.

CFD analysis has been used to provide reliable information regarding existing flow conditions around the required geometry and operating conditions. Particle trajectories within any flow geometry and conditions can

be predicted with good accuracy [83, 150] and with it impact data computed. Brown in 2002 [36], reported the successful application of CFD in addressing a significant erosion problem on the inner surfaces tee-junctions, part of a slurry pipeline system. Parslow et al. [81] used CFD methods to qualitatively predict erosion patterns in pipe components of complex geometry and reported good correlation to experimental observations. Principally CFD methods are approximations and do not provide an exact solution to the flow problem. Numerical errors are inherent and can be amplified if the flow problem is incorrectly specified [137]. Zhang et al. [92] also pointed out a few concerns present in the CFD approach and recommended modifications for improvements. Nevertheless, CFD has improved the ability to predict erosion behaviour despite its intrinsic limitations. It was suggested that with careful modelling approach good correlations can be obtained [83, 151].

The numerical recreation of erosion wear reproduced by a fluid based impingement test on a flat sample was carried out and the entire process can be grouped together into two major parts;

1. Solution of the flow field generated by the impinging jet (Section 4.2),

2. Particle motion and impact data calculations (Section 4.3).

All simulation work was carried out using commercially available CFD software, *Gambit and Fluent Inc.*, and is reported in the following sections.

4.2 CFD simulation of the jet impingement flow field

CFD simulation of a flow problem involves various steps as discussed in section 3.2.1 and can be generally grouped into three main elements, namely, 1 pre-processing; 2 flow solution; 3 analysis and optimisation. The objective here is to convert a given physical flow problem into a numerically compatible form for processing and subsequently obtaining a solution to the flow problem. Different stages require different set of operator skills and the work carried out during modelling the JIT based erosion is sequentially detailed as follows;

4.2.1 Creation of geometry

The first step in any CFD analysis is to describe the flow geometry (also referred to as the computational flow domain). In simple terms, this involves regeneration of the exact physical geometry using a capable computational tool. Replicating the geometry precisely is a criterion for accurate results; however, this can induce immense computing cost and resources during processing stage, thus minimising the beneficial aspects of CFD. Hence geometries are simplified to reduce computational cost without greatly comprising the accuracy of the numerical solution. The impinging jet and sample configuration simulated are assumed to be symmetrical about the centre line of the nozzle (axi-symmetrical). Hence, the resulting flow domain on any particular plane along this centre line and perpendicular to the test surface is expected to be representative of the entire flow domain. Henceforth only a 2D model (Figure 4.1) was used (for 90°) to minimise computing resources without comprising solution accuracies due to geometrical simplifications, whereas for the 105° and 135° flow geometries symmetrical 3D models were used.

Actual geometry   **Computational geometry**
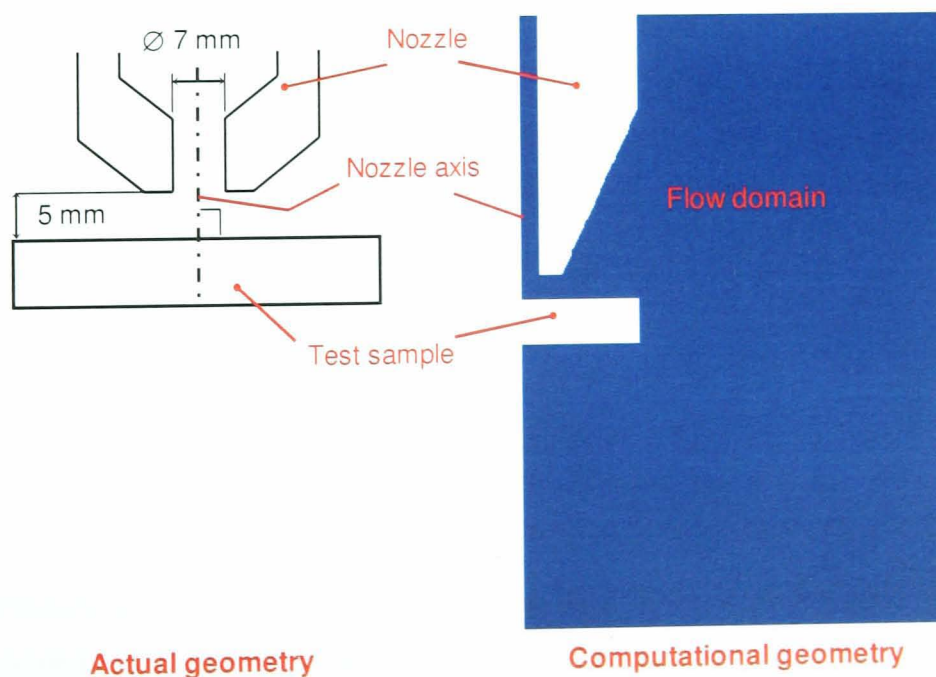
Figure 4.1 Schematic of the actual nozzle/sample configuration and the simplified 2-dimensional version generated using *Gambit*. Please note the sketch is not to scale.

4.2.2 Mesh generation

The second step; mesh generation or discretization of the numerical model is among the most important stages during pre-processing. CFD analysis requires the sub-division of the entire computational domain into a number of smaller, non-overlapping domains in order to solve the flow physics within the created geometry. These sub-divisions are termed as cells or elements (control volumes in 3-dimensional space) and the overlaying of these cells on the entire computational domain generates the grid/mesh. Governing flow equations are numerically solved and discrete values for flow variables are determined at each cell centre eventually yielding an overall solution to the flow problem (section 3.5). The accuracy of a CFD solution is governed by the number of cells in the mesh and in general, the prerequisite of a large number of cells leads to the attainment of a solution with high numerical accuracy.

Due to the strong dependency of solution accuracies with the interactions between the mean flow and the generated turbulence, adequate grid resolution is vital particularly for turbulent flows. In general, regions with major flow variations should be adequately resolved in order to accurately capture all possible substantial flow events and this demands the prior knowledge of the likely flow conditions.

An impingement jet and the resulting flow field has been a subject of intensive research and several studies has have reported [145, 152, 153]. Fluid exiting the nozzle undergoes severe changes in direction from normal to radial around the surface and velocity variations of small length scales can significantly affect the overall solution [144, 154]. It is hence suggested that a large number of computational cells should be used to adequately resolve this region. Variations in flow diffuse with increasing distance from the surface and a lower density mesh should suffice as suggested by Davis and Frawley [151]. This served as a guideline and a computational mesh with varying mesh density (defined as the total number of cells over a fixed area) was generated enveloping the entire flow domain as illustrated by Figure 4.2.
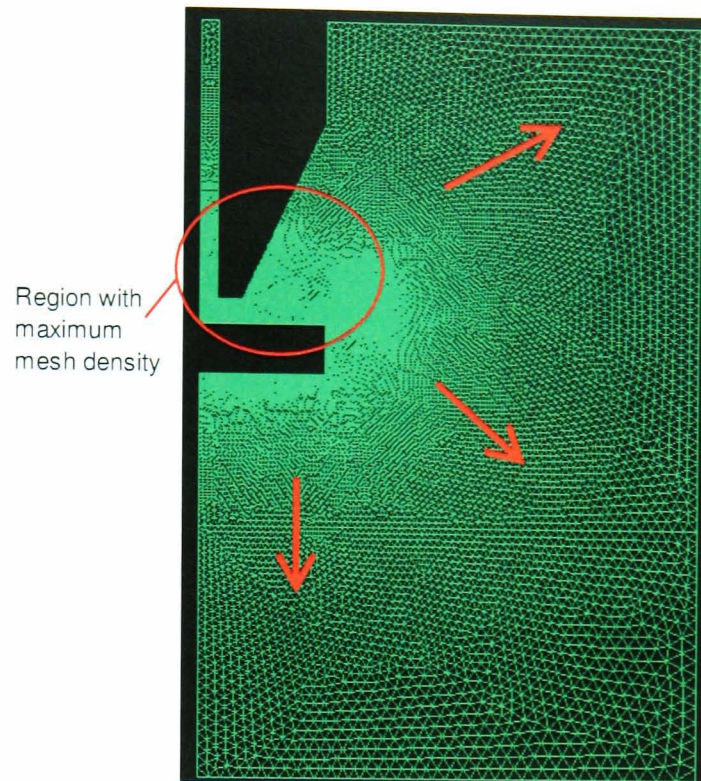
Figure 4.2 Computational mesh generated on the impingement jet flow geometry indicating regions of varying mesh density. Red arrows indicate the direction reducing mesh densities.

4.2.3 Specification of boundary conditions

The complex nature of fluid flow behaviour has important implications in directing the approach in prescribing the boundary conditions for a particular flow problem. It is required to define appropriate conditions that mimic the actual physical representation of a fluid problem into its numerical counterpart. This step in the pro-processing stage deals with the implementation of allowable boundary conditions for imminent simulations. Evidently the existence of a physical inlet and outlet boundary is impersonated by suitable boundary conditions with known values of flow variables. Appropriate boundary conditions are also required to be assigned to external solid walls bounding the flow and to any physical obstacles present within the domain. Surfaces of physical geometries can be represented in *Fluent* by 'wall boundary' condition which assign the physical condition of no flow across that surface.
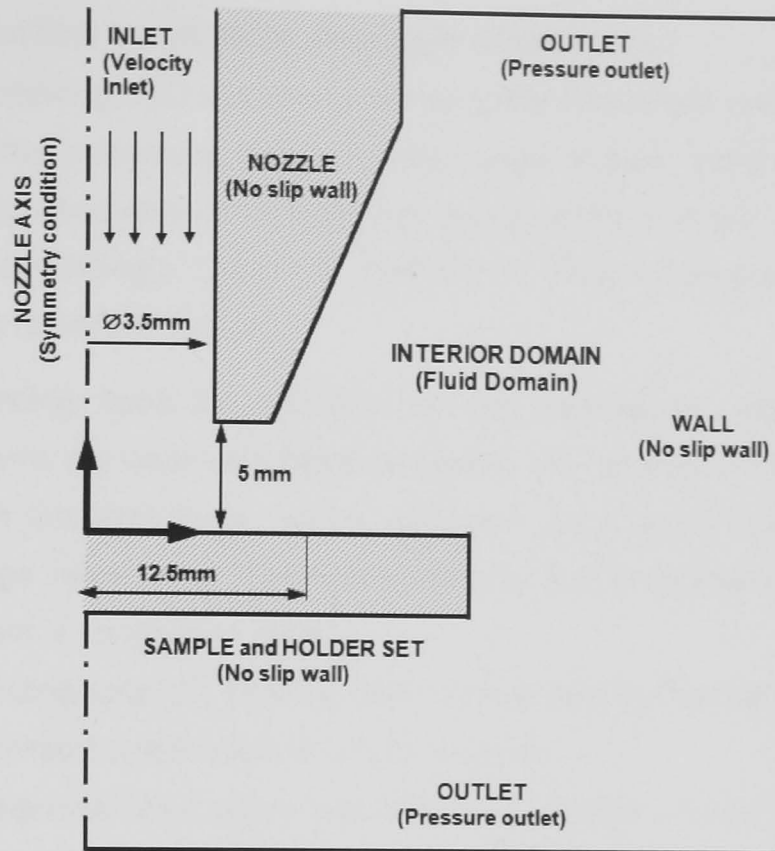
Figure 4.3 Approximated geometry of the JIT with boundary conditions imposed comprising the computational domain developed using Gambit.

The implementation of the above mentioned boundary conditions to our case is schematically illustrated in Figure 4.3. By definition, flow velocities on all solid walls are zero due to the implementation of no-slip condition [155]. For the inflow condition, the mean fluid jet velocity at which the fluid enters the domain is specified. Outflow boundaries indicate fluid exiting the domain and a known relative pressure (atmospheric pressure in our case) is typically associated with this boundary condition. Another boundary condition associated with this problem is the symmetrical axis boundary where all normal variations of flow parameters are zero and this axis is defined on the line representing the nozzle axis in the geometry. The final boundary condition to be associated is the interior of the computational flow domain which is representative of the fluid solution within the reservoir.

4.2.4 Selection of physics and fluid properties

The following CFD sub-processes described from here were carried out as part of the processing stage. A wide range of fluid problems exist and they are classified depending upon the nature of the problem and needs to be treated accordingly. Under the main title of CFD, a flow problem can be divided into many sub groups.

- Depending upon the variation of flow parameters with time, flow problems are described either as steady or unsteady. It must be noted that in turbulent flows, minute variations are present, however, if the average value of the flow variable (section 3.4) is constant with time the problem is considered *steady.*

- Depending upon the local variation of fluid density, the flow field can be considered compressible or incompressible.

- Subsequently the problem can further be divided into either *viscous or inviscid,* based on the effect of fluid viscosity.

- Viscous problems are further branched into *laminar* and *turbulent* flows.

The user is required to be fully aware of the physics involved in order to appropriately treat the flow problem and any simplifications implemented to reduce computational costs must justified with valid reasons.

• The recreated JIT is 3-dimensional in nature, however, the geometry was simplified to a 2-dimensional version as previously described (section 4.2.1.1) and the overall flow phenomenon was assumed to be invariant with time, hence the choice of a 2-D steady state model.

• The fluid re-circulated within the JIT rig is water, which by nature is incompressible and hence the problem was treated as incompressible.

• Water is viscous in comparison with air and it has been proven that wear rates can be radically reduced by high viscosity fluids. To model the effects of viscosity, viscid flow option was selected.

• The measure of the influence of viscosity over the entire flow domain can be provided by Reynolds number, defined in section 3.4.1 [156] and for our case can be determined using the equation,

$$Re = \frac{\rho \times V \times L}{\eta} \simeq 39{,}000,$$ (4.1)

where,

ρ, fluid density at 23°C= 998 kg/m³,

V, mean flow velocity = 5m/s,

L, characteristic length (Nozzle diameter in this case) = 7mm,

η, dynamic viscosity of fluid at 23°C = 0.9mPa-s.

Reynolds number of 40,000 confirms that the impingement flow regime is turbulent and the interactions between the turbulent eddy and the mean flow have to be accurately described.

4.2.5 Modelling turbulence effects

Dosnajh and Humphrey [90] examined the effects of flow turbulence on erosion due to impingement jets and concluded that rate of erosion decreases with increasing turbulence. Higher turbulence promotes better mixing and momentum exchange between various flow regions, thus reducing particle slip velocities (difference between local particle and fluid velocities) and in-turn reducing particle impact frequency. This results in an overall reduction in material removal rates and this effect was also observed by several other studies stressing the need to accurately capture the influence of turbulence on local fluid regime and hence erosion wear [90].

Due to the random nature of turbulence, which is characterised by local variations of flow variables occurring over a wide range of length and time scales, analysing a turbulent flow precisely would require computational resources which are virtually unattainable. Engineers and researchers resort to turbulence models which can provide an approximate yet reasonable solution and the accuracy of these solutions depends upon the ability of that particular model to capture all the important events of a certain flow phenomenon.

Several turbulence models are currently available and among which the two equation k-ε model is most widely used. Despite the many successful

applications in handling industrial problems, the standard k-ε model demonstrates only moderate agreement when predicting axis symmetric impingement jets due to the presence of extremely strained flow regions. This difficulty can be overcome by making improvised adjustments to model constants although this can reduce model robustness [141, 145, 157].

The Reynolds Stress Equation Model (RSM), which uses five additional equations to model turbulence, has been regarded as the most widely applicable turbulence models and has proved to be very accurate in many applications. However, the applicability and accuracy of this model is greatly compromised by the associated large computing costs [157]. It has also been reported that the RSM model performs similarly to the standard k-ε model when studying axis symmetric jet impingement flows [120].

Considerable research has been conducted over the evolution of turbulence modelling and advance k-ε models have been developed to counter the deficiencies (severely strained flow regions) of the standard k-ε model. Among the various advanced turbulence models, the renormalization group (RNG) developed by Yakhot et al. [158] has attracted considerable interest in academic and industrial circles for studying an axi-symmetric submerged impingement jet. Prediction accuracies of the RNG k-ε model has been reported to be significantly better than most of the turbulence models [140, 145, 159-161] and hence the RNG k-ε model (described in section 3.4.4.3) was used to numerically model the effects of turbulence on mean flow regime. Empirical model constants used were as per standard specifications [137].

4.2.6 Solution scheme

All numerical simulations were solved using the second order differential scheme for reduced numerical errors. Coupling between velocity and pressure were achieved using the SIMPLE scheme and all numerical simulations were converged when the residuals of all monitored flow parameters were below 1×10^{-4}. The solution obtained was further subjected to grid and domain size dependency studies to analyse the sensitivity of the

solution to modelling parameters as part of the verification process (section 3.5.7).

4.2.7 Flow modelling near the wall region

The overall effects of viscosity on mean flow in inertial flows (high Re) can be considered minimal, however, at regions close to wall boundaries it can be significant. Local fluid velocities at wall boundaries are zero (due to no-slip condition) and increase from zero to main stream condition. This increase occurs over a relatively thin region, known as boundary layer and the effects of viscosity in this region can be high. The events at the wall can have a major influence on the overall solution since walls act as the main source of turbulence and hence has to be accurately modelled [135]. Any compatible grid can be applied around the wall surface and a solution can be obtained, however, this may give unreasonable values for turbulent parameters which may subsequently lead to predictions of high particle impact velocities leading to inaccurate physical representation [130].

Traditionally, there are two approaches to modelling the near wall region. In one approach, the viscosity-affected inner region are not fully resolved, but semi-empirical formulas known as 'wall functions' are used to bridge the gap between the viscosity affected and fully turbulent regions [135]. In the other approach known as the near-wall modelling, turbulence models are modified to enable this region to be resolved with a mesh all the way to the wall [135]. The wall function approach is economical and reasonably accurate for industrial flow simulations, particularly for high Re flows and hence was opted in this study. A measure of the resolution of the viscosity affected layer is provided by y^+ (y-plus) value as defined by equation (4.2) [134];

$$y^+ = \frac{y}{\eta} \sqrt{\rho \tau_w} , \qquad (4.2)$$

where y is the distance from the centre of the nearest cell to the wall, η is the dynamic viscosity of fluid, ρ is fluid density and τ_w is the shear stress.

Two wall functions are available in Fluent: Standard and Non-equilibrium wall functions. For cases in which the surface is subjected to severe pressure gradients as in the case of an impingement flow or on an aircraft wing, the non-equilibrium wall function is recommended and as a guideline the y^+ values of the majority of the cells adjacent to the wall should be between $30 < y^+ < 300$. Simulations were conducted using the non-equilibrium wall function on the simplified geometry (Figure 4.1) with boundary conditions defined by Figure 4.3 for the conditions specified in Table 4.1. y^+ values of the cells adjacent to the wall was calculated to be mostly with the recommended range (Figure 4.4) and hence this approach was used in all further simulations.

Table 4.1 Conditions at which CFD simulations were carried out to study the sensitivity of flow solution with computational grid density.

Flow velocity (m/s)	Fluid: Water		Fluid pressure (Pa)	Turbulence model	Convergence criterion
	Density (kg/m³)	Viscosity (Pa-s)			
5	1000	1×10^{-3}	ATP (101325)	RNG $k\text{-}\varepsilon$	1×10^{-4}
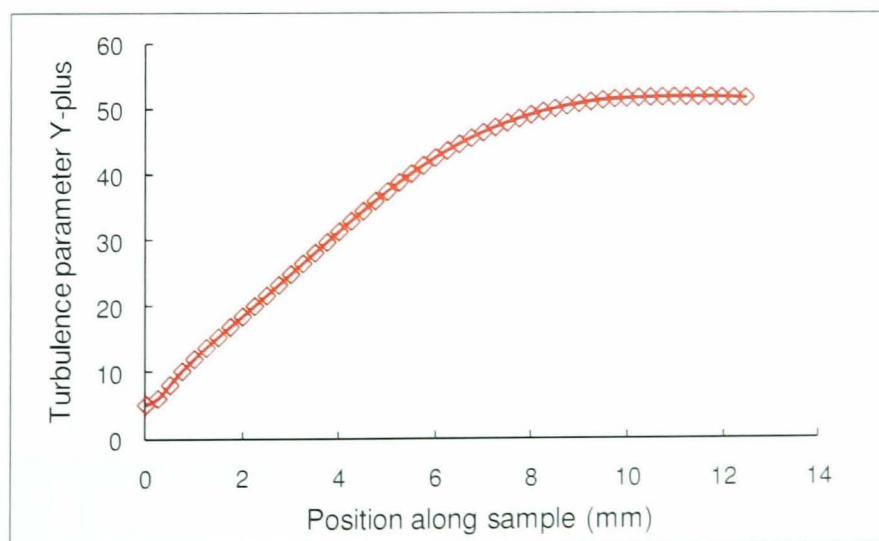
Figure 4.4 Variation of y^+ values along the test surface for a bulk flow velocity of 5m/s.

4.2.8 Verification and optimisation of computational mesh

A numerical grid with an adequate refinement does not ensure accurate representation of the physical problem but is considered a pre-requisite since the amount of numerical errors involved can be significantly reduced. However, the numerical accuracy of the solution is strongly dependent on the limitations imposed by computational costs and calculation times. Hence compromises are generally made between computational costs and numerical errors. As a good practice regions where flow variations are expected to have major influence on the overall solution are densely populated with cells and regions with minor variations are meshed with lesser number of cells which should ensures optimal utilization of computational resources with minimal numerical errors. This was followed for the study reported and the verification of the computational grid was carried out as described.

CFD simulations of the JIT geometry and with the boundary conditions defined in Figures 4.1 and 4.3 respectively, were conducted for the conditions specified in Table 4.1. Numerous simulations were conducted for computational grid with different number of cells and the variation of local fluid velocities 0.25mm above the surface and wall shear stress (described later) on the surface were recorded (Figures 4.5 and 4.6).

Wall shear stresses, according to Efrid [32] provides a direct measure of the viscous energy losses within the turbulent boundary layer and is related to the intensity of turbulence in the fluid acting on the wall, which can be expressed equation (4.3) [31],

$$\tau_w = \eta \left(\frac{\partial V}{\partial Y} \right)_{y=0} , \tag{4.3}$$

where, τ_w is the wall shear stress, η is dynamic fluid viscosity, V is the velocity component normal to the surface and Y is the normal distance from the wall.
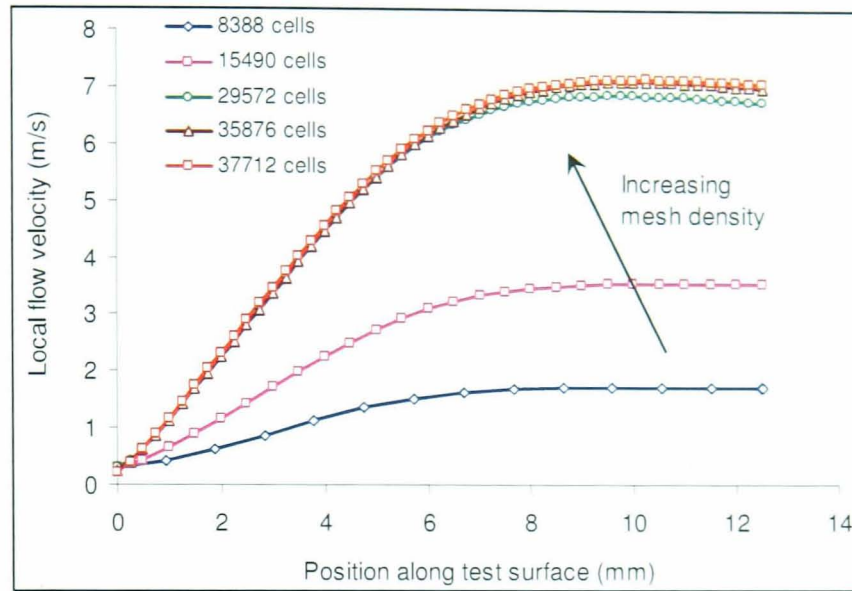
Figure 4.5 Variation of local fluid velocities, 0.25mm above the test surface, in the radial direction from the centre of the recreated test sample for different computational grid densities. Simulations were conducted on the computational geometry (Figures 4.1 and 4.3) and for conditions specified in Table 4.1.
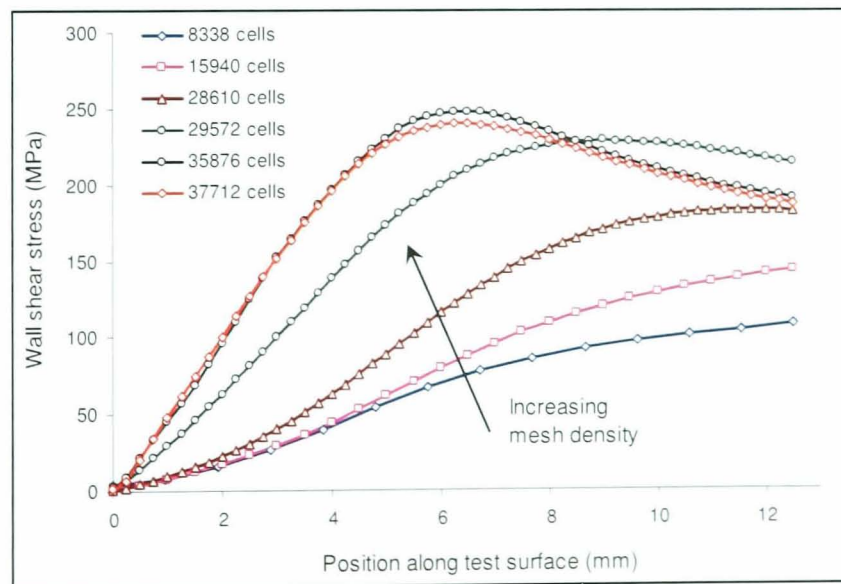
Figure 4.6 Variation of wall shear stress along the test surface in radial direction from the centre of the sample for different computational densities. Simulations were conducted on the computational geometry (Figures 4.1 and 4.3) and for conditions specified in Table 4.1.

Higher wall shear stresses correlates to large velocity gradients and differences in local particle-fluid velocities. This tends to weaker coupling between particles and the carrier fluid which can bring about severe particle impacts; thus the importance of carefully resolving the grid around the surface. Analogous to wall shear stresses, local flow velocities can also influence particle velocities and the numerical variation with elemental spacing was analysed.

Minimal differences in flow velocities (0.25mm above the surface) were observed with increasing grid elements beyond 29572 elements and the same was observed with wall shear stress values, but with computational grids comprising more than 35876 elements. Hence for optimum computational performance with negligible numerical errors (good resolution of significant flow regions), all CFD simulations were performed with a computational mesh comprising 35876 elements.

4.2.9 Specification of computational domain extent

The computational domain is defined by the entire flow field under examination and is an important parameter when analysing unconfined flows in particular. In external flow scenarios such as those encountered in automotive and aerospace applications, domain extents are set by a region/volume which allows for the total development of fluid flow and hence the overall size of the domain can be flexible [132]. For internal flow problems, examples of which are flow within conduits etc. physical walls generally define the extents of computational margins. However, for large geometries, domains of actual size need not be necessary but should be large enough to allow for the complete flow development (bringing boundaries closer to the test sample should not affect the resulting flow regime). However, large domains are associated with higher computing time and costs and hence optimisation of the domain extents is required.

Similar to mesh iterations, the sensitivity of flow variables (shear stresses along the surface and local flow velocities, 0.25mm above the surface) are monitored with different grid densities. CFD simulations of the JIT geometry and with the boundary conditions defined in Figures 4.1and 4.3

respectively, were conducted for the conditions specified in Table 4.1 for three different domain sizes and the ensuing variations of local flow velocities 0.25mm above the test surface (Figure 4.7a) and wall shear stresses (Figure 4.7b) on the surface were recorded. It was observed that increasing domain extents did not influence the monitored flow variables and the flow field was set to 70mm by 120mm. Solution run times for these three domains did not vary by much and hence domains of smaller sizes were not considered. Thus the domain of the size 70×120 mm^2 which allows for the full development of flow and is also computationally optimal was considered for further iterations.

(a)
(b)
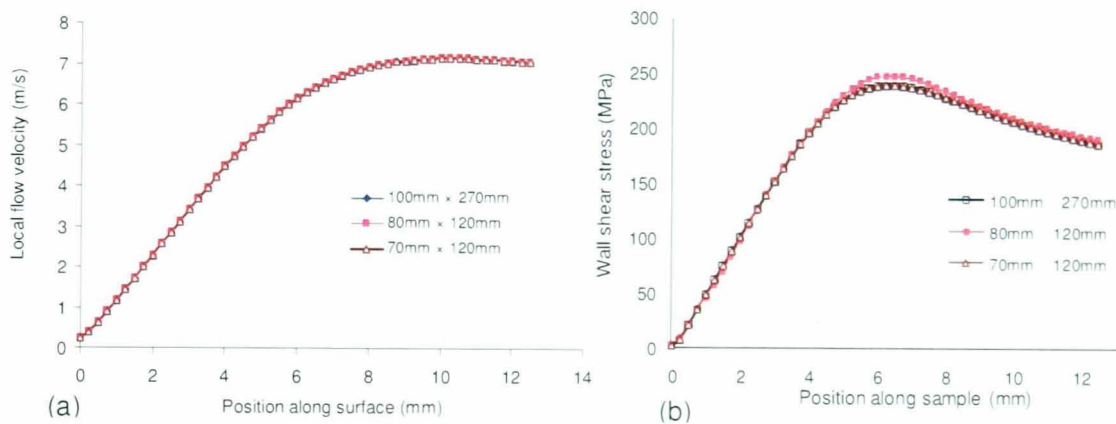
Figure 4.7 Variations of (a) local fluid velocity profile 0.25mm above the test surface and (b) wall shear stress on the test surface in radial direction with domain sizes. Simulations were conducted out on a simplified geometry (Figures 4.1 and 4.3) and at conditions specified in Table 4.1.

Another important feature in the domain is the length of the inlet pipe, i.e. the length of the nozzle. It is recommended that this length should be sufficient enough to allow for the flow to be fully developed prior to exiting the nozzle. CFD simulations using various inlet lengths suggested that beyond an inlet length of 70mm, the flow solution (local fluid velocities 0.25mm above the test surface) remained unaffected and hence the inlet length was set to 70mm (10 times the internal diameter) to allow for the flow to be fully developed within the nozzle.

4.2.10 Impingement jet flow simulation

The modelling approach and conditions at which CFD simulations are to be conducted to provide data for the wear map is summarised by Table 4.2. The final part of the CFD process involves assessing the fidelity of the flow solution by validating against experimental data. Practical flow visualisations and measurements are not conducted since it is beyond the scope of this study. An extensive range of impingement flow data has been reported, but the majority of these studies were conducted either for large ratios of H/D (H denotes stand-off distances and D is for nozzle diameters) or at low Reynolds numbers (<4,000). Flow measurement data reported by Cooper et al. [160] was used for qualitative validations since the conditions were found to be relatively similar (Re≃23,000 and H/D≃2 in Cooper et al. [160] study; Re≃39000 and H/D≃0.7 for our case study). Figure 4.8 presents the normalised velocity data within the flow field from published experimental data and CFD predictions conducted in our study

Table 4.2 Conditions at which impingement jet flow simulations were conducted as part of data accumulation for the development of the wear prediction method.

Inlet flow velocity	5, 7.5 and 10 m/s
Fluid density	1000 Kg/m^3
Fluid viscosity	1×10^{-3} Pa-s
Fluid temperature	23 °C
Fluid pressure	ATP (101325 Pa)
Nozzle diameter	7mm
Sample nozzle separation distance	5mm
Turbulence Model	RNG K-ε
Convergence criterion	1×10^{-4}
Number of mesh elements	35876
Domain Size	70 × 120 mm^2

The predictions are reasonably close to the actual data and variations can be attributed to differences in flow conditions (Re and H/D in particular) and modelling approximations. CFD of JIT forms a vital part of this research; however, further validations of flow features are not pursued since it is beyond the scope of the work. Reasonable agreement with experimental data and the careful modelling approach acts as assurance for the fidelity of the recreated flow problem.
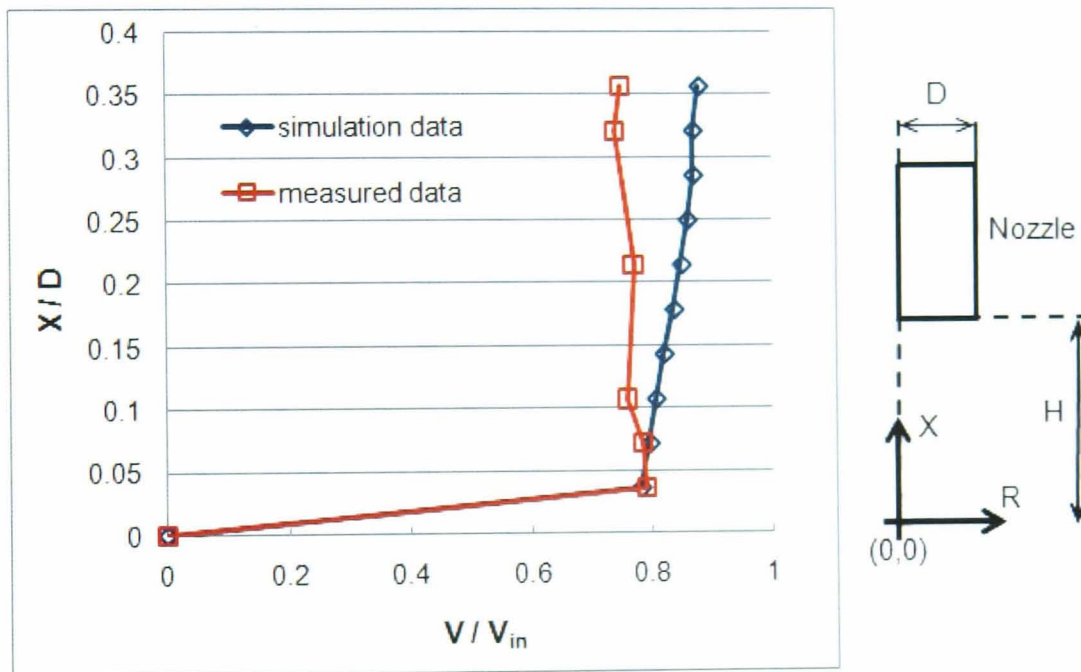
Figure 4.8 Profiles of normalised local flow velocity as predicted by CFD simulations of the impingement jet and as measured by Cooper et al. [160]. H= distance between surface and nozzle end; D= jet diameter, X= distance from stagnation point in vertical direction, R= distance from the stagnation point in radial direction, V= local flow velocity and V_{in}= Inlet velocity. Flow conditions: measured data case: H/D=2 and Re was 23,000. Simulation condition: H/D=0.7 and Re was nearly 39,000.

4.3 Prediction of particle motion and impact conditions

4.3.1 Particle phase modelling

The next step involves the calculation of particle motion within the already predicted flow field (section 4.2.10). Solid particle tracking equations

are either solved discretely over the already solved flow field or coupled together with the flow equations and solved together. This depends upon the extent to which the physical presence of particles affects the local flow regime. Two basic approaches are commonly used to predict particulate motion in fluid flows: Eulerian and Lagrangian.

- Eulerian models are generally referred to as continuum models because the particles are treated as an additional continuous phase within the main fluid phase. Along with the governing flow equations, an extra set of equations are solved for the particulate phase and coupling between the two phases takes place through inter-phase transfer terms. This approach is ideally suited to model slurries with moderate to high particulate concentrations where particle motion can possibly influence fluid flow. Since particulate phase equations are solved along with the main phase numerical iterations, computational resources used can be very high, which is the main drawback of this approach. For a particular simulation, particle properties are fixed and hence for particle parameter studies the simulations have to be re-run.

- In the Lagrangian formulation, the particles are assumed to be discrete. In this approach continuum fluid equations are solved for the fluid phase after which Newtonian equations of motion are solved over the already obtained solution to determine the trajectories of individual particles (or groups of particles). Particles of different size and densities can be studied for a given flow field without any re-runs. This approach is ideally suited for studying lightly loaded particulate flows where the presence of particles and its subsequent motion has no effect on the fluid phase. Using the Lagrangian method can reduce computational costs but determining particle impact data can consume a lot of user time.

It is thus essential to determine the appropriate model to describe particle motion, which can be aided by calculation of particle loading and stokes number. The particle mass loading is expressed as the ratio of

particulate mass per unit volume of flow to fluid mass per unit volume of flow [162] and is expressed by equation (4.4),

$$\beta = \frac{r_p \rho_p}{r_f \rho_f},$$ (4.4)

where r is the volume fraction, ρ is density and the subscripts p and f refer to particle and fluid phases respectively. Significant two way particle fluid coupling is generally expected for particle mass loadings greater than 0.2 [36]. The particle mass loading for our case study was 0.01 and hence it can be assumed that the effect of particles on flow regime is negligible and thus the Lagrangian approach was chosen to determine particle motion tracks.

4.3.2 Particle tracking equations

Based on Newton's law of motion, Clift et al. [163] proposed the governing equation (4.5) of particle motion given as;

$$m_p \frac{dV_p}{dt} = F_d + F_p + F_b + F_a,$$ (4.5)

where m_p is the mass of a particle, V_p is local particle velocity and t denotes time. The terms on the RHS (right hand side) are described below,

Equation (4.5) consists of,

- Drag force: The force acting on the surface of the body due to the viscous effects of the fluid medium and this force accounts to the cohesion between a particle and fluid streamlines. The drag force is given by equation (4.6),

$$F_d = C_d \frac{\pi d_p^2}{8} \rho_f (V_f - V_p) |V_f - V_p|,$$ (4.6)

V_f and V_p are local fluid and particle velocities respectively, where C_d is the drag force coefficient for a spherical particle defined as;

$$C_d = \frac{24}{Re_p} (1 + 0.15 Re_p^{0.687}),$$ (4.7)

where Re_p is the relative particle Reynolds number defined by,

$$Re_p = \frac{\rho_f}{\eta}|V_f - V_P|d_P, \tag{4.8}$$

where η and ρ_f are the dynamic viscosity and density of fluid respectively, d_p and ρ_p are particle diameter and density respectively.

• Pressure gradient force: The effect of the local pressure gradient gives rise to a force in the direction of the pressure gradient and is given as;

$$F_p = \frac{1}{4}\pi d_p^3 \nabla . P, \tag{4.9}$$

where $\nabla . P$ is the divergence of pressure and is defined similar to $\nabla . u$ by equation (3.2). It is assumed that the pressure gradient is constant over the volume of the particle.

• Buoyancy force: It is the upward force on the particle, due to fluid pressure, opposing the weight of the particle and is defined by equation (4.10).

$$F_b = \frac{1}{6}\pi d_p^3 (\rho_p - \rho_f)g, \tag{4.10}$$

where, g stands for acceleration due to gravity.

• Added mass or virtual force: An accelerating or decelerating particle in a fluid medium has to move some volume of the surrounding fluid in order to progress. The analogy here is that the added mass is the force the surrounding fluid will gain at the expense of the work done on it by a particle and is given by equation (4.11). This force can be a major factor if the fluid medium is denser than the particle.

$$F_a = -\frac{1}{12}\pi d_p^3 \rho_p \frac{dV_P}{dt}. \tag{4.11}$$

To solve the force balance equation (4.5), local particle (V_p) and Fluid (V_f) velocities are required. Particles are released into the fluid flow with zero velocities and the local fluid velocity at the release point is

given by CFD simulations. These data put into equations (4.5 to 4.11), would provide particle velocity until the next fluid velocity data point. where new values for particle velocities will be calculated based on local data. Equations (4.5 to 4.11) can be resolved into horizontal and vertical components and thus tracing the direction of motion.

4.3.3 Wall interactions

The type of particle impacts occurring within a flow field can be characterised using the momentum equilibrium constant, λ, as described in section 2.2.3.5. The momentum equilibrium constant can be expressed by equation (4.12) [162].

$$\lambda = \frac{\tau_p}{\tau_f} = \frac{\rho_p d_p^2 V_f}{18 \eta L_f},$$ (4.5)

where τ_p is the particle response time, τ_f is a characteristic time scale of the fluid motion, d_p and ρ_p are particle diameter and density respectively, η is the dynamic viscosity of the fluid phase and V_f and L_f are characteristic velocity and length scales in the flow respectively. It was discussed that for, $\lambda > 2.0$, particulate flows are highly inertial and in the presence of an obstruction would be dominated by particle-wall interactions. For $\lambda < 0.25$, minimal particle wall interactions can be expected and generally particles are tightly coupled to the fluid due to viscous drag.

The λ based on the velocity (5m/s), nozzle-sample separation (5mm) and mean particle size (250μm) was calculated to be approximately 4, indicating the dominance of particle inertia over viscous drag and hence high numbers of impacts are to be expected and hence wall interactions should be treated accordingly.

Particles are assumed to transfer the majority of their kinetic energy on to the impact surface prior to rebound. The post collision velocity depends on the particle properties, target material and the fluid phase and is provided by *restitution coefficient* (defined in 2.3.3.2) for that particular condition. Grant and Tabakoff [126] reported that restitution relations improved prediction capability especially when a particular particle undergoes several

impacts, which can be significant at low angles of impact. In the impingement flow field, particles can impact at a wide range of angles (numerically described later). Restitution factors vary locally depending upon local impingement angles, and for the case of JIT, the effect of secondary impacts can vary locally [120, 164] and needs to be captured accurately.

In *Fluent*, particles are presumed to be a point in the flow field. Although physical values for density and diameter are specified for calculations, the actual physical presence of a particle is not considered. This leads to impacts at the wall which should not occur in reality. Implying particle motion is determined all the way to the horizontal surface (Y= 0) whereas in reality rebound occurs at particle radius as illustrated in Figure 4.9.
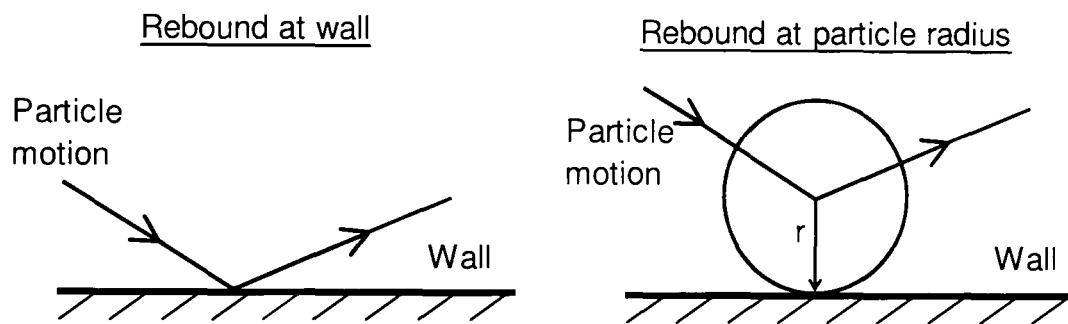
Figure 4.9 Schematics of particle rebound at wall and rebound at particle radius, with 'r' representing particle radius which set to125μm.

Non-physical impacts at the wall can result in erroneous wear predictions. Rebounding at particle radius increased predicted local impact velocities by nearly 8% in comparison to a particle treated as a point. Thus impact data was manually determined at y= 0.125mm in all the analysis. Due to this only the initial impact can be considered due to non-physical impacts (this also annuls the use of a *restitution factor*) and secondary impacts are not considered, although it is was pointed out that secondary impacts can have a significant effect [120, 122].

4.3.4 Turbulent interactions on particle motion

The flow field is assumed to be steady, although in reality local velocities for a turbulent flow varies with time and these variations are small but can be effective as described in section 3.4.2. At certain conditions these small variations (along with the mean flow) can also influence particle motion and the effect of which can be entirely random. To capture this, empirical models are suggested which considers the effect of turbulence on particle dispersion. Chen et al. [164] studied the erosion behaviour using a CFD based method in plugged tee-joints and observed that predictions were 15% greater than experimental results when turbulence dispersion was neglected. Zhang et al. [92] reported that including turbulence dispersion affected small sized particles (<100μm), but had negligible influence on larger sized particles and attributed this to high particle inertia. Considering the average size of particles used in our case (250μm), turbulence dispersion was not considered.

4.3.5 Initial conditions of particles

In *Fluent* the particle is released with zero velocity into the impingement jet and the subsequent motion is traced. The distance between the release point and the sample surface should be adequate enough for particles to acquire momentum and reach a dynamic state similar to its practical counterpart during testing. Inappropriate release positions can lead to impact conditions different from actual conditions and resulting in poor solution fidelity. Thus, a systematic study was carried out by releasing particles with zero velocity within the nozzle stream at various distances from the surface and particle velocities gradients close to the surface were monitored (Figure 4.10). Injecting particles into fluid at 5mm from the surface with zero velocity resulted in impacts occurring at nearly 2m/s. Releasing particles further away from the surface resulted in impacts at relatively low lower velocities. It was observed that particle velocity gradient when released at 20mm above the surface was similar to the case when released at a position 40mm from the surface. Thus all particles were released into the jet stream at a position 40mm above the surface. It must be noted that particle rebound in our

analysis is assumed to occur at 0.125mm above the surface (section 4.3.3). However, here particle motion is traced to the surface to study the sensitivity of predicted particle motion to release position.
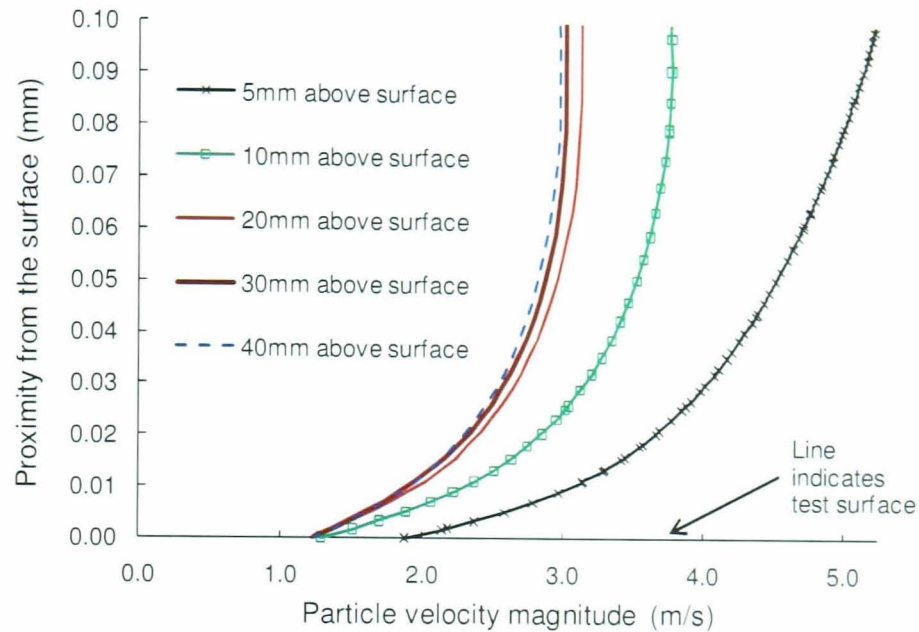
Figure 4.10 Variation of particle velocity gradient close to the test surface with increasing particle release distance. Predictions were carried out for a flow velocity of 5m/s and for conditions specified in Table 4.2 and for particle properties (density=2650kg/m^3, diameter=250µm and spherical in shape).

4.3.6 Summary of all assumptions

The following sections provides a summary of all the assumptions made during particle tracking and impact data calculations (few assumptions are already described in detail in the previous sections) and is listed as below;

1. The effect of particle shape factor on erosion rates was reviewed in section 2.2.2.2 and numerically describing it is extremely difficult and in most cases can be averaged out statistically. Thus particle shape was assumed to be spherical in order to develop a simple but robust method.

2. Particle size was set to 250μm which was considered to be a good representation of the average size of the sand distribution (212-300 μm) used for testing.

3. Particle-particle interactions were considered negligible, which has been shown to be reasonable assumption while simulating erosion wear at low particle flux [36].

4. Particles were released into the flow at zero velocities and 40mm from the surface (section 4.3.5).

5. It is assumed that rebound occurs at particle radius, contrary to the procedure suggested in *Fluent*. This annuls the use of restitution factors and hence secondary impacts of a particle are ignored (section 4.3.3).

6. The effect of local flow fluctuations due to turbulence on particle motion were assumed to be negligible (section 4.3.4) since particles were greater than 100μm [92].

7. Particle density was set to 2650kg/m³ which was similar to the sand particles used during experimental testing.

4.3.7 Impact data calculation procedure

Having established an appropriate flow and particle modelling scheme for our study, CFD simulations were conducted on the geometry (defined in Figure 4.1) with boundary conditions imposed as specified in Figure 4.3 and for conditions specified in Table 4.2. Lagrangian particle trajectory equations (section 4.3.2) were then solved on the obtained flow solution using the assumptions (section 4.3.6) to determine impact data (local impact velocity, angle and rate) as a function of radial position on the surface of the specimen. Particle impact angles are defined as the angle subtended by the tangent of particle path prior to impact to the horizontal as illustrated in Figure 4.11 and local particle impact velocity is defined as the relative magnitude of particle velocities at this point. These data were recorded for every impact along the surface.

Numerical predictions led to the observations that not all particles exiting the nozzle collide with the surface. A fraction of the total number of

particles is dragged away from impact by the fluid stream. To determine this, particles were uniformly spaced within the nozzle at release position and the subsequent predicted location of impact of every particle was noted. It was observed that all particles released beyond 2.59mm from the nozzle centre (as illustrated in Figure 4.12a) did not collide with the surface and it was estimated that only 74% of the total number of particles can proceed to impact the surface. This data was from simulations carried out for an inlet velocity of 5m/s and conditions stated in Table 4.2. This way the variation of impact number along the surface was determined.
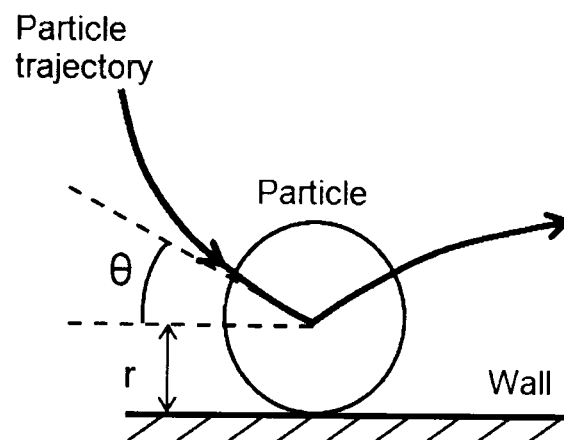
Figure 4.11 Schematic representation of a particle impact and graphical illustration of particle impact angle.

Particle impact data for a case of nozzle exit flow velocity of 5m/s and 90° nominal impingement angle determined using the above procedure is shown in Figure 4.12 (b, c and d) and this implemented for different nominal impingement conditions. It was predicted that for a nominal impact velocity of 5m/s, local particle impact velocities can vary between 1 to 5.5 m/s and for a nominal impingement angle of 90°, local angles varied approximately between 80° to 6°. This further stresses the fact that the submerged JIT can reproduce a wide range of local impact conditions. It must be noted that local impact velocity at the edge of the surface is slightly greater than the nominal impact velocity. This is attributed to the accelerating effects of the fluid at these regions.
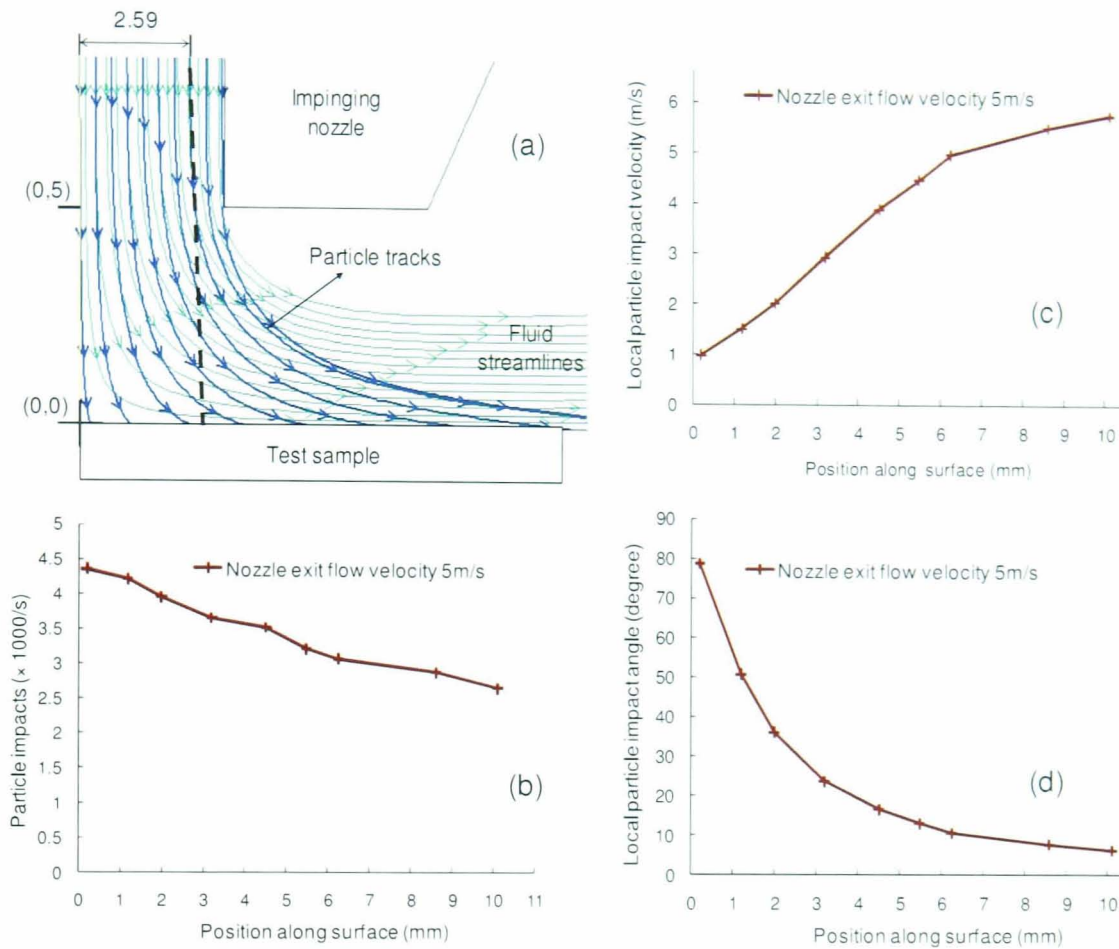
Figure 4.12 A half model of the JIT simulation showing the motion path of solid particles (thick arrow lines) crossing the fluid streamlines (thin arrow lines) and impacting the target plate in 'a' for a jet velocity of 5m/s. (All numerical units are in mm and sketch is not to scale). Also the variation of particle impact number, local impact velocity and angle with radial position is graphically shown in b, c and d.

Thus CFD simulations were able to provide relevant data pertaining to particle impact conditions for a range of operating conditions for correlations with material data. This material data was extracted from a minimum set of standard laboratory tests and the testing procedure is presented next.

Chapter 5

Standard laboratory jet impingement tests

Computational fluid dynamic (CFD) simulations enabled local flow and impact conditions to be predicted at the test surface (chapter 4). The second step in the development of the wear prediction method necessitates local material wear data to be acquired at these impact conditions and hence a minimum set of laboratory based experiments were executed for this purpose as presented in this chapter.

A standard submerged jet impingement test (JIT) apparatus was selected to conduct laboratory based slurry erosion tests and the features of the test rig are described in section 5.1. The functional characteristics of the JIT rig were analysed and carefully calibrated (section 5.2) to ensure uniformity between CFD and laboratory test conditions. Material loss due to erosion is affected by a number of parameters and the influence of critical factors on wear rates are practically investigated (section 5.3). A minimal set of standard JIT's were conducted under pre-determined nominal conditions to provide local material wear data (section 5.4) to conclude the second stage of the wear prediction method.

5.1 Standard Laboratory test equipment

Various laboratory based facilities designed for the purpose of analysing material behaviour under a range of erosion-corrosion conditions are currently used by researchers [40, 41, 58, 65, 68, 72, 107. 108, 112, 113, 117, 165, 166] and the most common tests were reviewed in chapter 2. It was earlier mentioned that the JIT can reproduce a wide range of local impact conditions on a flat surface and this was demonstrated numerically by CFD simulations (section 4.3.7). For this reason the JIT was selected for material wear data acquisition.
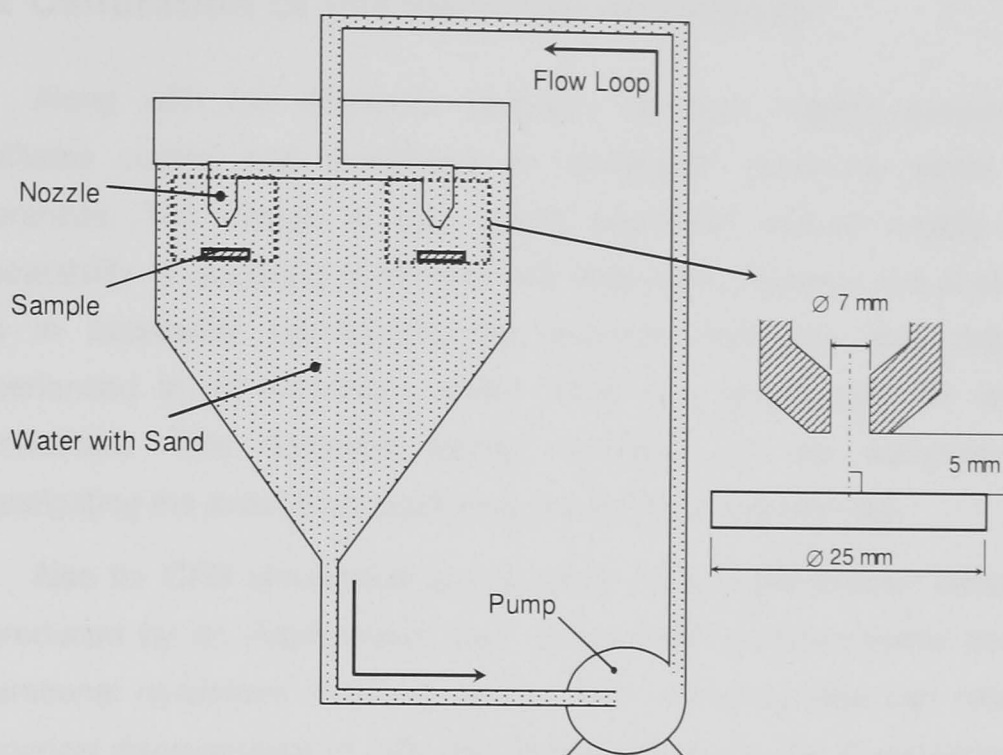
Figure 5.1 Cross-sectional diagram of the JIT used for generating erosion conditions on test surfaces in a laboratory.

A jet impingement test rig used to reproduce erosion-corrosion conditions typical of those found within an oil industry (sand concentration, flow rates, temperatures, corrosivity, particle size, etc.) was setup at the University of Leeds, comprising a centrifugal pump, a set of nozzles, sample holders, pipeline network and a holding tank, which works through impinging a suspension of particles within a liquid onto the test material which is submerged in the same liquid. Various configurations of the JIT have been used depending upon the conditions simulated [167, 168] and Figure 5.1 shows the diagram of the setup of the experimental rig, together with the nozzle arrangement, used in our study. If desired, corrosion of the sample can be reduced to negligible values either by cathodically protecting the surface or by controlling oxygen levels within the system [169]. The facility enables the dependence of different parameters such as the nominal impingement angle, sand concentration, temperature, flow velocity, etc. on material wear rates to be studied and hence to assess the critical factors which contributes to material degradation.

5.2 Calibration of impingement conditions

Along with the economic benefits, laboratory based experiments facilitates control and monitoring of operational conditions within high tolerances. The design of any testing equipment should enable good repeatability of operating conditions and wear data; however, the challenge lies in accurately reproducing the required conditions that may be experienced in an industrial context which is a prerequisite for reliable correlations. This demands robust calibration of the equipment by investigating the exact local conditions the facility is reproducing.

Also for CFD simulations to accurately capture the erosion behaviour reproduced by an impingement test, geometrical and operational nominal operational conditions must be similar. Any inconsistencies can result in numerical discrepancies in wear predictions. Thus it is vital to scrutinize and calibrate the test facility to obtain well defined data of the nominal operational conditions. This information can then be submitted to a CFD simulation to obtain local impact data. The wear method developed is based on three variables related to local impact conditions (angle, velocity and rate) and these nominal conditions were calibrated as described.

5.2.1 Nominal flow velocity

The average velocity at which fluid particle suspension exits the nozzle is defined as the nominal flow velocity and is also referred to as nozzle exit flow velocity. Impingement action is produced by the recirculation of the liquid suspension within the reservoir on to a tests surface and the energy required for this action is provided by a centrifugal pump. The pump is driven by an electric motor with a manually controlled frequency attenuator, the purpose of which is to enable easy control over the rotational speed of the pump and hence flow rates. Flow velocities exiting the nozzle can be calculated from flow rate data and hence flow measurements were conducted.

The centrifugal pump was operated at a certain frequency and flow rates were measured by physically collecting the fluid exiting the nozzle over

a fixed time interval. Flow rates were measured for various frequencies and the variation of nozzle exit flow velocities (calculated from flow rates) with frequencies are graphically illustrated in Figure 5.2. Observations suggested flow velocities varied linearly with the speed of the centrifugal pump. For a particular motor frequency, lower flow rates were observed with the inclusion of sand particles. Addition of sand particles increased the overall weight of the fluid suspension and hence accounting for minor drop in flow velocities. Flow rates were then measured with the addition of sand particles (1% by weight) and nozzle exit flow velocities were standardised against motor frequencies. Increases in fluid temperatures and sand particles affected flow velocities and were accounted for in subsequent velocity calibrations.
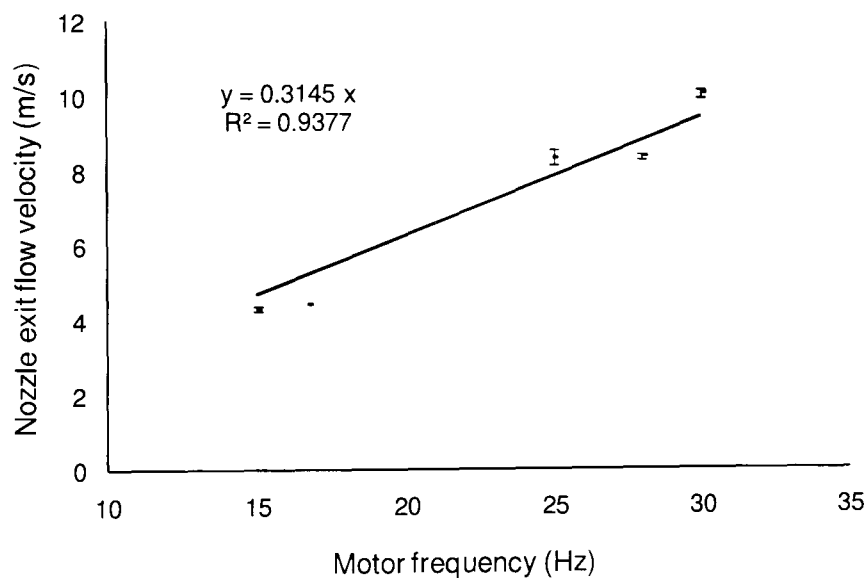
Figure 5.2 Illustration of the functional characteristic of the impingement rig. Variations of nozzle exit flow velocities with motor frequency for a 7mm diameter nozzle, 1% sand concentration by weight (defined later) and with water at 23°C as the fluid medium.

5.2.2 Sand Concentration

Sand concentrations are generally defined by the ratio of the total weight of the sand particles to the total weight of the fluid solution within the reservoir. The re-circulating impingement apparatus presents an issue in

determining the amount of sand particles impacting the test surface. It has been reported that not all sand particles added (particles here were added manually) to the reservoir of this configuration actually impact the surface [167] and can be attributed to three major reasons;

1. Inter particle collision at the surface,

2. Sweeping action of the liquid jet away from the surface,

3. Non uniform mixing of particles within the reservoir.

Quantifying inter particle collision has been regarded highly complicated since the entire phenomenon can be considered to be based on random events [89]. Particles can collide with other particles rebounding off the test surface or from the inner surfaces of the nozzle and these events can be abundant in the case of heavily loaded particle flows (high solid concentrations) [170].The number of particles swept away from the impact surface by the fluid can be quantified with reasonable accuracy using CFD (section 4.3.6) provided data regarding particle content within the nozzle is dependable. A systematic approach was thus ensued to determine the particle flow rates through the impingement nozzle.

Several questions have been previously raised regarding the quantity of sand particles circulating within the reservoir. Sand particles (density- $2650kg/m^3$) are denser than fluid (density- $1000kg/m^3$) which allows for particles to settle at the base of the pipe fittings. All these particles should ideally be dragged by the re-circulating fluid solution promoting uniform mixing. However, particles can be trapped at various pipe bend sections, obstructions (e.g. directional control valves) and misaligned pipe sections, etc. effectively reducing the number of particles flowing through the nozzle. This can be significant in very low concentration slurries.

To control the amount of sand particles flowing through the nozzle, the standard JIT was modified [58, 167]. This setup comprised an additional sand storing chamber with a flow control valve, which allowed for releasing a known quantity of sand particles into the fluid solution. This solution was then impinged against the test surface. After impact, particles were filtered

and the fluid solution was re-circulated. Fresh measured quantities of sand particles were constantly injected into the fluid stream at a controlled rate thus providing accurate particle flow rate data. The modified version of the JIT provided the ability to control and regulate sand concentrations within the fluid suspension; however, this greatly increased testing cost and required capital investment.

As an alternative to the improvised but expensive sand delivery system, a statistical approach was adopted to establish the approximate amount of particles exiting the nozzle. Here, the amount of sand particles contained within a particular amount of fluid exiting the nozzle for a fixed time duration is measured by manually collecting the slurry solution exiting the nozzle. Sand particles are then filtered and weighed when completely dried. It was noted that the sand concentration (the ratio of weight of dry sand/weight of fluid exiting the nozzle) was considerably lower in comparison to the sand loading (total weight of added dry sand/total weight of fluid in the reservoir). At very low sand loadings (also referred to as nominal concentration), the sand concentration exiting the nozzle was negligible. This reduction was attributed to particles getting trapped at various pipe fittings within the loop. According to this it was expected that sand concentrations (circulating in the rig) will be lower than sand loadings (added to the rig). Laboratory tests meant for wear data acquisition are designed to be conducted for sand concentrations of 1%, and thus it was required to determine the sand loading for which this condition is realised at the exit of the nozzle.

JIT trials were conducted for a nozzle exit flow velocity of 5m/s and for various nominal sand loadings. It was ensured that the test environment was very similar to those expected during testing for wear data accumulation. Sand concentrations were then recorded for various sand loadings for a nozzle exit flow velocity of 5m/s and is presented in Figure 5.3.

It was observed that for sand loading of 1% by weight, the sand concentration exiting the nozzle was nearly 8 times greater which was in sharp contrast to what was expected. This can be attributed to the non-uniform mixing of particles within the reservoir and to substantiate these sand trials were conducted at a different nozzle exit flow velocity of 10m/s

(presented in Figure 5.4). It was observed that for a sand loading of 1% by weight, sand concentrations measured exiting the nozzle for a velocity of 10m/s was around 3.93% which was nearly half the concentrations measured exiting the nozzle at 5m/s.
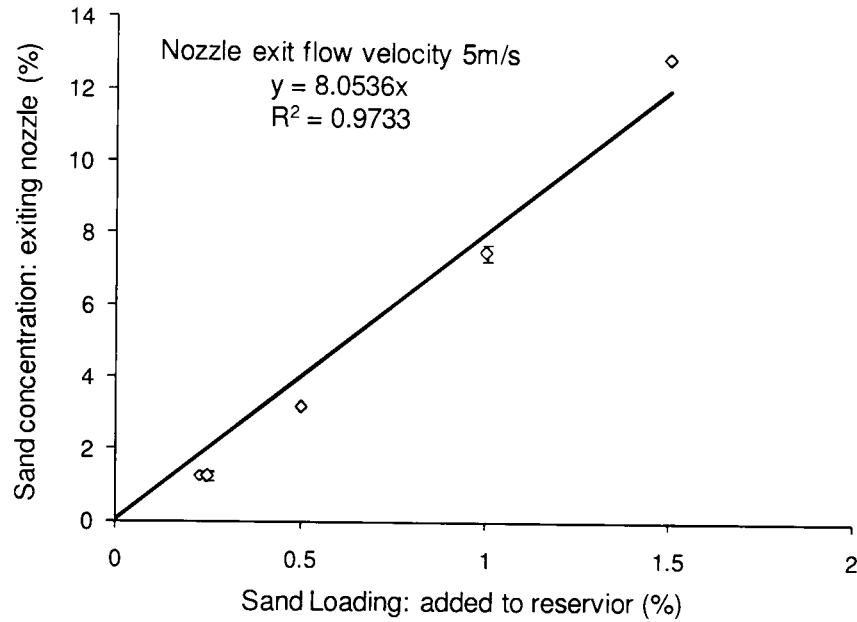
Figure 5.3 Variation of the sand concentration to sand loading for a nozzle exit flow velocity of 5m/s.
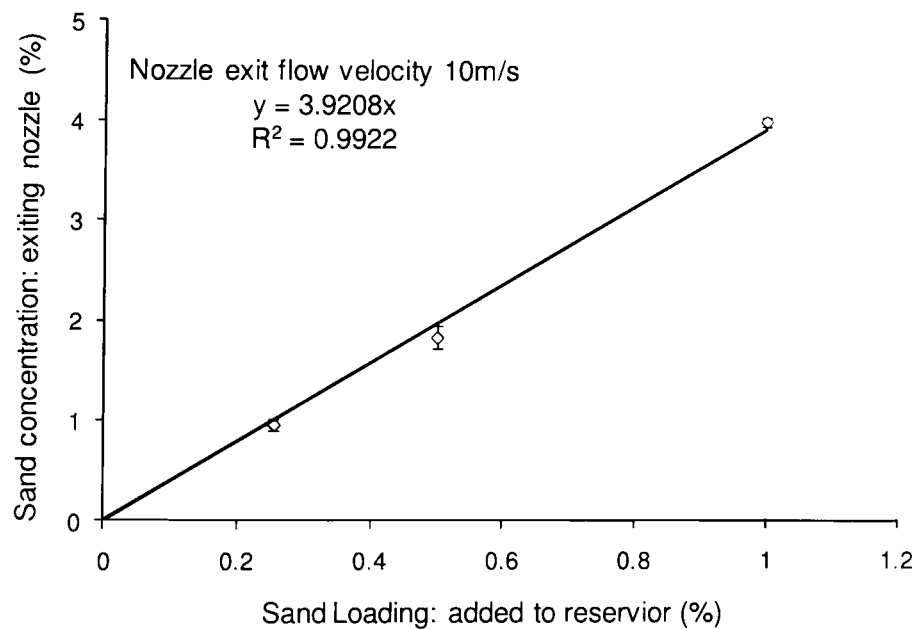
Figure 5.4 Variation of the sand concentration to sand loading for a nozzle exit flow velocity of 10m/s.

These differences can be explained by considering the effect of flow turbulence in agitating the surrounding fluid. The flow jet after impingement diffuses radially across the surrounding fluid carrying with it sand particles. Higher impingement velocities, means the jet stream diffuses through greater distances with sand particles. Thus sand particles are dispersed to greater extents within the reservoir promoting better mixing at higher impingement velocities as illustrated in Figure 5.5. Also other factors such as positioning of the sample holder, discharge pipe position and geometry of tank can affect the mixing of particles within the reservoir.
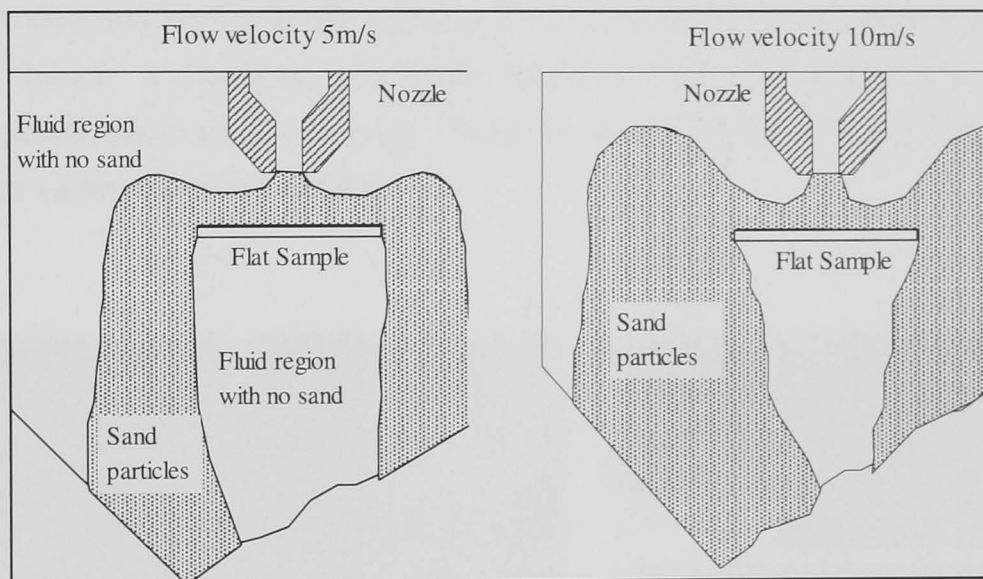
Figure 5.5 Mixing of sand particles within the reservoir for different nozzle exit flow velocity, suggesting higher flow velocities induces better mixing of sand particles.

The sand concentration data obtained at 5 and 10 m/s (Figures 5.4 and 5.5) enabled required particle mass flow rates to be reproduced. For 5m/s, addition of 0.125% by weight of sand to the reservoir should reproduce a sand concentration of 1% by weight and 0.25% for 10m/s. This data coupled with CFD simulations can provide an estimation of the total number of particles flowing within the nozzle.

5.2.3 Nominal impingement angle

The differences between the nominal and local impact angles were illustrated by Figure 2.19 in section 2.3.4. The recreation of nominal impingement angles are dependent on the physical configuration of the nozzle-sample arrangement and require accurate positioning and measurement of orientation angles and separation distances. Wear tests were conducted at 90° to obtain data for the wear map and also at 105° and 135° for validating the wear prediction method. Special purpose holders were designed (Figure 5.6) and test samples were mounted and aligned under the nozzle. Measuring these orientation angles and separation distances was done visually with the aid of a Vernier scale as described later and hence a possible difference between test geometries and CFD simulated geometries can exist. However, at this stage it is assumed that these variations are negligible.
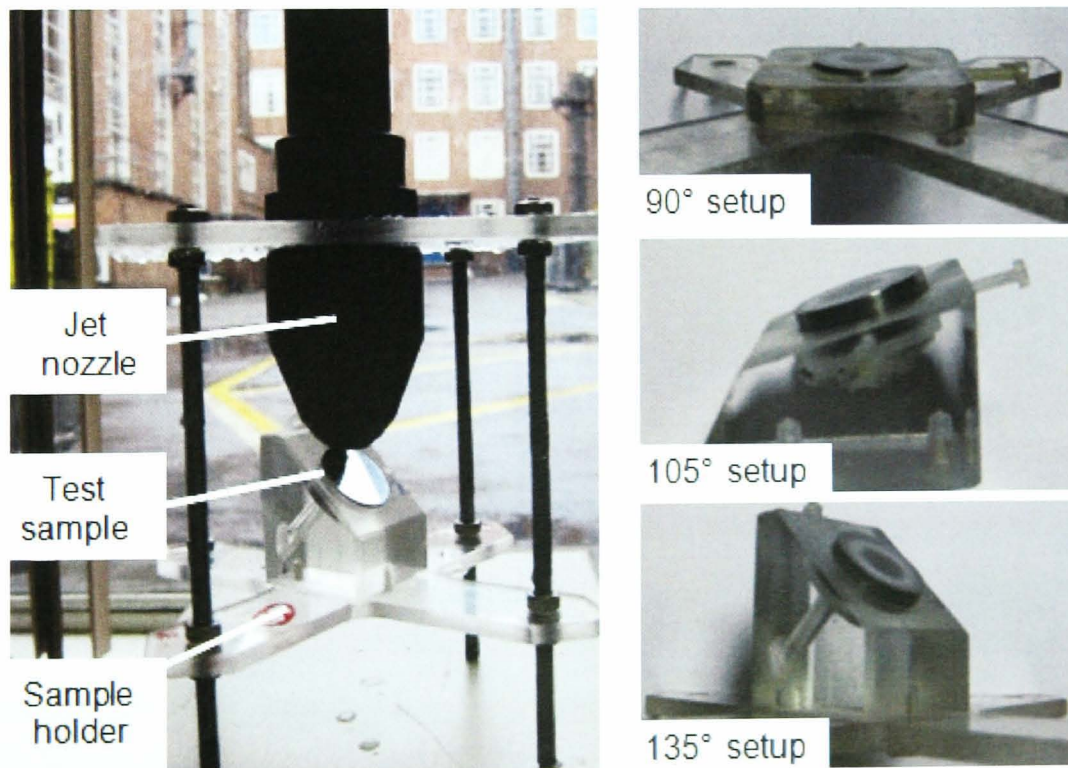
Figure 5.6 Images of different sample holders fabricated to reproduce controlled nominal impingement angles and the setup used to conduct laboratory based erosion-corrosion testing.

Meticulous calibration of operational aspects of the JIT facility provide well defined data regarding nominal operational conditions and this data is submitted to CFD simulations which can predict local impact data. This offers a good starting point for erosion tests to be conducted and with the confidence that the test apparatus can faithfully reproduce the required nominal operating conditions.

5.3 Variation of erosion parameters during testing

Erosion wear is a multivariate physical phenomenon and the majority of the principle factors can be segregated into four groups as suggested by Clark [16] and discussed earlier (section 2.2). It was proposed that for a set combination of sand-material in a specific fluid medium, the major variable parameters affecting erosion wear are connected to the local flow conditions. Using this as the premise, the wear prediction method was proposed. It is assumed that factors such as the erosion power of an erodent does not change with time, however, this can change during testing [6, 11, 52]. It is vital to verify whether the contribution of factors assumed to have no influence on erosion wear is valid throughout the entire test duration and this is done experimentally as described in the next section.

5.3.1 Influence of corrosion on wear losses

Thermodynamics controls system equilibrium by affecting the initiation of corrosion reactions on the surface leading to material loss [6]. Within this work it is required to restrict the contribution of corrosion to negligible levels, which can be attained by regulating operating conditions and by careful selection of the fluid-material combination. Stainless steel 316L (UNS S31603) was selected as the test material and a decisive feature in material selection was the enhanced corrosion resistance of this material in water at temperatures below 25°C. UNS S31603 is ductile in nature and since the majority of hydro-transport equipment materials are ductile, this was preferred. High corrosion resistance of this material in fluid is attributed to

development of a strong passive layer inhibiting corrosion [171]. However, it has been reported that corrosion losses can be greater that 50% of total mass loss under particle impingement under certain conditions [172]. Corrosion under these conditions can be constrained by the application of Cathodic protection (CP) to the specimen.

Cathodic protection and erosion-corrosion tests [18]

For certain materials, any unwanted electrochemical reactions at the surface of a material can be suppressed by the application of an external potential and this method is known as Cathodic Protection. From a thermodynamic perspective, CP pushes the potential of the working electrode (test sample) to a point where corrosion cannot occur. For corrosion to be restricted, a material has to be maintained at the correct potential during operation in that environment. This potential is environment specific and has to be experimentally determined by conducting Cathodic Polarisation tests. The erosion-corrosion behaviour of UNS S31603 has been extensively studied and it has been recommended that by applying an external voltage of -0.8V the chemical attack on a surface can be reduced but without the potential for complications with hydrogen embrittlement [17].

Erosion-corrosion tests were then conducted on UNS S31603 coupons for the conditions specified in Table 5.1, with and without the application of CP. For CP tests, an external voltage of -0.8V was applied to every sample. Differences in mass loss with and without the application of CP was around 0.6mg (<1% of total mass loss). Although corrosion contribution to total material loss can be high as discussed in section 2.1.3, it was observed to be very low these conditions which are attributed to a combination of high corrosion resistance of UNS S31603, low corrosivity of water at 23°C and erosion dominated wear regime. It can hence be concluded that losses due to corrosion at these conditions are negligible (anywhere within 5% can be considered negligible due to possible experimental errors and deviations) and further tests are conducted without the application of CP.

Table 5.1 Operating conditions for which erosion-corrosion tests were conducted on UNS S31603 samples to study the effect of corrosivity of an environment on total mass losses.

Fluid	Temp.	Fluid Density	Impact angle	Test duration	Flow velocity	Sand density	Sand content	Sand size
Water	23 °C	1000 kg/m^3	90°	120 minutes	5 m/s	2650 kg/m^3	1% by weight	212-300 μm

5.3.2 Degradation of abrasivity of sand particles

An important time dependent factor in the test system is the degradation of the abrasivity of suspended particles. Industrial flows are passed through the geometry once and a particular abrasive can collide with a specific section only once. Whereas in the impingement test rig, recirculation of the fluid suspension causes a particle to impact the test surface several times during the entire test duration. Repeated particle impacts can lead to modifications to particle size and shape, which can considerable influence wear rates as reported by Masden [52].

Hu et al. [17] eroded UNS S31603 surfaces using AFS50/70 (American foundry society) particles suspended in water and by employing the same apparatus used here to study the degradation of particles with time. After 8 hours of testing with the same fluid suspension, the shape and size of the particles were examined by Hu et al. [17]. Microscopic images of particles revealed that the general shape of the particles were maintained but with reduced sharpness. The variations in size distribution pre and post tests were within 10% as shown in Figure 5.7. Hu et al. [17] also monitored erosion rates by measuring test samples at fixed intervals of time and replacing it back into the test rig without replacing the test fluid for the entire test duration. It was observed that erosion wear rates were approximately constant throughout the entire test duration, similar to observations made by Reza et al. [6]. This can be used as evidence to substantiate the assumption that changes in particle shape and size with time due to repeated impingement can be considered negligible to our specific case study.
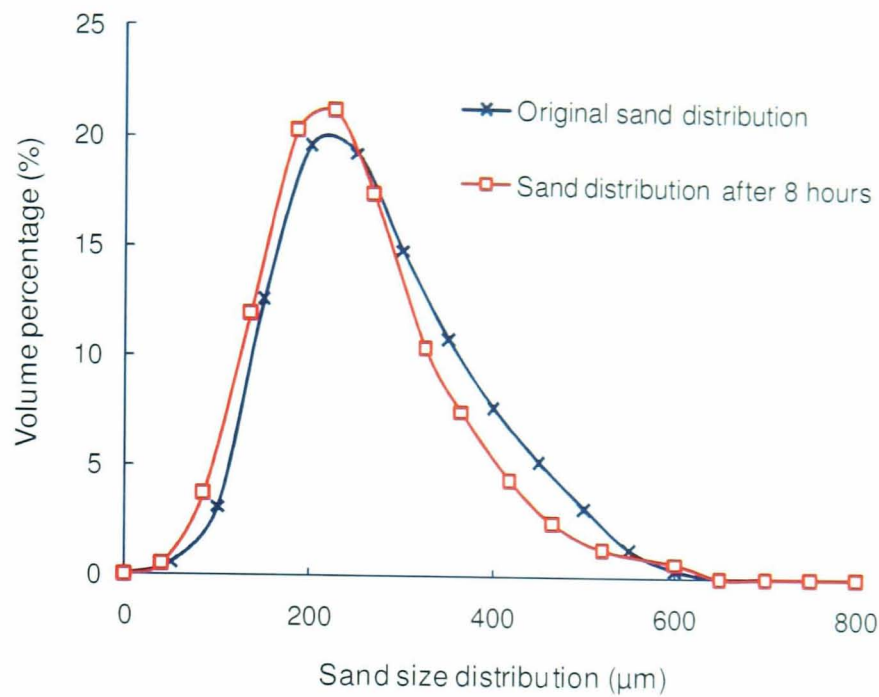
Figure 5.7 Size distributions of AFS 50/70 sand particles measured before and after impingent based erosion tests. Tests were conducted for the duration of 8 hours, at a nozzle exit flow velocity of 5m/s, using water as fluid at room temperatures, without the application of CP, UNS S31603 as the test sample, AFS 50/70 was the sand particles and the particles were not recycled. Image reproduced from Hu et al. [17].

5.3.3 Material behaviour with time

Tilly [78] conducted airborne erosion impingement tests on steel and aluminium surfaces and reported the existing of a small incubation period at the initial stages of material degradation. During this period, erosion rates were not linear and these materials resisted damage resulting in minimal losses before settling down to a steady state of material loss. The incubation period relates to the time during which the test surface is within the plastic zone and material removal occurs locally immediately after reaching the elastic limit [35, 78]. It was suggested that 'incubation time' was a function of that specific material, abrasive and test conditions (e.g. impact velocity, angle, etc.) [78]. It is essential to establish the magnitude of this non-linear state for the investigated conditions in order to ensure that most of the testing involves steady state erosion. Erosion tests were carried out on UNS S31603 surfaces in a submerged impingement rig for the conditions

specified in Table 5.1 and material loss as a function of time was monitored. Steady state erosion conditions were established after 15 minutes of testing as shown in Figure 5.8 and hence all tests were performed for durations longer that 30 minutes to nullify what could be the effect of material incubation. This could also be because the magnitude of wear was low and hence difficult to measure.
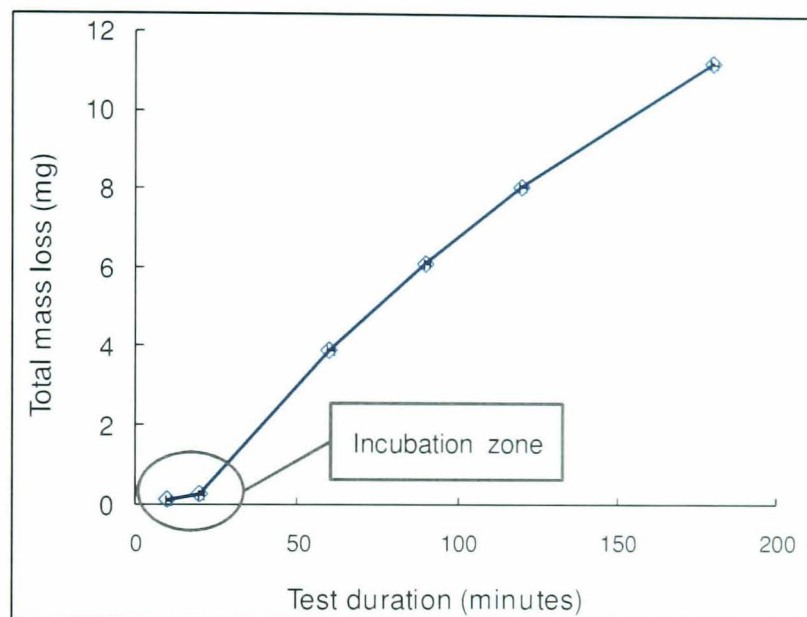
Figure 5.8 Variation of UNS S31603 total mass loss with time for test conditions specified in Table 5.1 recreated in an slurry impingement test facility.

5.3.4 Effect of changing flow geometry

Erosion mechanisms are progressive which relates to constant change in geometries due to attrition and these geometrical modifications can have a significant effect on wear rates [37]. Postlethwaite and Nesic [11] conducted erosion tests within a pipeline with varying cross sections for a time period of 12 hours. The test was interrupted every two hours allowing erosion rates and profiles to be measured. It was observed that sharp edges within the flow geometry, was rounded due to erosion over time which promoted smooth fluid flow leading to fewer impacts and hence reduced erosion rates. Reduction in wear rates over time due to change in geometry

is dependent on that particular geometry, resulting wear depths and test durations.

From Figure 5.8, beyond the 'incubation' period erosion rates are steady with time which indicates that changes to the surface geometry due to wear has minimal consequence on the overall outcome. Although the surface does change with time, the extent of this is deemed to have minimum effect on the overall outcome.

Post test surface contours provided information regarding local wear depths (described later) and maximum wear depth observed over a radial distance of 6mm on the test surface from the centre of the sample was 60µm (for a jet velocity of 10m/s), which translates to a change in the surface inclination by 0.6°. The effect of this undulation on local impact conditions was analysed by conducting CFD simulations of the modified geometry. Figures 5.9 and 5.10 provide CFD data regarding the variation of local impact conditions for geometry incorporating the eroded profile and for a flat surface. CFD simulations were conducted for a nozzle exit flow velocity of 5m/s and using the approach described in section 4.3 and conditions specified in Table 4.2. Differences in local impact velocities for the case of flat and eroded surfaces were within 0.25 m/s overall. However, differences (a maximum of less than 4° and an overall average of 1°) were observed between local impact angles predicted for flat and eroded surfaces which are considered to be negligible. These differences could also be due to numerical errors inherent in the CFD code, however, the effect of geometrical variations are analysed and discussed later. CFD simulations are conducted assuming both the surfaces are smooth and this is due to the high degree of complexities involved to include surface roughness effects.

Negligible variations of erosion rates with time (within 5%) asserts the low influence of geometrical variations on erosion rates, however, testing for longer durations can drastically modify inner wall contours affecting erosion wear rates significantly which necessitates the development of unsteady state predictive models accounting for changes in geometry.
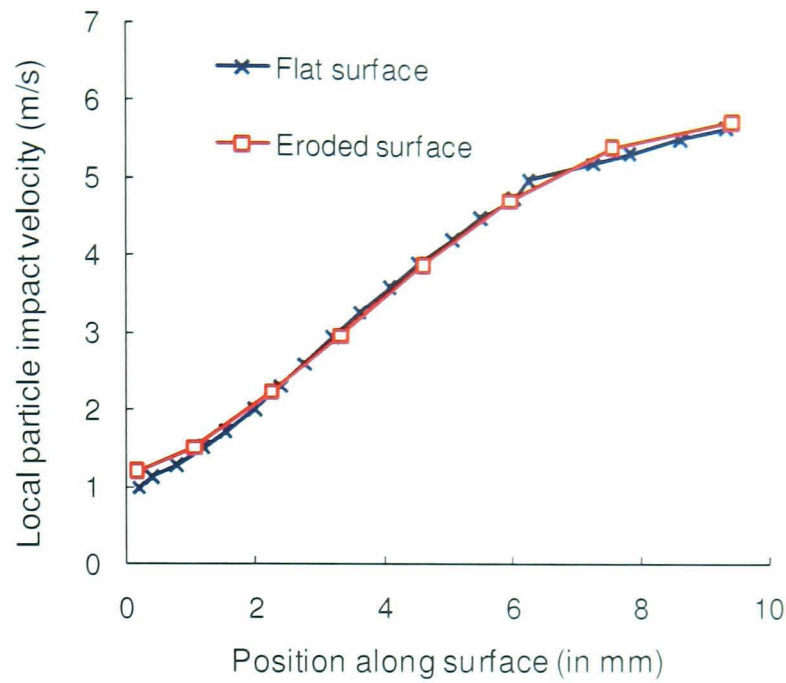
Figure 5.9 Variation of local particle impact velocities along the length of a test surface as predicted by CFD for flat and fully eroded geometries. Simulations were conducted for a nozzle exit flow velocity of 5m/s and at conditions specified in Table 4.2.
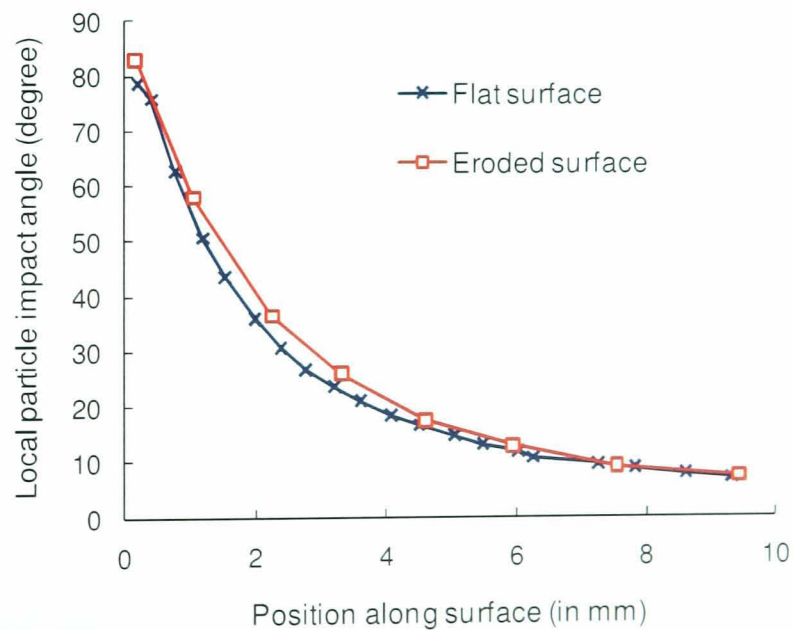
Figure 5.10 Variation of local particle impact angles along the length of a test surface as predicted by CFD for flat and fully eroded geometries. Simulations were conducted for a nozzle exit flow velocity of 5m/s and at conditions specified in Table 4.2.

5.4 Impingement tests for wear data

Experimental observations from the previous set of trials (section 5.3) provided evidence regarding the influence of various factors on erosion wear losses. Variations in surface geometry and particle abrasivity with time were negligible and the corrosion contribution was restricted. A short period of material incubation time was detected and to minimise the effects of this on wear predictions, tests are conducted for longer durations. Impingement based erosion tests were then performed on flat UNS S31603 samples for the conditions specified in Table 5.2. Prior to testing, the surface of every sample was ground and polished using an automatic polishing machine. Successive finer grades of Silicon Carbide sand papers (200, 400. 600 & 800 grit size; increasing grit size denotes finer sand papers) were used to obtain a featureless profile on all samples.

The test sample was fully submerged in water and the motor was started to re-circulate the water. A small amount of delay (approximately 30 seconds) was present before sand particles were added. This was to allow for any gas bubbles which may have accumulated within the system during non-circulation to be purged out and also for the entire system to be reach a steady state. After which sand particles were added to the reservoir steadily. Care was taken not to drop all the amount of sand into the system at once since this might lead to clogging of the pipe work and the time taken to add all the particles within the reservoir was approximately 30 seconds. After the completion of each test, the test sample was thoroughly rinsed with water and cleaned using acetone, to remove any possible dirt or contamination due to the environment. The test sample was quickly dried and immediately weighed using the same weighing balance as before and then stored away in vacuum.

The test equipment was then thoroughly cleaned and all the sand particles were flushed out of the system. The reservoir was refilled with mains water and fresh batch of sand particles and test materials were used for every test. Every material wear test at a specific operating condition was repeated at least thrice to ensure reliability of the test data.

Table 5.2 Operating conditions under which laboratory based impingement tests were conducted on flat UNS S31603 samples to provide material wear data for the development of the material-sand particle specific wear map.

Fluid	Temp.	Fluid Density	Impact angle	Test duration	Exit velocity	Sand density	Sand content	Sand size
Water	23 °C	1000 kg/m^3	90°	120 minutes	5, 7.5, 10 m/s	2650 kg/m^3	1% by weight	212-300 µm

Variation of mass loss with nozzle exit flow velocities of 5, 7.5 and 10 m/s are graphically portrayed in Figure 5.11. It was observed that the total weight losses of UNS S31603 increased linearly with V^n (where V is the nozzle exit velocity and n, an empirical constant, in this case was around 3) [63]. This corresponds exceedingly well with erosive wear studies conducted in the past for stainless steels in which the velocity exponential ranged in values between 2 to 3 ascertaining the reliability of experimental data [169].

$$y = 0.0567x^{3.1049}$$
$$R^2 = 0.9944$$
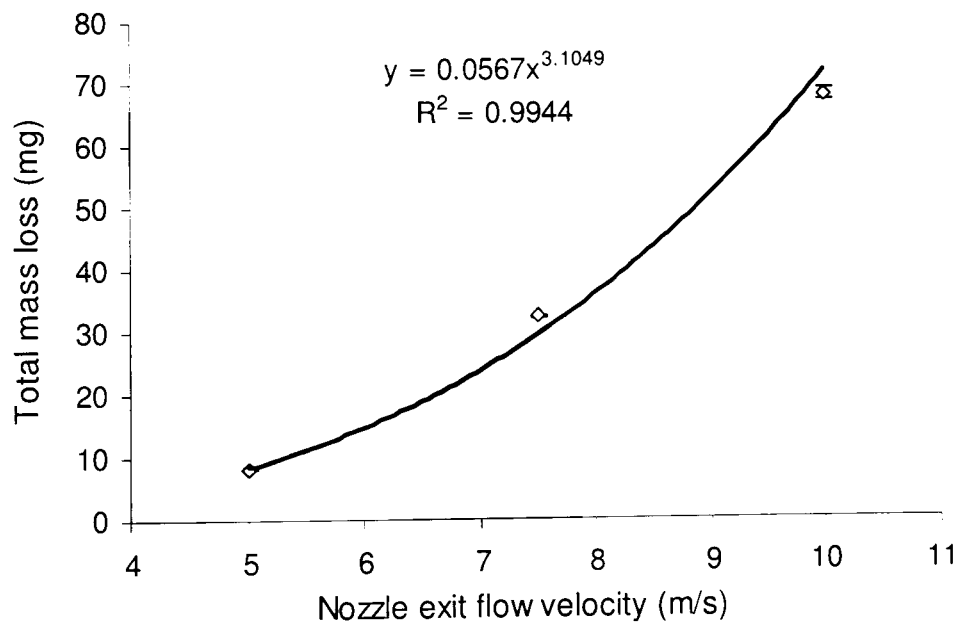
Figure 5.11 Variation of UNS S31603 total mass loss with nozzle exit flow velocities for conditions specified in Table 5.2.

5.5 Summary

A standard configuration of jet impingement test facility was chosen to provide material wear data for particle impact conditions predicted by CFD simulations. The JIT facility was attuned to standardise the operating conditions and hence the fidelity of the apparatus in reproducing the required conditions is optimised. Wear tests were then conducted to study the sensitivity of erosion mass losses with various factors other than impact angle, velocity and number of particle. It was concluded that factors such as degradation of particle abrasivity, variation of geometry with time, particle-particle interactions, effect of corrosion and work hardening did affect material wear rates but can be neglected under these conditions.

Chapter 6

Wear scar morphology studies and development of wear map

Sand based erosion tests were conducted on flat UNS S31603 samples oriented at 90° and for nozzle exit velocities of 5 and 10 m/s to provide local material wear data (section 5.4). This chapter presents the second stage in the development of the wear prediction method which involves correlating this local material wear data to available local particle impact conditions (section 4.3). The reliability of computational fluid dynamic (CFD) simulations were qualitatively validated by comparing local wear pattern on post test surfaces with expected wear pattern based on particle impact data supported by material degradation theories. Available CFD and experimental wear data were interlinked providing a range of erosion parameters to develop a wear map for a specific sand-material combination. The systematic development of a UNS S31603 wear map which can associate local particle impact conditions to average material wear rates for a specific sand particle (AFS 50/70) is presented in this chapter.

6.1 Surface characterisation of test samples

Wear surfaces from impingement tests were observed under a scanning electron microscope (SEM) to study the nature of the entire wear scar and in particular, local wear patterns. Impact conditions at the surface, especially impact angles, dictate local wear mechanisms and the variation of which results in diverse wear patterns. Impact conditions predicted by CFD and classical ductile material wear mechanism theories [30, 33. 34, 86. 87. 99] provided an insight into expected local wear patterns. Experimentally observed local wear patterns were compared with predicted wear patterns to assess the cohesion of CFD simulations and the experimental facility in

accurately reproducing erosion conditions, prior to conducting any extensive numerical analysis. A typical ductile material wear scar under 90° impingement can effectively be divided into three major regions as demonstrated by Lapides and Levy [173] and Hu et al. [17] depending on the range of particle impact angles which directly influences material removal mechanisms.

6.1.1 Impingement flow field characterisation

The three main regions on the test surface as illustrated in Figure 6.1 within a typical impingement flow field can be defined on the basis of local flow dynamics translating to particle impacts at a wide range of angles and grouped as listed below;

- Region 1: Impact angle 90° to 40° (high to medium range),
- Region 2: Impact angle 40° to 15° (medium to low range),
- Region 3: Impact angle < 15° (low to sliding range).
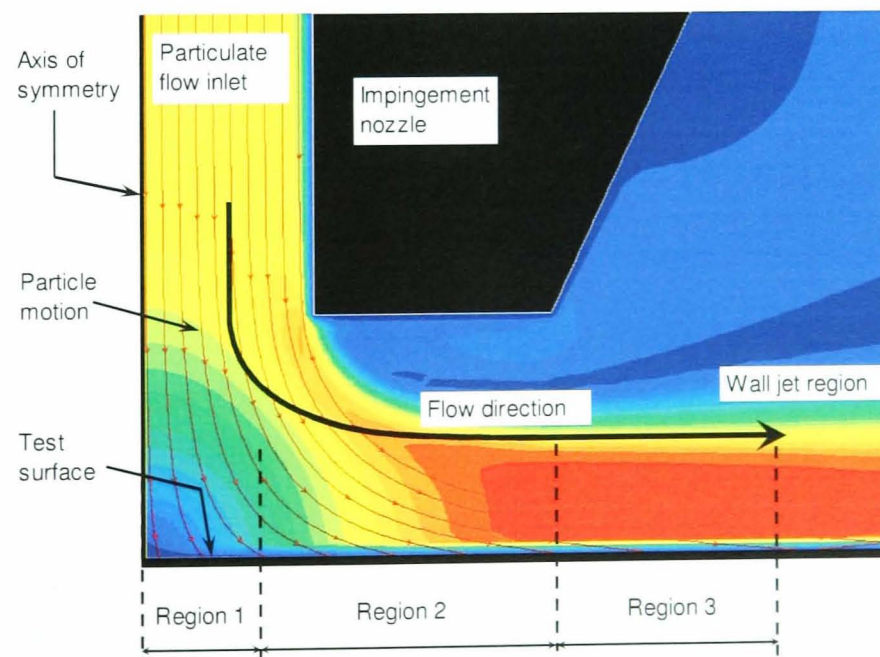
Figure 6.1 Particle motion (red coloured arrow lines) within impingement jet flow as predicted by CFD and subsequent impact on the test surface. The wear region on the test surface is divided into three secondary regions based on impact angles.

- Region 1 lies immediately next to the stagnation point (defined as the intersection point of nozzle axis and the surface for this configuration) and is typified by low local flow velocities. The oncoming fluid jet decelerates rapidly due to an orthogonal obstruction presented by the test surface prompting a rapid change in the flow direction leading to a significant drop in flow momentum (in the direction normal to the surface). The consequence of this conjoined with particle inertia and momentum, drives an erodent towards the surface by crossing fluid streamlines [31]. High impact angles are to be endured at this region but impact velocities can be low due to the decelerating effect of the fluid [16, 68, 174]. CFD simulations predicted a similar trend of particle impact conditions with the lowest flow velocities (Figure 4.12b) observed around the stagnation region (less than 1.5m/s for a free stream velocity of 5m/s) and high impact angles (nearly 80° around the stagnation region). Fluid flow in this region has the least effect on the direction of particle motion (due to low particle-fluid coupling) and within this region flow with a high tendency to impact the surface presuming no interactions with other particles.

- Region 2 can be characterised by particles impacting at medium to low angles ranging between 40-15°. Local turbulence levels are high in this region as the fluid jet accelerates along the radial direction by aligning itself to the test surface. Particle inertia drives the particles to impact the surface whereas the fluid drags particles away from the surface. Particles are required to travel longer distances to impact and the sweeping action of accelerating fluid jet improves inter-phase coupling and thus reduces impact angles. However, particles derive energy from the mean flow which leads to impact at higher velocities.

- In region 3 defined in Figure 6.1, flow velocities remain fairly high while turbulence energy decays to the surrounding. This occurs at regions very close to the edge of the sample and with the primary flow vector aligned parallel to surface. Particle motion in this region is

almost entirely dominated by fluid flow and adheres to streamlines leading to minimum impacts. Particles that do impact this region glance or slide along the surface enacting a scratching motion and impacts occur at angles well below $15°$. Particles post impact from the previous regions are dragged by the fluid and the probability of these particles striking the surface again [15, 175] and interfering with oncoming particles leading to inter-particle collisions [128] are high. Hence quantifying the particle impact number can be a difficult task around this region.

6.1.2 Local impact wear mechanism

Several theories relating to ductile erosion wear at local levels have been postulated. Finnie [33, 95] put forth a theory which accounted erosion due to cutting and ploughing mechanisms at low impact angles. Bitter [34, 86] attributed wear at high impact angles due to plastic deformation caused by repeated heavy blows on the surface. Tilly postulated a two stage ductile erosion mechanism in which particles on contact rupture and the secondary particles further damage the surface [30, 78]. Sundararajan [35] pointed out that erosion is due to the localization of plastic flow beneath the particle surface contact and formation of material lips and eventual dislocation of these lips. Jennings et al. [121] suggested that the kinetic energy per impacting particle can be sufficient to melt the volume of target material removed and on this basis put forth two mechanisms of material removal: melting of the surface beneath an impacting particle followed by splashing of this material; and bonding of solidified material to imbedded particles which in turn were removed by subsequent impacts. Due to the intricate nature of particle erosion, no single theory exists since a particular mechanism is specific to conditions which further complicate the understanding of local wear mechanism. However it is widely accepted for slurry erosion conditions, wear on a ductile material is predominantly due to cutting and deformation mechanisms which are described in the following sections.

6.1.2.1 'Cutting' wear mechanism

Hutchings and Winter [87] performed individual impact tests on ductile materials using spherical shaped particles and demonstrated that at oblique impacts material flows plastically to create a small raised formation known as material lip, which can be detached above certain impact velocity. This mechanism has been referred to as a ploughing or cutting action of the particle leading to shallow and lengthy surface indentations which are relatively smooth in nature [22, 87] asserting the theory proposed by Finnie [33, 95]. Figure 6.2a demonstrates loss of material due to ploughing and cutting action occurring due to low angle impacts. Particles travel at high velocities almost parallel to the surface and hence cutting wear is associated to the horizontal velocity component. Not all energy possessed by particles are consumed for material removal and particles subsequent to impact rebound with high residual energy [30, 33, 95].
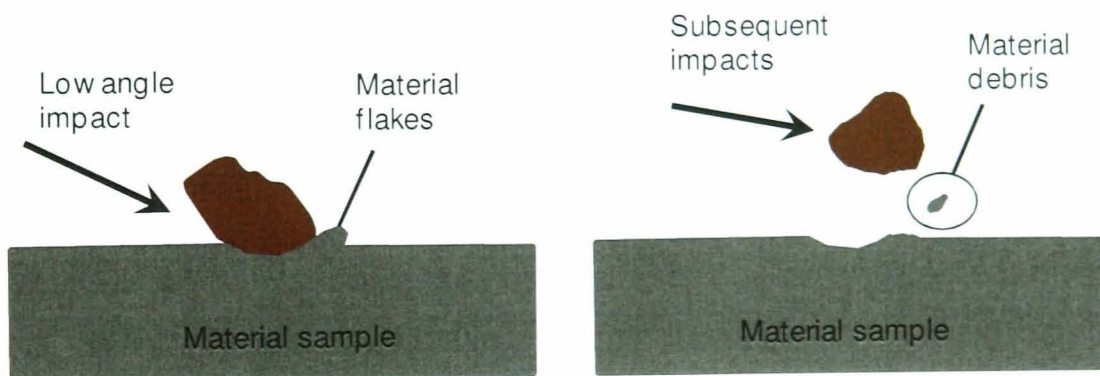
Figure 6.2a Material removal mechanism due to impact of solid particles at high and medium to low impact angles for a ductile material–(for example UNS S31603).

6.1.2.2 'Deformation' wear mechanism

In another pioneering work, Bitter [34, 86] accounted for damage at high angles of attack by demonstrating the predominance of wear by 'deformation' on ductile materials. Particles penetrate deeply into the material surface which leads to material being raised along the edge of the particle leading to the formation of 'material flakes'. These flakes are

removed from the surface due to subsequent particle impacts and deformation wear phenomenon is illustrated in Figure 6.2b. Particle indentations due to high angle impacts are deep with high surface roughness [34, 86, 95]. Certain non eroded material surfaces tolerate impacts initially accounting for minimal wear by absorbing the impact energy attributed to the effects of work hardening. Repeated heavy blows increase the local hardness of the surface and material removal is initiated when the limit of plasticity is reached [35]. A major fraction of particle energy is dispensed during wear by deformation and particles almost stop at the end of the impact event and can present an obstruction to oncoming particles leading to inter particle collisions [12, 28, 47, 64].
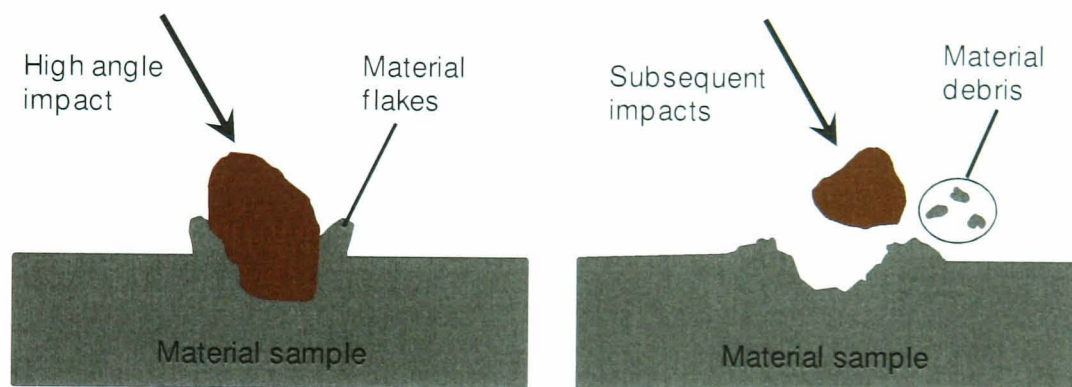
Figure 6.2b Material removal mechanism due to impact of solid particles at high and medium to low impact angles for a ductile material (for example UNS S31603).

At intermediate angles, it was proposed that both cutting and deformation can exist contributing to wear [4, 82]. Erosion wear theories described were formulated and validated based on the assumption that impact angle is the angle subtended between the surface and the leading face of the cutting object and is equal to the angle subtended by particle trajectory with the surface. Considering particle angularity and alterations in surface roughness due to indentation, it is highly impractical that such a condition exists at all instances. Finnie [33] suggested that this might lead to discrepancies in numerical correlations and the effect of which could be

negated using an experimentally determined correction factor. Nevertheless these theories offer a good starting point to compare qualitatively the local wear pattern with the impact conditions as predicted by CFD simulations.

6.1.3 Wear scar on 90° impingement test surface

The morphology of the erosion wear scar of UNS S31603 samples tested at 90° nominal impingement angle and for a nozzle exit flow velocity of 5m/s was observed under a scanning electron microscope (SEM) to assess and study the nature of local impacts and wear patterns. The conditions at which erosion tests described in the following sections were conducted are specified in Table 6.1.

Table 6.1 Operating conditions for which laboratory based impingement tests were conducted on flat UNS S31603 samples.

Fluid	Temp.	Fluid Density	Test duration	Stand-off distance	Sand density	Sand content	Sand size
Water	23°C	1000 kg/m^3	120 minutes	5mm	2650 kg/m^3	1% by weight	212-300µm

Figure 6.3 shows the top view (approximate) of the test sample on which three regions in the form of concentric halo were distinguished and a half computational model of the impinging jet indicating particle motion with line-arrows. Based on CFD predicted particle impacts the entire test surface can be divided into three major regions (as described in 6.1.1). An additional area at the edge of the surface where wear is negligible was observed and can be defined as region 4. The concentric dotted lines approximately mark the subdivision of the surface depending on impact angles and the morphology of the surface was studied in between these limits.

Visual observation of 90° impingement test sample	Particle impacts simulated using CFD
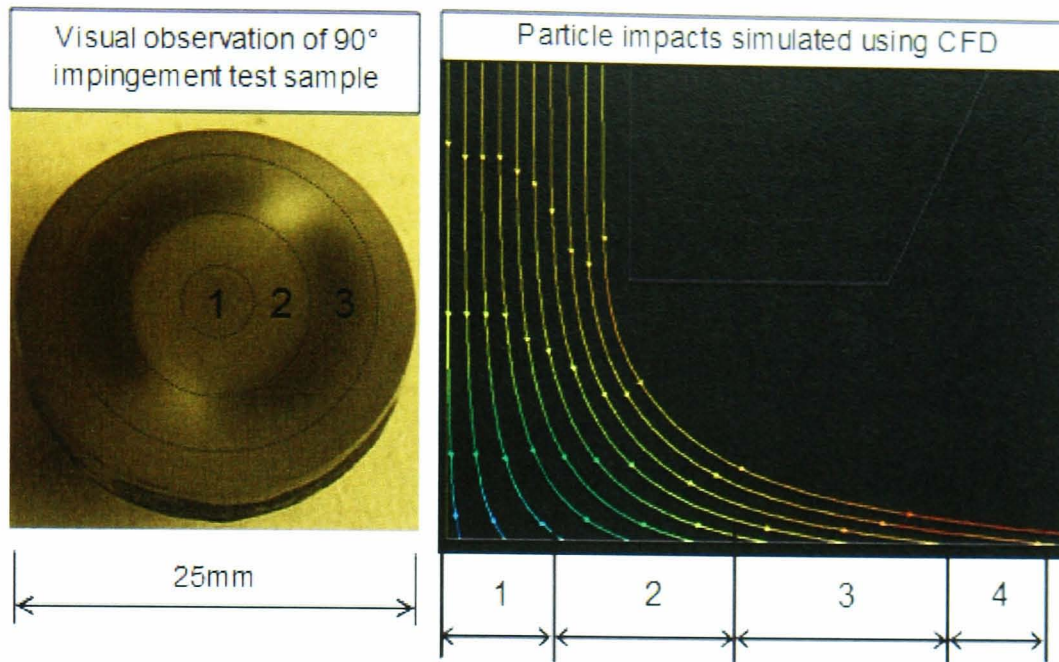
Figure 6.3 Approximate top view of the test sample after testing viewed under the naked eye indicating three distinctive regions of wear and also the CFD predictions of particle motion in the JIT. CFD simulations and experiments were conducted at conditions specified in Table 4.2 and Table 6.1 respectively for nominal flow velocities of 5m/s and 90° impingement angle.

Figure 6.4 presents the local wear pattern in region 1 close to the stagnation point. Area A annotated in the picture indicates what appears to be a deep impact scar and B shows material flakes elevated due to plastic deformation and flattened by ensuing particle impacts. Close examination indicates that material flakes are evenly spread out thoroughout this region, asserting the incidence of sand at high inclinations.

Figure 6.5 shows the SEM image of the wear scar within region 2 where CFD simulations predict particles to impact at medium-low angles. Area C highlights heavy indentation and material plastically raised around it. This indicates that this was a consequence of high angle impacts.
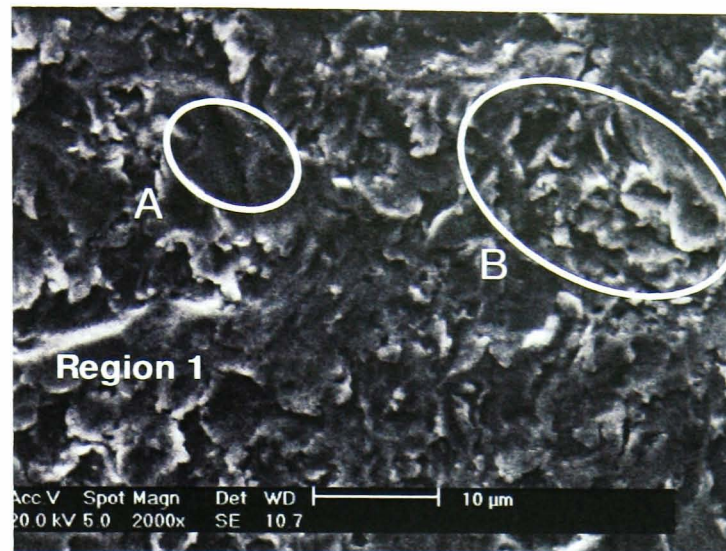
Figure 6.4 A SEM image of the wear scar at vicinity of the stagnation point, within region 1 as defined in Figure 6.3. A indicates a possible discrete heavy indentation scar and B shows material flakes generated due to plastic deformation induced by repeated particle impacts. Experiments were conducted at 90° nominal impingement angle, nozzle exit flow velocities of 5m/s and conditions specified in Table 6.1.
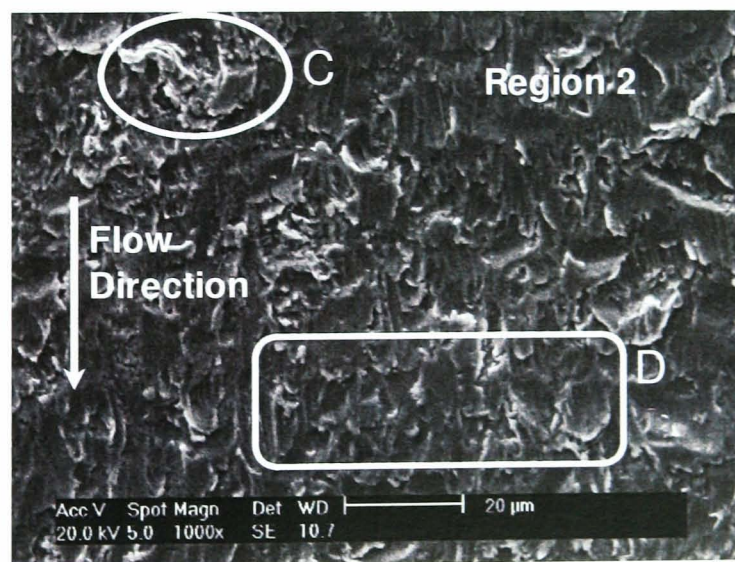
Figure 6.5 SEM image of the local wear pattern within region 2. C (closer to region 1) indicates material flakes formed due to repeated particle impacts and D shows material flakes aligned towards the flow direction. Experiments were conducted at 90° nominal impingement angle, nozzle exit flow velocities of 5m/s and conditions specified in Table 6.1.

The region enveloped by D positioned further along radial direction away from the stagnation point within region 2 presents longer indentations. Surface local indentations are primarily aligned along flow direction with raised material flakes at the edge of the dents. This shows that material is locally removed by both plastic deformation and cutting action, with cutting action predominating further away from the centre of the sample. The CFD simulation predicts particle impacts to occur at medium-low angles within this region, in line with earlier discussions.

Similarly, Figure 6.6 shows the SEM image of local wear pattern as observed on region 3, where CFD predictions imply particles to impact at low inclinations. Area E indicates a local dent with a small raised pattern at the tip of the cavity formed due to oblique impacts. Further along the radial direction, an elongated depression is underlined by area F which again emphasises that impacts predominately occurred at low angles (again the CFD predictions are in accordance with this).
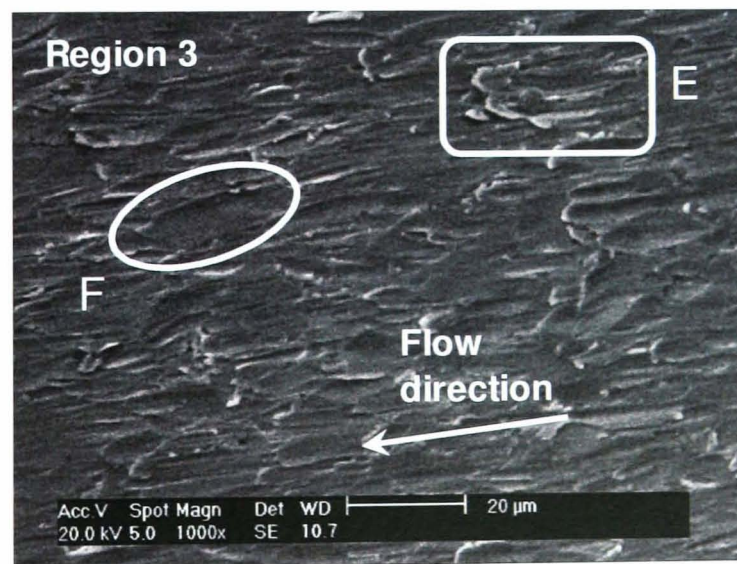
Figure 6.6 SEM photo of the local wear pattern in region 3. Area E indicates material flakes formed due to particle impacts and F shows a long shallow crater formed due to low angle impacts. Experiments were conducted at 90° nominal impingement angle, nozzle exit flow velocities of 5m/s and conditions specified in Table 6.1.

These observations demonstrated that the morphology of the wear scar at different regions are wide-ranging and also the material removal mechanism as predicted by CFD are in accordance previous observations in this area - thus endorsing prediction and experimental synchronization.

6.1.4 Wear scar on 105° impingement test surface

Further to tests conducted at 90° impingement, sand based impingement tests were performed at 105° and 135° for quantitative wear predictions which are described in Chapter 7. This section presents the work done on asserting the cohesion of experimental and numerical simulations by the qualitative comparison of anticipated and observed local wear indentations and overall pattern.
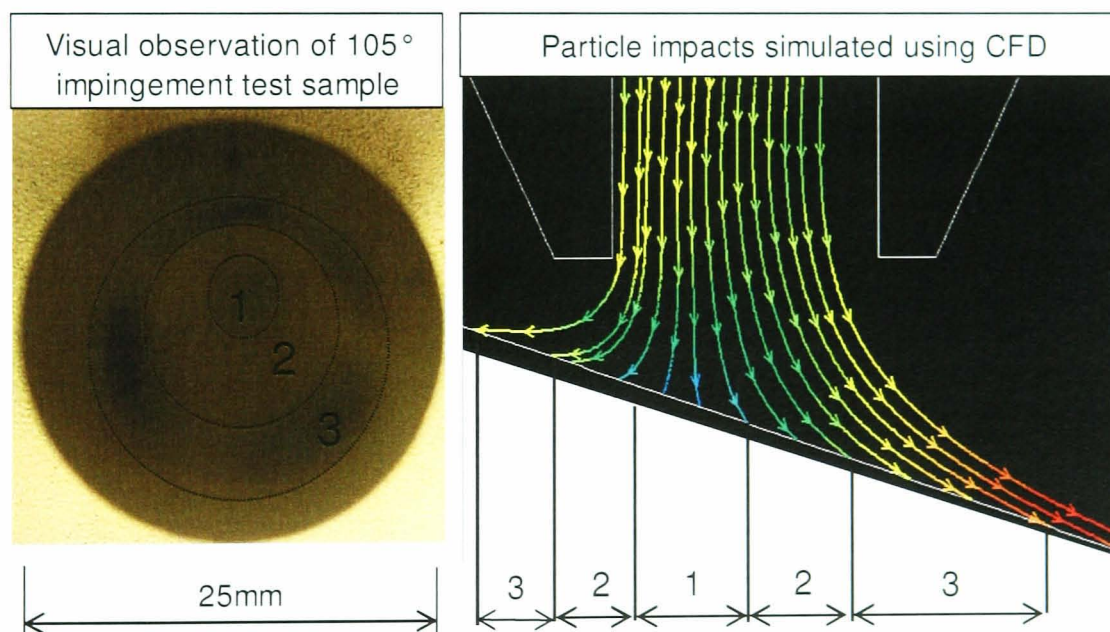
Figure 6.7 Top view of a post-test sample viewed under the naked eye indicating three distinctive regions of wear and CFD predictions of particle motion. CFD simulations and experiments were conducted at conditions defined in Table 4.2 and Table 6.1 respectively for nominal flow velocities of 5m/s and 105° nominal impingement angle.

Figure 6.7 shows the top-view of the surface tested at 105° nominal impingement angle sub-divided into three primary regions depending upon

impact angles. The regions are divided by elliptical lines, unlike the circular lines in 90° case due to non-symmetrical flow regime [85]. The three regions were examined under a SEM (Figures 6.8-6.10) to study the morphology of the surface and qualitatively determine the mode of impact wear. Figure 6.8 shows the local wear pattern on region 1 where indentations are anticipated to occur predominantly due to plastic deformations caused by repeated heavy blows, an example of which is annotated by area G. Around the top right hand edge of the image (annotated by H) it can be observed that minimal heavy indentations are present suggesting that impact angles here are not as high as around the stagnation point and flow effects tend to dominate the wear pattern.
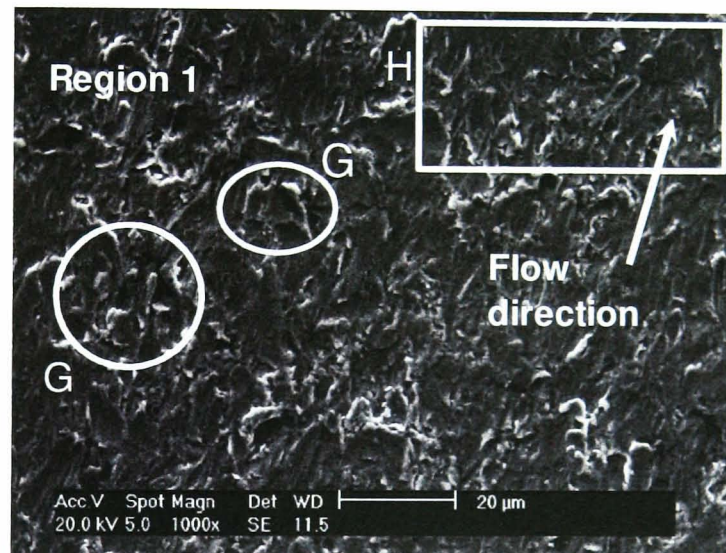
Figure 6.8 SEM picture of the wear pattern in region 1 where area G indicates surface indentation due to high angle impact and wear is due to heavy blows inflicted by sand particles. Testing was conducted for a nominal impingement angle of 105°, nozzle exit flow velocity of 5m/s and at conditions specified in Table 6.1.

Figure 6.9 shows the image of the surface with local wear craters in region 2 as observed under a SEM. According to impact data and classical wear theories, both plastic deformation and cutting action should occur in this region with cutting action predominating wear contribution. This can be confirmed by the presence of lengthy wear scars with a raised material lip

around the edge of the scar. Also the majority of the discrete impact sites and indentations are aligned with flow direction resulting in an overall wear pattern similar to what is expected at regions bombarded with medium to low angle impacts.
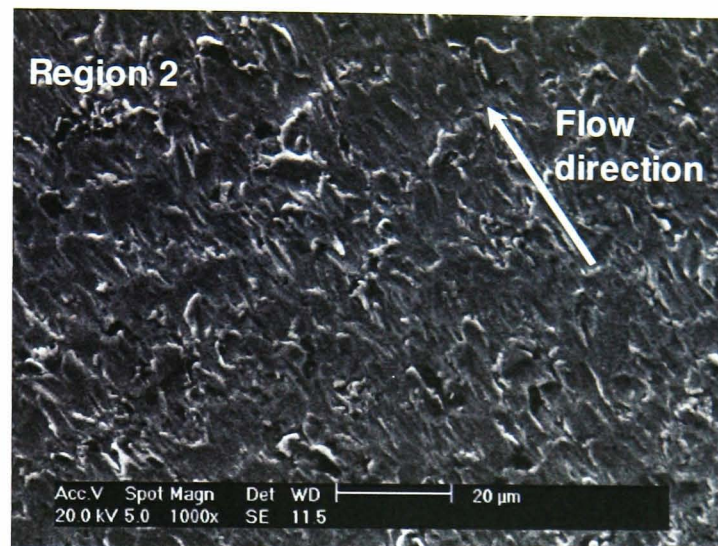
Figure 6.9 SEM picture of the wear pattern in region 2 showing majority of the surface indentations along the direction of fluid flow. Testing was conducted for a nominal impingement angle of 105°, nozzle exit flow velocity of 5m/s and at conditions specified in Table 6.1.

Figure 6.10 shows the wear pattern in region 3 where the particles are predicted to impact at glancing or sliding angles from CFD simulations. On comparing Figures 6.9 and 6.10, it can be seen that material damage (based on visual observations of surface roughness) and indentations are visually less compared to region 2 signifying sliding angle impacts leading to only scratches on the surface which is representative of an overall wear region dominated by low angle particle impacts.
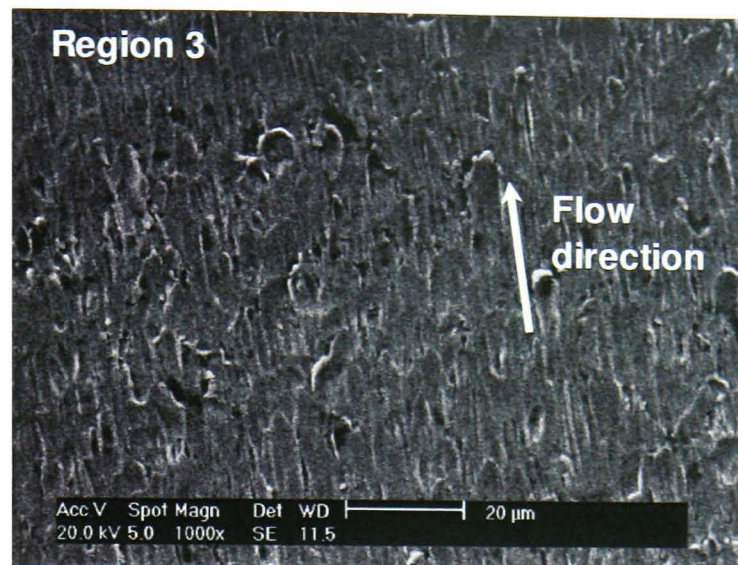
Figure 6.10 SEM picture of the wear pattern in region 3 showing surface indentations and crater along the direction of fluid flow. Testing was conducted for a nominal impingement angle of 105°, nozzle exit flow velocity of 5m/s and at conditions specified in Table 6.1.

6.1.5 Wear scar on 135° impingement test surface

Similar to the previous cases the sample surface was characterised on basis on impact angles as extracted from particle motion obtained from CFD simulation of 135° impingement test as shown in Figure 6.11. Based on the particle trajectory data obtained under this condition the overall expected wear region was subdivided into two main regions comprising primarily of medium to low angle collisions. Particle impacts at high angles were not predicted to occur which is attributed to the acutely angled flow geometry promoting smooth diversion of fluid flow.

Observing region 2 of the surface using a SEM, shown in Figure 6.12 at two different positions for local wear pattern, it was seen that material lips formed due to the cutting action of particles were aligned along flow direction. Impacts leading to heavy indentation were hardly seen, emphasizing few particle impacts at high angles as predicted by CFD simulations.
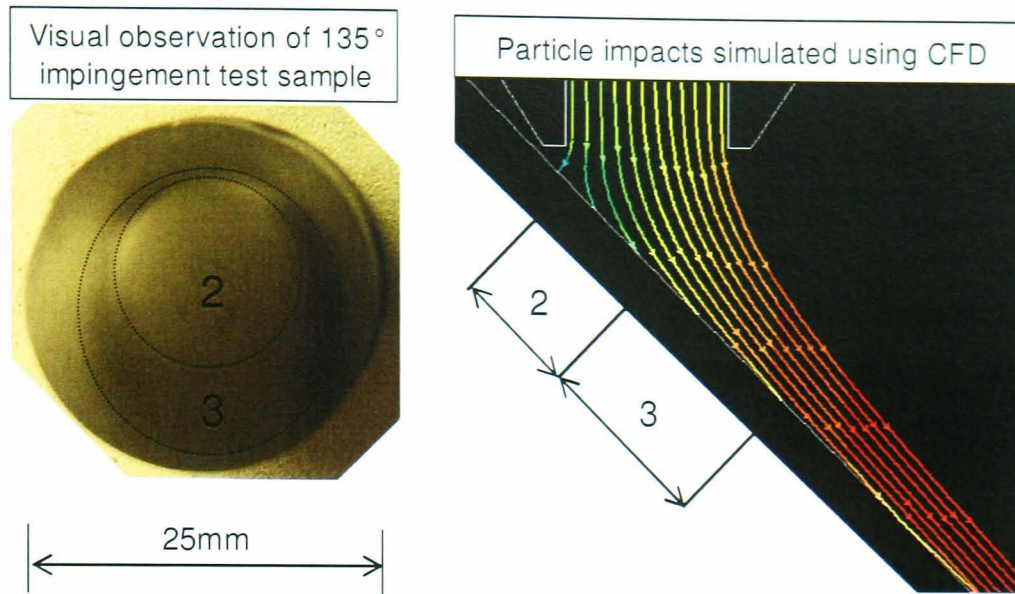
Figure 6.11 Top view of a post-test sample viewed under the naked eye indicating two distinctive regions of wear and also the CFD predictions of particle motion in the JIT at 45° along the horizontal. CFD simulations and experiments were conducted at conditions defined in Table 4.2 and Table 6.1 respectively for nominal flow velocities of 5m/s and 135° nominal impingement angle.
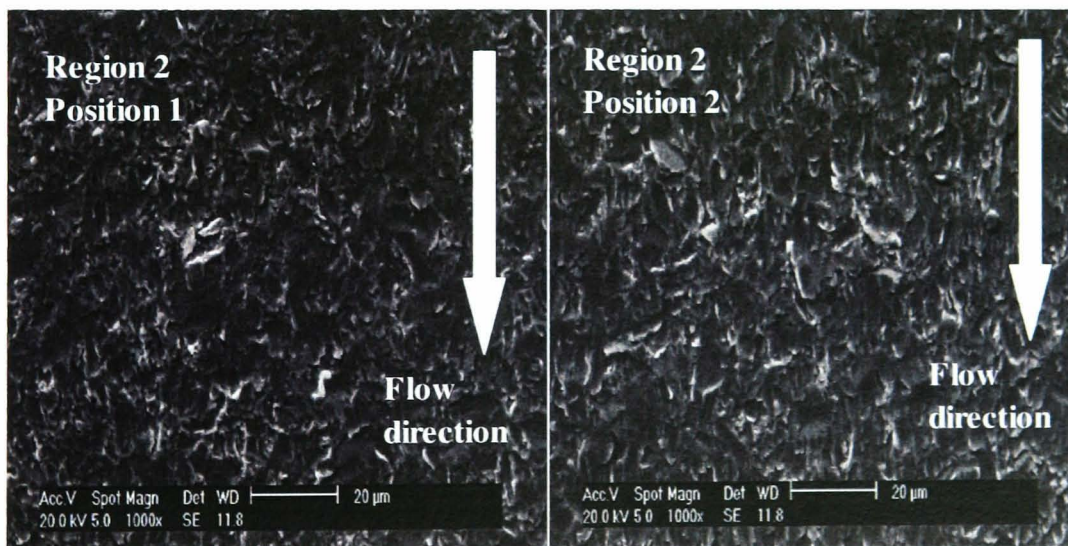
Figure 6.12 SEM photos of the local wear pattern in region 2 (defined by medium-low particle impact angles based on CFD predictions) at two different positions (position 2 is radially away from position 1 and the stagnation region). Testing was conducted for a nominal impingement angle of 135°, nozzle exit flow velocity of 5m/s and at conditions specified in Table 6.1.

Figure 6.13 shows SEM images of the surface of the test sample on region 3 at two different positions (position2 was radially away from position 1 and the stagnation region). CFD simulation data predicted particles to impact the surface at low-sliding angles and this can be seen from long craters as indicated by H in Figure 6.13. The flakes formed by material deformation are well directed towards flow direction, which stresses the fact that particles in this region impacted at very low angles as predicted by CFD simulations.
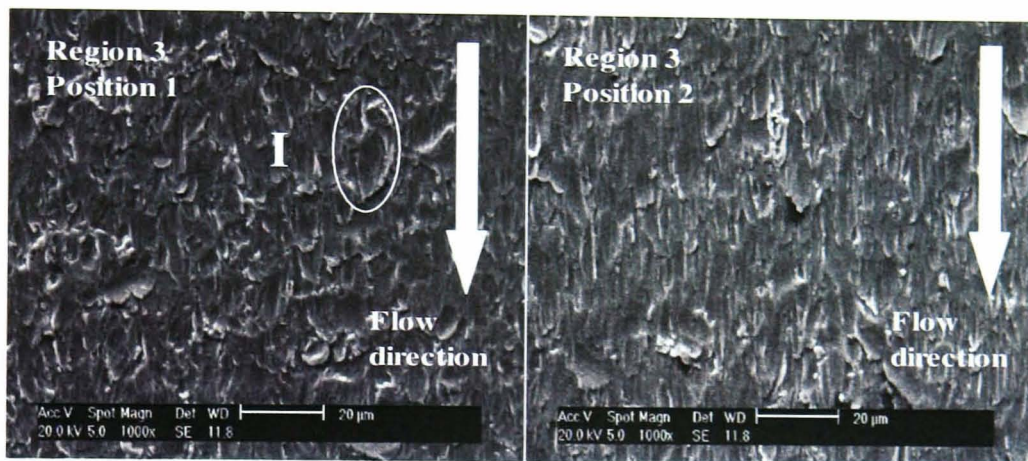
Figure 6.13 SEM image of the local wear pattern in region 3 (defined by low-sliding impact angles based on CFD predictions) at two different positions. Testing was conducted at a nominal impingement angle of 135°, nozzle exit flow velocity of 5m/s and at conditions specified in Table 6.1.

SEM images of the wear regions at several locations on the wear scar suggested wear was approximately due to wear mechanisms as dictated by impact conditions. These results can be used as evidence of accuracy in the integration of CFD simulations and experiments into a singular unit and the ability to qualitatively predict erosion mechanisms. Specifically it illustrates that for a given test it is possible to define the local conditions that exist on the surface. It was observed that for the case of 90° impingement angle, a full range of local impact conditions (which includes impacts conditions predicted to occur at 105° and 135°) existed. This emphasises the versatility of the 90° impingement test, in qualitatively capturing a broad range of erosion parameters which can exists in different geometry.

6.2 Material specific wear map development

6.2.1 Wear profile measurement

A general purpose profilometer, commercially named Talysurf probe, with the capability of measuring the profile with high resolution (resolutions below 0.1µm were achieved) was used to quantify the contour of wear samples tested at 90° nominal impingement angles and for nozzle exit flow velocities of 5 and 10 m/s along two perpendicular radial lines (passing through the centre of the wear scar) over the surface (Figure 6.14 illustrates this for the case of 5m/s). Since the test coupons and the impinging jet were perpendicular, it was initially assumed that the profile would be axis-symmetric and hence the outline on only one radius was considered for analysis. However, it was observed that the profiles were not exactly mirror images about the nozzle centre line as illustrated in Figures 6.14a and 6.14b. This non-symmetry is attributed primarily to the misalignment between the impinging jet nozzle and the test sample which is inherent of this particular apparatus (this was also reported by Wang et al. [42]). The surface profile of the specimen was then measured at various radial positions and the profile was averaged as shown in Figure 6.15.
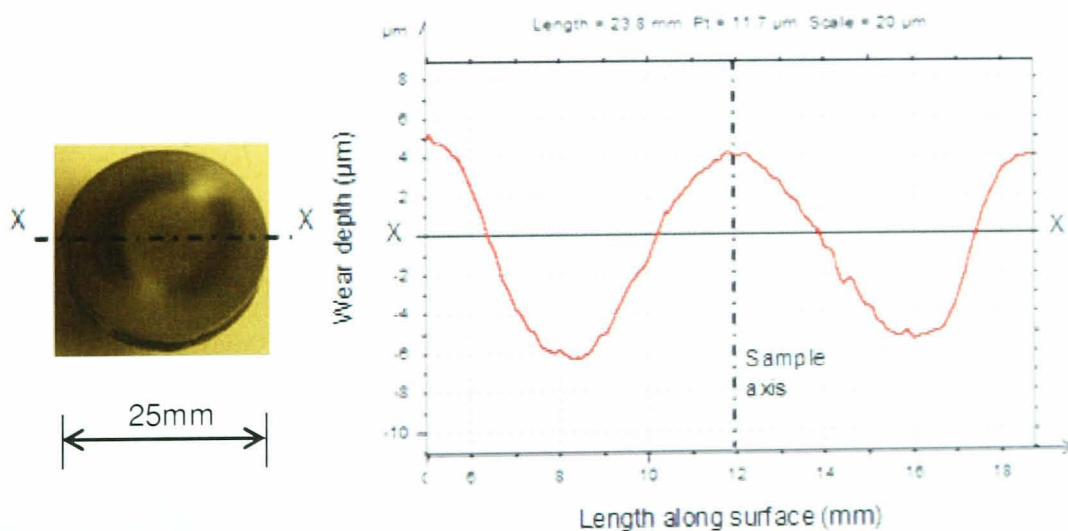
Figure 6.14a The profile of the wear scar measured along the horizontal diameter on a post test sample tested for 120 minutes using a JIT at 90° nominal impingement angle, nozzle exit flow velocity of 5m/s and conditions specified in Table 6.1.
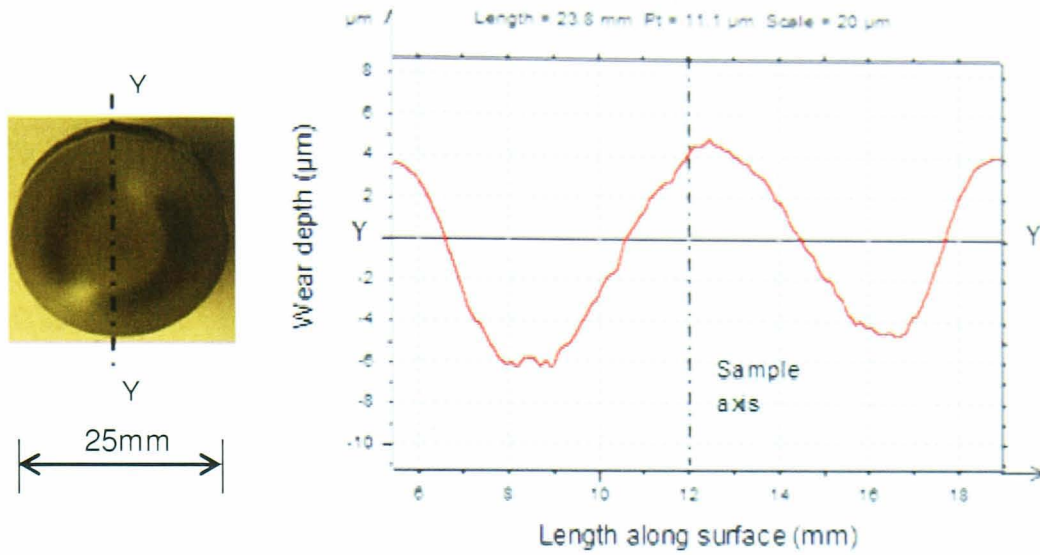
Figure 6.14b The profile of the wear scar measured along the vertical diameter on a post test sample tested for 120 minutes using a JIT at 90° nominal impingement angle, nozzle exit flow velocity of 5m/s and conditions specified in Table 6.1.
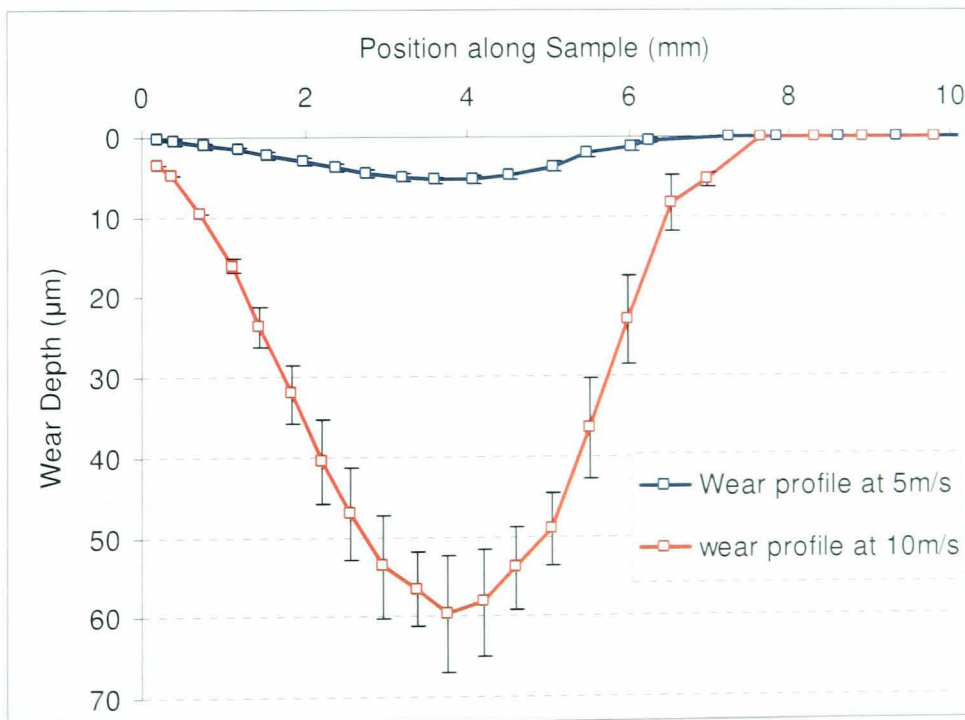
Figure 6.15 The average wear profiles along 3 different radii on wear surfaces from impingement based tests conducted at 90° nominal impingement angle, nozzle exit flow velocities of 5 and 10 m/s and at conditions specified in Table 6.1.

6.2.2 Local impact and wear data correlation

CFD simulations of the JIT test at 90° and 5 and 10 m/s flow velocities enabled local particle impact data (velocity, angle and rate) to be predicted as a function of radial position. This data (V_p and θ only) is represented graphically in Figure 6.16 and the construction of the wear map requires local wear data for each point on the two curves illustrated. The position on the surface is a decisive factor since it presents the only common factor between CFD impact data and experimental wear data. Using this as a starting point, an array of local wear data was directly associated to local impact conditions to populate Table 6.2 as illustrated by Figure 6.17.
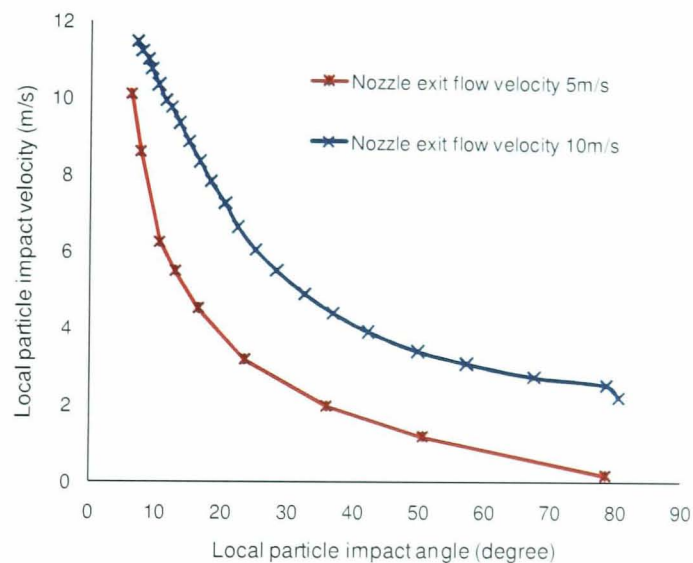
Figure 6.16 Predicted local particle impact conditions on a flat surface at nozzle exit flow velocities of 5 and 10 m/s for which average wear data has to be correlated. Please note impact rates are not shown here.

Impact angle and velocity was directly obtained from particle motion data (post-processing stage), whereas, further calculations were made to determine impact rate. Assuming equal distribution of particles within the nozzle (at 70mm from the exit of the nozzle), for a nozzle exit flow velocity of 5m/s it was observed that only particles released within a radius of 2.6mm from the nozzle axis (illustrated in Figure 4.12a) would impact the surface (i.e. approximately 75% of the total number of particles in the system). The

release position was further divided into various sections (for example; 0.0-0.5mm, 0.5-1mm, etc.) and the corresponding impact position was recorded. This enabled the percentage of particles impacting a particular region of the test surface. This was then normalised taking into account the average particle velocity to give the local impact rates (n).
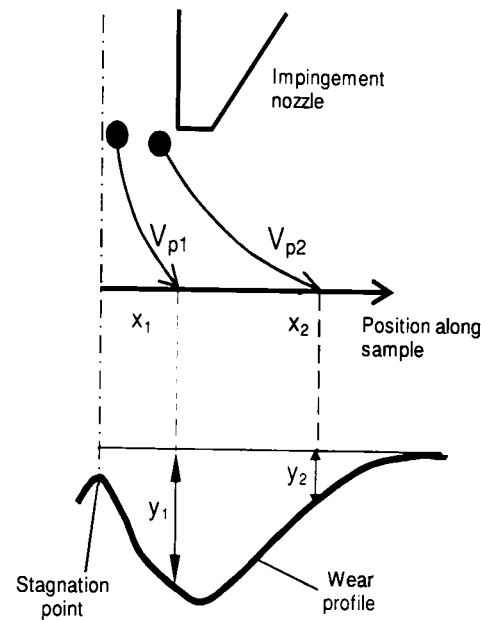
Figure 6.17 A schematic representation of correlation between local impact parameters and experimental wear data.

Table 6.2 Correlation of local impact conditions to average wear depth for exact same positions as predicted using CFD. Here and in Figure 6.16, Vp and θ are local particle impact velocity and angle, n is the number of impacts at that position, x is the radial distance from the centre of the scar, y is the average wear depth and n is the total number of available local impact data set.

Local position	Impact conditions	Average wear depth
x_1	V_{p1}, θ_1, n_1	y_1
x_2	V_{p2}, θ_2, n_2	y_2
x_i	V_{pi}, θ_i, n_i	y_i

Using mathematical software, Minitab 15, a local average wear map (shown in Figure 6.18) was obtained and for every impact data set within the envelope of this map, an average local wear data can be predicted for that specific abrasive-material combination.
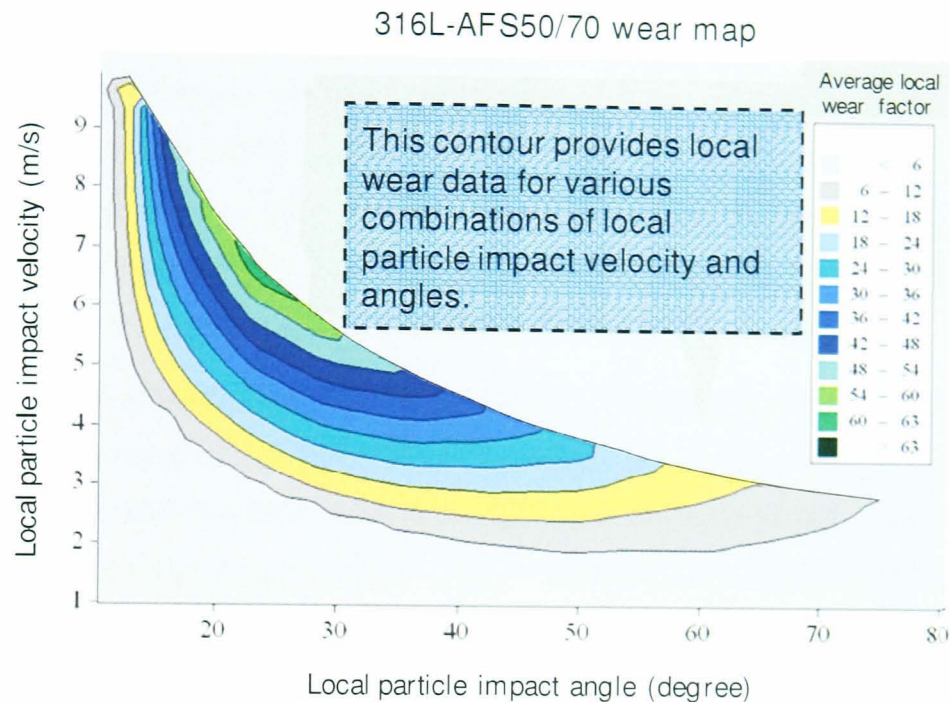
Figure 6.18 The material-abrasive specific wear map translates local particle impact data to local average wear per impact.

6.2.3 Characteristics of the developed wear map

There are various regions within the confines of the wear map, which can be characterised by the local particle impact angles and velocities. For an impact data point which lies within any of the contours, a local wear depth can be obtained and each contour in the wear map corresponds to a range of local wear rate as shown in Figure 6.18. This range specifies the upper and lower limit for a particular predicted local wear value and this is represented as standard deviations in some of the predicted wear profiles presented in subsequent chapters (standard deviations are shown only on few profiles to enhance graphical visualisation). This range within which the local wear rates varies for a specific impact condition (angle and velocity) is

dependent on the resolution of the wear map (the highest possible resolution was used in this study).

However, the JIT is unable to reproduce particles impacting at both high velocity (close to the nominal flow velocity) and perpendicular angles. High angle impacts generally occur around the stagnation region where the decelerating effect of the fluid retards particle motion leading to low velocity impacts. Nonetheless for the same reason, the probability of particles impacting material surfaces at both high angles and velocities in hydro-transport equipment is also low. The area covered by the wear map can be increased by increasing the nozzle exit velocities, which then would provide wear data for higher impact particle impact velocities.

Also for certain particle impact conditions such as very low impact, sliding or glancing angles (<10°) the map predicts no wear. This is attributed to the lack of material wear data for particle impacts below 10°. From Figure 4.12d (local impact angle data for 5m/s nozzle exit flow velocity) it can be seen that impacts below 10° occur at beyond 6mm from the centre. At these regions for the case of 5m/s, negligible wear data was observed from experiments (Figure 6.15). On the contrary for the case of 10m/s, for impacts below 10° (Figure 6.19 shows impact angle data as a function of position: impacts below 10° occur beyond 7mm from the centre) measurable wear data was observed (from Figure 6.15). Although the wear volume was relatively low compared to overall damage for 10m/s, but relative to 5m/s it was considerable.

The wear map requires a minimum of two local impact velocity data points with wear data associated with, for a particular local impact angle to predict the variation of material wear with impact velocities for that angle. However, for impact angles below 10° we have only one set of impact velocity data (from the nominal jet velocity of 10m/s) for which wear data is available (example, for an local impact of 10°, wear data exists only for an impact velocity at 11m/s). It is possible to construct the wear map with only one velocity data point for 10°. However, this presents a situation in which for an impact angle of 10°, for different impact velocities only one value of

local wear data would be predicted and hence during construction of the map impacts below 10° were not included.
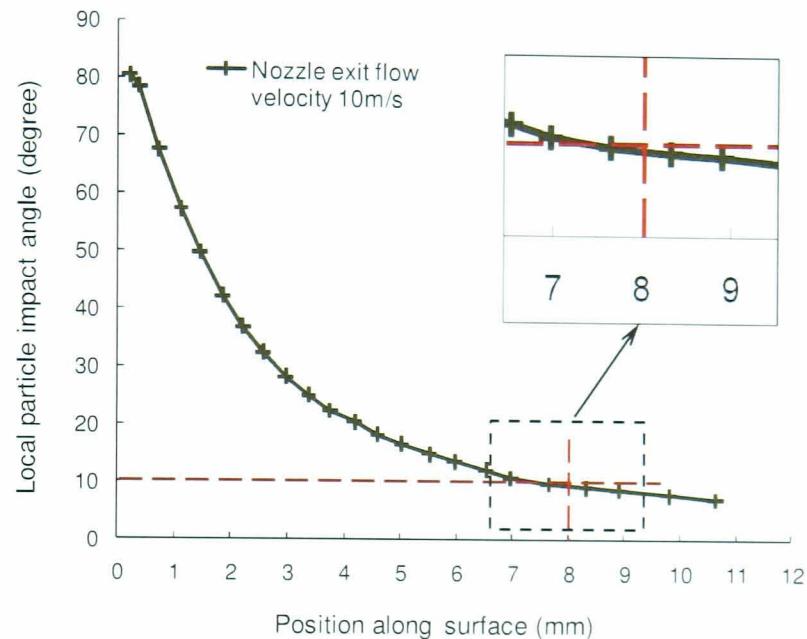
Figure 6.19 Variation of local impact angle with radial position from the centre of an impingement based erosion wear scar. Tests were conducted at 90° nominal impingement angle, 10m/s nozzle exit flow velocities and conditions specified in Table 6.1.

This raises another issue in the form of variations in wear volume for similar impact angles (<10°) but at different velocities. For the case of low flow velocities, measured wear volumes at this region (<10° impact region) is considered negligible, however, at 10m/s wear in this region is amplified and hence is significant. Also it is postulated that the effect of secondary impacts can be major around this region. Neilson and Gilchrist [82] pointed out that at shallow impact angles, particle residual velocities (velocity at which a particle exits post collision) can be very close to impact velocities. This corresponds to very low impact energies and hence negligible wear. Increases in impact velocities lead to a possibility of higher wear due to greater impact energies.

Particles post collision preceding this location tend to get dragged away from the surface by the fluid which can lead to inter-particle collisions [36].

The effect of this can be pronounced with increasing overall concentration as observed by Reza [6]. Along the surface, local particle concentrations can be highest at the edge of the surface (due to rebounding and oncoming particles) and hence the effects of collisions can be higher. The effect of particle collisions and residual velocities can lead to very low wear and hence for attainment of measureable wear data, higher velocities are to be employed or test durations can be prolonged for low flow velocity case.

6.3 Summary

A systematic approach to developing a material specific wear map with the function of rendering wear data for a range of erosion parameters has been presented and can be summarised as follows.

- Post test surfaces conducted at nominal impingement angles of 90°, 105° and 135° were examined under a scanning electron microscope to study local wear patterns at different regions. The regions were spatially characterised by different impact regimes as defined by CFD simulations aided by impact wear theories. It was observed that local wear patterns were qualitatively in accordance with CFD predictions.

- Another significant observation was that all material removal modes prevalent on 105° and 135° existed on 90° surface. Thus a standard submerged 90° impingement test with CFD can be useful in predicting wear damage on various geometrical configurations.

- Wear data obtained from testing conducted at 90° nominal angle with flow velocities of 5m/s and 10m/s was correlated to local impact conditions to obtain a material specific wear map. It is proposed that this map can provide an average material loss due to erosion for a specific sand-test material combination for a wide range of impact angle and velocity.

- Testing at higher nozzle exit flow velocities can increase the confines of the wear-map and it is suggested that this map is material-sand specific and not universal.

- The wear-map does not predict any wear for impacts at high angles and velocities. This is attributed primarily to local fluid regime, however, due to the fact that these conditions rarely exist in practice, this drawback is not considered significant.

- Also, the wear-map does not predict any wear for impacts below $10°$ and this is attributed to the lack of substantial wear data from material tests. For the construction of the wear map, every local impact angle should be associated with two velocity points with wear data, however, this was not the case and hence the wear-map fails at this juncture (predicting effects of sliding angles).

- It is proposed that the wear-map, barring a few deficiencies due to experimental shortcomings and lack of clear understanding of secondary effects, can be resourceful in providing wear data for a range of erosion conditions by mapping the data obtained from just two simple laboratory tests.

Chapter 7

Results: Wear predictions using CFD and the wear map

7.1 Erosion wear predictions on flat samples and 90° bend

In chapter 5, sand based erosion tests were conducted on flat UNS S31603 specimens at 90° and nozzle exit flow velocities of 5 and 10 m/s. Wear data was interpreted using particle impact data obtained from CFD simulations as described in chapter 4. A material and sand specific wear map was developed (chapter 6) with the capability of predicting local wear rate for a wide range of impact parameters.

Using this data, the ability of this wear map in predicting wear on complex geometries and conditions is explored. To validate the proposed method, CFD simulations of the impingement test on a flat specimen were performed under a variety of configurations (section 7.2 to 7.4) and also on pipe bends (section 7.5).

Numerical simulations of the impingement test at configurations listed below were performed using the modelling approach described in chapter 4 and conditions specified in Table 4.2.

   i. 90° nominal impingement angle and 7.5m/s nozzle exit flow velocity,

   ii. 105° nominal impingement angle and 5m/s nozzle exit flow velocity,

   iii. 135° nominal impingement angle and 5m/s nozzle exit flow velocity.

Laboratory tests were carried out on flat UNS S31603 samples at these configurations and also for conditions specified in Table 6.1 to validate wear predictions and the accuracy of each case is presented in the following sections.

7.2 90° angle and 7.5m/s nozzle exit flow velocity

7.2.1 Description of CFD predicted flow field and impact data

CFD simulation and experiments of the JIT for a nozzle exit velocity of 7.5m/s was conducted on the geometry defined in Figure 5.1, using similar approaches for modelling (chapter 4) and laboratory tests (section 5.4). The hydrodynamic flow regime is qualitatively similar to the case of 90° at 5m/s since the geometry remains the same. The flow field is previously described in section 6.1.1 and the variation of local impact conditions along the surface can be expected to be similar to the case of 90° at 5m/s (Figure 4.13) and is illustrated in Figure 7.1.

(a) Particle impact velocity
(b) Particle impact angle
(c) Particle impact rate
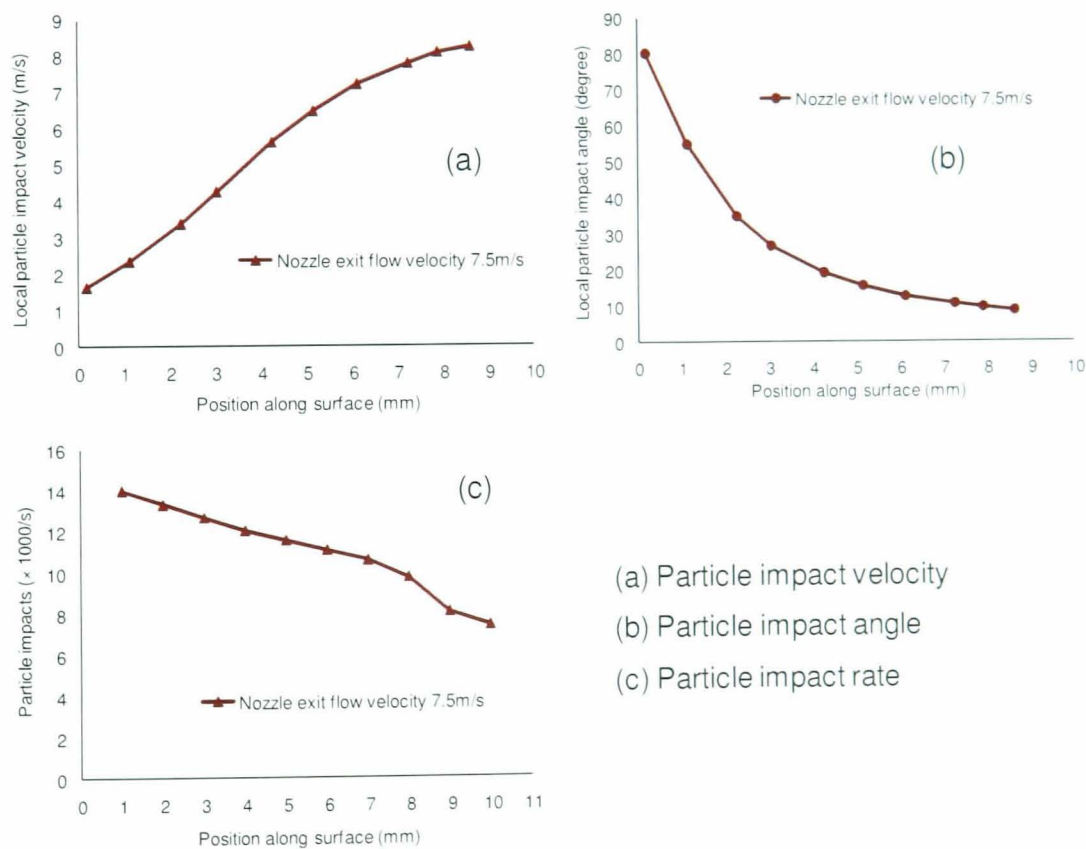
Figure 7.1 Variation of local impact data as a function of position from the centre of the wear scar as predicted by CFD for 90° angle at 7.5m/s.

7.2.2 CFD predicted and experimentally measured wear scar for 90° and 7.5m/s

From the particle impact data (Figure 7.1) average local wear profile was predicted for this configuration using the UNS S31603-AFS50/70 wear map (Figure 6.18) which is shown in Figure 7.2. The experimental wear scar at this condition was profiled at three randomly picked radii which were averaged to obtain an experimental profile as illustrated in Figure 7.2. The wear profiles resembled the classical w-shape appearance as observed on post erosion test surfaces on ductile specimens, e.g. Lapides and Levy [173] and Hu et al. [17]. It is previously mentioned that the wear map can provide a range of wear data (depending on the resolution of the map) for a set of local impact condition which accounts for the standard deviations in predictions (section 6.2.3). Good agreement was seen between both the profiles except at the edges of the wear scar, as illustrated in Figure 7.2. The error bars shown in the measured profile gives the limits of the wear depth along the length of the post test surface from the centre of the specimen.
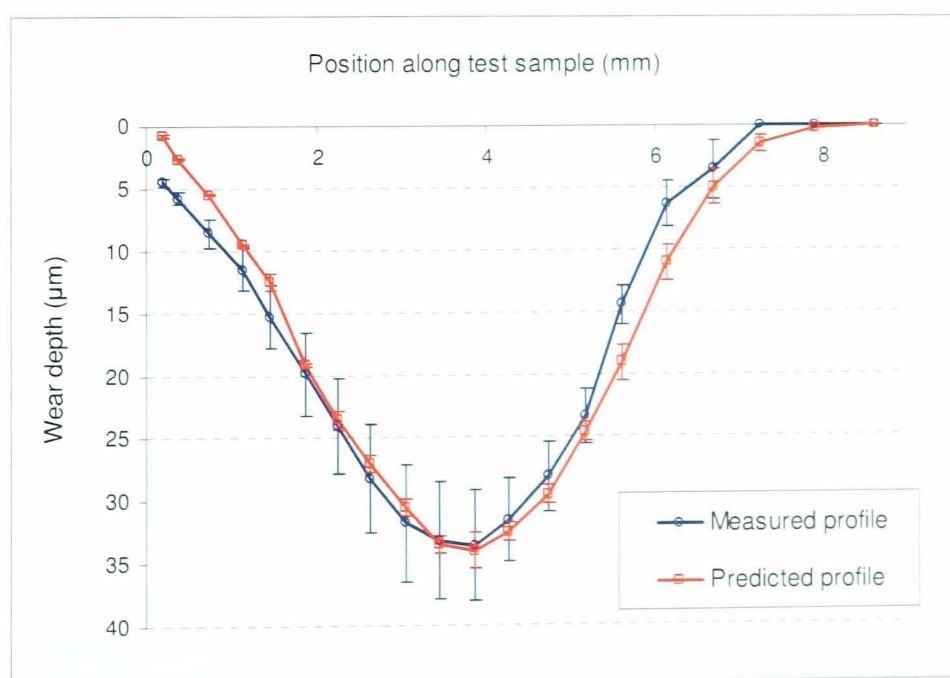
Figure 7.2 Predicted and experimentally obtained wear profiles on flat UNS S31603 samples for a JIT configuration of 90° and flow velocities of 7.5m/s.

7.2.3 Misalignments within sample and nozzle configurations

It was earlier mentioned that although the sample and nozzle were assumed to be perpendicular in CFD simulations, misalignments are inherent in this system and measured wear profiles were not mirror images about the stagnation point axis. Misalignments were primarily due to difficulties in measuring the surface nozzle separation distances. For the case of 90° impingement angles, a flat reference plate (5±0.2 mm thickness) was used to separate the surface and the nozzle. The sample holder was at this position as illustrated in Figure 7.3a. For the case of 105° and 135°, measuring the separation distances and maintaining the orientation was fraught with difficulties. This is primarily due to the geometry and the simple nature of the setup (Figure 7.3b), which also posed a problem in fixing and maintaining the sample holder in position.
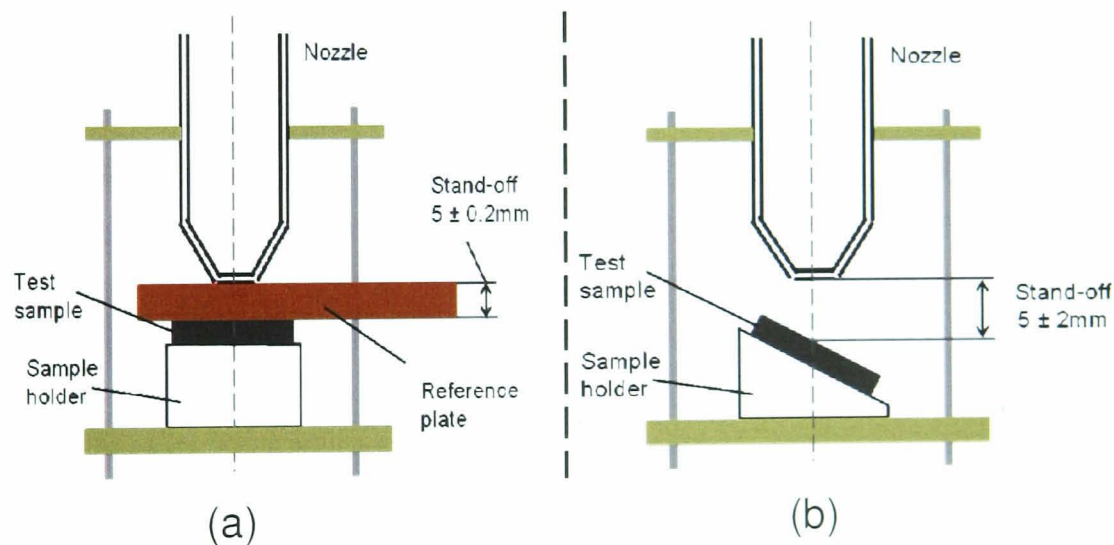
Figure 7.3 Methods used to maintain the separation distance between the surface and the nozzle.

Differences between CFD and experimental geometries are inherent and since close tolerances were difficult to achieve in the experimental setup, it is suggested that the experimental geometry can vary within a certain range set as acceptable and is provided in Table 7.1

Table 7.1 The range within which geometrical parameters of nozzle-sample setup can vary for different configurations.

Parameter	Case 1- 90° and 7.5m/s	Case 2- 105° and 5m/s	Case 3- 135° and 5m/s
	Tolerance range		
Nominal impingement angle	90 ± 5°	105 ± 5°	135 ± 5°
Stand-off distance	5 ± 0.2 mm	5 ± 2 mm	5 ± 2 mm

7.2.4 Prediction discrepancies at 90° and 7.5m/s

The wear map was developed from data obtained from tests conducted under similar geometry and hence the existing flow regime at 90° and 7.5m/s is qualitatively similar and can be perceived to be a scaled up version of the 90° test at 5m/s. Figure 7.4 shows good numerical agreement in positions between 1-5 mm with the numerical errors within ± 20%. High prediction divergence was observed towards the edge of the wear scar and around the stagnation region. Wear at these regions are low and hence any possible errors of measurement in this test or in developing the original wear map, can be amplified to elevated values. Low wear depths at these regions can be attributed to the effect of the flow field (described in Chapter 6). Theoretically no impacts occur at the stagnation point and hence zero wear; however, tests results indicate positive wear. This can be accounted for particles altering trajectories due to inter-particle collisions and impacting the surface at the stagnation point leading to material wear [87, 119].

At the edge of the wear scar, where particles predominantly slide along the surface, wear is low. This is attributed to lack of material wear data required to build the during wear map at sliding angles (<10°) as previously discussed in section 6.2.3.
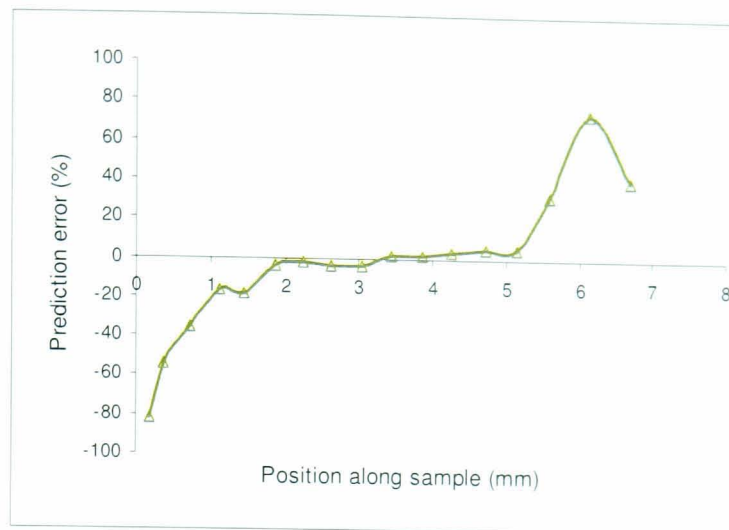
Figure 7.4 Predicted deviations along the surface of the test sample with zero representing the stagnation point.

Prediction error can also be accredited to possible misalignment between sample surface and nozzle edge during testing. To determine the sensitivity of minute variations of impingement angle on wear predictions, simulations were conducted with the surface inclined at several nominal angles within the allowed range of orientation (Table 7.1). Figure 7.5 shows the predicted profile at 92.5° (CFD was conducted at 92.5°) as compared with measured profile (original nozzle-sample configuration) and the numerical variations of predictions is graphically represented in Figure 7.6. Also the previous prediction discrepancies (Figure 7.4) are shown alongside for comparison.

Visual observation of both the profiles suggests that for the CFD configuration of 92.5°, predicted and measured profiles are closely matched with differences vastly reduced (more than 50%) near the stagnation region and at the edge of the wear scar (Figure 7.6) while the accuracy between positions 1 to 5 mm is retained. This suggests that there could be possibility of impingement angle while testing was not strictly 90° and the effect of this geometrical variation is to alter the stand-off distance, surface orientation, particle impact distribution all of which can contribute to differences in wear profiles. This demonstrates the sensitivity of predictions towards minor geometrical variations, particularly in regions with low material wear.
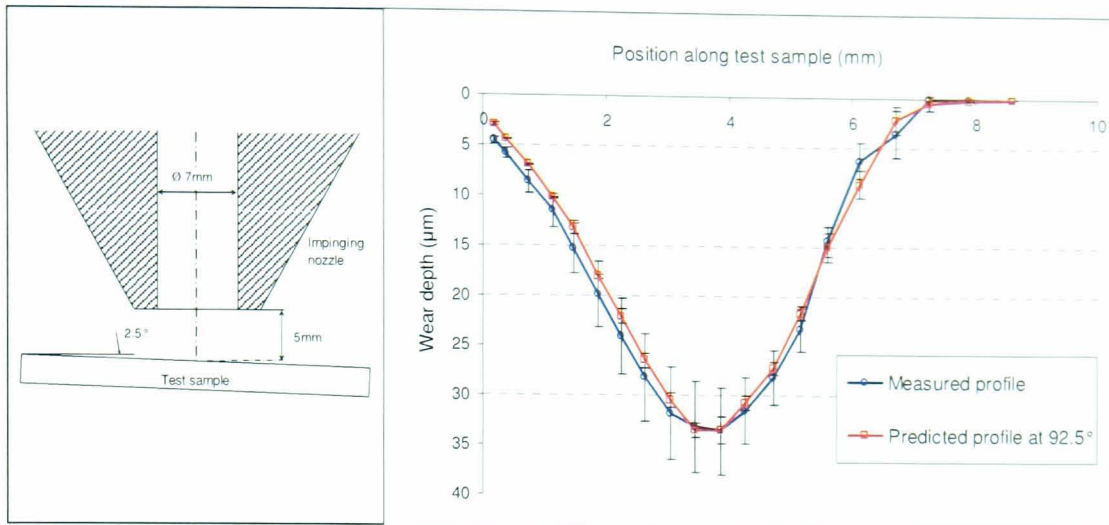
Figure 7.5 Wear profile predicted using the CFD-wear map method at 92.5° impingement angle and measured profile under an apparent 90° nominal impingement angle and flow velocity of 5m/s.
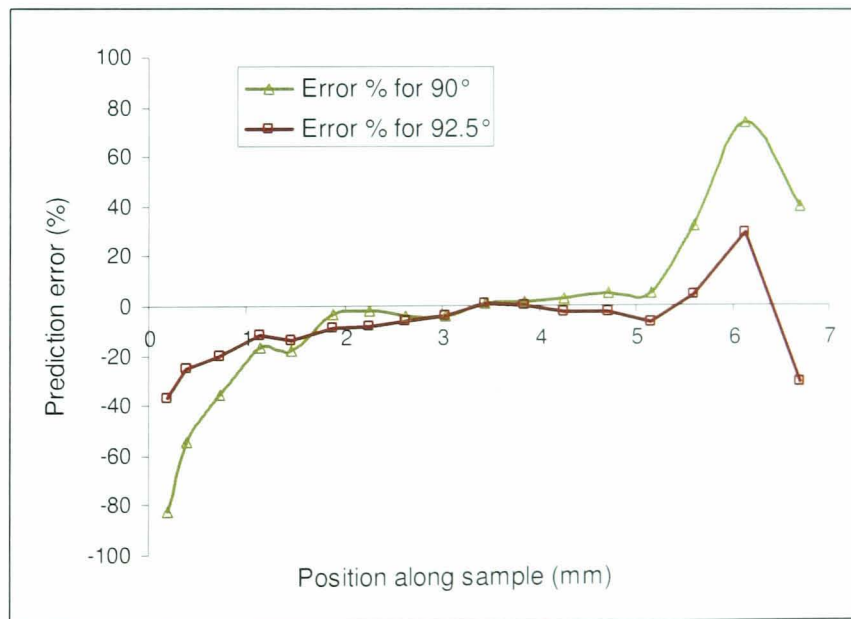
Figure 7.6 Prediction differences at various surface locations between CFD and wear-map predicted profiles at 90° and 92.5° nominal impingement angles and experimentally measured profile.

This could very well mean that the nominal impingement angle in any one of the three 90° laboratory tests was not exactly 90°. Minor alignment

errors affected accuracies at low wear regions but had minimum influence on remaining regions and hence the total average mass loss during testing did not fluctuate vastly (section 5.4) with low standard deviations. This related to good repeatability of laboratory tests and as a result of this it was highly improbable to isolate any particular test data due to inappropriate definition of conditions. However, without considering the possibility of misalignments predictions were quantitatively good. The flow regime for this case was similar to the ones from which the wear map developed (both at 90° nominal impingement angle) and hence this scenario presents a case of interpolating available wear data.

7.3 105° angle and 5m/s nozzle exit flow velocity case study

Unlike the 90° case, the 105° is not axis-symmetric and hence a 3-D model had to be used in simulations and for optimum utilization of computational only a half model (represented in Figure 7.7) was developed and simulations for nozzle exit flow velocity of 5m/s was conducted. Particle tracking equations were solved on the obtained single flow solution adopting the approach described previously (section 4.3) to predict local impact data and subsequently wear profile using the material-sand specific wear map. JIT were conducted on the same geometry at exact nominal flow parameters and conditions specified in Table 6.1.
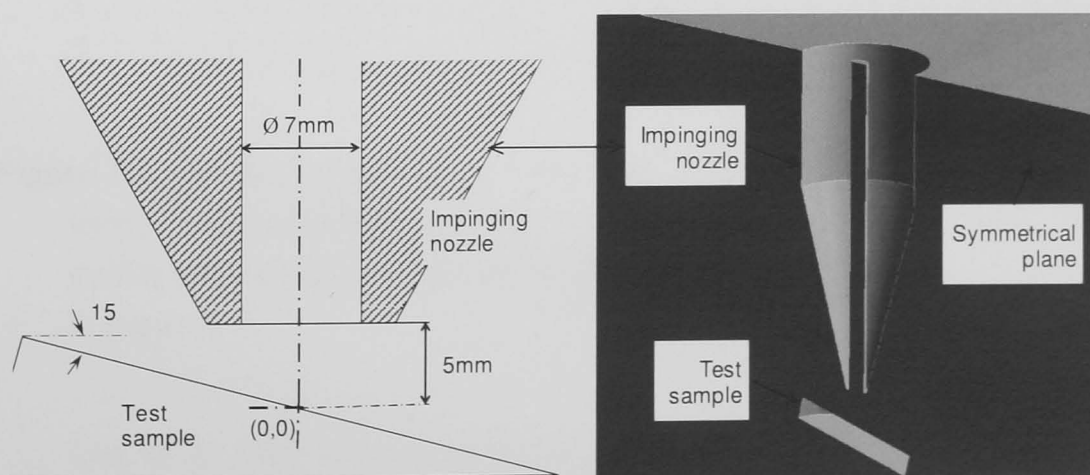
Figure 7.7 A schematic of the cross sectional view of nozzle/sample and the flow geometry used in CFD simulation as an approximation of the actual test geometry.

7.3.1 Description of CFD predicted flow field and impact data

Since the geometrical configuration is not axis-symmetric, the resulting flow field is not similar on either sides of the stagnation point. This leads to an asymmetrical distribution of particle impacts and wall shear stress (significance of this is previously described in 4.2.8) about the stagnation point as illustrated in Figures 7.8a and 7.8b (local particle impact data are shown in Figure 7.8c and 7.8d).
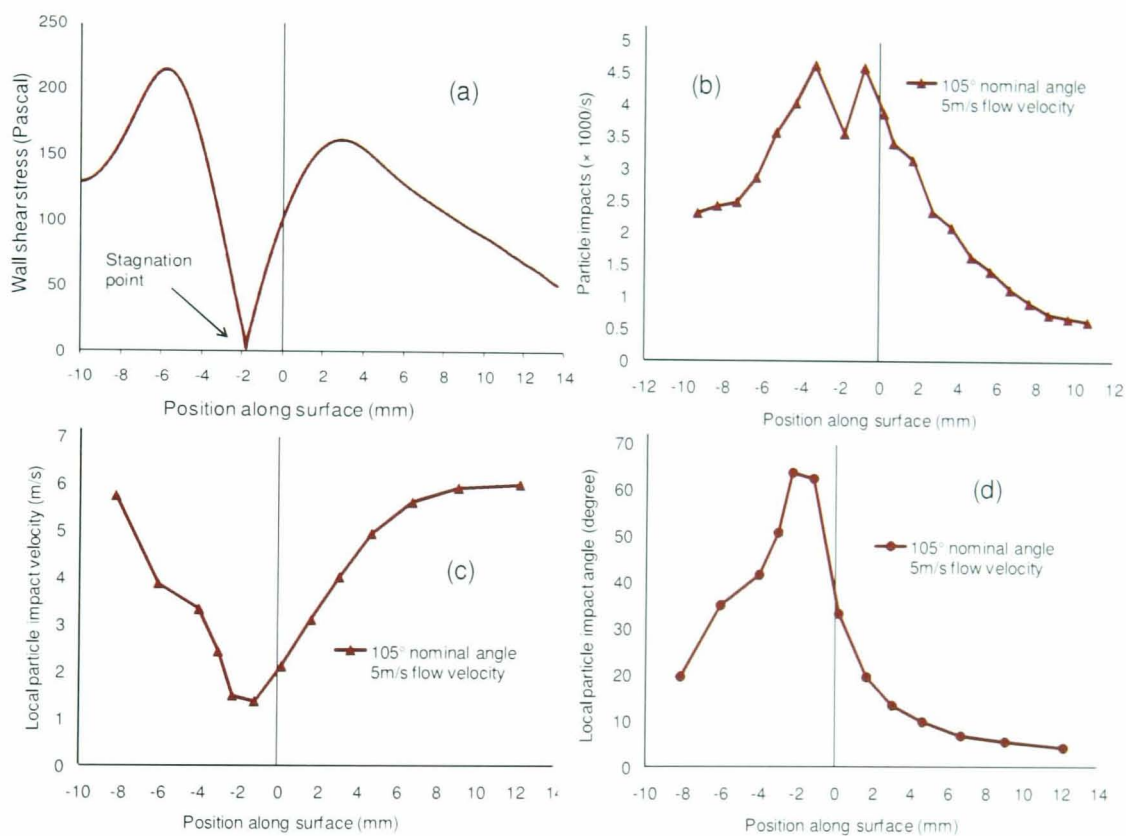
Figure 7.8 Variation of wall shear stress and particle impact data along the length of a surface oriented at 105° to an impinging multiphase flow exiting the nozzle at 5m/s, as predicted by CFD on a geometry defined in Figure 7.7.

Oka et al. [85] eroded aluminium samples using SiO_2 abrasives with the surface oriented at various nominal angles (90°, 120°, 150° and 160°) to the impinging multi-phase flow and post-test surface analysis revealed wear scars to be 'pear' shaped. It was observed that maximum wear depths occurred on the major axis of the pear shape and hence all analysis

described further (CFD and wear measurements) in our study are performed on this axis. The geometry chosen for analysis was a 2-d plane normal to the sample and intersecting both the nozzle and the sample (i.e. the symmetrical plane); such that the line representing the sample (in this plane) in CFD simulations coincides with the expected line of maximum physical wear depth. The fluid jet exiting the nozzle branches into two streams about the stagnation point. Streamlines flowing towards the negative side (left hand) of the stagnation point are highly curved compared to the streamlines on the positive/right hand side. This is due to the acute angle geometry on the negative side, whereas the fluid jet on the positive side slides relatively smoothly along the surface. This leads to larger velocity gradients and shear stress on the negative side, which leads to high angle impacts [31, 32, 176]. Impact velocities at these regions are, however, low due to the severe deceleration of the fluid [48] (section 6.1.1) as encountered on either side of the stagnation point.

The asymmetric condition also leads to non uniform distribution of particle impacts on either side of the stagnation point (Figure 7.8b). Although the general trends of particle impact rates predicted by CFD on both sides were similar, calculations suggested the positive side endured more number of impacts. This is due to high particle-flow coupling around the positive side promoted by the relatively gradual change in flow directions and total number of impacts on this side was estimated to be greater than 20%.

Particle impact velocity and angle data, graphically presented in Figures 7.8 (d and c), suggests that velocities on either side of the stagnation point (approximate position -2.0mm) is at the lowest and impact angles are of the highest values. High to medium angle impacts (65-30°) on the right side are predicted to occur only over a small region (-2 to 0 mm). The sample nozzle separation distances on the right hand side increases with radial distance thus reducing the tendency of high angle impacts [16]. Consequently impact velocities increase and angles reduce along the length of the specimen away from the stagnation point.

Particles impacting on the edge of wear scar at the right hand side (6 to 12 mm) tend travel at high velocities and impacts are predicted to occur at

sliding angles (<10°). However, impact angles on the negative side (positioned between -2 to -8 mm) are in general between high and medium (65-30°), which is due to smaller nozzle/sample separation distances.

7.3.2 CFD Predicted and experimentally measured wear scar for 105° and 5m/s

Using the UNS S31603-AFS50/70 wear map, an average local wear rate was associated for almost all impact data (no data was available for <10° impacts) and wear profile was predicted (shown in Figure 7.9). Low values of wear were observed on either side of the stagnation point, due to a combined effect of high impact angles (>60°, ductile materials endure high angle impacts [28, 177]) and low impact velocities. The predicted wear profile has the shape of two valleys of different depths on either side of the stagnation point. The different depths can be explained with the help of Figures 7.8 (c and d), illustrating the variation of particle impact data along the surface. Maximum wear depth is predicted to occur on the right hand side between 0-2 mm where impacts are predicted to occur at 20-35°, which is within the range of peak ductile material loss [98, 178]. However, on the left hand side impacts at 20-35° are predicted to occur around the edge of the surface where impact rates are low (Figure 7.8b). Maximum wear depth on the negative side is predicted to occur between points -3 to -5 mm where the impacts occur at medium angle range (30-50°: a combination of deformation and cutting mechanisms work here) and is lower compared to the right hand side's wear depth (approximately 50% of the maximum depth).

7.3.3 Prediction discrepancies at 105° and 5m/s

Qualitative comparisons suggests good agreement between predictions and measurements, in particular the two different wear depths on either side of the stagnation point. However, numerical differences between local wear depths along surface length indicated major inconsistencies between the two

wear profiles (Figure 7.10), especially around 0-3 mm where maximum wear depth is predicted and around the stagnation point.
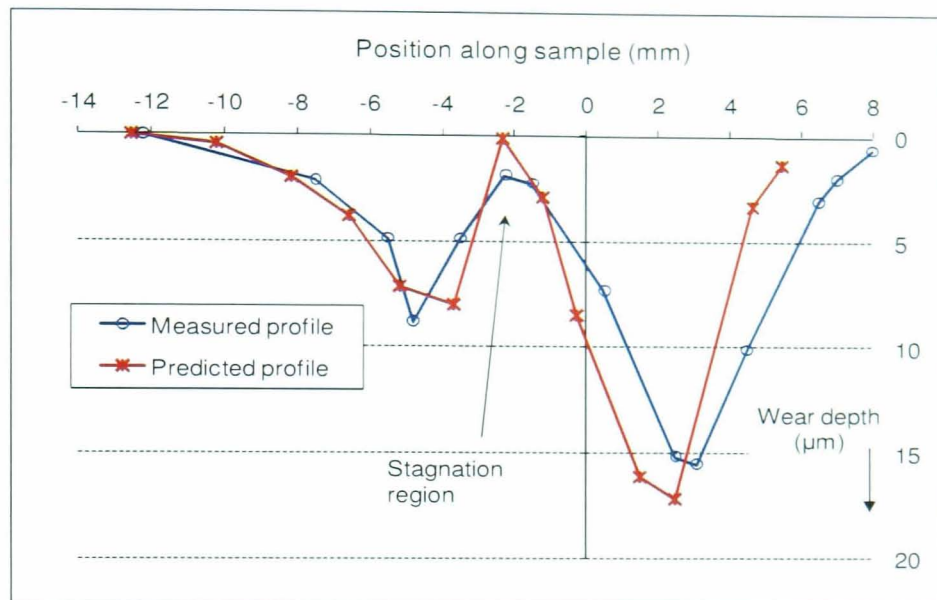
Figure 7.9 CFD predicted and experimentally measured wear profiles on a flat sample oriented at 105° nominal impingement angle and for a nozzle exit flow velocity of 5m/s. Please note the standard deviations for predictions are not represented to improve clarity.
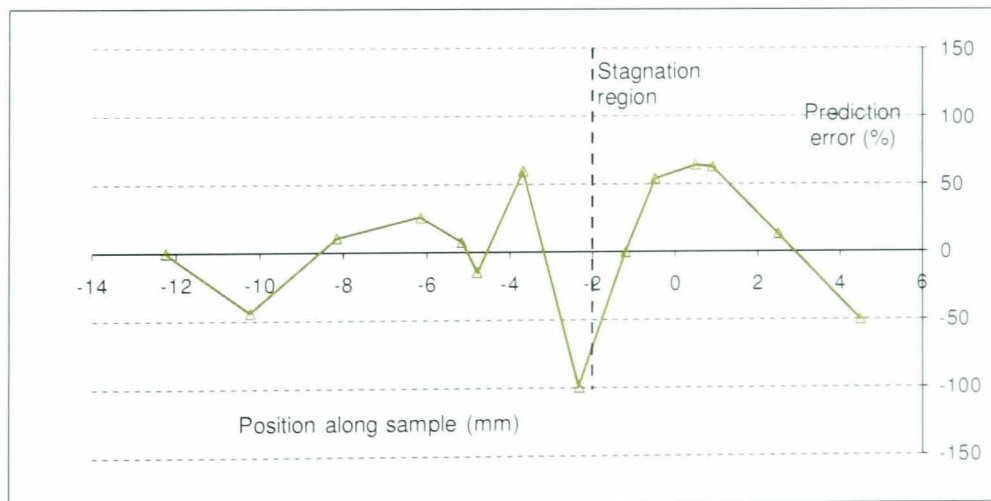
Figure 7.10 Quantitative variations amid CFD predicted and experimentally measured wear profiles along the surface of the test sample for the configuration of 105° nominal angle, 5m/s nozzle exit flow velocity and for a stand-off distance of 5mm.

In general, the model was over predicting wear and the quantitative variations in the profiles are attributed to a combination of two possible factors described as follows,

Misalignment between nozzle and sample surface

The major contributor to prediction errors has been associated with the difficulty encountered during spatial arrangement of the surface at 105° to the nozzle and also in accurately measuring the distance between the surface and the nozzle. Purpose based sample holders were designed (Figure 5.6), however, differences between experimental and CFD recreated geometries are inherent as discussed earlier (section 7.2.3). To study the sensitivity of stand-off distances on wear predictions, CFD simulations were performed at different stand-off distances within the tolerance range provided in Table 7.1. Predictions for new stand-off distance of 6mm (for the geometry defined in Figure 7.7) are presented in comparison with the original experimental profile in Figure 7.11.
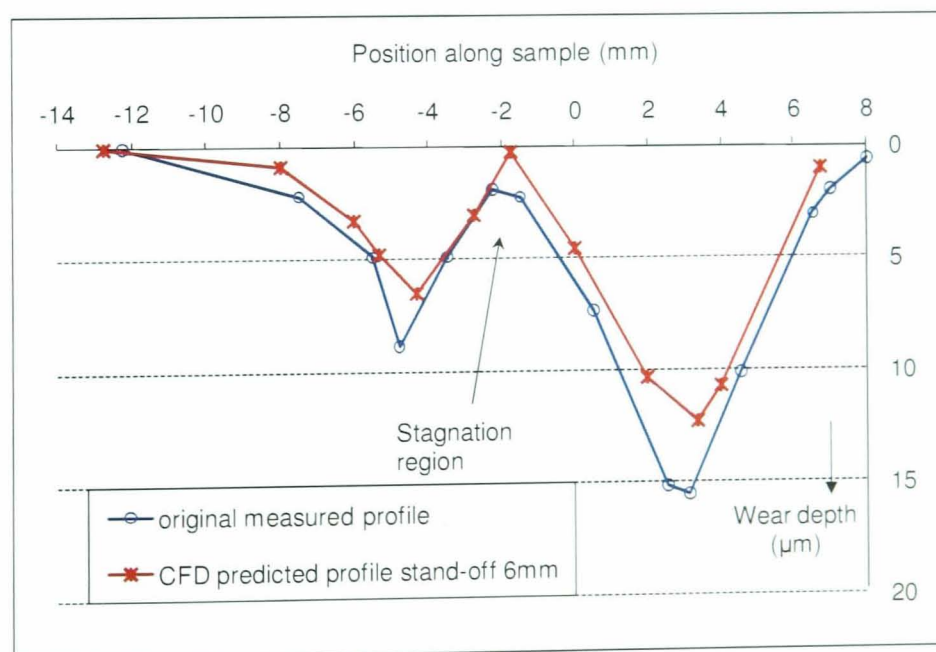
Figure 7.11 Measured wear profile on a flat sample oriented at 105° under an impinging solid suspension at flow velocities of 5m/s and predicted profile (stand-off distance 6mm). Please note standard deviations for predictions are not represented to improve clarity.

Lowering the surface increases the distance particles travel before impact. This shifts particle impacts from the zone of high-medium angles to medium-low impact angles regime which is attributed to better particle-fluid cohesion (drag effect of the fluid flow). This pushes the stagnation point for the new configuration further towards the positive side (Figure 7.11, but only by a small distance). Analysing the originally predicted wear profile (Figure 7.9), it could be seen that maximum wear depths on both sides of the stagnation point were over predicted and also positioned closer to stagnation point in comparison with measured wear profile. This is an indication that CFD simulation (with 5mm stand-off distance) could have been performed with the surface position higher in relation to experimental position (here we suggest that the experimental stand-off distance was greater than 5mm). At elevated positions, particles tend to impact at relatively higher velocities and at medium angles. Impacts under these conditions correlate to greater material damage located close to the stagnation region due to higher impact energies and hence over predicted wear rates. CFD calculations based on new stand-off distances (6mm) a suggested better correlation (location and value of the wear depths on either side of the stagnation point) which is a sign of improved prediction accuracy.

Figure 7.12 Prediction errors along the surface length of two sets of predictions made by CFD-Wear map method (i) 105° impingement angle and 5mm stand-off (ii) 105° impingement angle and 6mm stand-off distance.

Figure 7.12 illustrates the numerical variations among predictions made for two stand-off distances and measured profiles. With the new stand-off distances, the overall accuracy of predictions are improved, with the maximum error approximately within 20% along the sample length (excluding stagnation point-impacts caused due to change in particle trajectories as an account of possible inter-particle collisions and also at regions where wear volumes are very low). This establishes the fact that alignment might well be a major reason for prediction differences. One region is of particular interest: beyond 6mm on the positive side. where no wear is predicted. This is attributed to lack of material wear data during the wear map development stage and it is proposed that here the effect of sliding impacts predominate.

Variation in hydrodynamic regime

Sand concentrations used in these tests were considered to be low enough not to have any effect on the fluid regime. However, at regions closer to the sample surface particles after impact lose almost all energy and come to a stop momentarily before exiting the surface [82]. Rebounding particles can form a bed of slow moving particles which act as a protective bed and hindering oncoming particles. The effect of this can be pronounced as we move away from the region of high angle impacts. Comprehensive studies related to this effect have rarely been undertaken due to the complexities involved, in particular the length scales at which these events can occur.

The wear data used to develop the wear map is based on statistical averaging of local mass loss obtained from impingement tests conducted at 90° nominal impingement angle. For the case of 90° and 5m/s, substantial wear data was not available for impacts <10° and this was previously accounted for effects of high angle particle impacts occurring upstream and eventually hindering the motion of particles en route to impact at low angles (at the edge of the wear scar). However, due to change in geometry the local flow regime varies. If the geometry promotes smooth transition of fluid flow. the possibility of heavy impacts can be low and hence the effect of particles

shielding sliding angle impacts can be inconsequential. Conversely, if the geometry promotes highly curved flows, then significant shielding can be encountered at the regions where particles predominantly glance/slide along the surface and lead to minimal damage.

7.4 135° angle and 5m/s nozzle exit flow velocity case study

CFD simulation of the impingement test with the surface oriented at 135° to the nozzle axis was carried out on the geometry schematically represented in Figure 7.13 for nozzle exit flow velocity of 5m/s. Similar to the case of 105° a symmetrical 3-D model was used for simulations. The first stage of CFD involved solving the flow problem considering only the single phase medium (water), assuming negligible effect of particle motion on the resulting fluid regime. Lagrangian particle tracking models were used to numerically predict erodent motion through the already solved fluid regime and extract impact data at the surface (described in detail in section 4.3). Actual JITs were conducted on the same geometry for exact nominal flow parameters and at conditions specified in Table 6.1.
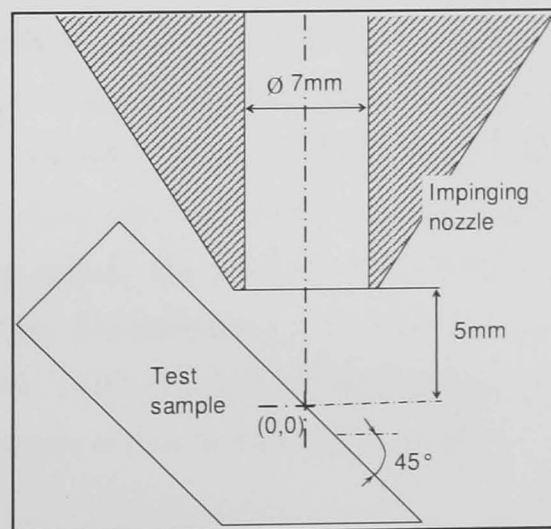
Figure 7.13 A schematic representation of the nozzle-sample arrangement used in CFD simulation as an approximation of the experimental configuration of the impingement test with the flow oriented at 135° to the surface.

7.4.1 Description of CFD predicted flow field and impact data

On analysing the fluid regime, it was observed that majority of the fluid traversed along the downward direction of the sample (right hand side) and the position of the stagnation region was 5mm towards the left of the reference point (coordinate 0,0), defined by wall shear stress profiles (Figure 7.14b). On the basis of shear stresses, gradual transitions in flow direction on the right side of the stagnation point were predicted in comparisons to the flow events on the left side of the stagnation point (due to highly curved nature of the fluid streamline). Maximum wall shear stress, particularly on the positive side, is very low in comparison with the case of 105° (approximately 100Pa and 150Pa for 135° and 105° respectively). This suggests better particle-fluid coupling on the right side for the case of 135° and can result in majority of the particles exiting the nozzle to flow towards this region. Particle impact data along the surface predicted by CFD (Figure 7.14a) confirms this fact and it was calculated that almost 90% of the total number of possible impact events (it was predicted by CFD that only 17% of the particles flowing within the nozzle has the possibility of colliding with the surface) occur on this side suggesting maximum attrition to be expected in on the right side and minimum wear on the left side of the stagnation point.

Variation of particle impact velocities and angles along the length of the surface are illustrated in Figures 7.14 c and d. Impact velocities are lowest around the stagnation region are very low and increases radially outward along the surface. The flow regime around the surface on the right side of the stagnation point is qualitatively similar to region 2 and 3 defined in Figure 6.1 where wear by cutting mechanism predominates. In accordance with this, predicted impacts are between 10-35° which are particularly severe on ductile materials [40, 179]. Impacts at high angles are not predicted, as a result of smooth change in flow directions [37, 148].
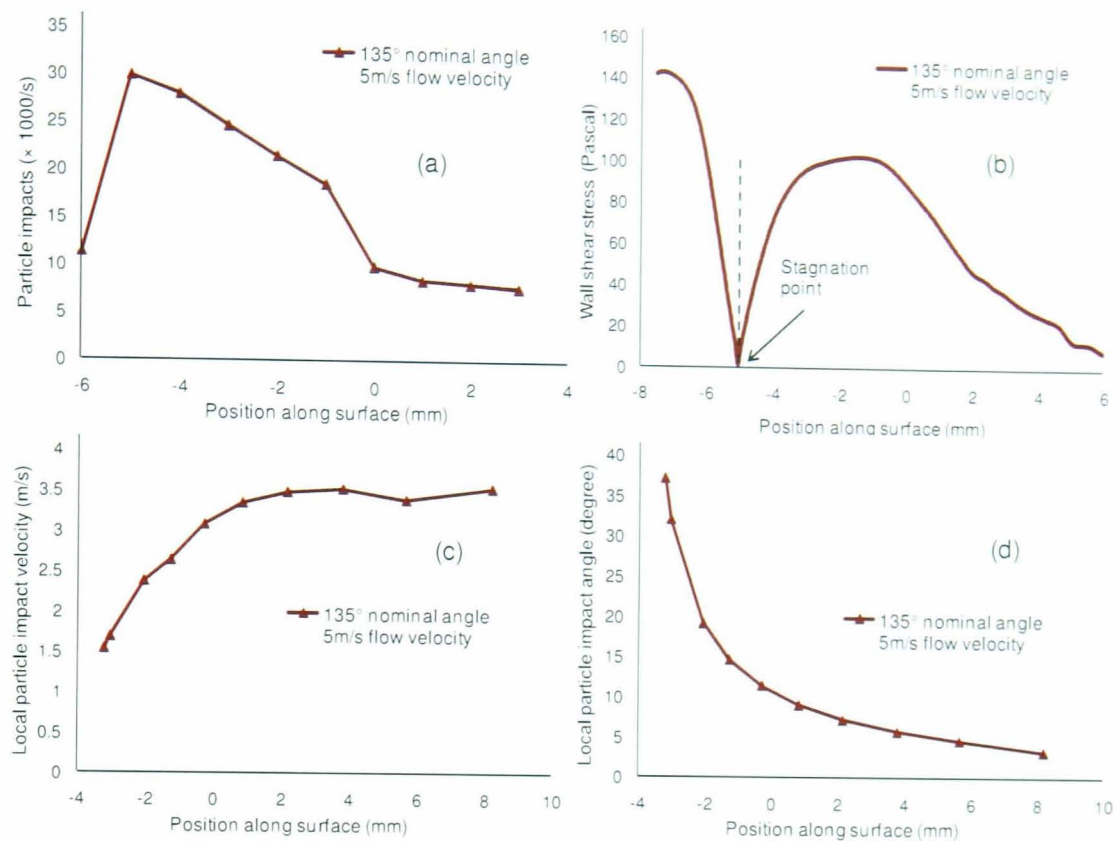
Figure 7.14 Variation of wall shear stresses and impact data along the length of the surface oriented at 135° to an impinging flow exiting the nozzle at 5m/s as predicted by CFD on a geometry defined in Figure 7.13.

7.4.2 CFD Predicted and experimentally measured wear scar for 135° and 5m/s

Average local wear was predicted for these impact data using the wear-map, and expected wear profile (maximum wear depth) for a flat UNS S31603 surface oriented at 135° to the fluid jet exiting the nozzle at 5m/s, eroded by AFS50/70 particles for a total time duration of 120 minutes is shown in Figure 7.15. Sand based impingement erosion tests were conducted using the configuration of the JIT (Figure 5.1) for a sample nozzle geometry defined in Figure 7.13 on flat UNS S31603 at 5m/s nozzle exit fluid velocities and at conditions specified in Table 6.1. The post test wear scar was contoured using a contact probe (6.2.1) along the line where material wear is expected to be the highest. It is noted that this line was an approximation and hence possible variations in predictions could exist.

Experimentally obtained and CFD based wear-map predicted wear profiles for these conditions are illustrated in Figure 7.15.
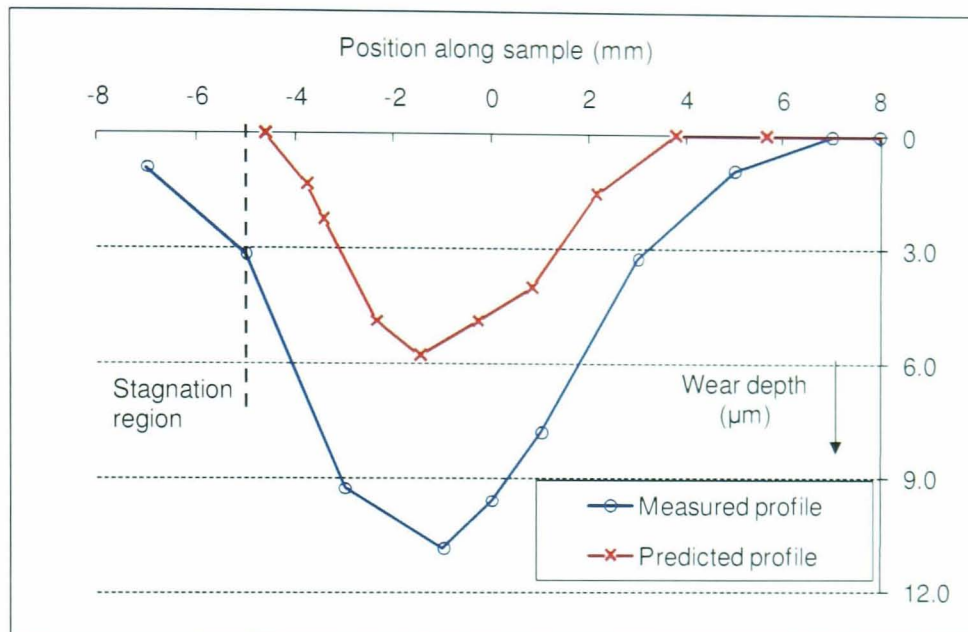
Figure 7.15 CFD predicted and experimentally measured wear profiles on a flat sample oriented at 135° nominal impingement angle and for a nozzle exit flow velocity of 5m/s. Please note standard deviations for predictions are not represented to improve clarity.

On analysing Figure 7.15, very low volume of wear was observed towards the left of the stagnation point, which can be explained by the low number of particle impacts. Towards the right of the stagnation region, maximum wear occurs at regions (between -2.5 to 0 mm) where particles impact at angles between 25-10° corresponding to maximum ductile material loss theory. However, comparisons with experimentally measured wear concluded wear was severely under predicted (differences were greater than 50% in almost all local positions), as illustrated by Figure 7.16.
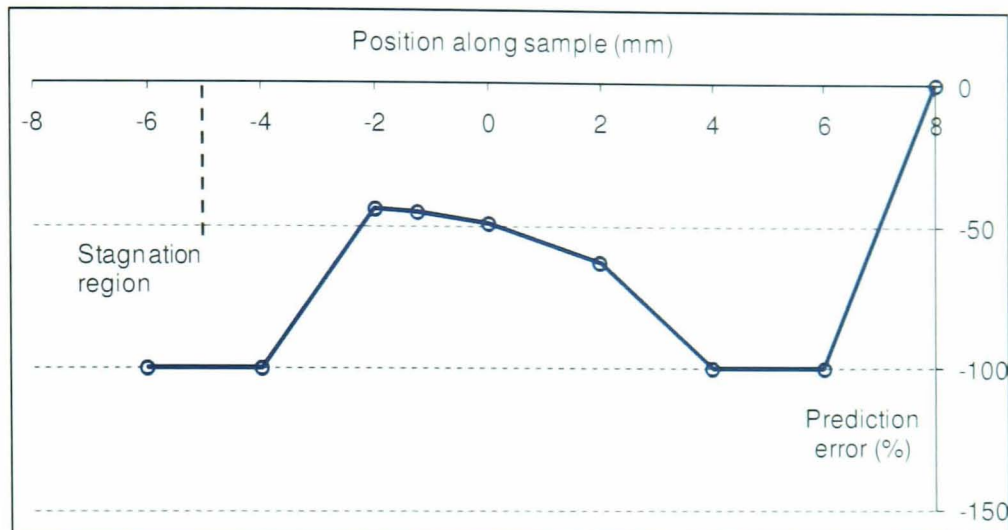
Figure 7.16 Numerical variations between measured and CFD predicted wear profiles along the surface of the test sample for the configuration of 135° nominal angle, 5m/s nozzle exit flow velocity and for a stand-off distance of 5mm.

7.4.3 Prediction discrepancies at 135° and 5m/s

Similar to the case of 105° tests, the primary reasons for this difference can be attributed to misalignment issues and the different hydrodynamic regime. To assess the sensitivity of the predicted wear profile with test surface position, various CFD simulations were performed for different stand-off distances within the allowable range (Table 7.1). Figure 7.17 presents the predicted wear profile for a stand-off distance of 4mm (surface was moved up in the CFD simulations) along with the experimentally obtained profile, improvements in correlations can be visually observed. The accuracy of the predictions for the stand-off distance of 4mm suggests that the impingement tests could have been conducted with the surface closer to the nozzle than previously assumed.
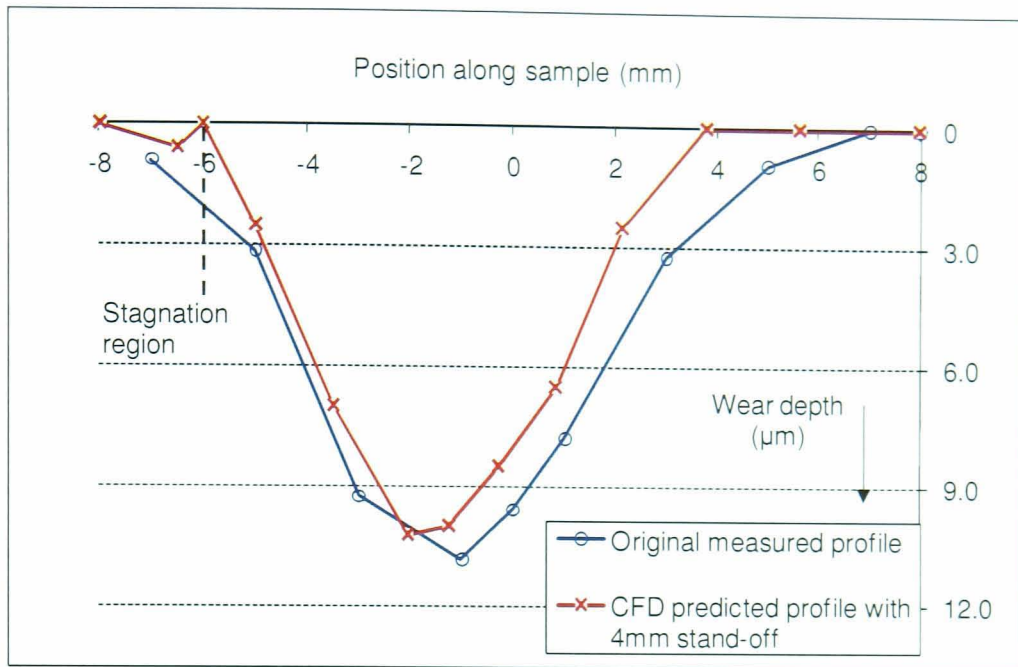
Figure 7.17 Measured wear profile on a flat sample oriented at 135° under an impinging solid suspension at flow velocities of 5m/s and predicted profile (stand-off distance 4mm). Please note standard deviations for predictions are not represented to improve clarity.
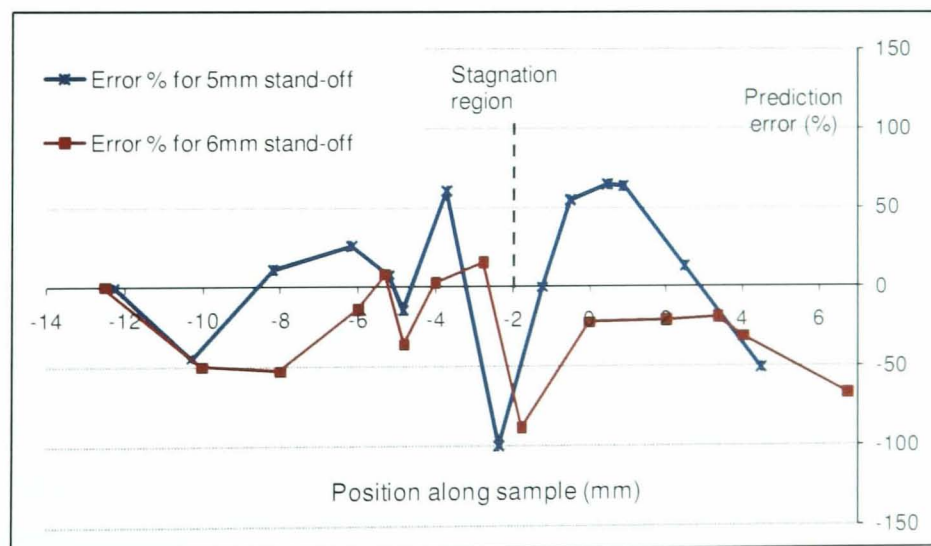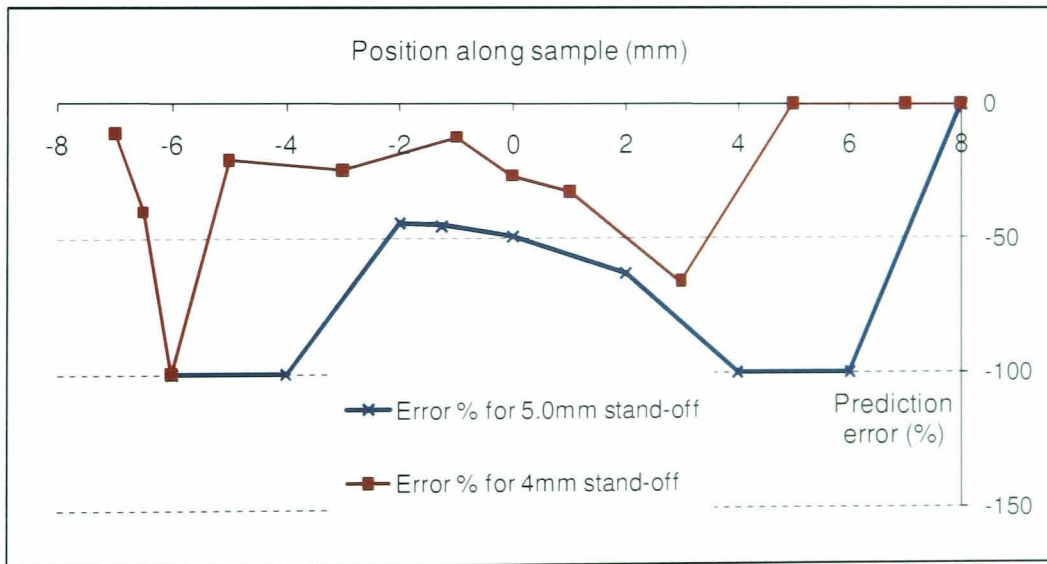

Figure 7.18 Prediction error's along the surface length of two sets of predictions made by CFD-Wear map method (i) 135° impingement angle and 5mm stand-off (ii) 135° impingement angle and 4mm stand-off distance.

Prediction disparities for the new stand-off distance (4mm) had a similar trend to previous case as shown in Figure 7.18, with 100% variations at stagnation points (described earlier) and at regions where particles impact predominantly at sliding angles (<10°). Particles impacting upstream of this region (where sliding impacts are predicted), might rebound with higher residual velocities in comparison to the case of 105° and quickly moves away from the surface. Thus the probability of particles moving slowly around the surface due to high angle impacts around the stagnation region and providing a protective shield at the edge of the wear scar can be very low. This effect is postulated to account for wear measured around this region, where zero wear is predicted by the wear-map (this was attributed to lack of wear data).

It is also mentioned that a fraction of the disparity between predictions and measurements could be due to the locations on which experimental wear scar were profiled. Although there are certain uncontrollable factors such as particle-particle interactions, secondary impacts, particle size and shape variations which can affect the accuracy of wear predictions, it was demonstrated that the CFD based wear map method can be effectively used to provide material wear data for a range of impact conditions using data from two standard laboratory tests.

7.5 Preliminary application of the method to plant equipment

A typical 1.5D 90° bend (20mm internal diameter) used in plant operations (Figure 7.19), was fabricated from the material (UNS S31603) based on which the wear-map was developed. Initially commercially available bends were used for this purpose, however, due to issues encountered during post-test analysis in the form of referencing and also with the accuracy of the actual geometry, these components were rejected and hence purpose based pipe bends were fabricated to facilitate profile measurements and for improved accuracy. This was also done with an impetus to improve alignment which was a major learning from the earlier

wear predictions, where misalignments between test surface and the impinging nozzle caused severe discrepancies.
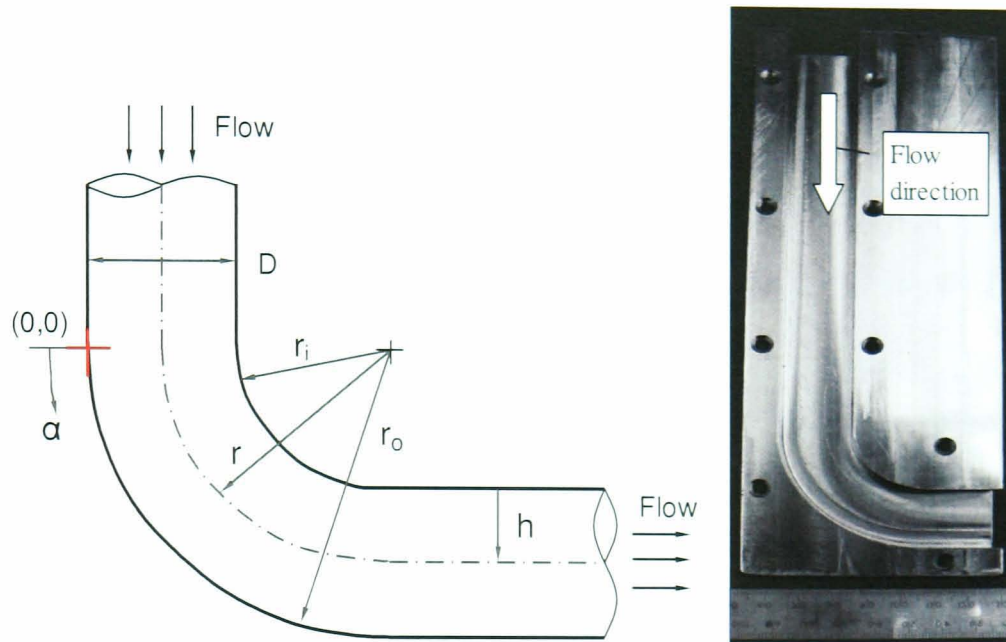
Figure 7.19 A schematic of the 90° 1.5D pipe bend geometry used in CFD simulations as an approximate representation of the actual pipe bend used in wear testing. Actual pipe bend is also shown alongside. Here, h= radial distance from the inner surface of the bend, r_o and r_i is the outer and inner radius of curvature respectively, r is the quoted radius of curvature, D is the inner diameter of the pipe cross-section and α is angle of the bend measured from (0,0).

7.5.1 Flow field within a 1.5D 90° pipe bend (elbow) simulated using CFD

CFD simulations were conducted on the geometry (Figure 7.19) to obtain a solution for single phase flow (fluid-water) using the modelling approach described previously (section 4.2). Since fluid phase has a major influence on particle motion and hence wear, accurate solution of the fluid phase is vital for credible particle impact data predictions. For this purpose the resulting flow solution is to be validated with practical measurements obtained from well defined experiments.

Sudo et al. [180] investigated the flow through a 90° section of a curved square duct with a 2D turning radius using hot wire anemometer with the intention to study the effect of turbulence on flow field. The Reynolds number for the flow field studied by Sudo et al. [180] was reported to be 4×10^4 (Reynolds number in our case study was 10×10^4). The credibility of the 90° square pipe bend flow simulation was assessed by qualitatively comparing the predicted flow field with the data reported by Sudo et al. [180]. Though the geometries in comparison are not exactly similar, due to the lack of availability of measured flow data for the case of 1.5D 90° bend and at similar flow regimes, this data was used for qualitative validations.
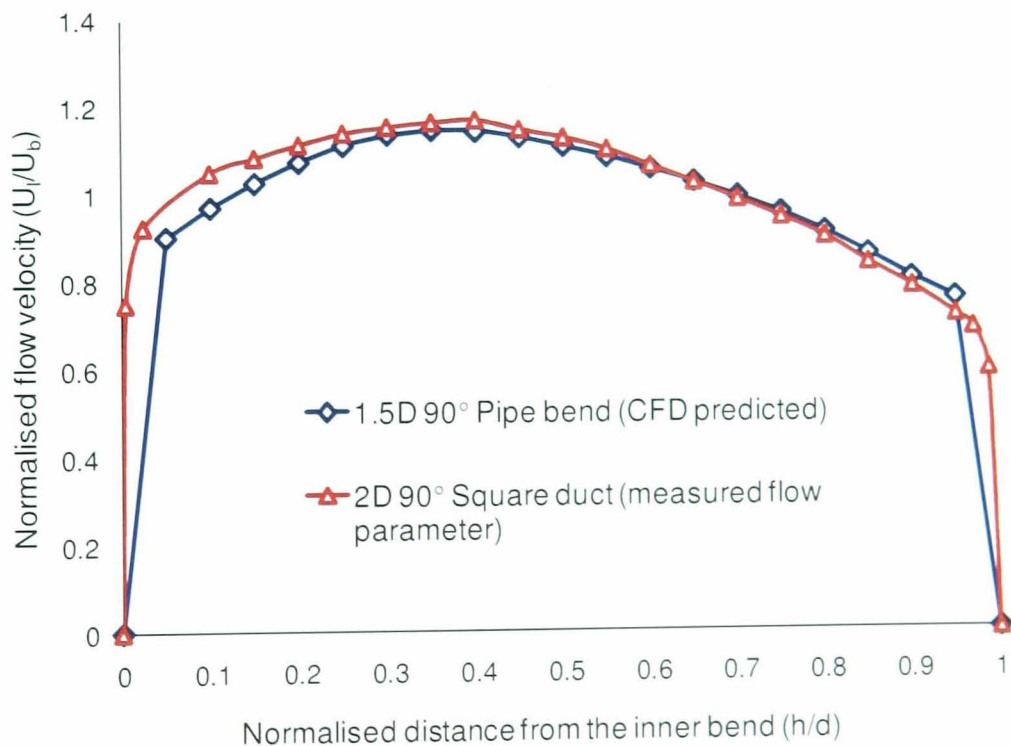
Figure 7.20 Variation of normalised flow velocities with normalised distance from the inner bend as predicted by CFD simulations and measured experimentally by Sudo et al. [180]. CFD simulations were conducted on a 90° pipe bend with a 1.5D bend with water as the fluid and for Reynolds number of 10×10^4. Measurements were conducted for a 90° square pipe bend with a 2D radius, using air as fluid and for a Reynolds number of 4×10^4. Flow measurements and predictions were made on line across the cross section at a bend angle $\alpha = 30°$.

Variations among measured and predicted flow parameters were observed near both the inner surfaces of the bend, no attempt is made to account for this variations due to the complex nature of turbulent flow and analysing this is beyond the scope of the current study. Good overall agreement was observed between CFD predicted and measured flow parameters as illustrated in Figure 7.20 which asserts the validity of the CFD approach followed and the credibility of the flow data.

7.5.2 Particle impact data within a 1.5D 90° pipe bend (elbow)

Particle tracking models were then used to determine the sand trajectories within the geometry. Evenly placed particles were released into the upstream section at a distance of 10D from the start of the bend with no initial velocity (section 4.3.4). Particle-particle and particle-flow interactions were assumed to be negligible at these solid concentrations and the effects of turbulent eddies on particle motion were considered negligible at these conditions as recommended [15, 36] (also section 4.3.4). Particle impact data was obtained and it was calculated that only 25% of the total number of sand particles within the nozzle can in all probability impact the inner wall of the pipe bend. The variation of particle impact angle and velocity along the sample length in radial direction is illustrated in Figure 7.21.

(a)

(b)
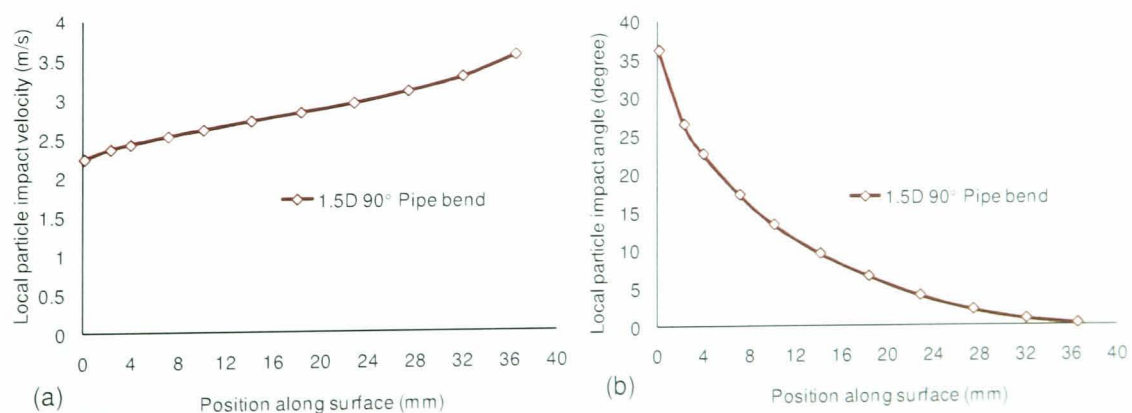
Figure 7.21 Variation of particle impact velocity and angle along the length of the elbow in the radial direction for the configuration shown in Figure 7.19 for a bulk inlet flow velocity of 5m/s.

The smooth geometry of the elbow promotes gradual change in flow direction and enhances particle-fluid coupling. A consequence of which is particle impacts occurring within a narrow range of velocities (2.25 to 3.5 m/s) throughout the entire geometry (Figure 7.21). Particle impact data under these conditions are very similar to impact conditions observed under 135° impingement test (Figure 7.14) which can be used as evidence for in using the 135° impingement test to recreate impact conditions within a 90° elbow.

7.5.3 CFD predicted and experimental wear for a 1.5D 90° pipe bend (elbow)

Using the wear map and CFD predicted impact data; expected wear profile on the inner surface of the elbow for the duration of 120 minutes was predicted and is shown in Figure 7.22. Sand based laboratory experiments were conducted on the geometry defined in Figure 7.19, using water at room temperature exiting the nozzle with a flow velocity of 5m/s and 1% by weight of sand concentration (measured as the amount of sand exiting the pipe bend for a total duration of 120 minutes. The abrasive used was AFS50/70 which had the nominal size distribution of 212-300 μm and average density of 2650kg/m³. The wear surface was contoured using a profilometer to determine an average wear profile which was compared with predicted wear as shown in Figure 7.22. The accuracy of the predictions are generally good up to a radial distance of 15mm. Beyond this point, the wear map method fails which is again attributed to the lack of material wear data at sliding impacts. Almost all impacts downstream of the bend (beyond 16mm as shown in Figure 7.21b) was predicted by CFD to occur at sliding angles (<10°) and it is proposed that at these regions the effects of secondary impacts can be significant.

The ability of this method to accurately predict the magnitude and location of maximum wear demonstrates the capability of the proposed wear map, however, to improve the prediction capability at sliding angles further developments are needed which are suggested in the later section of this work.
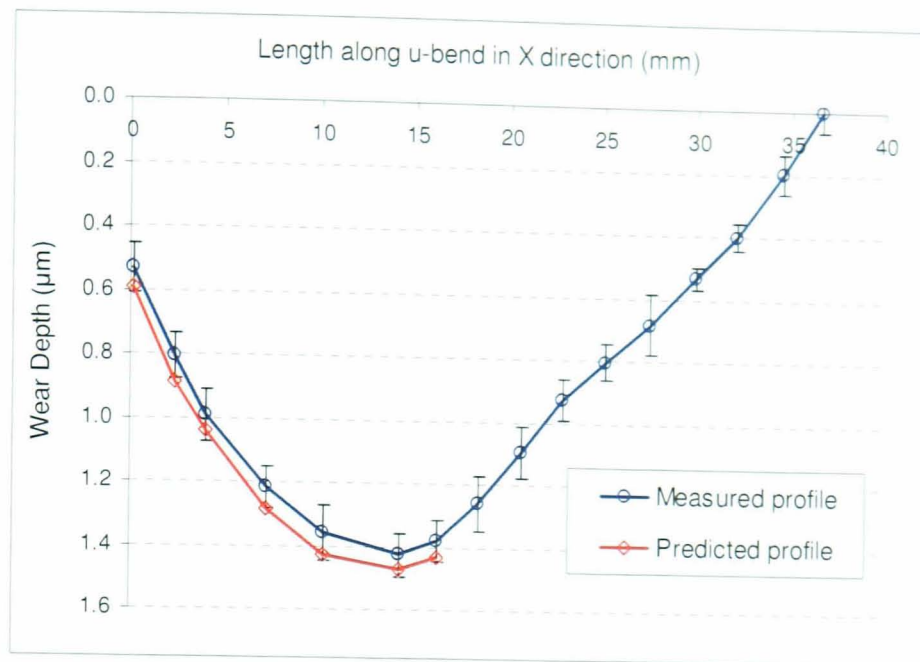
Figure 7.22 The CFD predicted and experimentally measured wear profile on a 90° 1.5D pipe bend geometry tested using the JIT facility for flow velocities of 5m/s and the duration of 120 minutes.

7.6 Summary

- Erosion wear was predicted on flat samples oriented at different angles to the oncoming fluid suspension (105° and135°) using the material-abrasive specific wear map.

- Predictions were qualititavely similar in comparison to experimental wear profiles, however, large numerical variations were encountered.

- Numerical disimilarities were primarily attributed to incorrect recreation of nozzle-sample configurations in CFD simulations. Sensitivity of predicted wear with apparent differences between CFD simulated and experimental geometry (nozzle-sample separation distances and angular orientation) was conducted and significant improvements in predcition accuracies were detectd.

- No wear was predicted at stagnation point but physical wear was observed post erosion tests. This was accounted to change in particle trajectories around stagnation region due to particle collisions during actual testing leading to impacts.

- Wear for sliding impacts were not predicted by CFD-Wear map method which was in contrast to experimental data. The wear map does not predict wear at low impact angles (<10°) due to lack of data. For 90° test case, particles enroute to impact at sliding angles can be hindered by rebounding particles upstream of this region and very low wear for these angles. However, the effect of this can be low in geometries promoting smooth transition of flow and hence measurable wear data is observed for impacts lower than 10° for the case of 105° and 135°.

- Wear on 1.5D 90° pipe bend was predicted with the location and magnitude of the maximum wear point accurately estimated. However, the effects of sliding impact events are significant in this geometry and the wear-map breaks down at these locations. Further modifications are suggested to improve prediction capability at low impact angles.

Chapter 8

Discussion: Erosion wear models- A comparative study

8.1 Introduction

A review of various erosion prediction methods was presented earlier (section 2.3) and with the focus on predicting erosion wears numerically. Several conceptual and empirical models which profess to capture wear characteristics as a function of material has been developed. The challenges presented in implementing these models were highlighted in section 2.3.4 and hence a new CFD integrated experimental method was developed. The objective of this method was to acquire sufficient erosion parameters from a minimum set of tests and to be able to accurately map these on a more realistic scenario for similar conditions.

The comparisons between wear predictions made using the wear-map method and experimental testing suggested good predictive power of the method. Further numerical analysis are conducted using the experimental data to develop a semi-empirical model which captures the features of the wear map at conditions similar to those generating the co-relation. An investigation of two 'fundamental' models (purported to capture wear as a function of material properties) and an empirical model is conducted and presented in this chapter.

8.2 Numerical treatment of local impact and wear data

Erosion wear rate is a function of particle impact kinetics (velocity and angle), properties of target-abrasive materials and geometrical features of the erodent: and can be numerically expressed by an empirical equation

(8.1) [81]. This equation forms the fundamental block on which majority of the empirical wear models were developed.

$$E_r = A \times V_P^n \times f(\theta), \tag{8.1}$$

where 'A' is generally a constant depending on the mechanical properties of target-abrasive materials and erodent shape, E_r is the local erosion rate, V_p and θ are local impact velocity and angle respectively and n is the velocity exponent.

Using equation (8.1) as a premise, an empirical model which generates the best mathematical correlation between local impact and experimental wear data for our study (wear-map data) was developed as described;

1. Local impact data determined from CFD simulations and wear data obtained from experimental tests conducted at exact conditions from a single test are entered into equation (8.1).

2. Second step is to choose a value for 'n' to use in equation (8.1). Practically this exponent can be anywhere between 1 to 5 as suggested by Clark [65], however, values between 2 and 3 are generally considered to be good [63]. It is impossible to determine this exponent based on one test result since the effects of velocity and angle are coupled together and requires more test data. Although, the total mass loss was observed to vary as a function of V^3 (Figure 5.11), it does not necessarily mean that n is 3. This is because the total weight loss in a slurry based impingement system is a function of both angle and velocity. Thus as a starting point, n was taken as 2 in our formulations and this was also due to the fact that it is reported that wear rates are a function of the kinetic energy of an impacting particle which in turn is a function of the velocity squared [5].

3. Substituting these data (E_r, U_p and n) into equation (8.1) results in a set of numerical relations for $f(\theta)$ and 'A'. 'A' is associated with the physical properties of the material and abrasive, the value should be fixed. The angular dependence of erosion wear for a ductile material has been reported to be a trigonometric function of the impact angle [33, 81].

4. Using appropriate mathematical fitting functions a relationship for $f(A, \theta)$ which provides a good fit for the local impact and wear data within the premises of equation (8.1) can be obtained.

For this purpose, data for nominal impingement conditions of 90° and 7.5m/s were selected. The conditions at which CFD simulations and laboratory based erosion tests were conducted are specified in Table 8.1 and 8.2 respectively. An empirical formulation (equation 8.2) between experimental and impact data was generated using a mathematical software *Minitab 15*.

$$E_r = AV_p^2 \left[b(\sin \theta)^4 + c(\sin \theta)^3 + d(\sin \theta)^2 + e \sin \theta + f \right] \qquad (8.2)$$

In equation (8.2), A, b, c, d, e and f are all coefficients which provide the best fit for E_r and (V_p, θ, A) in equation (8.1). These correlation factors were obtained using a regression analysis sub-routine in *Minitab 15* and are presented in Table 8.3. These constants will be dependent on the physical characteristics and properties of both the target and abrasive, although no attempt is made to associate any physical meaning to these numbers. Also equation (8.2) can work only for UNS S31603-AFS50/70 combinations and for the conditions within the envelope of the wear-map.

Table 8.1 Conditions at which CFD simulations of the JIT geometry were performed to predict particle impact data as a function of position.

Fluid	Temp. (°C)	Fluid Density (kg/m³)	Nominal Impact angle	Fluid viscosity (Pa.s)	Stand-off distance (mm)	Particle density (kg/m³)	Particle shape	Particle size (μm)
Water	23	1000	90°	1×10^{-3}	5	2650	Sphere	250

From equation (8.2), local wear rates for the combination of UNS S31603-AFS50/70 for a range of local impact conditions (velocities between 1-8 m/s and angles between 10-80°) were predicted and are represented graphically by Figure 8.1. These boundary conditions cover the region enveloped by the wear-map, i.e., the local impact conditions predicted by CFD for which statistical wear data is available. Extrapolation beyond these data points resulted in non-physical wear data and hence should be avoided.

Table 8.2 Conditions at which erosion mass loss tests on flat UNS S31603 samples were conducted for data acquisition and validation purposes.

Fluid	Temp. (°C)	Fluid Density (kg/m³)	Nominal Impact angle	Test duration (minutes)	Nozzle exit velocity (m/s)	Sand density (kg/m³)	Sand content	Sand size distribution (μm)
Water	20	1000	90°	120	7.5	2650	1% by weight	212-300

Table 8.3 Values for coefficients in equation (8.2) which provide the best correlation between local wear, impact data and surface-abrasive properties obtained for nominal impingement angle of 90° and velocity of 7.5m/s.

A	b	c	d	e	f
0.434×10^{-16}	-0.396	8.38	-16.92	10.747	-1.765

Predictions made using equation (8.2), as represented by the surface plot in Figure 8.1 is referred to as the wear map predictions and is compared with the available experimental local wear data for all three conditions (nozzle exit flow velocities of 5, 7.5 and 10 m/s with the angle set at 90°) as shown in Figure 8.2. Some scatter between both the data sets was observed which is attributed to a combination of factors such as CFD modelling errors (due to approximations), variations in particle size, evolution of surface profile with time, differences between experimental and CFD geometries.

neglecting secondary impacts and also because the empirical coefficients are approximations. Overall the correlation was good (majority of the data was within 75% of experimental data as shown in Figure 8.2) and from this it can be conclusively shown that data from a single test can be used to predict erosion rates over a set of conditions using the wear-map method.
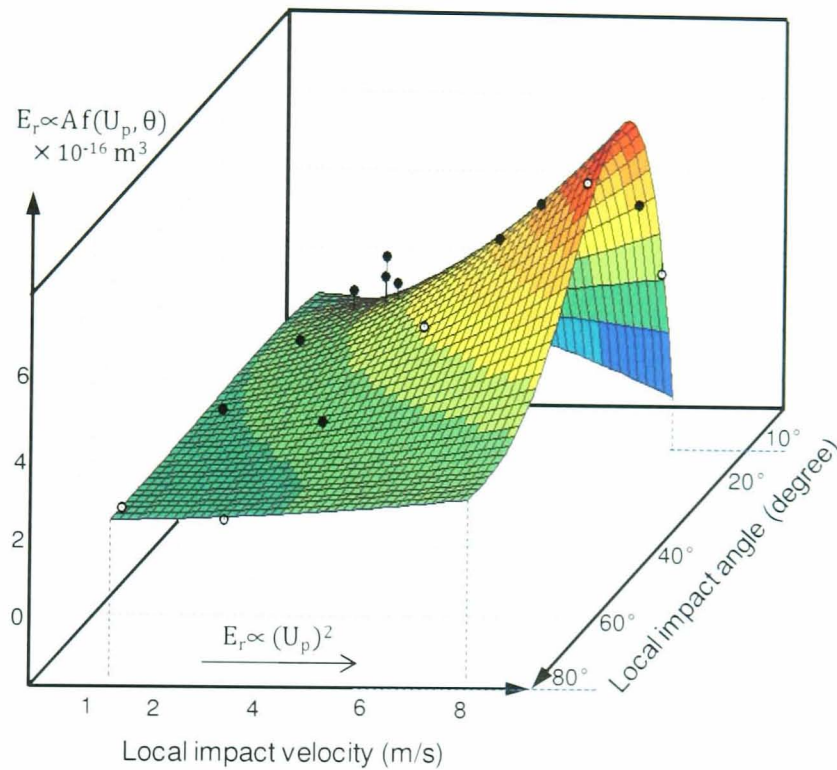
Figure 8.1 Erosion rates as predicted from equation (8.2) for local impact conditions between 1-8 m/s for velocity and 10-80° for angles. Dots on the 3-D surface plot represent the position of available experimental data.

Subsequent to this, the entire procedure (step 1 to 4) was repeated choosing different values for the velocity exponent, n. Iterations using 2.5 and 3 for n provided a different set of coefficients for equation (8.2), and using these new equations wear predictions were made. It was observed for these velocity exponents, the numerical fit varied only by 6% relative to the values obtained for an exponent of 2. Thus an exponent value of 2 is deemed appropriate and further predictions were made with n taken as 2.
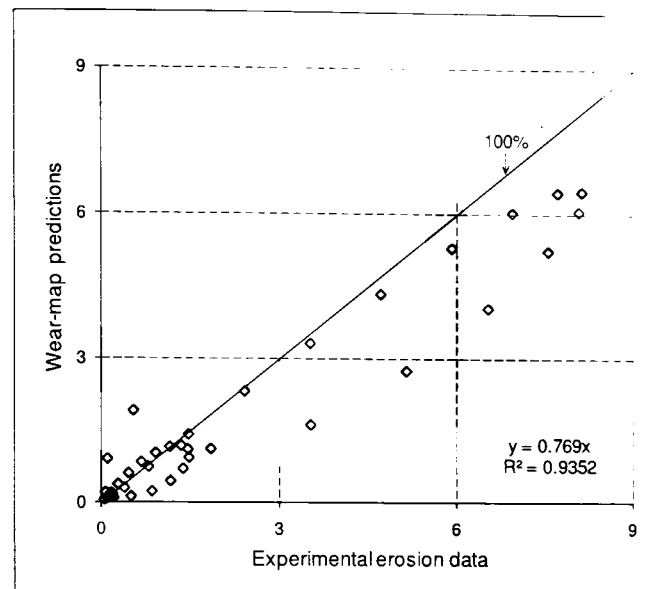
Figure 8.2 Comparisons between predictions and experimental erosion data for a set of local impact conditions (these local conditions correspond to nominal conditions of 5, 7.5 and 10 m/s and 90°). Predictions were made using a model developed using data from one standard test (90° and 7.5m/s).

8.3 A numerical review of erosion wear models

This section describes the numerical analysis conducted using three erosion wear models and the capability of these models to capture the wear-map data. Three models were chosen for this purpose:

1. Model of Neilson and Gilchrist (NG model) [82]
2. Model of Huang et al. [24]
3. Wear model correlations made by Alhert [124]

The above listed wear models were modified to be able to predict local wear rates for the combination of UNS S31603-AFS50/70. These wear models comprised constants and correlations factors and values were to be determined from experimental data. Subsequent to this. the available local impact conditions predicted using CFD (chapter 4) for different nominal impact conditions were integrated with these modified wear models to predict local wear rates as illustrated by Figure 8.3. All CFD simulations were conducted following the approach described in Chapter 4 and for the

conditions specified in Table 8.1. The geometry on which simulations were conducted is defined in Figure 8.4 which is a close representation of the actual laboratory test geometry. Wear experiments were conducted at conditions similar to these (also specified in Table 8.2). It is mentioned here that additional tests or simulations were not performed and all the data used for the described analysis were previously acquired as described in chapters 4 and 5. Predictions were compared with experimental data the performance of each model is assessed as follows;
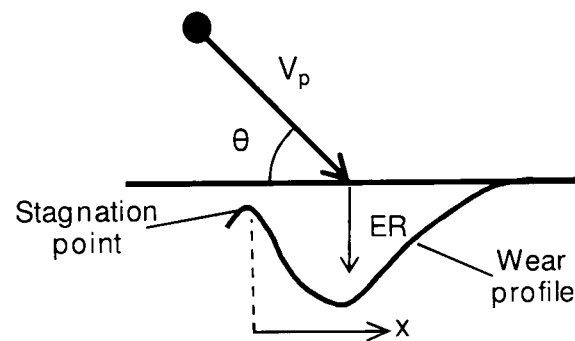
Figure 8.3 A schematic of ER prediction using data obtained from CFD simulations and a numerical wear equation.
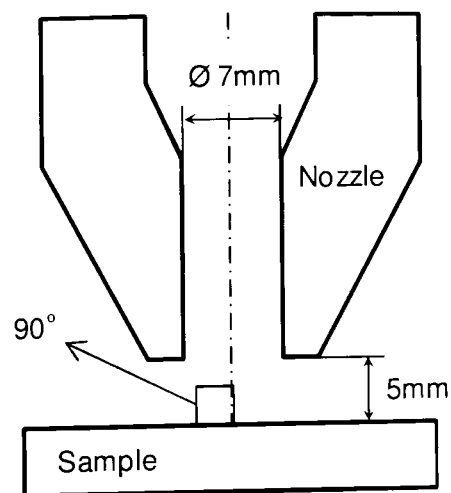
Figure 8.4 A schematic of the nozzle/sample geometry used in CFD simulations as an approximation of the actual test geometry for a nominal impingement angle of 90°.

8.3.1 Model of Neilson and Gilchrist (NG model) [82]

As discussed previously, the combined Finnie-Bitter wear model was one of the earliest complete erosion wear model to be formulated [34, 86] (*section 2.3.2.2*). The complexities involved in finding various parameters for the implementation of this model was pointed out and hence proposed a simpler wear model described by equation (8.3) was proposed by Neilson and Gilchrist [82].

$$E_r = \frac{m_p V_p^2}{2} \frac{(\cos^2 \theta \sin n\theta)}{\varnothing} + \frac{m_p}{2} \frac{(V_p \sin \theta - V_n)^2}{\delta}, \qquad \theta \leq \theta_{p0},$$

$$E_r = \frac{m_p V_p^2}{2} \frac{\cos^2 \theta}{\varnothing} + \frac{m_p}{2} \frac{(V_p \sin \theta - V_n)^2}{\delta}, \qquad \theta \geq \theta_{p0},$$

(8.3)

where V_p is local impact velocity, θ is local impact angle, m_p is the mass of impact particle and V_n is the normal velocity component below which no erosion occurs (critical velocity and is material specific). It was suggested that δ, $\varnothing$ and n are constants dependent on various factors such as material-abrasive properties and local conditions. Values of 4.85 for n, $\theta_{p0}=18.5°$ and $V_n=0$ (since it is usually small relative to particle velocity) were recommended [82] and the model was further simplified as,

$$E_r = \alpha V_p^2 (\cos^2 \theta \sin 4.85\theta) + \beta (V_p \sin \theta)^2, \qquad \theta \leq 18.5°,$$

$$E_r = \alpha V_p^2 \cos^2 \theta + \beta (V_p \sin \theta)^2, \qquad \theta \geq 18.5°,$$

(8.4)

where $\alpha = M_p/2\varnothing$ and $\beta = M_p/2\delta$.

Local impact data obtained from CFD simulations for nozzle exit flow velocities of 7.5m/s with the nominal impingement angle set at 90° were entered into equation (8.4). Local E_r associated with these local impact conditions, determined experimentally for the same nominal conditions were also keyed into equation (8.4) which provided a set of algebraic equations for α and β. Using the linear regression analysis routine available in a mathematical software, *Minitab 15,* values for α and β which provided the

best curve fits for E_r and local impact conditions as defined by equation (8.4) were determined (α=0.074119 and β=0.069142). CFD predicted local impact conditions for nominal conditions (90°; 5 and 10 m/s) were submitted to the NG wear model (equation 8.4) and local erosion rates were determined. Predictions were compared with available wear data (section 5.4) as shown by Figures 8.5 and 8.6. The values of α =0.074119 and β =0.069142 were used in equation (8.4) and all predictions are truncated at 6mm from the centre of the surface due to lack of credible wear and impact rate data (section 6.2.3).

From Figures 8.5 and 8.6 it can be inferred that the NG model fails to capture the erosion wear on the flat surface at 5 and 10 m/s. One possible reason for this can be attributed to the coefficients. α and β, used in equation (8.4). α and β are associated with the cutting and deformation components of total erosion wear respectively. The extent of material removed by cutting and deformation factors depends on the local wear mechanism which is governed by local impact conditions. Thus cutting and deformation factors should vary with impact angles [127]. The NG model, however, has been used to predict steady state erosion with good correlations; although validations were predominantly conducted in dry conditions (local impact angle and velocity vary within a tight range). In dry conditions. one set of α and β can generate good correlations since local impact angles vary within a smaller range, however, for slurry wear as pointed out by Huang et al. [24] and Haugen et al. [127]. α and β has to be carefully chosen since local impact angle can vary over a larger range for a single experiment.

Figure 8.5 Variation of erosion rates along the radial direction from the stagnation point as computed using the model proposed by the model of Neilson and Gilchrist [82] and wear map method for nominal conditions (90° and 5m/s). Local experimental wear data extracted at similar nominal conditions are also shown.

Figure 8.6 Variation of erosion rates along the radial direction from the stagnation point as computed using the model proposed by the model of Neilson and Gilchrist [82] and wear map method for nominal conditions (90° and 10m/s). Local experimental wear data extracted at similar nominal conditions are also shown.

8.3.2 Model of Huang et al. [24]

Huang et al. [24] argued that several existing models do not consider the variation of impact angles over the length of surface and the dependence of cutting and deformation factors on this variation as discussed earlier. A new phenomenological model was hence theoretically derived for erosion of materials in slurry flow which was implemented in conjunction with CFD by Wang et al. [42] and wear rates were determined using equation (8.5).

$$E_r = \frac{K_1 \, m_p^{1.125} \, V_p^{2.25} \, (\cos\theta)^2 \, (\sin\theta)^{0.25}}{(1+B)^{0.125} \, E_B^{0.125} \, \sigma_B^{0.7} \, \varepsilon_B^{1.2}} + \frac{K_2 \, E_B^{1.1} \, d_p^{0.05}}{\sigma_B^{0.98} \, \varepsilon_B^{1.44}} \left(\frac{m_p \, V_p^2 \, \sin^2\theta}{1+B} \right)^{1.15} \quad \text{(8.5)}$$

This equation (8.5) was previously described (section 2.3.2.5) and the comprehensive derivation of this provided elsewhere [24]. Equation (8.5) can be simplified to equation (8.6) by grouping all material parameters together. Since α and β in equation (8.6) are connected to material parameters, the values for these should be constant for a specific material. It was suggested that the values for α and β are to be experimentally determined for a different set of material [24].

$$E_r = \alpha \, V_p^{2.25} \, (\cos\theta)^2 \, (\sin\theta)^{0.25} + \beta \, V_p^{2.3} \, (\sin\theta)^{2.3} \quad \text{(8.6)}$$

Local impact data obtained from CFD simulations for nozzle exit flow velocities of 7.5m/s with the nominal impingement angle set at 90° were entered into equation (8.6). Local erosion rate associated with these local impact conditions, determined experimentally the same nominal conditions were also keyed into equation (8.6) which provided a set of algebraic equations for α and β. Using the linear regression analysis routine available in a mathematical software, *Minitab 15,* values for α and β which provided the best curve fits for E_r and local impact conditions as defined by equation (8.4) were determined ($\alpha=0.102$ and $\beta=0.00947$). CFD predicted local impact conditions for nominal conditions (90°; 5 and 10 m/s) were submitted to the modified model of Huang et al. [24] (equation 8.6) and local erosion rates were determined. Predictions were compared with available wear data

(section 5.4) as shown by Figures 8.7 and 8.8. The values of α =0.102 and β =0.00947 were used in equation (8.6).

Figure 8.7 Variation of erosion rates along the radial direction from the stagnation point as computed using the model of Huang et al. [24] and wear map method for nominal impingement angle of 90° and nozzle exit flow velocity of 5m/s. Also experimental wear rates are shown.

Figure 8.8 Variation of erosion rates along the radial direction from the stagnation point as computed using the model of Huang et al. [24] and wear map method for nominal impingement angle of 90° and nozzle exit flow velocity of 10m/s. Also experimental wear rates are shown.

Figures 8.7 and 8.8 suggests the model of Huang et al. [24] performs comparatively better than the NG model. Erosion rates are fairly close to experimental rates, but beyond 3-4 mm from the centre of the specimen, predictions began to deviate away from experimental results. This was observed for both the case (5 and 10 m/s) and it can be said that the model of Huang et al. [24] also fails to capture the erosion features predicted by the wear-map method.

8.3.3 Wear model correlations made by alhert [124]

The third model in this review is the empirical wear equation developed by Alhert [124] given by equation (8.7). A description of this model and the conditions in which this was developed is given in section 2.3.3.1.

$$ER = A F_s V_p^n f(\theta), \qquad (8.7)$$

where F_s is the particle shape coefficient, ($F_s = 1.0$ for sharp particle, 0.53 for semi-rounded or 0.2 for fully rounded sand particles), V_p is the local impact velocity; 'A' and 'n' are empirical coefficients. Alhert [124] used two functional forms of the angle dependence, with matching conditions applied at 15°. The dependence on impingement angle, $f(\theta)$ is given by equations (8.8 a and b).

$$f(\theta) = a\theta^2 + b\theta, \qquad \text{for } \theta \leq 15°, \qquad (8.8a)$$

$$f(\theta) = x \cos \theta^2 \sin \theta + y \sin \theta^2 + z, \qquad \text{for } 90° > \theta > 15°. \qquad (8.8b)$$

For predicting wear using the model of alhert [124] it is required to determine values for empirical coefficients, A, a, b, x, y and z. This was done by using CFD impact and local wear data available for nominal conditions (90° and 7.5m/s), similar to the two previous cases and values of which are tabulated in Table 8.4. Local wear rates were then predicted using equations (8.7 and 8.8) with the empirical factors specified in Table 8.4 for the nominal

conditions (90° angle and velocity of 5 and 10 m/s). Wear predictions were compared with the available experimental data for the same nominal conditions and portrayed by Figures 8.9 and 8.10.

Table 8.4 Empirical coefficients which provide the best mathematical fit for local erosion rate predicted by (equation 8.7 and 8.8) and impact data for the nominal conditions of 90° and 7.5m/s.

A	a	b	x	y	z
6.28×10^{-16}	-146	573	-5.28	-2.12	6.56

Erosion rate (E_r) predictions obtained using the alhert model [124] are portrayed by Figures 8.8 and 8.9, illustrating good qualitative correlations with experimental data especially with the positioning of the maximum E_r for both the cases (5 and 10 m/s) were similar to those on the test sample. Numerical comparisons suggested that wear rates for 5m/s were over-predicted and for the case of 10m/s, E_r at majority of the locations were under-predicted. Overall the prediction accuracy of this model was calculated to be within 70% of experimental results at almost all the locations and thus suggesting good performance of this model in our case. Good correlations by ahlert (1994) model can be accounted for by the fact that the conditions under which this model was developed and validated was very similar to the one where the wear map model was built (similar material-abrasive property and geometries, impact kinetics, etc) as discussed earlier (section 2.3.3.1). Also this model does not try to associate any system parameter to the coefficients (Table 8.4) obtained thus improving the robustness and hence good performance in our case study. This does not assure that this model will perform well for a different case.
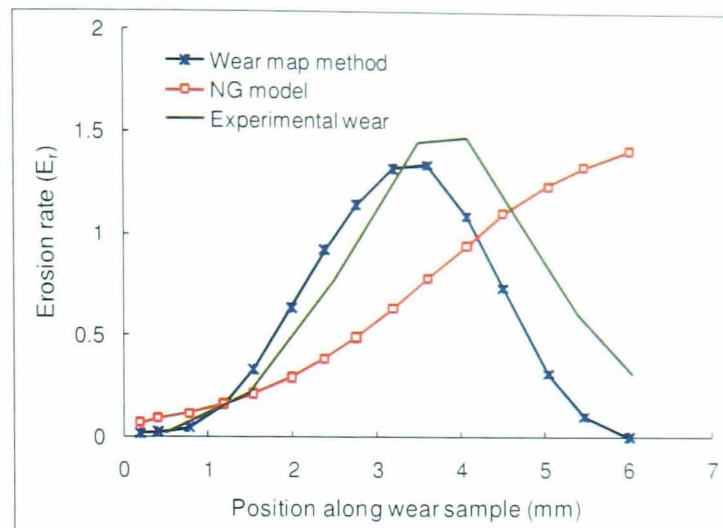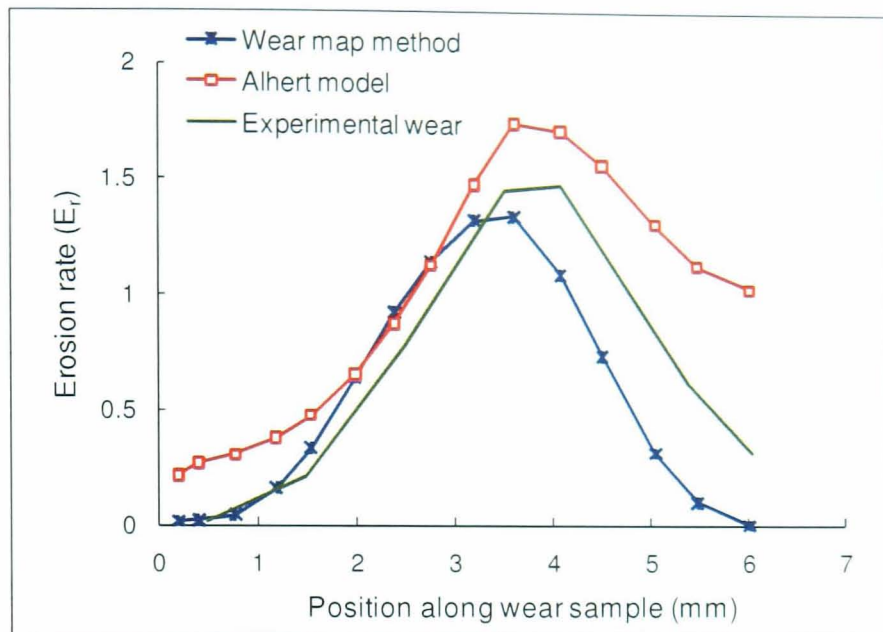
Figure 8.9 Variation of erosion rates along the radial direction from the stagnation point as computed using the model proposed by the model of alhert [124] and wear map method for nominal conditions (90° and 5m/s). Local experimental wear data extracted at similar nominal conditions are also shown.
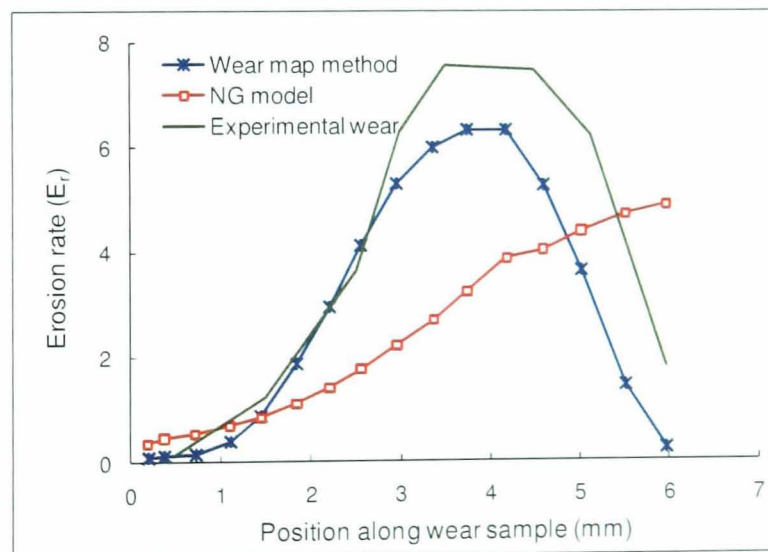

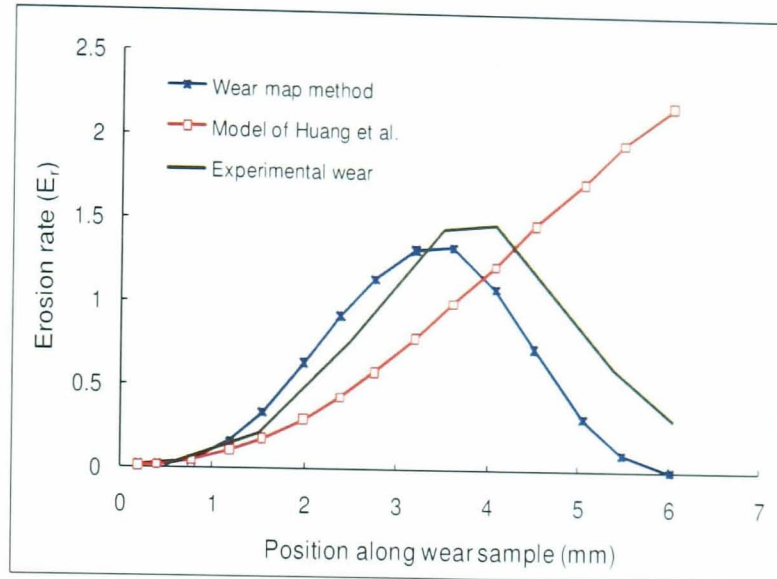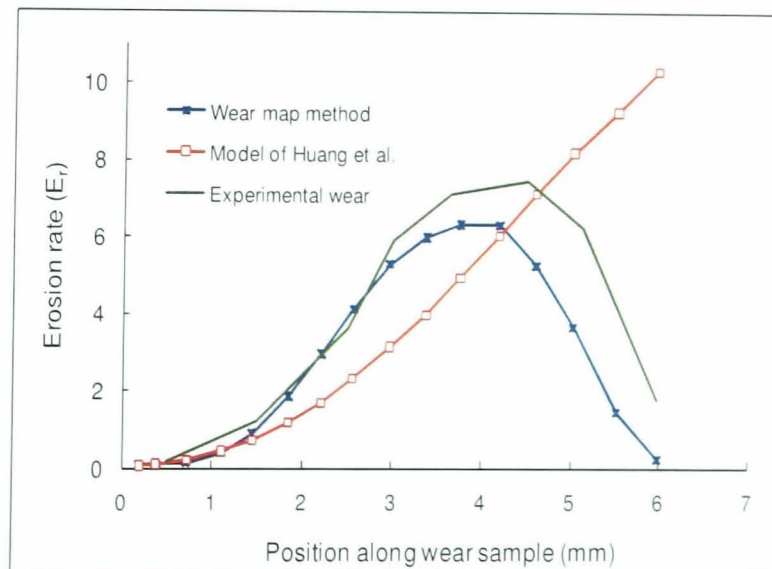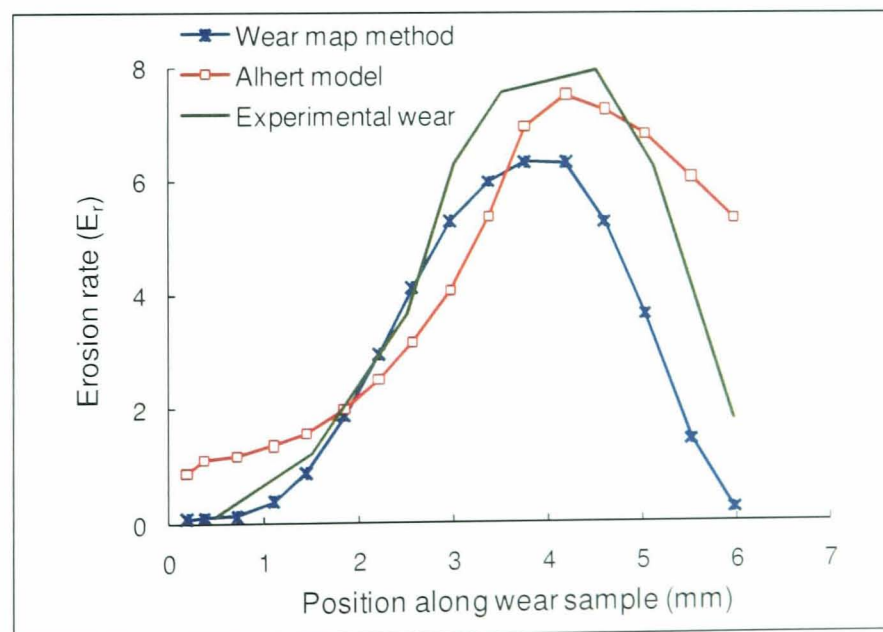**Figure 8.10** Variation of erosion rates along the radial direction from the stagnation point as computed using the model proposed by the model of alhert [124] and wear map method for nominal conditions (90° and 10m/s). Local experimental wear data extracted at similar nominal conditions are also shown.

8.4 Summary

A range of erosion parameters were obtained from a single well-defined experimental test (90° angle and 7.5m/s) characterised by CFD simulations. Mathematical fitting functions were used to obtain empirical constants which provided a best fit for experimental and local impact data related by the equation (8.1). The developed equation (8.2) was able to capture the features of the wear map with good correlations and thus demonstrating that a single test can indeed provide adequate data to map erosion wear on different conditions provided these conditions are similar in nature under which the correlations were generated.

In the next stage, predictions were made using three different available wear models and it was observed that the Huang et al. [24] and Neilson and Gilchrist [82] models failed to capture erosion wear while the model of Alhert [124] performed considerably well. However, this does not necessarily mean that the models are robust enough to work under all conditions and this was echoed by Dobrowolski and Wydrych [123] and Lester et al. [84]. Considering the nature of erosion wear, to obtain repeatability in inter-laboratory tests were shown to be difficult [29]. On similar lines, it can be extremely hard to make wear models developed at one set of conditions to work for all possible wearing condition with uncertainties around the choice of models and the numbers of experiments required within the parameter space to accurately find the constants. Furthermore, there are no models for advanced structures, for example, metal-matrix composites, where fundamental wear mechanisms may prove to be difficult than the conventional balance of cutting and deformation wear factors used for ductile materials. Consequently, the proposed wear-map method is a useful tool for capturing the behaviour of material under erosion conditions, and when linked with CFD a useful component of material specification and plant design.

Chapter 9

Conclusions and future work

9.1 Major conclusions and findings

The aim of this research work is to develop a method to predict wear and is presented in this thesis. The major conclusions of this work are listed as follows;

- Material wear data from a minimum set of carefully selected laboratory experiments can be used together with CFD to predict actual wear rates (wear profiles) on different flow geometries at different conditions.

- Existing numerical wear models which profess to predict material wear as a function of various erosion parameters and variables (example: particle diameter, surface hardness, particle density, material strength) fail to do so when the test conditions are different from the conditions at which the wear model coefficients was generated.

- To effectively use an existing wear model, it is necessary that operating conditions and target-abrasive characteristics are similar to those at which the model coefficients were generated.

9.2 General Discussion

This thesis presents the work carried out to develop a geometry independent wear prediction method to predict absolute wear rates due to particle impacts for a specific combination of material and abrasive. The method is an integration between a standard laboratory test and CFD

simulations. A range of erosion data is obtained from a minimal series of laboratory tests and are interpreted using CFD to ensure the maximum amount of data is made available from each test. Data obtained from both the CFD simulations and wear tests are then used to build a wear-map, specific to the material and abrasive. Once established, CFD simulations are used to predict flow for different geometries and conditions (i.e. the plant equipment) which, using the wear map can be interpreted to give actual wear predictions.

The wear-map method was developed on the foundation that the major factors affecting erosion wear due to particle impacts are the local impact angle, velocity and frequency, provided the combination of material type and abrasive are set. The first developmental part, as described in chapter 4, involved numerically determining the local particle impact conditions (angle, velocity and frequency) of a given wear test surface. CFD simulations of the slurry jet impingement test was carried out with the nominal jet angle set at 90° and for flow velocities of 5 and 10 m/s. A systematic modelling approach was followed to ensure the CFD model closely resembled the actual physical phenomenon. Numerical simulations provided an array of local impact data for which material wear values had to be obtained experimentally.

In chapter 5, the work carried out during the experimental stage was described and the slurry jet impingement test was chosen for this purpose. The test equipment was calibrated in order to ensure that the local impact velocity, angle and frequencies were the major factors affecting wear. Although various other factors such as degradation of erodent abrasivity, modifications to wear geometry, non-linearity in material behaviour and effects of corrosion can all affect erosion wear rates, experiments were designed to ensure that these factors had negligible influence. Tests were then carried out on flat test coupons with the nominal impingement angle set at 90°and for flow velocities of 5 and 10 m/s, corresponding to the CFD simulations.

Post test profile measurements of the experimental study provided local wear depth which was correlated to local particle impact data (velocity, angle and frequency taken from the CFD simulations) as described in chapter 6.

Material wear data was linked to particle impact data to build a wear-map, which can associate a wear rate for any local impact condition for that specific material and abrasive combination. The power of the wear-map lies here, in such that further CFD simulations of any geometry where hydrodynamic particle impact is the predominant wear mechanism is sufficient to predict wear rates due to erosion, provided the material and abrasive are the same as that used to develop the wear map, without further testing. The major findings and contributions to the field of erosion wear predictions based on this method are described as follows;

- To assess the wear predictive capabilities of the wear-map method, wear on a flat specimen angled 90° to an impinging slurry medium at 7.5m/s was predicted using CFD simulations interlinked with the wear-map. Experiments were conducted at similar conditions to validate all predictions and very good correlations were observed. Based on these results it was suggested that for any flow velocities between 5 and 10 m/s (the jet velocities used to build the wear-map), this method would be able to predict wear very accurately. This high degree of accuracies was attributed to the fact that the flow regime is qualitatively similar in both the cases.

- Subsequent to this, the geometry was modified by changing the angle of nominal impingement to 105° and 135°. The nozzle exit flow velocity was set at 5m/s so as to study the effect of change in geometry only. Good qualitative correlations were observed between predictions and experiments, however, numerical differences were high. Prediction discrepancies were attributed primarily to possible misalignments between nozzle-sample arrangement and variations in hydrodynamic regime due to change in geometries.

  - To study the effect of possible misalignments introducing variations in CFD and experimental geometries and hence prediction errors, CFD simulations were conducted at different orientations (with

small changes in stand-off distances and inclination angles) and it was observed that minor changes can significantly affect local erosion wear profiles. Subsequent CFD and wear-map predicted profiles (with different geometries) were much closer to experimentally measured profiles and errors were reduced by more than 50% thus emphasizing the influence on small changes in geometry on erosion profile.

- Prediction errors were also attributed to the changes in the hydrodynamics brought about by the change in geometry. During the development of the wear-map, only the initial impact of the particle was considered on the assumption that the particle would lose majority of its energy after the first impact. However, with the change in the geometry from 90° to 105 and 135° it could be possible that a secondary impact of a particle does contribute to material loss. This could well explain the divergence observed in wear profiles around the edge of the wear scars for 105° and 135° samples.

- Subsequent to these observations, it was concluded that although there were numerical errors in the predicted profiles, with an experimental setup in which closer tolerances can be achieved and by the use of appropriate restitution factors (Section 2.3.3.2), data from a few simple standard tests can be effectively used to predict wear profiles on different geometries.

- Further to this, wear on a typical plant geometry (1.5D 90° elbow bend) was predicted using CFD simulations and the wear map. To prevent any possible misalignment, an elbow bend was fabricated in order to reduce any possibly geometrical variations between CFD and experimental geometries. Good correlations were observed between predicted and measured wear profiles, with the magnitude and location of maximum wear accurately predicted by the wear-map. However beyond a certain point the wear-map method fails to predict any

material wear. This was attributed to the inability of the wear-map to predict wear due to sliding impacts (impacts below 10°) and also wear due to secondary impacts of particles.

- A further observation based on the test results of the flat samples and the elbow bend is that to build a wear map which covers the wide range of conditions encountered in plant equipment more than one geometry should be considered. It is proposed that along with the 90° configuration, tests should be performed at 135° and the data obtained could be collated to enhance the predictive ability of the wear-map. Although these data were available from the tests conducted in this programme due to time restrictions this was not pursued any further.

- In Chapter 8, three different existing wear models were assessed based on their ability to capture the features of the wear-map. It was observed that two wear models, the model of Neilson and Gilchrist [83] (NG) and the model of Huang et al. [24] failed to capture the features of the wear-map. However, the model of Alhert et al. [124] performed well in that it was able to correlate the data; although these three models were purported to predict absolute wear rates over the entire spectrum of the operating conditions as a function of material and abrasive properties, only the Alhert et al. [124] model behaved satisfactorily over the examined range. It does not necessarily infer it is robust enough to work for all conditions. Given the uncertainties around the choice of a suitable mode, the mode general wear model (and wear-map) is proposed as an useful tool to be able to predict erosion wear for a set of conditions by using CFD as an interpretation tool.

9.3 Suggestions for future work

In section 2.1.3, the effects of particle impacts on corrosion was described and a natural extension of the wear-map method would be to include erosion enhanced corrosion loss and advance the model to be more applicable for erosion-corrosion environment. A starting point to this would

be to experimentally determine the material loss due to corrosion for a single particle impact event and to superimpose this data on to the wear-map.

The wear-map predictions on the elbow bend (section 7.5.3) failed to capture wear due to low angle and secondary impacts of particles. As suggested, wear data from an additional slurry jet test in which particles predominantly impact at glancing angles (<10°) could be incorporated into the wear-map to further its envelope of applicability. This can then improve the accuracy of wear predictions on geometries (such as valves, chokes, long radius pipe-bends) where secondary impacts of particles contribute considerably to wear loss.

Also a more detailed estimation of errors (the contribution of a specific factors to the overall error) at a given particle impact velocity and angle are required to improve prediction accuracies. Also a wider set of flow predictions can be used as a guide to design the series of experiments (geometry and conditions) based on the local impact data predicted to build the wear-map.

Accounting for wear due to secondary impacts of particles would require the use of appropriate restitution functions. However, due to the non physical rebound of particles (section 4.3.3) as assumed by *Fluent* during particle trajectory calculations, the use of restitution factors would be compromised. Hence this shortcoming of the numerical code has to be corrected and the efficient use of restitution factors could be investigated.

In Chapter 5, it was numerically and experimentally shown that changes in surface geometry due to wear had minimal effect on overall wear rates. However, for longer test durations it is suggested that profile changes can have a significant effect on local impact conditions and subsequently the overall wear profile. It was also assumed that the presence of particles did not have any effect on the flow conditions; however, with increases in particle concentrations this assumption may not be valid. Hence the effect of time and particle concentrations on absolute wear rates and the possibility of incorporating them into the wear model could also be considered.

Another part of the future work could be examining and building a database of material behaviour (example: a range of steels for a given abrasive) and also to extend the work to complex materials such as MMCs.

References

1. Alboudwarej, H., et al., *Highlighting Heavy Oil.* 2006: Alberta, Canada.

2. Flores, J.F., *Erosion and Erosion-Corrosion Mechanisms of PTA Coatings for Application in the Oilsands Industry*, in *Mechanical Engineering.* 2008, University of Leeds: Leeds. p. 85.

3. Revega, T. and S. Chiovelli, *Syncrude Oil Sand Mine, Alberta- Mining Technololgy.* 2009: Alberta.

4. Wallace, M.S., W.M. Dempster, T. Scanlon, J. Peters, and S. McCulloch, *Prediction of impact erosion in valve geometries.* Wear, 2004. **256**(9-10): p. 927-936.

5. Hutchings, I.M., *Wear by particulates.* Chemical Engineering Science, 1987. **42**(4): p. 869-878.

6. Reza, F., *Corrosion and Erosion-Corrosion Behaviour of Materials used for Oilsands applications*, in *Mechanical Engineering.* 2005, Heriot-Watt University: Edinburgh. p. 234.

7. Roco, M.C. and G.R. Addie, *Erosion wear in slurry pumps and pipes.* Powder Technology, 1987. **50**(1): p. 35-46.

8. Poloski, A.P., A.W. Etchells, J. Chun, H.E. Adkins, A.M. Casella, M.J. Minette, and S.T. Yokuda, *A pipeline transport correlation for slurries with small but dense particles.* The Canadian Journal of Chemical Engineering, 2010. **88**(2): p. 182-189.

9. Matousek, V. *The Pipeline Transport of Different Sand Fractions in Dense Slurries.* 2002: ASCE.

10. Jacobs, B.E.A., ed. *Design of Slurry Tranport Systems.* 1991.

11. Postlethwaite, J. and S. Nesic, *Erosion in disturbed liquid/particle pipe flow: Effects of flow geometry and particle surface roughness.* Corrosion 1993. **49**(10): p. 850-857.

12. Levy, A.V. and P. Yau, *Erosion of steels in liquid slurries.* Wear, 1984. **98**: p. 163-182.

13. Worster, R.C. and D.F. Denny. *The Hydraulic Transport of Solid Material in Pipes.* in *General Meeting of the Institution of Mechanical Engineers.* 1955. London.

14. Tuzson, J.J., *Laboratory slurry erosion tests and pump wear rate calculations.* J. Fluids Eng. ; Vol/Issue: 106:2, 1984: p. Pages: 135-140.

15. Humphrey, J.A.C., *Fundamentals of fluid motion in erosion by solid particle impact.* International Journal of Heat and Fluid Flow, 1990. **11**(3): p. 170-195.

16. Clark, H.M., *The influence of the flow field in slurry erosion.* Wear. 1992. **152**(2): p. 223-240.

17. Hu, X., *The corrosion and Erosion-Corrosion Behaviour of High Alloy Stainless Steels*, in *Department of Mechanical and Chemical Engineering*. 2003, PhD thesis, Heriot-Watt University: Edinburgh.

18. Roberge, P.R., ed. *Corrosion Engineering Principles and Practice*. 2008.

19. Reyes, M. and A. Neville, *Degradation mechanisms of Co-based alloy and WC metal-matrix composites for drilling tools offshore*. Wear. 2003. **255**: p. 1143-1156.

20. Neville, A. and X. Hu, *Mechanical and electrochemical interactions during liquid-solid impingement on high-alloy stainless steels*. Wear, 2001. **251**(1-12): p. 1284-1294.

21. Li, Y., G.T. Burstein, and I.M. Hutchings, *The influence of corrosion on the erosion of aluminium by aqueous silica slurries*. Wear, 1995. **186-187**(Part 2): p. 515-522.

22. Flores, J.F., A. Neville, N. Kapur, and A. Gnanavelu, *Erosion-corrosion degradation mechanisms of Fe-Cr-C and WC-Fe-Cr-C PTA overlays in concentrated slurries*. Wear, 2009. **267**(11): p. 1811-1820.

23. Poulson, B., *Complexities in predicting erosion corrosion*. Wear, 1999. **233-235**: p. 497-504.

24. Huang, C., S. Chiovelli, P. Minev, J. Luo, and K. Nandakumar, *A comprehensive phenomenological model for erosion of materials in jet flow*. Powder Technology, 2008. **187**(3): p. 273-279.

25. Heine, O.R. and P.M. Riede, *Wear Resistant Pipe Bend for Slurry Transport*, U.S. Patent, Editor. 1984, R & H Technologies Inc.: United States.

26. McLaury, B.S. and S.A. Shirazi, *An Alternate Method to API RP 14E for Predicting Solids Erosion in Multiphase Flow*. Journal of Energy Resources Technology, 2000. **122**(3): p. 115-122.

27. Levy, A., ed. *Solid Particle Erosion and Erosion-Corrosion of Materials*. 1995, ASM International.

28. Levy, A.V. and G. Hickey, *Liquid-solid particle slurry erosion of steels*. Wear, 1987. **117**(2): p. 129-146.

29. Ruff, A.W., *Analysis of interlaboratory test results of solid particle impingement erosion*. 1985.

30. Tilly, G.P., *A two stage mechanism of ductile erosion*. Wear, 1973. **23**(1): p. 87-96.

31. Efird, K.D., E.J. Wright, J.A. Boros, and T.G. Hailey. *Experimental Correlation of Steel Corrosion in Pipe Flow with Jet Impingement and Rotating Cylinder Tests*. in *NACE 93*. 1993. New Orleans.

32. Efird, K.D., *Jet impingement testing for flow accelerated corrosion*, in *Corrosion 2000*. 2000, Nace International Paper 00052: Texas, U.S.A.

33. Finnie, I., *Erosion of surfaces by solid particles.* Wear, 1960. **3**(2): p. 87-103.

34. Bitter, J.G.A., *A study of erosion phenomena: Part II.* Wear, 1963. **6**(3): p. 169-190.

35. Sundararajan, G., *A comprehensive model for the solid particle erosion of ductile materials.* Wear, 1991. **149**(1-2): p. 111-127.

36. Brown, G.J., *Erosion prediction in slurry pipeline tee-junctions.* Applied Mathematical Modelling, 2002. **26**(2): p. 155-170.

37. Wang, J. and S.A. Shirazi, *A CFD Based Correlation for Erosion Factor for Long-Radius Elbows and Bends.* ASME, 2003. **125**: p. 26-34.

38. Nesic, S., *Using computational fluid dynamics in combating erosion-corrosion.* Chemical Engineering Science, 2006. **61**(12): p. 4086-4097.

39. Bozzini, B., M.E. Ricotti, M. Boniardi, and C. Mele, *Evaluation of erosion-corrosion in multiphase flow via CFD and experimental analysis.* Wear, 2003. **255**(1-6): p. 237-245.

40. Tian, H.H., G.R. Addie, and K.V. Pagalthivarthi, *Determination of wear coefficients for erosive wear prediction through Coriolis wear testing.* Wear, 2005. **259**(1-6): p. 160-170.

41. Shook, C.A., D.B. Haas, W.H.W. Husband, and M. Small, *Relative Wear Rate Determinations for Slurry Pipelines.* Journal of Pipelines, 1981. **1**: p. 273-280.

42. Wang, M.-H., C. Huang, K. Nandakumar, P. Minev, J. Luo, and S. Chiovelli, *Computational fluid dynamics modelling and experimental study of erosion in slurry jet flows.* International Journal of Computational Fluid Dynamics, 2009. **23**(2): p. 155 - 172.

43. Schaan, J., N. Cook, and R.S. Sanders, *On-line wear measurements for commercial-scale, coarse-particle slurry pipelines.* 2006, Syncrude Canada Ltd.

44. Hu, X. and A. Neville, *An examination of the electrochemical characteristics of two stainless steels (UNS S32654 and UNS S31603) under liquid-solid impingement.* Wear, 2004. **256**(5): p. 537-544.

45. Wood, R.J.K., *Erosion-corrosion interactions and their effect on marine and offshore materials.* Wear, 2006. **261**(9): p. 1012-1023.

46. Engel, P.A., ed. *Impact Wear of Materials.* 1976.

47. Kleis, I. and P. Kulu, eds. *Solid Particle Erosion: Occurence, Prediction and Control.* 2008, Springer-Verlag London Limited.

48. Laitone, J.A., *Aerodynamic effects in the erosion process.* Wear, 1979. **56**(1): p. 239-246.

49. Fontana, M.G., ed. *Corrosion Engineering.* 1985, McGraw-Hill book company.

50. Neville, A., T. Hodgkiess, and J.T. Dallas, *A study of the erosion-corrosion behaviour of engineering steels for marine pumping applications.* Wear. 1995. **186-187**(Part 2): p. 497-507.

51. Neville, A., M. Reyes, and H. Xu, *Examining corrosion effects and corrosion/erosion interactions on metallic materials in aqueous slurries.* Tribology International, 2002. **35**(10): p. 643-650.

52. Madsen, B.W., *Measurement of erosion-corrosion synergism with a slurry wear test apparatus.* Wear, 1988. **123**(2): p. 127-142.

53. Lu, B.T. and J.L. Luo, *Synergism of Electrochemical and Mechanical Factors in Erosionâ¨Corrosion.* The Journal of Physical Chemistry B, 2006. **110**(9): p. 4217-4231.

54. Burstein, G.T. and K. Sasaki, *Effect of impact angle on the slurry erosion-corrosion of 304L stainless steel.* Wear, 2000. **240**(1-2): p. 80-94.

55. Burstein, G.T. and K. Sasaki, *Detecting electrochemical transients generated by erosion-corrosion.* Electrochimica Acta, 2001. **46**(24-25): p. 3675-3683.

56. Matsumura, M., Y.I. Oka, H. Hiura, and M. Yano, *The role of Passivating Flim in Preventing Slurry Erosion-Corrosion of Austenitic Stainless Steel.* ISIJ International, 1991. **31**(2): p. 168-176.

57. Ekambara, K., R.S. Sanders, K. Nandakumar, and J.H. Masliyah, *Hydrodynamic Simulation of Horizontal Slurry Pipeline Flow Using ANSYS-CFX.* Industrial & Engineering Chemistry Research, 2009. **48**(17): p. 8159-8171.

58. Cooke, R., G. Johnson, and P. Goosen, *Laboratory Apparatus for Evaluating Slurry Pipeline Wear.* Proceedings of the 14th International Conference on Slurry Handling and Pipeline Transport 2000. **14**: p. 1-17.

59. Elghobashi, S., *On predicting particle-laden turbulent flows.* Applied Scientific Research, 1994. **52**(4): p. 309-329.

60. Goodwin, J.E., W. Sage, and G.P. Tilly, *Study of erosion by solid particles.* ARCHIVE: Proceedings of the Institution of Mechanical Engineers 1847-1982 (vols 1-196), 1969. **184**(1969): p. 279-292.

61. Hanson, R., D. Allsopp, T. Deng, D. Smith, M.S.A. Bradley, I.M. Hutchings, and M.K. Patel, *A model to predict the life of pneumatic conveyor bends.* Proceedings of the Institution of Mechanical Engineers, 2002. **216**(3): p. 143-149.

62. Hussainova, I. and K.-P. Schade, *Correlation between solid particle erosion of cermets and particle impact dynamics.* Tribology International. 2008. In **Press, Corrected Proof**: p. 330.

63. Meng, H.C. and K.C. Ludema, *Wear models and predictive equations: their form and content.* Wear, 1995. **181-183**(Part 2): p. 443-457.

64. Levy, A.V., N. Jee, and P. Yau, *Erosion of steels in coal-solvent slurries.* Wear, 1987. **117**(2): p. 115-127.

65. Clark, H.M., *On the impact rate and impact energy of particles in a slurry pot erosion tester.* Wear, 1991. **147**(1): p. 165-183.

66. Jepsen, R., J. Roberts, and W. Lick, *Effects of bulk density on sediment erosion rates.* Water, Air, & Soil Pollution, 1997. **99**(1): p. 21-31.

67. Hojo, H., K. Tsuda, and T. Yabu, *Erosion damage of polymeric material by slurry.* Wear, 1986. **112**(1): p. 17-28.

68. Benchaita, M.T., P. Griffith, and E. Rabinowicz, *Erosion of Metallic Plate by Solid Particles Entrained in a Liquid Jet.* ASME, 1983. **105**(3): p. 215-222.

69. Lynn, R.S., K.K. Wong, and H.M. Clark, *On the particle size effect in slurry erosion.* Wear, 1991. **149**(1-2): p. 55-71.

70. Misra, A. and I. Finnie, *On the size effect in abrasive and erosive wear.* Wear, 1981. **65**(3): p. 359-373.

71. Desale, G.R., B.K. Gandhi, and S.C. Jain, *Effect of erodent properties on erosion wear of ductile type materials.* Wear, 2006. **261**(7-8): p. 914-921.

72. Clark, H.M., *Specimen diameter, impact velocity, erosion rate and particle density in a slurry pot erosion tester.* Wear, 1993. **162-164**(Part 2): p. 669-678.

73. Dhar, S., T. Krajac, D. Ciampini. and M. Papini, *Erosion mechanisms due to impact of single angular particles.* Wear, 2005. **258**(1-4): p. 567-579.

74. Chen, Q. and D.Y. Li, *Computer simulation of solid particle erosion.* Wear, 2003. **254**(3-4): p. 203-210.

75. Carmichael, G.R., *Estimation of the drag coefficient of regularly shaped particles in slow flows from morphological descriptors.* Industrial & Engineering Chemistry Process Design and Development, 1982. **21**(3): p. 401-403.

76. Goossens, D., *A drag coefficient equation for natural, irregularly shaped particles.* CATENA, 1987. **14**(1-3): p. 73-99.

77. Sapate, S.G. and A.V. RamaRao, *Effect of Erodent Particle Hardness on Velocity Exponent in Erosion of Steels and Cast Irons.* Materials and Manufacturing Processes, 2003. **18**(5): p. 783-802.

78. Tilly, G.P., *Erosion caused by airborne particles.* Wear, 1969. **14**(1): p. 63-79.

79. Sari, N.Y., *Influence of erodent particle types on solid particle erosion of polyphenylene sulphide composite under low particle speed.* Polymer Composites, 2008. **30**(10).

80. Levy, A.V. and P. Chik, *The effects of erodent composition and shape on the erosion of steel.* Wear, 1983. **89**(2): p. 151-162.

81. Parslow, G.I., D.J. Stephenson, J.E. Strutt, and S. Tetlow. *Investigation of solid particle erosion in components of complex geometry.* Wear, 1999. **233-235**: p. 737-745.

82. Neilson, J.H. and A. Gilchrist, *Erosion by a stream of solid particles.* Wear. 1968. **11**(2): p. 111-122.

83. Zhang, Y., E.P. Reuterfors, B.S. McLaury, S.A. Shirazi, and E.F. Rybicki. *Comparison of computed and measured particle velocities and erosion in water and air flows.* Wear, 2007. **263**(1-6): p. 330-338.

84. Lester, D.R., L.A. Graham, and J. Wu, *High precision suspension erosion modeling.* Wear, 2010. **269**(5-6): p. 449-457.

85. Oka, Y.I., M. Nishimura, K. Nagahashi, and M. Matsumura, *Control and evaluation of particle impact conditions in a sand erosion test facility.* Wear, 2001. **250**(1-12): p. 736-743.

86. Bitter, J.G.A., *A study of erosion phenomena part I.* Wear, 1963. **6**(1): p. 5-21.

87. Hutchings, I.M. and R.E. Winter, *Particle erosion of ductile metals: A mechanism of material removal.* Wear, 1974. **27**(1): p. 121-128.

88. Clark, H.M. and K.K. Wong, *Impact angle, particle energy and mass loss in erosion by dilute slurries.* Wear, 1995. **186-187**(Part 2): p. 454-464.

89. Shipway, P.H. and I.M. Hutchings, *A method for optimizing the particle flux in erosion testing with a gas-blast apparatus.* Wear, 1994. **174**(1-2): p. 169-175.

90. Dosanjh, S. and J.A.C. Humphrey, *The influence of turbulence on erosion by a particle-laden fluid jet.* Wear, 1985. **102**(4): p. 309-330.

91. Levy, A. and Y.-F. Man, *Elevated temperature erosion-corrosion of 9Cr-1Mo steel.* Wear, 1986. **111**(2): p. 135-159.

92. Zhang, Y., B.S. McLaury, and S.A. Shirazi, *Improvements of Particle Near-Wall Velocity and Erosion Predictions Using a Commercial CFD Code.* Journal of Fluids Engineering, 2009. **131**(3): p. 031303.

93. Finnie, I. and Y.H. Kabil, *On the formation of surface ripples during erosion.* Wear, 1965. **8**(1): p. 60-69.

94. Finnie, I. and D.H. McFadden, *On the velocity dependence of the erosion of ductile metals by solid particles at low angles of incidence.* Wear, 1978. **48**(1): p. 181-190.

95. Finnie, I., *Some reflections on the past and future of erosion.* Wear, 1995. **186-187**(Part 1): p. 1-10.

96. Levy, A.V., *The solid particle erosion behavior of steel as a function of microstructure.* Wear, 1981. **68**(3): p. 269-287.

97. Soderberg, S., S. Hogmark, U. Engman, and H. Swahn, *Erosion classification of materials using a centrifugal erosion tester.* Tribology International, 1981. **14**(6): p. 333-343.

98. Sheldon, G.L. and A. Kanhere, *An investigation of impingement erosion using single particles.* Wear, 1972. **21**(1): p. 195-209.

99. Tilly, G.P., *Sand erosion of metals and plastics: A brief review.* Wear, 1969. **14**(4): p. 241-248.

100. Divakar, M., V.K. Agarwal, and S.N. Singh, *Effect of the material surface hardness on the erosion of AISI316.* Wear, 2004. **259**(1-6): p. 110-117.

101. Chacon Nava, J.G., F.H. Stott, and M.M. Stack, *The effect of substrate hardness on the erosion-corrosion resistance of materials in low-velocity conditions.* Corrosion Science, 1993. **35**(5-8): p. 1045-1051.

102. Sapate, S.G. and A.V.R. Rao, *Effect of material hardness on erosive wear behavior of some weld-deposited alloys.* Materials and Manufacturing Processes, 2002. **17**(2): p. 187 - 198.

103. Chauhan, A., D. Goel, and S. Prakash, *Erosion behaviour of hydro turbine steels.* Bulletin of Materials Science, 2008. **31**(2): p. 115-120.

104. Sundararajan, G., *The effect of temperature on solid particle erosion.* Wear, 1984. **98**: p. 141-149.

105. Goretta, K.C., R.C. Arroyo, C.T. Wu, and J.L. Routbort, *Erosion of work-hardened copper, nickel, and 304 stainless steel.* Wear, 1991. **147**(1): p. 145-154.

106. Naim, M. and S. Bahadur, *The significance of the erosion parameter and the mechanisms of erosion in single-particle impacts.* Wear, 1984. **94**(2): p. 219-232.

107. Clark, H.M., J. Tuzson, and K.K. Wong, *Measurements of specific energies for erosive wear using a Coriolis erosion tester.* Wear, 2000. **241**(1): p. 1-9.

108. Xie, Y., H.M. Clark, and H.M. Hawthorne, *Modelling slurry particle dynamics in the Coriolis erosion tester.* Wear, 1999. **225-229**(Part 1): p. 405-416.

109. Hawthorne, H.M., *Some Coriolis slurry erosion test developments.* Tribology International, 2002. **35**(10): p. 625-630.

110. Hawthorne, H.M. and Y. Xie, *On particle interactions with target materials of different mechanical properties in a long specimen Coriolis slurry erosion tester.* Wear, 2005. **258**(1-4): p. 470-479.

111. Tuzson, J.J., *Laboratory Slurry Erosion Tests and Pump Wear Rate Calculations.* Journal of Fluids Engineering, 1984. **106**(2): p. 135-140.

112. Tian, H.H., G.R. Addie, and E.P. Barsh, *A new impact erosion testing setup through Coriolis approach.* Wear, 2007. **263**(1-6): p. 289-294.

113. Clark, H.M., *The influence of the squeeze film in slurry erosion.* Wear, 2004. **256**(9-10): p. 918-926.

114. Desale, G.R., B.K. Gandhi, and S.C. Jain, *Improvement in the design of a pot tester to simulate erosion wear due to solid-liquid mixture.* Wear, 2004. **259**(1-6): p. 196-202.

115. Wong, K.K. and H.M. Clark, *A model of particle velocities and trajectories in a slurry pot erosion tester.* Wear, 1993. **160**(1): p. 95-104.

116. Been, J., B. Lu, J. Wolodko, and D. Kiel, *Predicting Wear of HydroTransport PipeLines in Oil Sand Slurries*. 2008, Alberta Research Council / Coanada Research and Development Corporation.

117. Wood, R.J.K., T.F. Jones, J. Ganeshalingam, and N.J. Miles, *Comparison of predicted and experimental erosion estimates in slurry ducts*. Wear, 2004. **256**(9-10): p. 937-947.

118. Postlethwaite, J., S. Nesic, G. Adamopoulos, and D.J. Bergstrom, *Predictive models for erosion-corrosion under disturbed flow conditions*. Corrosion Science, 1993. **35**(1-4): p. 627-633.

119. Hutchings, I.M., *A model for the erosion of metals by spherical particles at normal incidence*. Wear, 1981. **70**(3): p. 269-281.

120. Forder, A., M. Thew, and D. Harrison, *A numerical investigation of solid particle erosion experienced within oilfield control valves*. Wear, 1998. **216**(2): p. 184-193.

121. Jennings, W.H., W.J. Head, and C.R. Manning Jr, *A mechanistic model for the prediction of ductile erosion*. Wear, 1976. **40**(1): p. 93-112.

122. Keating, A. and S. Nesic, *Particle tracking and erosion prediction in three-dimensional bends*. ASME Fluids Engineering, 2000. **10**(1).

123. Dobrowolski, B. and J. Wydrych, *Evaluation of numerical models for prediction of areas subjected to erosion wear*, in *Fourth International Tribology Conference ITC 2006*, International Journal of Applied Mechanics and Engineering, Editor. 2006. p. 735-749.

124. Ahlert, K.R., *Effects of Particle Impingement Angle and Surface Wetting on Solid Particle Erosion on ANSI 1018 Steel*, in *Mechanical Engineering*. 1994, University of Tulsa.

125. McLaury, B.S., S.A. Shirazi, J.R. Shadley, and E.F. Rybicki, *Modelling erosion in chokes*. ASME Fluids Engineering, 1996. **236**(1): p. 773-781.

126. Grant, G. and W. Tabakoff, *An experimental investigation of the erosive characteristics of 2024 aluminium alloy*. 1973: p. 73-37.

127. Haugen, K., O. Kvernvold, A. Ronold, and R. Sandberg, *Sand erosion of wear-resistant materials: Erosion in choke valves*. Wear, 1995. **186-187**(Part 1): p. 179-188.

128. Crowe, C., M. Sommerfeld, and Y. Tsuji, eds. *MULTIPHASE FLOWS with DROPLETS and PARTICLES*. 1998.

129. Tu, J., H.G. Yeoh, and c. Liu, eds. *Computational Fluid Dynamics: A practical Approach*. 2008.

130. Wilkes, J.O., ed. *Fluid mechanics for chemical engineers: with Microfluidics and CFD*. 2006.

131. Nakayama, Y. and R.F. Boucher, eds. *Introduction to fluid mechanics*. 1999. John Wiley and Sons Inc.

132. Gilkeson, C.A., *Ventilation of Small Livestock Trailers*, in *Mechanical Engineering*. 2009, University of Leeds: Leeds.

133. Massey, B. and J. Ward-Smith, eds. *Mechanics of Fluids*. 1998.

134. Davidson, P.A., *Turbulence: An introduction for scientists and Engineers*. 2004, Oxford.

135. Launder, B.E. and D.B. Spalding, *The numerical computation of turbulent flows*. Computer Methods in Applied Mechanics and Engineering, 1974. **3**(2): p. 269-289.

136. Spalart, P.R., *Strategies for turbulence modelling and simulations*. International Journal of Heat and Fluid Flow, 2000. **21**(3): p. 252-263.

137. Versteeg, H.K. and W. Malalasekera, eds. *An Introduction to Computational Fluid Dynamics- The Finite Volume Method*. 2007.

138. Spalart, P.R. and S.R. Allmaras, *A one-equation turbulence model for aerodynamic flows*. AIAA-Paper 92-0439, 1992(1): p. 5-21.

139. Nallasamy, M., *Turbulence models and their applications to the prediction of internal flows: A review*. Computers & Fluids, 1987. **15**(2): p. 151-194.

140. Wolfshtein, M., *Some comments on turbulence modelling*. International Journal of Heat and Mass Transfer, 2009. **52**(17-18): p. 4103-4107.

141. Murakami, S., *Comparison of various turbulence models applied to a bluff body*. Journal of Wind Engineering and Industrial Aerodynamics, 1993. **46-47**: p. 21-36.

142. Yakhot, V. and L.M. Smith, *The renormalization group, the ε-expansion and derivation of turbulence models*. Journal of Scientific Computing, 1992. **7**(1): p. 35-61.

143. Shih, T.-H., W.W. Liou, A. Shabbir, Z. Yang, and J. Zhu, *A new k-[epsilon] eddy viscosity model for high reynolds number turbulent flows*. Computers & Fluids, 1995. **24**(3): p. 227-238.

144. Baydar, E. and Y. Ozmen, *An experimental and numerical investigation on a confined impinging air jet at high Reynolds numbers*. Applied Thermal Engineering, 2005. **25**(2-3): p. 409-421.

145. Craft, T.J., L.J.W. Graham, and B.E. Launder, *Impinging jet studies for turbulence model assessment--II. An examination of the performance of four turbulence models*. International Journal of Heat and Mass Transfer, 1993. **36**(10): p. 2685-2697.

146. Nishino, K., M. Samada, K. Kasuya, and K. Torii, *Turbulence statistics in the stagnation region of an axisymmetric impinging jet flow*. International Journal of Heat and Fluid Flow, 1996. **17**(3): p. 193-201.

147. Yakhot, V. and S.A. Orszag, *Renormalization group analysis of turbulence. I. Basic theory*. Journal of Scientific Computing, 1986. **1**(1): p. 3-51.

148. Wood, R.J.K., T.F. Jones, N.J. Miles, and J. Ganeshalingam, *Upstream swirl-induction for reduction of erosion damage from slurries in pipeline bends.* Wear, 2001. **250**(1-12): p. 770-778.

149. Feyerl, J., G. Mori, S. Holzleitner, J. Haberl, M. Oberndorfer, W. Havlik, and C. Monetti, *Erosion-Corrosion of carbon steels in a laboratory: Three-Phase flow.* Corrosion Engineering, 2008. **64**(2): p. 175-186.

150. Leduc, S., C. Fredriksson, and R. Hermansson, *Particle-tracking option in Fluent validated by simulation of a low-pressure impactor.* Advanced Powder Technology, 2006. **17**(1): p. 99-111.

151. Davis, C. and P. Frawley, *Modelling of erosion-corrosion in practical geometries.* Corrosion Science, 2009. **51**(4): p. 769-775.

152. Barata, J.M.M., D.F.G. Durao, M.V. Heitor, and J.J. McGuirk, *The turbulence characteristics of a single impinging jet through a crossflow.* Experimental Thermal and Fluid Science, 1992. **5**(4): p. 487-498.

153. Dianat, M., M. Fairweather, and W.P. Jones, *Predictions of axisymmetric and two-dimensional impinging turbulent jets.* International Journal of Heat and Fluid Flow, 1996. **17**(6): p. 530-538.

154. Virdung, T. and A. Rasmuson, *Hydrodynamic properties of a turbulent confined solid-liquid jet evaluated using PIV and CFD.* Chemical Engineering Science, 2007. **62**(21): p. 5963-5978.

155. Jambunathan, K., E. Lai, M.A. Moss, and B.L. Button, *A review of heat transfer data for single circular jet impingement.* International Journal of Heat and Fluid Flow, 1992. **13**(2): p. 106-115.

156. Fox, R.W. and A.T. McDonald, eds. *Introduction to Fluid Mechanics.* Fourth Edition ed. 1994.

157. Angioletti, M., E. Nino, and G. Ruocco, *CFD turbulent modelling of jet impingement and its validation by particle image velocimetry and mass transfer measurements.* International Journal of Thermal Sciences, 2005. **44**(4): p. 349-356.

158. Yakhot, V., S.A. Orszag, S. Thangam, T.B. Gatski, and C.G. Speziale, *Development of turbulence models for shear flows by a double expansion technique.* Physics of Fluids A: Fluid Dynamics, 1992. **4**(7): p. 1510-1520.

159. Chen, Q., *COMPARISON OF DIFFERENT <i>k</i>-Îµ MODELS FOR INDOOR AIR FLOW COMPUTATIONS.* Numerical Heat Transfer, Part B: Fundamentals: An International Journal of Computation and Methodology. 1995. **28**(3): p. 353 - 369.

160. Cooper, D., D.C. Jackson, B.E. Launder, and G.X. Liao, *Impinging jet studies for turbulence model assessment--I. Flow-field experiments.* International Journal of Heat and Mass Transfer, 1993. **36**(10): p. 2675-2684.

161. Gupta, P.K. and K.V. Pagalthivarthi, *Comparison of Three Turbulence Models in Wear Prediction of Multi-Size Particulate Flow through Rotating*

Channel. International Journal of Mechanical, Industrial and Aerospace Engineering, 2010. **4:1**.

162. Tu, J.Y., *Numerical Investigation of Particulate Flow Behavior in Particle-Wall Impaction.* Aerosol Science and Technology, 2000. **32**(6): p. 509 - 526.

163. Clift, R., J.R. Grace, and M.E. Weber, eds. *Bubbles, Drops, and Particles.* 1978.

164. Chen, X., B.S. McLaury, and S.A. Shirazi, *Application and experimental validation of a computational fluid dynamics (CFD)-based erosion prediction model in elbows and plugged tees.* Computers & Fluids, 2004. **33**(10): p. 1251-1272.

165. Been, J., B. Lu, J. Wolodko, and D. Kiel, *Predicting Wear of HydroTransport PipeLines in Oil Sand Slurries.* 2008, Alberta Research Council / Coanada Research and Development Corporation.

166. Neville, A. and T. Hodgkiess, *Characterisation of high-grade alloy behaviour in severe erosion-corrosion conditions.* Wear, 1999. **233-235**: p. 596-607.

167. Wood, R.J.K. and D.W. Wheeler, *Design and performance of a high velocity air-sand jet impingement erosion facility.* Wear, 1998. **220**(2): p. 95-112.

168. Zu, J.B., I.M. Hutchings, and G.T. Burstein, *Design of a slurry erosion test rig.* Wear, 1990. **140**(2): p. 331-344.

169. Meng, H., X. Hu, and A. Neville, *A systematic erosion-corrosion study of two stainless steels in marine conditions via experimental design.* Wear, 2007. **263**(1-6): p. 355-362.

170. Neville, A., F. Reza, S. Chiovelli, and T. Revega, *Erosion-corrosion behaviour of WC-based MMCs in liquid-solid slurries.* Wear, 2005. **259**(1-6): p. 181-195.

171. Kwok, C.T., F.T. Cheng, and H.C. Man, *Synergistic effect of cavitation erosion and corrosion of various engineering alloys in 3.5% NaCl solution.* Materials Science and Engineering A, 2000. **290**(1-2): p. 145-154.

172. Hu, X. and A. Neville, *The electrochemical response of stainless steels in liquid-solid impingement.* Wear, 2005. **258**(1-4): p. 641-648.

173. Lapides, L. and A. Levy, *The halo effect in jet impingement solid particle erosion testing of ductile metals.* Wear, 1980. **58**(2): p. 301-311.

174. JOSEPH, G.G., R. ZENIT, M.L. HUNT, and A.M. ROSENWINKEL, *Particle—wall collisions in a viscous fluid.* Journal of Fluid Mechanics, 2001. **433**(-1): p. 329-346.

175. El-Sayed, A.F., R. Lasser, and W.T. Rouleau, *Effects of secondary flow on particle motion and erosion in a stationary cascade.* International Journal of Heat and Fluid Flow, 1986. **7**(2): p. 146-154.

176. Efird, K.D., *Flow accelerated corrosion testing basics,* in *Corrosion NACE expo 2006, 61st Annual conference and exposition.* 2006, Nace International Paper06689: Texas, United States.

177. McKibben, M.J. and C.A. Shook, eds. *Erosive Wear of Pipeline Systems in Slurry Handling: Design of Solid-Liquid Systems*. ed. N.P. Brown and N.I. Heywood. 1991.

178. Tsai, W., J.A.C. Humphrey, I. Cornet, and A.V. Levy, *Experimental measurement of accelerated erosion in a slurry pot tester*. Wear, 1981. **68**(3): p. 289-303.

179. Gandhi, B.K., S.N. Singh, and V. Seshadri, *A study on the effect of surface orientation on erosion wear of flat specimens moving in a solid-liquid suspension*. Wear, 2003. **254**(12): p. 1233-1238.

180. Sudo, K., M. Sumida, and H. Hibara, *Experimental investigation on turbulent flow in a square-sectioned 90-degree bend*. Experiments in Fluids, 2001. **30**(3): p. 246-252.

181. Hsu, S.M., M.C. Shen, and A.W. Ruff, *Wear prediction for metals*. Tribology International, 1997. **30**(5): p. 377-383.

182. Gnanavelu, A., N. Kapur, A. Neville, and J.F. Flores, *An integrated methodology for predicting material wear rates due to erosion*. Wear, 2009. **267**(11): p. 1935-1944.

183. Brown, G.J., *Use of CFD to predict and reduec erosion in an industrial slurry piping system*, in *Fifth International Conference on CFD in the Process Industries*. 2006: CSIRO, Melbourne, Australia.

184. Edwards, J.K., B.S. McLaury, and S.A. Shirazi, *Modeling Solid Particle Erosion in Elbows and Plugged Tees*. Journal of Energy Resources Technology, 2001. **123**(4): p. 277-284.

185. Sato, S., A. Shimizu, and T. Yokomine, *Numerical prediction of erosion for suspension flow duct*. Wear, 1995. **186-187**(Part 1): p. 203-209.

186. Hutchings, I.M., *Prediction of the resistance of metals to erosion by solid particles*. Wear, 1975. **35**(2): p. 371-374.